Alignment of the ATLAS Inner Detector and Single Top studies

Vicente Lacuesta Miquel

Doctoral Thesis under the supervision of

Salvador Martí i García

and

Jose Enrique García Navarro

Doctorado en Física
Valencia, Septiembre 2015

Facultat de Física
Departament de Física Atòmica, Molecular i Nuclear
Universitat de València

VNIVERSITAT DE VALÈNCIA

El **Dr. Salvador Martí i García** y el **Dr. Jose Enrique García Navarro** y, Investigador Científico y Contratado Ramón y Cajal, respectivamente, del CSIC

CERTIFICAN:

Que la presente memoria, "***Alignment of the ATLAS Inner Detector and Single Top studies***", ha sido realizada bajo nuestra dirección en el *Departament de Física Atòmica, Molecular i Nuclear* de la *Universitat de València* por Vicente Lacuesta Miquel y constituye su tesis para optar al grado de doctor en Física por la *Universitat de València*.

Y para que conste, en cumplimiento de la legislación vigente, firmamos el presente Certificado en Burjassot a 24 de Septiembre de 2015.

Dr. Salvador Martí i García

Dr. Jose Enrique García Navarro

Declaration

This dissertation is the results of my own work, except where explicit reference is made to the work of others, and has not been submitted for another qualification to this or any other university.

Vicente Lacuesta Miquel

Contents

Chapter 1

Theoretical motivations

The Standard Model (SM) is the theoretical framework that provides the most accurate description of the interactions among elementary particles to date [1]. During the last decades, its predictions have been confirmed by a high number of accurate experimental measurements, including the existence of the Higgs boson, one of the motivations for the building of the Large Hadron Collider (LHC).

1.1 The Standard Model

1.1.1 The fundamental fermions

According to the SM, all matter is built from a small number of fundamental spin $\frac{1}{2}$ particles called *fermions*: six *quarks* and six *leptons*. For each particle, its symbol and charge Q is given in the Table 1.1.

The three charged leptons are the electron (e), the muon (μ) and tauon (τ), all of them with unit negative charge. The μ and τ are heavy versions of the electron. The muon and tauon are both unstable and they decay spontaneously. The neutral leptons are called neutrinos. Each neutrino is paired with its correspondent charged lepton. The *quarks* carry fractional charges of $+\frac{2}{3}$ or $-\frac{1}{3}$. In the table the quark masses increase

Particle	Flavour			Q/$\lvert e\rvert$
leptons	e	μ	τ	-1
	ν_e	ν_μ	ν_μ	0
quarks	u	c	t	$+\frac{2}{3}$
	d	s	b	$-\frac{1}{3}$

Table 1.1: Chart of fundamental fermions according to the SM.

leptons	Mass (MeV/c^2)	quarks	Mass (MeV/c^2)
e	0.511	u	2.3
ν_e	$< 2 \times 10^{-6}$	d	4.8
μ	105.7	c	1.275
ν_μ	< 0.19	s	95
τ	1.777	t	173.21
ν_μ	< 18.2	b	4.18

Table 1.2: Masses of the leptons and quarks as shown in 2014 PDG[2].

Interaction	Theory	Mediator	Coupling constant	Range (m)
strong	QCD	gluon, g	$\alpha_S = 1$	10^{-15}
electromagnetic	QED	photon, γ	$\alpha = 1/137$	∞
weak	EW	$W^\pm$, Z^0	$\alpha_W = 10^{-1}$	10^{-18}
gravity	GR	graviton, G	$\alpha_g = 6 \times 10^{-39}$	∞

Table 1.3: Fundamental interactions

from left to right as for the leptons. The masses of the fermions are showed in Table 1.2. Like the leptons, the quarks are grouped into pairs differing by one unit of electric charge. The quark type or flavour is denoted by a symbol: u for up, d for down, s for strange, c for charm, b for bottom and t for top. While leptons exist as free particles, quarks appears only in bound states. Quarks have a different charge called *colour* and the quarks appear only forming colour singlets. It is a peculiarity of the strong forces between the quarks that they can be found only in combinations. This phenomenon is called quark confinement. Protons and neutrons consist of three of the lightest u and d quarks: a proton consists of uud and a neutron udd. The common material of the universe is the stable particles, electrons, quarks u and quarks d. The heavier quarks also combine to form particles but much heavier than the proton and neutron. They are unstable and decay rapidly to u and d combinations. Only in very high energy collisions at accelerators or naturally in cosmic rays, the heavy varieties are observed.

1.1.2 The fundamental interactions

The SM also explains the interactions of the particles. The different interactions are explained in terms of the exchange of characteristic bosons (particles of integral spin) between the fermion constituents. These boson mediators are listed in the table Table 1.3.

The four fundamental interactions are:

- Strong interactions are responsible for binding the quarks into protons, neutrons and other hadrons. It is also the responsible of the binding of the neutrons and protons within a nucleus. It is mediated by a massless particle, the gluon.

- Electromagnetic interactions are responsible for almost all the phenomena in extra-nuclear physics, in particular for the bound states of electron with nuclei and for the intermolecular forces. These interactions are mediated by the massless photon (γ) exchange.

- Weak interactions are responsible for both the radioactive decay and nuclear fusion of subatomic particles. The mediators of the weak interactions are the $W^{\pm}$ and Z^0 bosons, with masses almost 100 times the proton mass.

- Gravitational interactions act between all types of particle with mass. This is by far the weakest of all the fundamental interactions, although it is dominant on the scale of the universe. It is supposedly mediated by exchange of a spin 2 boson, the graviton.

1.1.3 The SM

The SM is a gauge quantum field theory based on the symmetry group:

$$SU(3)_C \otimes SU(2)_L \otimes U(1)_Y \tag{1.1}$$

which describes strong, weak and electromagnetic interactions, via the exchange of gauge fields. The colour group $SU(3)_C$ implies 8 gluons. The EW sector $SU(2)_L \otimes U(1)_Y$ is governed by $W^{\pm}$ and Z^0 bosons for the weak interaction and photons for the electromagnetic interaction ass seen in previous section. Matter is built up with three types of particles: leptons and quarks (fermions) and gauge bosons. The fermionic particles are organised in 3 families as seen in Table 1.1 and each family can be classified according to the EW symmetry in the following way:

$$\begin{bmatrix} \nu_l & q_u \\ l^- & q_d \end{bmatrix} \equiv \begin{pmatrix} \nu_l \\ l^- \end{pmatrix}_L , \begin{pmatrix} q_u \\ q_d \end{pmatrix}_L , l^-_R, (q_u)_R, (q_d)_R \tag{1.2}$$

where subindexes R and L refer to the left and right chirality. Quarks appear in 3 different charges called *colours*. All particles have antiparticle partners. The 3 fermionic families have identical properties, differing only in the mass values. The concept of gauge invariance is a necessary piece in the SM and it will be explained in the frame of the simplest model, Quantum Electrodynamics (QED).

1.1.4 Quantum Electrodynamics

Gauge invariance refers to the invariance of the theory under certain transformations for which the theory has internal symmetries. This transformations can be applied in all space-time locations (global) or vary from one point to another (local). The Dirac Lagrangian is a relativistic Lagrangian that describes a fermion with mass m and spin 1/2. In the free-particle form, the Dirac Lagrangian is:

$$\mathcal{L}_0 = i\bar{\psi}(x)\gamma^\mu \partial_\mu \psi(x) - m\bar{\psi}(x)\psi(x) \tag{1.3}$$

where ψ is the wave function of the particle and γ^μ are the Dirac matrices. The first term is the kinematical term and the second one, the mass term. Since the observables depend on $|\psi|^2$, the phase of ψ should be invariant under a local $U(1)$ transformation:

$$\psi(x) \xrightarrow{U(1)} \psi()'(x) \equiv e^{iQ\theta(x)}\psi(x) \tag{1.4}$$

the exponent contains a local phase dependent on the point x. If the transformation is applied to the Lagrangian, new terms appear, so the Lagrangian appears to be not invariant. But the Gauge principle is the requirement that the $U(1)$ phase invariance should hold locally. To make the Lagrangian invariant, it is necessary to introduce a vector gauge field A_μ transforming as:

$$A_\mu(x) \xrightarrow{U(1)} A'_\mu \equiv A_\mu + \frac{1}{e}\partial_\mu\theta \tag{1.5}$$

and a new covariant derivate:

$$D_\mu\psi(x) = [\partial_\mu - ieQA_\mu]\psi(x) \tag{1.6}$$

This new derivative has the correct behaviour under the $U(1)$ transformation. Then the Lagrangian can be defined by replacing the partial derivative in equation 1.3 by the covariant derivative:

$$\mathcal{L} = \mathcal{L}_0 + eQA_\mu(x)\bar{\psi}(x)\gamma^\mu\psi(x) \tag{1.7}$$

The resulting Lagrangian is invariant under $U(1)$ local transformations. Now there is an additional term describing an interaction between the fermion ψ and the gauge field A_μ. The requirement of a $U(1)$ invariance has lead to the introduction of this new interaction. The interaction is mediated by the vector particle A_μ and the strength is proportional to the charge eQ. Since there is not term proportional to $A^\mu A_\mu$, the intermediate particle is massless. The new interaction is the electromagnetic force, which is mediated by photon and the value eQ is the electromagnetic charge. It is necessary to add the gauge invariant kinetic term of the field A_μ

$$\mathcal{L}_{\text{Kin}} = -\frac{1}{4}F^{\mu\nu}_{\mu\nu} \text{ with } F_{\mu\nu} \equiv \partial_\mu A_\nu - \partial_\nu A_\mu \tag{1.8}$$

Finally, the total Lagrangian is the Lagrangian of Quantum Electrodynamics:

$$\mathcal{L} = i\bar{\psi}(x)\gamma^\mu\partial_\mu\psi(x) - m\bar{\psi}(x)\psi(x) + eQA_\mu(x)\bar{\psi}(x)\gamma^\mu\psi(x) - \frac{1}{4}F^{\mu\nu}_{\mu\nu} \tag{1.9}$$

1.1.5 EW interactions

The weak interaction is mediated by the massive gauge bosons $W^\pm$ and Z. The simplest gauge theory is based on the $SU(2)$ group. As the particles with electric charge also have weak interactions, the next logical step is to unify the weak and electromagnetic forces. The group $U(1)$ is needed, so the electroweak interaction is obtained with the symmetry group $SU(2)_L \otimes U(1)_Y$. L refers to left-handed fields and Y to *weak hyper-charge*. The free Lagrangian is defined:

$$\mathcal{L} = \sum_{j=1}^{3} i\bar{\psi}_j(x)\gamma^\mu\partial_\mu\psi_j(x) \tag{1.10}$$

The Lagrangian should be invariant under the local transformations $SU(2)_L \otimes U(1)_Y$, and this implies four different gauge fields. These gauge fields correspond to the gauge bosons needed to describe electroweak interactions. The electroweak covariant derivate is defined as:

$$D_\mu \psi_j \equiv \left[\partial_\mu - ig\frac{\vec{\sigma}}{2}\vec{W}\mu - ig'\frac{y_j}{2}B_\mu \right] \psi_j(x) \tag{1.11}$$

The gauge fields $\vec{W}$ (3D vector) and B (scalar) can be identified with the $W^\pm$, Z, and γ bosons. The $\vec{\sigma}$ matrices are the Pauli matrices, generators of the $SU(2)$ group, g and g' are the interaction couplings and y_i the weak hyper-charge values. Finally the electroweak SM Lagrangian can be written is compact form as:

$$\mathcal{L}_{\mathrm{EW}} = \sum_{j=1}^{3} i\bar{\psi}_j(x)\gamma^\mu D_\mu \psi_j(x) - \left(\frac{1}{4}B_{\mu,\nu}B^{\mu\nu} + \frac{1}{4}\vec{W}_{\mu\nu}\vec{W}^{\mu\nu} \right) \tag{1.12}$$

where

$$B_{\mu\nu} \equiv D_\mu B_\nu - D_\nu B_\mu, \qquad \vec{W}_{\mu\nu} \equiv D_\mu \vec{W}_\nu - D_\nu \vec{W}_\mu + g\vec{W}_\mu \times \vec{W}_\nu \tag{1.13}$$

This Lagrangian describes electroweak interactions between gauge bosons and fermions. It can be divided in two different parts corresponding to the interactions of gauge bosons with fermions: charged currents and neutral currents. Using terms of the Lagrangian connected with a charged interaction, the $W^\pm$ bosons can be identified as a combination of the charged $\vec{W}$ components:

$$W_\mu^\pm \equiv \frac{1}{\sqrt{2}}(W_\mu^1 \mp iW_\mu^2) \tag{1.14}$$

Using the neutral gauge fields W_μ^3 and B_μ it is possible to construct the Z and γ bosons, but as long as both fields are massless, any arbitrary combination of them is allowed. The adopted parametrisation is:

$$\begin{pmatrix} W_\mu^3 \\ B_\mu \end{pmatrix} \equiv \begin{pmatrix} \cos\theta_W & \sin\theta_W \\ -sin\theta & \cos\theta_W \end{pmatrix} \begin{pmatrix} Z_\mu \\ A_\mu \end{pmatrix} \tag{1.15}$$

The relation between fields is a rotation of angle θ_W, known as the Weinberg angle. In order to recover QED from the $\mathcal{L}_{\mathrm{EW}}$, the following requirements are necessary:

$$g\sin\theta_W = g'\cos\theta_W = e \qquad Q = T_3 + \frac{Y}{2} \tag{1.16}$$

where T_3 is the third component of the weak isospin. In this way, the electromagnetic and electroweak couplings are connected. An additional quantum number Y or weak hyper-charge appears as the combination of weak isospin and electric charge. The table Table 1.4 shows the values of the different electroweak quantum numbers for fermions.

There are no mass terms present in the Lagrangian, so all particles in the theory as it stands are massless. Since most fermions and bosons are experimentally observed to have mass, this is a serious problem in $\mathcal{L}_{\mathrm{EW}}$. A satisfactory SM theory must include an alternative mechanism to generate the particle masses.

leptons	T	T_3	Q	Y	quarks	T	T_3	Q	Y
ν_e	1/2	1/2	0	-1	u_L	1/2	1/2	2/3	1/3
e_L^-	1/2	-1/2	-1	-1	d_L	1/2	-1/2	-1/3	1/3
e_R^-	0	0	-1	-2	u_R	0	0	2/3	4/3
					d_R	0	0	-1/3	-2/3

Table 1.4: Electroweak quantum numbers for leptons and quarks

1.1.6 Spontaneous Symmetry Breaking

The idea of Spontaneous Symmetry Breaking (SSB) is to introduce a scalar field to give mass to fermions and gauge bosons. Let consider the simplest case of a complex scalar field $\phi(x)$. A potential term $V(\phi)$ is added to the Lagrangian of a free particle. The potential is chosen to preserve the invariance under the transformation $\phi(x) \to \phi(x) \equiv e^{i\theta}\phi(x)$. The resulting Lagrangian is:

$$\mathcal{L} = \partial_\mu \phi^\dagger \partial^\mu \phi - V(\phi) \quad V(\phi) = \mu^2 \phi^\dagger \phi + \lambda(\phi^\dagger \phi)^2 \tag{1.17}$$

where λ and μ are arbitrary couplings. In order to get a non-trivial solution, the parameters should be $\lambda > 0$ and $\mu^2 < 0$. With this choice, the potential $V(\phi)$ has a minimum at $\phi_0 = \frac{v}{\sqrt{2}} e^{\imath\theta}$ with $v = \sqrt{-\mu^2/\lambda}$. Selecting a particular solution as $\theta = 0$ as the ground state, the symmetry gets spontaneously broken. Parametrising the excitations above the ground state as:

$$\phi(x) \equiv \frac{1}{\sqrt{2}}[v + \phi_1(x) + \phi_2(x)] \tag{1.18}$$

where ϕ_1 and ϕ_2 are real fields, the potential becomes

$$V(\phi) = V(\phi_0) - \mu^2\phi_1^2 + \lambda v \phi_1(\phi_1^2 + \phi_2^2) + \frac{\lambda}{4}(\phi_1^2 + \phi_2^2)^2 \tag{1.19}$$

Here, ϕ_1 describes a massive state with mass $m_{\phi_1}^2 = -2\mu^2$, but ϕ_2 is massless. The fact that there are massless excitations associated with the SSB mechanism is a general result known as the Goldstone theorem[3]: *if a Lagrangian is invariant under a continuous symmetry group G, but the vacuum, is only invariant under a subgroup, there must exist as many spin-0 particles as broken generators.* But another consequence of the SSB is that some massless fields become massive, like the ϕ_1 field in the previous case. The SSB mechanism in the SM can be implemented using scalar field multiplets of the $SU(2)_L \otimes U(1)_Y$ group. The simplest case is a $SU(2)_L$ doublet of scalar fields ϕ:

$$\phi = \begin{pmatrix} \phi^+ \\ \phi^0 \end{pmatrix} \tag{1.20}$$

where the fields can be written as:

$$\phi^+ = \frac{1}{\sqrt{2}}(\phi_0 + i\phi_1) \quad \phi^0 = \frac{1}{\sqrt{2}}(\phi_0 + i\phi_2) \tag{1.21}$$

The part of the Lagrangian containing ϕ and its interactions,

$$\mathcal{L}_{\rm SB} = (D_\mu\phi)^\dagger D^\mu\phi - \mu^2\phi^\dagger\phi - \lambda(\phi^\dagger\phi)^2 \quad \mu^2 < 0 \text{ and } \lambda > 0 \tag{1.22}$$

is invariant under local $SU(2)_L \otimes U(1)_Y$ transformations by coupling the field ϕ to the vector bosons through the covariant derivative D_μ:

$$D_\mu \equiv \partial_\mu - ig_w\frac{\sigma^i}{2}W_\mu^i - ig'_w Y_\phi B_\mu \tag{1.23}$$

where g_w and g'_w are respectively the $SU(2)_L$ and $U(1)_Y$ gauge couplings, σ^i, the Pauli matrices and $Y_\phi = 1/2$ the scalar hyper-charge. There is an infinite number of configurations each with the same minimal potential energy. By choosing a particular ground state among the infinite number of degenerate states, the symmetry gets spontaneously broken:

$$| < 0|\phi|0 >= \begin{pmatrix} 0 \\ \frac{v}{\sqrt{2}} \end{pmatrix} \tag{1.24}$$

where $v = \sqrt{\frac{-\mu^2}{\lambda}}$. The choice of the vacuum expectation breaks spontaneously the electro weak symmetry to the electromagnetic subgroup $U(1)_{\rm QED}$ where it preserves the vacuum. The three generators of the $SU(2)_L \otimes U(1)_Y$ broken symmetry give rise to three massless Goldstone bosons, providing extra longitudinal degrees of freedom to the weak gauge bosons, Z and $W^\pm$, which have acquired mass:

$$M_W = M_Z \cos\theta_w = \frac{1}{2}vg_w \tag{1.25}$$

where the angle θ_w (the Weinberg angle or electroweak mixing angle) is fixed by the relative strengths of the coupling constants. The remnant scalar boson, the Higgs boson, has a mass $M_H = \sqrt{-2\mu^2} = \sqrt{2\lambda}v$. One combination of the parameters of the Higgs potential $\mu^2/\lambda = v^2 = 2G_F^2 \approx (246 \text{ GeV})^2$ is fixed by the measured parameters of the electroweak theory. The other parameter is arbitrary, thus M_H remains a free parameter in the SM. The Higgs mechanism generates also masses to leptons and quarks according to $m_f = g_f v/\sqrt{2}$, g_f is the coupling of the fermion and the Higgs particle. And this proportionality makes that the coupling strength to the Higgs field increases with the mass of the fermion.

1.1.7 Quantum Chromodynamics

The quarks carry a strong interacting charge that can take 3 values. This charge is known as *color*. Since this property is not seen in nature, the colours of the quarks must be combined such that they produce colourless hadrons. The hadrons are gauge singlets representations of the colour group $SU(3)_C$. The theory derived from the $SU(3)_C$ group is called Quantum Chromodynamics (QCD) which is the gauge theory for the strong interactions and has provided many successful predictions so far. The local colour transformations leave the Lagrangian invariant. The QCD Lagrangian is:

$$\mathcal{L}_{\rm QCD} = \sum_f \bar{q}_f(i\gamma^\mu D_\mu - m_f)q_f - \frac{1}{2}T_r(G^{\mu\nu}G_{\mu\nu}) \tag{1.26}$$

where q_f are the fermions and f the colour index. D_μ and $G_{\mu\nu}$ are matrices defined as:

$$D_\mu = \delta_\mu + ig_S G_\mu \qquad \text{and} \qquad G_{\mu\nu} = \delta_\mu G_\nu - \delta_\nu G_\mu + ig_S[G_\mu, G_\nu] \tag{1.27}$$

with $G_\mu = \sum_f G_\mu^f \lambda_f/2$ being λ_f the 8 Gell-Mann (3×3) matrices. The gluons are the gauge bosons associated to this symmetry. There are eight gluons corresponding to the number of generators of $SU(3)_C$. Gluons are the massless mediators of the strong interactions. There is a distinct feature with respect to the photons, while the later do not carry electric charge, the gluons do carry colour charge. Therefore gluons can interact themselves. The interaction strength is governed by the coupling constant g_S or equivalently $\alpha_S = g_S^2/(4\pi)$.

1.1.8 Standard Model measurements in the LHC experiments

The LHC program is quite precisely defined, mainly based on proton-proton collisions but also with short periods of heavy-ions collisions. Many LHC physic studies emphasise discoveries and validation of new theories, there are a lot of measurements of the SM predictions.

Figure 1.1 shows the measured and predicted production cross-sections for individual SM processes in ATLAS detector at 7 and 8 TeVcollision energy.

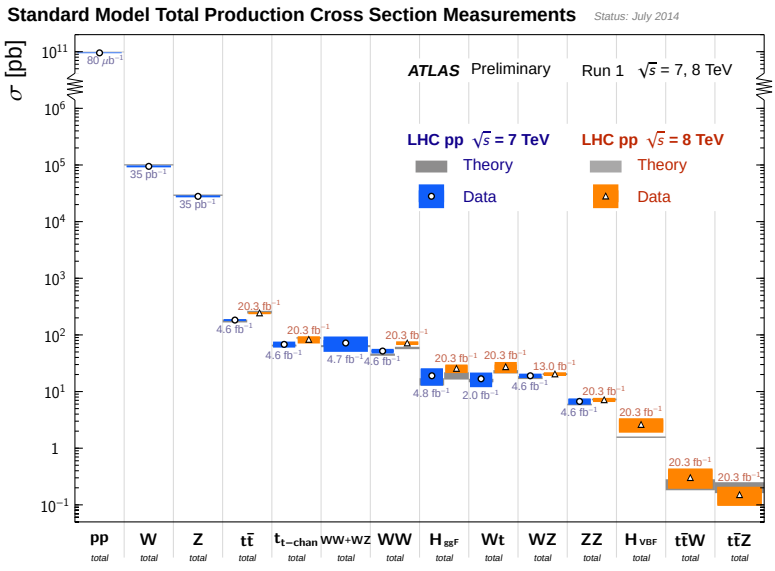

Figure 1.1: Summary of several Standard Model total and fiducial production cross section measurements, corrected for leptonic branching fractions, compared to the corresponding theoretical expectations. All theoretical expectations were calculated at NLO or higher.

On July 4th 2012, a new particle compatible with the SM Higgs with a mass of 125 GeV was discovered [4, 5], being confirmed after as the Higgs boson. Figure 1.2 shows the combined search results with the observed limits in the signal strength, the local p0 and the best-fit signal strength as function of the Higgs mass.

1.2 Beyond the Standard Model

1.2.1 Problems of SM

Although the SM is the most precisely tested theory, everything cannot be explained through the SM. The Large Electron Positron (LEP) the Standford Linear Collider (SLC) and Tevatron have established that the physic is understood up to energies of 200 GeV. Now, the physics should be understood at the LHC energies (TeVscale) and try to understand the nature of the SM problems. The most important problems are:

- The SM does not unify the strong and EW forces. The success of the EW model opened the possibility that the strong interactions might also be included in a unifying scheme. The basic idea is that the $SU(2) \times U(1)$ electroweak symmetry and the $SU(3)$ colour symmetry of the strong interactions might be encompassed by a more global symmetry at some high unification energy, well above the electroweak scale, called Grand Unification Theory (GUT) scale.

- Another problem is the hierarchy problem which is the huge gap between two fundamental scales of physics: the EW scale ($\sim 10^2$ GeV) and the Planck scale ($\sim 10^{19}$ GeV) where the gravity becomes important. More technically, the question is why the Higgs boson is so much lighter than the Planck mass, one would expect that the large quantum contributions to the square of the Higgs boson mass would make the mass huge, unless there is an incredible fine tuning cancellation between the radiative corrections and the bare mass. One proposed solution is that one may solve the hierarchy problem via Super Symmetry (SUSY) (1.2.2). SUSY can explain how a low mass Higgs can be protected from large quantum corrections.

- The neutrinos are supposed to be massless and to exist in only one helicity state: $\nu = \nu_{\mathrm{L}}$, while $\bar{\nu} = \bar{\nu}_{\mathrm{R}}$. There is still a question about the nature of the neutrinos. The Dirac description treats the neutrinos as 1/2 spin particles with one of the two spin substates missing. The Majorana description supposes that the neutrino is it own antiparticle, so that $\nu \equiv \bar{\nu}$. So there is only one spin 1/2 particle with two substates ν_{L} and ν_{R}. The difference in behaviour of ν and $\bar{\nu}$ is then merely a consequence of the different helicities in the two cases.

- Gravity is not included in the SM, while a 'theory of everything' should contain that also. Attempts to incorporate gravity with the other fundamental interactions are the so-called supergravity theories.

- Cosmological observations tell us the SM explains about the 4% of the energy present in the universe. Of the missing 96%, about 27% should be dark matter, which should behave just like ordinary matter but only interacting weakly with

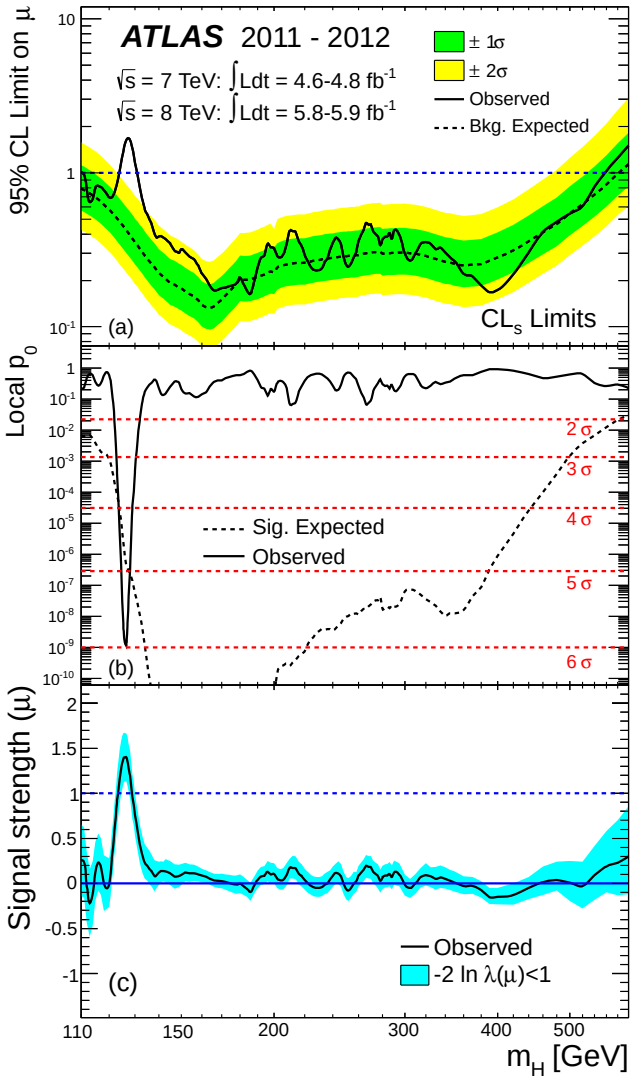

Figure 1.2: Combined search results: (a) The observed (solid) 95% CL limits on the signal strength as a function of m_H and the expectation (dashed) under the background-only hypothesis. The dark and light shaded bands show the $\pm 1\sigma$ and $\pm 2\sigma$ uncertainties on the background-only expectation. (b) The observed (solid) local p_0 as a function of m_H and the expectation (dashed) for a SM Higgs boson signal hypothesis ($\mu = 1$) at the given mass. (c) The best-fit signal strength as a function of m_H. The band indicates the approximate 68% CL interval around the fitted value.

the standard model fields. Also, the SM does not supply any fundamental particle that are good dark matter candidates.

- The SM predicts that matter and antimatter should have been created in equal amounts. But today everything is made almost entirely of matter.

All of these problems need new theories which should solve them. Actually, these theories are being subject of extensive searches and studies at the LHC experiments. The most promising theory beyond the SM is SUSY

1.2.2 SUSY

SUSY is a proposed type of space-symmetry that relates the bosons and fermions. Each particle from one group is associated with particle from the other, called super-partner, whose spin differs by a half-integer. In a theory with perfectly unbroken supersymmetry, each pair of super-partners shares the same mass and internal quantum number besides spin. However, since no super-partners have been observed yet, supersymmetry must be a spontaneously broken symmetry if it exists. If supersymmetry is a true symmetry of nature, it will explain many mysterious features of particle physics and would help solve paradoxes such as the cosmological constant problem. A central motivation for supersymmetry close to the TeV energy scale is the resolution of the hierarchy problem of the SM. Other features of TeV-scale supersymmetry are the fact that it provides a candidate dark matter particle, provides a natural mechanism for electroweak symmetry breaking and allows for the high-energy unification of the weak, the strong and electromagnetic interactions. Until now, no meaningful signs of the super-partners have been observed.

1.3 Single Top

One of the objective of this thesis is the study of the single top physics. The theoretical framework for the chapter 5 will be summarised in this section and all the details are in Ref. [6].

At hadron colliders, top quarks are produced mainly in pairs via the flavour-conserving strong interaction. Alternative production modes proceed via the weak interaction involving a Wtb vertex, leading to a single top quark in intermediate state before hadronisation. The single top quark production can be described by three different processes:

- The exchange of a virtual W boson in the t-channel (Figure 6.1a with 2 particles to 2 and Figure 6.1b with 2 particles to 3).
- The exchange of a virtual W boson in the s-channel (Figure 6.1c).
- The production of a top quark in association with an on-shell W boson in the Wt-channel. (Figure 6.1d).

At the LHC, colliding protons at $\sqrt{s} = 7$ TeV, the production cross-sections for the single top processes are calculated at next-to-leading order (NLO) QCD with resumed next-to-next-to-leading logarithmic (NNLL) accuracy, called approximate next-to-next-to-leading order (NNLO) in the following. They are found to be:

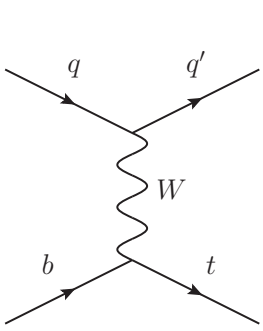

(a) Single top t-channel (2 to 2)

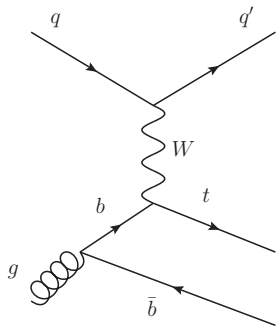

(b) Single top t-channel (2 to 3)

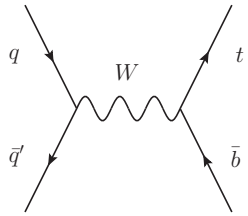

(c) Single top s-channel

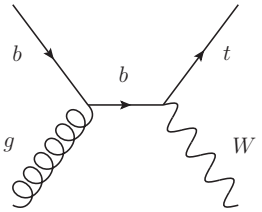

(d) Single top Wt channel

Figure 1.3: Feynman diagrams single top quark production.

- $64.6^{+2.7}_{-2.0}$ pb [7] for the t-channel
- $4.63^{+0.19}_{-0.17}$ pb [8] for the s-channel.
- 15.7±1.1 pb [9] for the Wt-channel

As the heaviest known elementary particle and due to its short lifetime (about 20 times shorter than the timescale for strong interactions) the top quark decays before hadronising and in the SM it decays almost exclusively to a W boson and a b-quark. Probing the couplings of the Wtb vertex offers an interesting window to new physics. This way single top quark events provide a direct probe of these couplings.

In the most general effective operator framework the Wtb vertex can be written as [10, 11]:

$$\mathcal{L}_{Wtb} = -\frac{g}{\sqrt{2}}\bar{b}\gamma^{\mu}(V_L P_L + V_R P_R)tW^{-}_{\mu} - \frac{g}{\sqrt{2}}\bar{b}\frac{i\sigma^{\mu\nu}q_{\nu}}{M_W}(g_L P_L + g_R P_R)tW^{-}_{\mu} + \text{h.c} \quad (1.28)$$

In this formula, g is the weak coupling constant, m_W is the mass and q_ν the four momentum of the W boson. $P_{LR} \equiv (1 \mp \gamma^5)/2$ are the left and right-handed projection operators and $\sigma^{\mu\nu} = [\gamma^{\mu}, \gamma^{\nu}]/2$. $V_{\mathrm{L,R}}$ and $g_{\mathrm{L,R}}$ are the left and right-handed vector and tensor couplings.

In the SM at tree level, the coupling V_{L} is close to one and is identical to V_{tb} which is one of the quark-mixing elements in the Cabibbo–Kobayashi–Maskawa (CKM) matrix [2], while the anomalous couplings V_{R} and $g_{\mathrm{L,R}}$ are all zero. Deviations from these values can be probed by measuring W polarisation fractions or angular asymmetries in the decay products of the top quark decay. Angular asymmetries are defined as:

$$A_z \equiv \frac{N_{\mathrm{evt}}(\cos\theta > z) - N_{\mathrm{evt}}(\cos\theta < z)}{N_{\mathrm{evt}}(\cos\theta > z) + N_{\mathrm{evt}}(\cos\theta < z)} \ , \quad (1.29)$$

where z is an arbitrary but fixed point in the angular distribution (within -1 and 1), θ is a decay angle and N_{evt} is the number of events where $\cos\theta$ is below (or above) z. For the choice of $z = 0$ the asymmetry is called the forward-backward asymmetry (A_{FB}). In top quark decays θ is defined as the angle between the direction of the lepton from the W decay, in the W boson rest frame, and a certain reference direction. For unpolarised top quark production [12] the only meaningful reference direction is the momentum $\vec{q}$ of the W boson (or $-\vec{q}$ of the b-quark) in the top quark rest frame (helicity basis) and the corresponding angle is called θ^* as shown in Figure 1.4.

ATLAS has set limits on the Wtb couplings in top quark pair ($t\bar{t}$) events [13] using the angle θ^*. However, asymmetries (or helicity fractions) derived with θ^* are not sensitive to all anomalous couplings, especially to their complex phases that would imply that the top quark decay has a $\mathcal{CP}$-violating component.

In the single top quark t-channel, the top quarks are expected to be produced highly polarised along the direction of the spectator quark with a predicted degree of polarisation of $P \approx 0.9$ at $\sqrt{s} = 7$ TeV as shown in Ref. [14, 15]. With this direction of polarisation ($\vec{s}_t$) two new reference directions can be defined in the helicity basis:

$$\vec{N} = \vec{s}_t \times \vec{q} \ , \quad (1.30)$$

$$\vec{T} = \vec{q} \times \vec{N} \ , \quad (1.31)$$

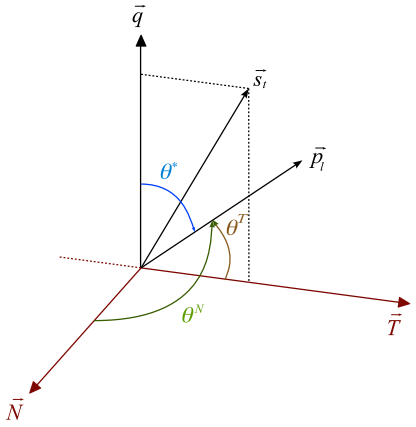

Figure 1.4: Definition of the two directions $\vec{N}$ and $\vec{T}$ given the direction of polarisation of the top quark, $\vec{s}_t$, and the momentum of the W boson, $\vec{q}$ in the helicity basis. The angles which are shown are defined as the angles between their reference directions and the momentum direction of the charged lepton, $\vec{p}_l$.

where $\vec{N}$ is the normal and $\vec{T}$ the transverse direction (see Figure 1.4), $\vec{s}_t$ is the spin direction (direction of the spectator quark in the top quark rest frame) and $\vec{q}$ is the W boson momentum in the top quark rest frame (helicity basis). In a similar way to θ^*, the angles θ^{N} or θ^{T} are defined between the lepton in the W boson rest frame and the new directions $\vec{N}$ or $\vec{T}$, respectively. In order to measure these angular distributions, the top quark and W boson need to be fully reconstructed since boosts to their rest frames are performed.

It is shown in Ref. [6] that the forward-backward asymmetry in the trasnversal direction, $A_{\mathrm{FB}}^{\mathrm{T}}$, is sensitive to the real part of the anomalous coupling g_{R}. After several calculations the asymmetry is given by the equation:

$$A_{\mathrm{FB}}^{\mathrm{T}} = \frac{1.98P\mathbb{R}(g_{\mathrm{R}})^2 - 5.19P\mathbb{R}(g_{\mathrm{R}})V_L + 1.99PV_L^2}{8.03\mathbb{R}(g_{\mathrm{R}})^2 - 10.11\mathbb{R}(g_{\mathrm{R}})V_L + 5.19V_L^2} \tag{1.32}$$

For small values of g_{R} and taking $V_{\mathrm{L}} = 1$ and $V_{\mathrm{R}} = g_{\mathrm{L}} = 0$, the relation can be approximated to:

$$A_{\mathrm{FB}}^{\mathrm{T}} \approx 0.38P - 0.26 * P\mathbb{R}(g_{\mathrm{R}}) \tag{1.33}$$

In the chapter 5 the measurement of the forward-backward asymmetry $A_{\mathrm{FB}}^{\mathrm{T}}$ and the real part of the anomalous coupling g_{R} will be presented.

Chapter 2

CERN, LHC and the experiments

2.1 CERN

The European Organization for Nuclear Research (CERN) is the biggest scientific laboratory in the world. Located in the border between France and Switzerland (Figure 2.1), CERN was funded in 1954 to study the atomic nucleus. Later its goal was redirected towards High Energy Physics, reaching several scientific achievements as the discovery of the W and Z bosons or the most recent discover of the Higgs boson. There are several different experiments based at CERN, like Isotope mass Separator On-Line facility (ISOLDE), neutron time-of-flight facility (nTOF), Common Muon and Proton Apparatus for Structure and Spectroscopy (COMPASS), Antihydrogen Laser Physics Apparatus (ALPHA) or the biggest particle accelerator in the world, the Large Hadron Collider (LHC).

2.2 LHC

The LHC[16] is the world largest and most powerful particle accelerator. The LHC consists of a 27 kilometre ring of superconducting magnets and Radio frequency (RF) cavities that accelerates two beams in opposite directions and collides them in four different points of the circumference. The idea of LHC began in the early 1980s. Although the LEP was not built yet, scientists already were looking further into the future of particle physics. Scientists imagined a machine using the existing 27 kilometre Large Electron Positron (LEP)[17] ring for an even more powerful machine. To reach highest energies and intensities, it was proposed to use two beams of protons. The project was approved in December 1994. In 2005 the first of the 1232 superconducting dipole magnets was lowered into the LHC tunnel. The last of the magnets was installed in May 2007. Finally, the beams were circulated on 10 September 2008 for the first time.

The main goal of the LHC is to allow to test the predictions of different theories of particle physics and High Energy Physics and particularly prove the existence of the

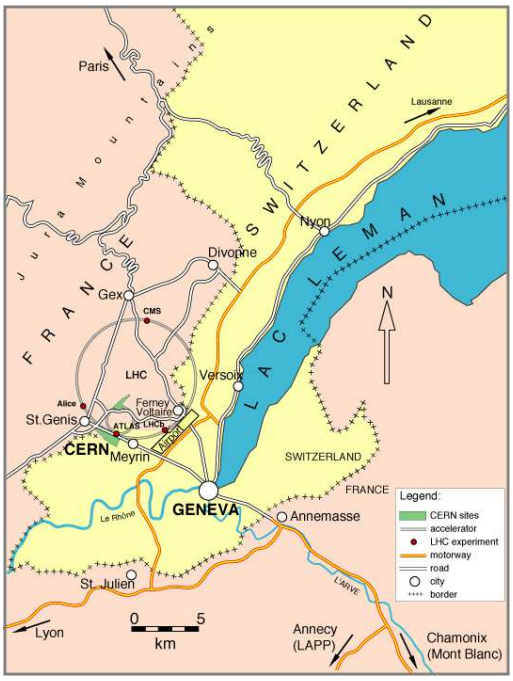

Figure 2.1: CERN location map in the border between France and Switzerland

Higgs boson or new physic phenomena beyond the SM. The SM has been tested by several experiments but it leaves many unsolved questions, which the LHC is helping to solve.

In the LHC, the particles circulate in a vacuum tube and are manipulated using electromagnetic devices: dipole magnets to keep the particles in the orbits, quadrupole magnets to focus the beam and accelerating cavities with alternating electric fields to accelerate the particles.

The LHC is made of 8 arcs and 8 insertions. Each arc contains 154 dipoles magnets that are able to bend the particle trajectories. Each insertion consists in a straight section plus two transition sections. The layout of the straight section depends on the specific use: collisions, injection, beam dumping, etc. There are in total 1232 dipole magnets in the LHC. The dipole magnets are superconducting electromagnets able to provide a high field of 8.3 T over their length. To create this high magnetic field, a current of 11850 A is needed in the dipoles. The LHC dipoles use niobium-titanium (NbTi) cables, which become superconducting below a temperature of 10 K. Currently, the LHC is operating at 1.9 K, which is even lower than the temperature of outer space (2.7 K). Fluid helium is needed to achieve this low temperatures. The dipoles have a weight around 35 tons and a length of 15 meters. A diagram of one dipole is shown in the Figure 2.2. The insertion quadrupoles are special magnets used to focus the beam down to the smallest possible size at the collision points.

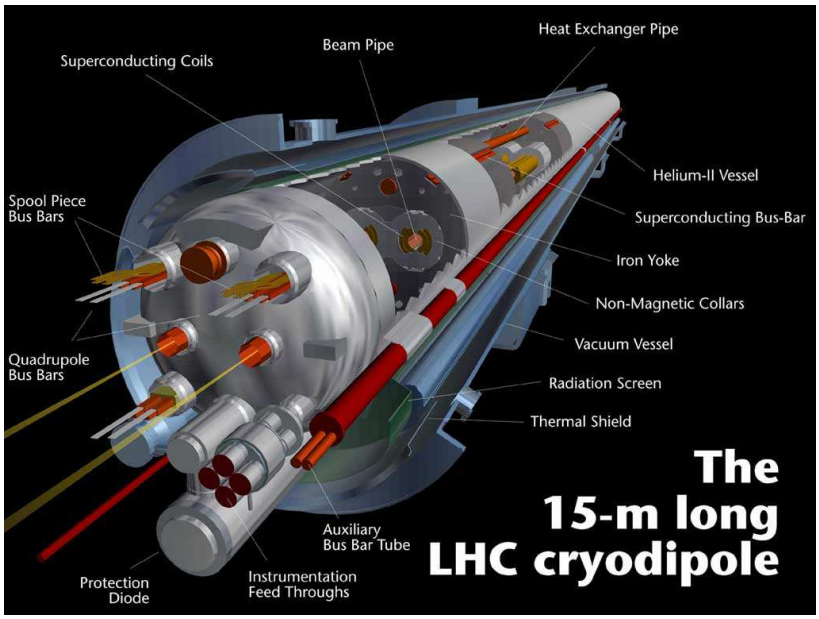

Figure 2.2: Diagram of one of 1232 dipoles used in the LHC.

The main role of the LHC cavities is to keep the 2808 proton bunches tightly packed to ensure high luminosity. They also deliver RF power to the beam during acceleration to the working energy. The LHC has eight cavities per beam, each delivering 2 MV at 400 MHz. This cavities operate at a temperature of 4.5 K.

The protons of the LHC circulate around the ring in well defined bunches. In the LHC each proton beam has 2808 bunches, with each bunch containing about 10^{11} protons. Bunches of particles measure a few centimetres long and a millimetre wide when they are far from a collision point. However, as they approach the collision points, they are squeezed to about 16 μm to allow for a greater chance of proton-proton collisions. Increasing the number of bunches is one of the ways to increase the luminosity of the LHC. Bunches crosses on average about 30 million times per second, so the LHC generates up to 600 million particle collision per second.

The most important parameters of the LHC are summarised in the table 2.1.

2.2.1 CERN accelerator complex

The accelerator complex at CERN (Figure 2.3) is a chain of machines that accelerate particles to higher and higher energies. Each machine boosts the energy of a beam of particles and then injects the beam into the next one. The LHC is the last element in this chain where the particles can be accelerated nominally up to 7 TeV. Most of the other accelerators in the chain have experimental halls where the beams are used for other experiments at lower energies. The proton source is a simple bottle of hydrogen

Quantity	**number**
Circumference	26659 m
Dipole Operating Temperature	1.9 K
Number of magnets	9593
Number of main dipoles	1232
Number of main quadrupoles	392
Number of RF cavities	8 per beam
Nominal energy, protons	7 TeV per beam
Nominal energy, ions	2.76 TeV/u
Peak magnetic dipole field	8.33 T
Min. distance between bunches	7 m
Design luminosity	$10^{34}\text{cm}^{-2}\text{s}^{-1}$
No. of bunches per proton beam	2808
No. of protons per bunch (at start)	1.1×10^{11}
Number of turns per second	11245
Number of collisions per second	600 million

Table 2.1: Main parameters of LHC collider.

gas. An electric field strips the atoms of their electrons to yield protons. Linac 2 is the first accelerator in the chain and accelerates the protons up to 50 MeV. The beam is then injected into the Proton Synchrotron Booster (PSB) which accelerates the protons to the energy of 1.4 GeV, followed by the Proton Synchrotron (PS) up to 25 GeV. The beam is accelerated to 450 GeV in the Super Proton Synchrotron (SPS). Finally the beams are transferred to the two beam pipes of the LHC. It takes 4 minutes and 20 seconds to fill each LHC ring and 20 minutes for the protons to reach the energy of 4 TeV. The beams can circulate for many hours inside the LHC beam-pipes. The two beams are brought into collision inside four detectors where the total energy at the collision point is equal to 8 TeV (as in 2012).

The accelerator complex includes the Antiproton decelerator (AD) and ISOLDE facility and feeds the CERN Neutrinos to Gran Sasso (CNGS) project and the Compact Linear Collider (CLIC) test area, as well as the nTOF. Lead ions can be also accelerated in the LHC. A source of vaporised lead is accelerated in the Linac 3 before being collected and accelerated in the Low Energy Ion Ring (LEIR). They then follow the same route as the protons.

2.2.2 LHC experiments

There are 7 experiments installed at LHC:

- A Large Ion Collider Experiment (ALICE)
- ATLAS
- Compact Muon Solenoid (CMS)

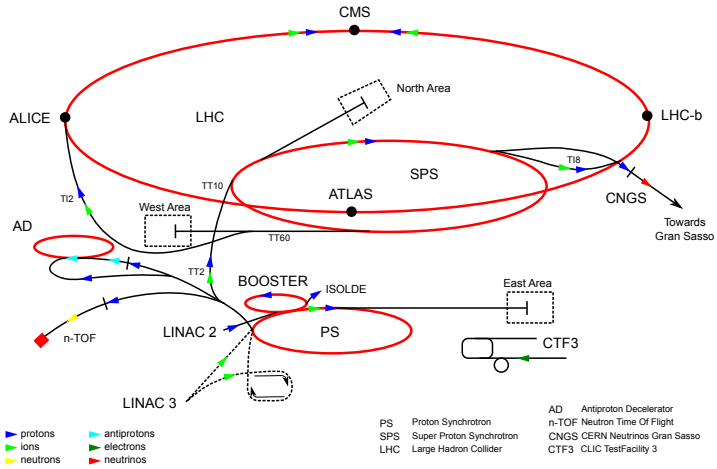

Figure 2.3: Diagram of the CERN accelerator complex

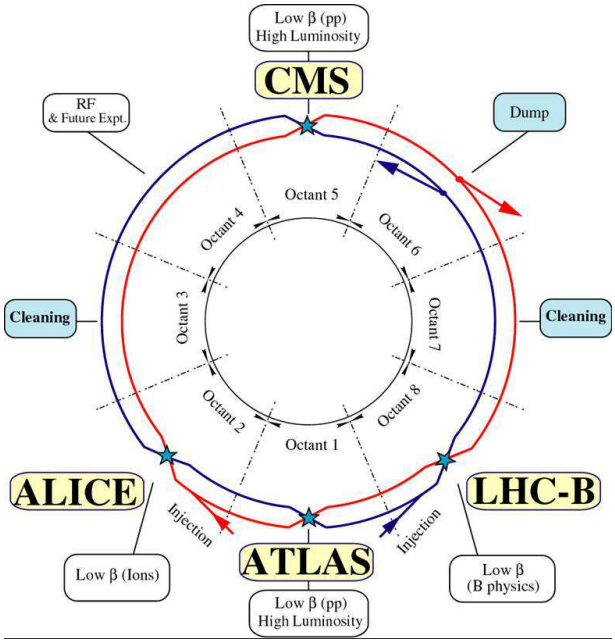

Figure 2.4: Schematic overview showing the four main experiments and the two ring structure of the LHC

- Large Hadron Collider beauty experiment (LHCb)
- Large Hadron Collider forward experiment (LHCf)

- TOTal Elastic and diffractive cross Section Measurement (TOTEM)
- Monopole and Exotics Detector at the LHC (MoEDAL)

The biggest experiments are ALICE, ATLAS, CMS and LHCb (Figure 2.5). They are placed in four huge underground caves built around the four collision points of the LHC beams as shown in the figure 2.4.

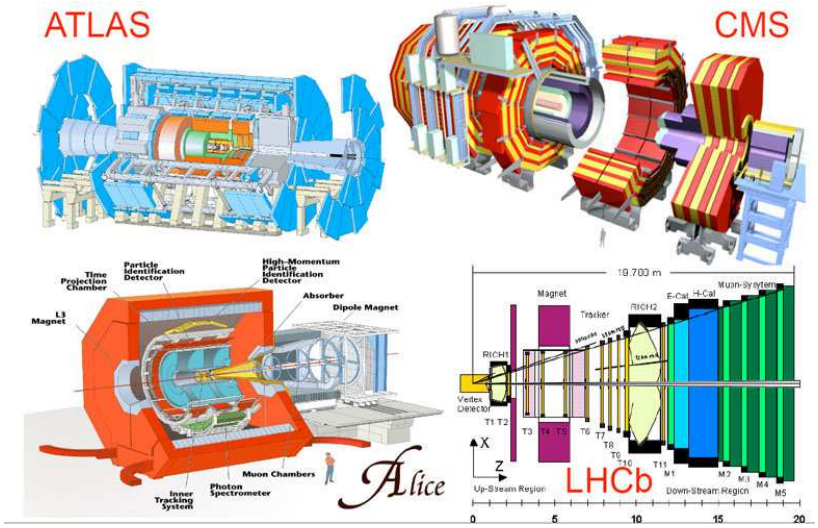

Figure 2.5: Schematics of the detectors of the main physics experiments at the LHC.

2.2.2.1 ALICE experiment

ALICE is a heavy-ion experiment [18]. It is designed to study the physics of strongly interacting matter at high energy densities, where a phase of matter called quark-gluon plasma forms. Collisions in LHC generate temperatures up to 1.6×10^{12} K. For part of each year the LHC provides collision between lead ions, recreating in the collisions the conditions similar to those just after the big bang. Under these extreme conditions, protons and neutrons free the quarks from their bonds with the gluons creating quark-gluon plasma. The existence of such a phase and its properties are key issues in the theory of QCD, for understanding the phenomenon of confinement, and for a problem called quiral-symmetry restoration [19]. The ALICE collaboration studies the quark-gluon plasma as it expands and cools, observing how it progressively gives rise to the particles that constitute the matter of our universe as it is known today.

The ALICE detector has a weight of 10,000 tonnes, a length of 26 m, a height of 16 and a width of 16 m. The detector is placed in a cavern 56 m below ground.

2.2.2.2 ATLAS experiment

The ATLAS is a general-purpose detector [20]. The experiment is designed to take advantage of the unprecedented energy available at the LHC and observe phenomena that involve highly massive particles which were not observable using earlier lower-energy accelerators. It might shed light on new theories of particle physics beyond the Standard Model. As this thesis has been performed within the ATLAS experiment, it will be explained with more detail in section 2.3.

2.2.2.3 CMS experiment

The CMS is the other general-purpose detector [21]. It is designed to investigate a wide range of physics, including the search of the Higgs boson, extra dimensions and particles that could make up dark matter. It has the same scientific goals as the ATLAS experiment but it uses different technical solutions and a different magnet system design.

The CMS detector is built around a huge solenoid magnet. It is a cylindrical coil of superconducting cable that generates a field of 4 T. The complete detector is 21 metres long, 15 metres wide and 15 metres high, with a weight of 15000 tons. The muon chambers are inside the return yoke and in the center there are silicon detectors (strips and pixels) for track reconstruction.

2.2.2.4 LHCb experiment

The LHCb experiments specialises in investigating the slight differences between matter and antimatter by studying the properties of the B hadrons (which contain the b-quark) and of their antiparticles [22]. The LHCb experiment uses a series of sub-detectors to register mainly forward particles. The first sub-detector is mounted close to the collision point with the others following one behind the other over a length of 20 metres. To catch the b-quarks, LHCb has developed sophisticated movable tracking detectors close to the path of the beams. The 5600 tonne LHCb detector is 21 metres long, 10 metres high and 13 metres wide, and sits 100 metres below ground.

2.2.2.5 Other experiments

LHCf is a small experiment that measures the particles produced very close to the direction of the beams. It has the detectors 140 m from the ATLAS collision point [23]. TOTEM measures the cross-section of the proton at LHC [24]. Like LHCf, TOTEM must be able to detect particles produced very close to the LHC beam. It is located at four locations near CMS. MoEDAL is an experiment to directly search for the Magnetic Monopole or Dyon and other highly ionising Stable (or pseudo-stable) Massive Particles (SMPs) at the LHC.

2.3 The ATLAS experiment

The ATLAS experiment is an experiment located at point one of the LHC. Like the CMS, it investigates a wide range of physics, as precision SM physics measurements, the search of the Higgs boson, physics phenomena beyond the SM like SUSY, extra

dimensions, dark matter, etc. ATLAS is the largest-volume collider-detector ever constructed. ATLAS is 45 meters long, 25 meters of diameter and has a weight about 7000 tonnes. The collaboration consists on more than 3000 members from 175 institutes in 38 countries.

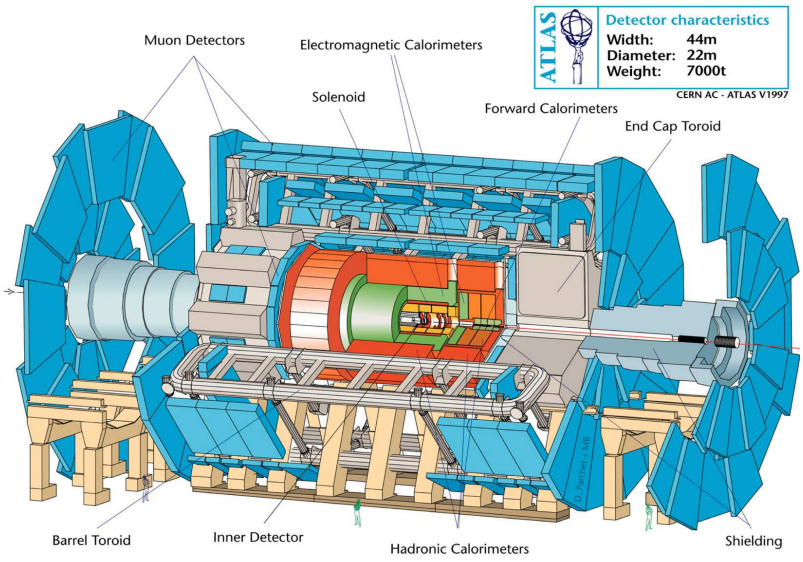

Figure 2.6: Overview of the ATLAS detector. All the subdetectors are shown.

The ATLAS experiment is composed of several parts as seen in Figure 2.6:

- The ID or tracking system.
- The Calorimeters.
- The MS.
- Solenoidal and Toroidal Magnets (ATLAS Magnet System).
- Trigger and DAQ.
- Reconstruction software.
- Computing GRID.

2.3.1 The Inner Detector (ID)

The ID is the innermost detector system in ATLAS. It is able to measure the tracks of hundred of charged particles that are produced in the proton-proton collisions. It consists of concentric layers of tracking detectors, with the highest precision detectors closest to the collision point. The colliding beams produce intense levels of radiation,

making radiation hardness a top priority for the detector and readout electronics. At the same time, the amount of material in the ID must be minimised to avoid disturbing the trajectories of the particles. The ID is composed by three sub-systems located inside of a solenoid which produces a magnetic field of 2 T. The magnetic field causes the charged particles to bend their trajectory. The curvature of these tracks provides the information for determining the momentum and electric charge of each particle. The three sub-systems are:

- The Pixel detector
- The Semi Conductor Tracker (SCT)
- The Transition Radiation Tracker (TRT)

A sketch of the ID is showed in the figure 2.7 and it will be explained with more detail in section 2.4.

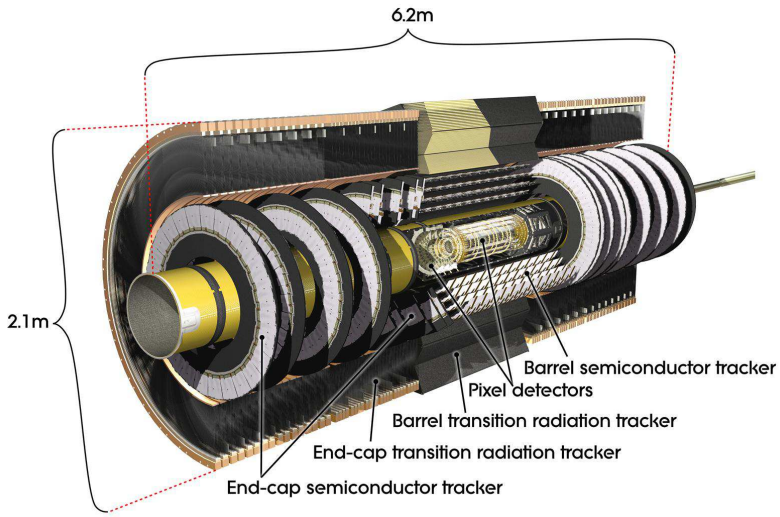

Figure 2.7: Overview of the ATLAS ID. The pixel, SCT and TRT modules are drawn. It is also possible to distinguish between the concentric layers of the barrel and the disks of the end-caps.

2.3.2 The calorimeters

The calorimeters, which surround the ID and the solenoid, absorb and measure the energies of most charged and neutral particles produced in the collisions. Energy deposits in the calorimeter are detected and converted to electrical signals that are read out by data-taking electronics. The ATLAS calorimeters consist of many layers of dense plates

that absorb incident particles and transform their energies into large showers of lower-energy particles. Between the absorber plates there are thin layers of particle sensitive detectors that register the particle showers and produce signals proportional to the energy. There are two types of calorimeters:

- The Electromagnetic Calorimeter preferentially absorbs and measures the energies of electrons and photons. It consists of absorber layers of lead with liquid argon as the sampling material.
- The Hadronic Calorimeter measures the particles that are not stopped by the Electromagnetic Calorimeter. The absorber layers are made of steel, and particle showers are sampled by tiles of scintillating plastic, which emit light when charged particles pass trough them.

A sketch of the ATLAS calorimeters is showed in the figure 2.8.

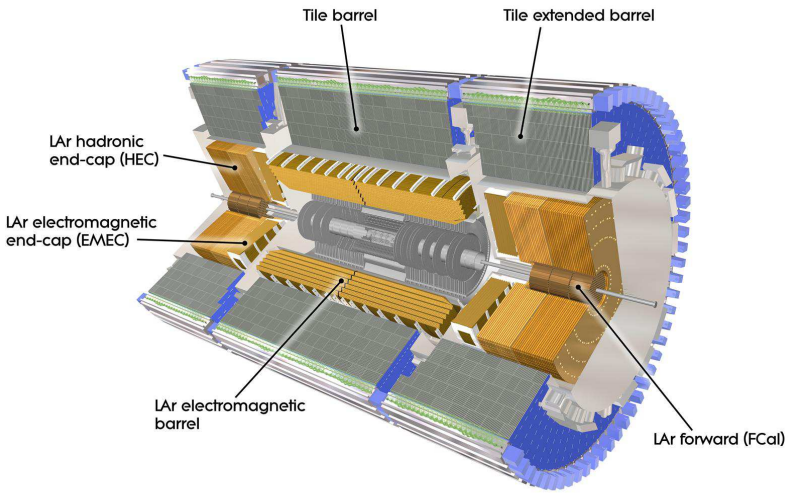

Figure 2.8: Overview of the ATLAS calorimeters.

2.3.3 MS

The Muon Spectrometer (MS) is a large tracking system designed to detect and track muons. It consists in 3 parts:

- The magnetic field provided by eight barrel loops and two end-cap toroidal magnets.
- 1200 chambers measuring with high spatial precision the tracks of the outgoing muons

- A set of triggering chambers with accurate time-resolution.

This sub-detector extends from a radius of 4.25 meters to 11 meters. This enormous size is required to accurately measure the momentum of muons, which first go through all the other parts of the detector before reaching the MS. The MS has roughly one million readout channels and the chamber cover has an area of 12000 mm^2. It has a hardware alignment system to continuously measure the muon chamber positions and deformations during data-taking based on optical and temperature sensors. The layout of the MS is shown in figure 2.9.

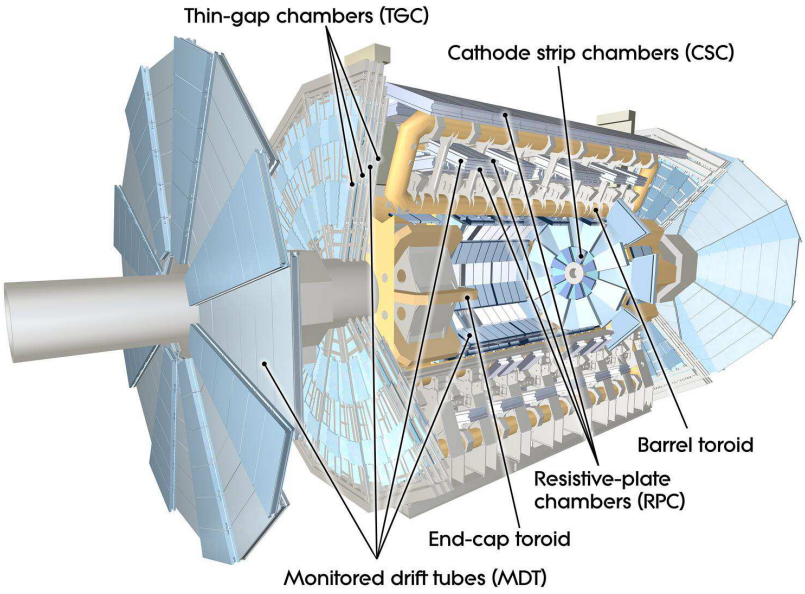

Figure 2.9: Overview of the ATLAS MS

2.3.4 ATLAS Magnet System

The ATLAS Magnet System consists of the Central Solenoid (CS) which provides the magnetic field for the ID, and eight large scale air-core superconducting toroids, the Barrel Toroid (BT) and two End-Cap Toroids (ECT), providing a toroidal field configuration. The CS is designed to provide an axial magnetic field of 2 T at the center of the ID in volume of 2.5 m in diameter and 5.3 m in length. The BT extends over a length of 25 m, with an inner bore of 9.4 m and outer diameter of 20.1 m. The two ECT are inserted in the barrel at each end, and have a length of 5 m, an inner bore of 1.65 m and an outer diameter of 10.7 m. The magnetic field provided is 3 Tm in the barrel and 6 Tm in the end-caps.

2.3.5 Trigger and DAQ

During the 7 TeVrun in 2011, the LHC proton bunches collided at a frequency of 40 MHz and an average of 23 collision were produced each bunch crossing. The trigger system needed to efficiently reject a large rate of events and select potentially the interesting ones with high efficiency. To deal with this amount of data, the ATLAS trigger is based on three levels of online event selection as shown in the figure 2.10 where each level refines the decisions made at the previous level. The level-1 trigger (LVL1) trigger, hardware based, is responsible for the first level of event selection reducing the event rate to 75 kHz. The next two levels are software based and are called the High Level Trigger (HLT), and it reduces to a final data-taking rate of approximately 200 Hz.

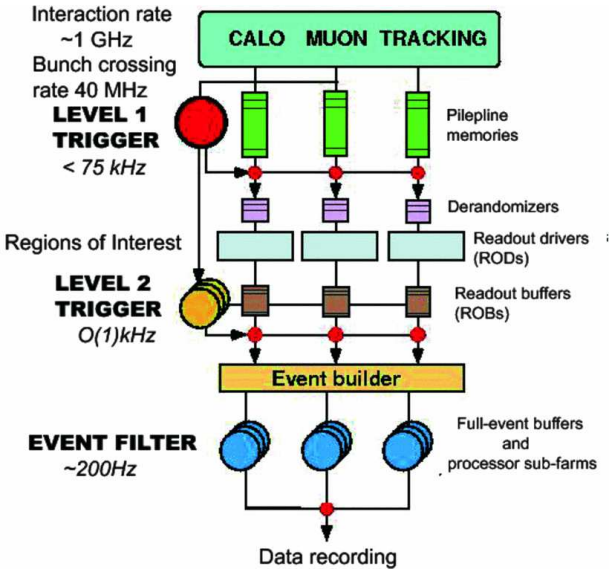

Figure 2.10: Overview of the ATLAS Trigger/DAQ system.

2.4 The Inner Detector

The ID is the innermost sub-detector of ATLAS. It combines high resolution silicon discrete detectors in the inner radii with continuous tracking detectors at outer radii. The ID has a diameter of 2.1 m and a length of 6.2 m. It has been designed to provide a robust pattern recognition, excellent momentum resolution and good vertex measurements for charged particle tracks. To achieve this goals the ID is composed by three systems: the Pixel Detector, the SCT and the TRT. These systems are surrounded by a superconducting solenoid that provides a 2T magnetic field as seen in the section 2.3.4. The Pixel detector provides three 3-dimensional space-points per track. The SCT surrounds the PIXEL detector and can provide at last eight 2-dimensional precision space-points (two per module). Finally, the TRT, a straw tracker, surrounds the other two and

provides up to 30 measurements in the bending plane. The figure 2.11 shows a plan view of a quarter-section of the ATLAS ID where the exact position and dimensions of each barrel layer and discs are showed. The operating specifications imply requirements

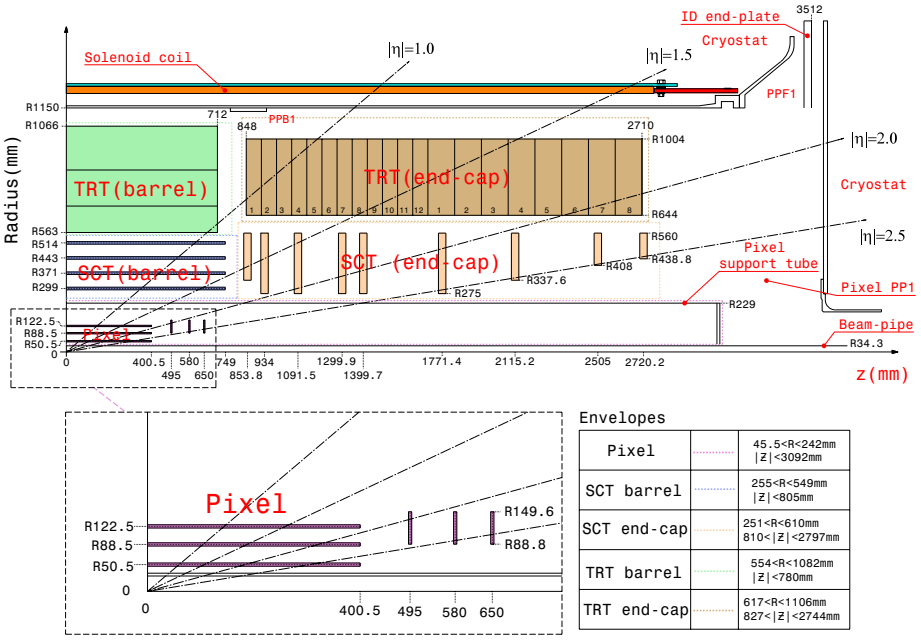

Figure 2.11: Plan view of a quarter-section of the ATLAS ID

on the alignment precision (which are summarised in the table 2.2) and which serve as limits on the silicon module building precision, the TRT straw-tube position, and the measured module placements accuracy and stability. This leads to:

- a good building accuracy with radiation-tolerant materials having adequate detector stability and well understood position.
- an ability to monitor the position of the detector elements using charged tracks and, for the SCT, laser interferometric monitoring (FSI).
- a trade-off between the low material budget needed for optimal performance and the significant material budget resulting from a stable mechanical structure.

The ID performance requirements imply the need for a stability between alignment periods which is high compared with the alignment precision.

The pixel and SCT sensors are required to maintain adequate signal performance over the detector lifetime at design luminosity. The integrated radiation dose has important consequences for the sensors of both detectors. The sensor leakage current also increases linearly with the integrated radiation dose. The n-type bulk material effectively becomes p-type after a fluence of F_{neq} of $2 \times 10^{13} cm^{-2}$. The effective doping concentration then

Item	**Intrinsic accuracy** (μm)	**Alignment tolerances** (μm)		
		Radial (R)	**Axial (z)**	**Azimuth ($R-\phi$)**
Pixel				
Layer-0	10 (R-ϕ) 115 (z)	10	20	7
Layer-1 and -2	10 (R-ϕ) 115 (z)	20	20	7
Disks	10 (R-ϕ) 115 (R)	20	100	7
SCT				
Barrel	17 (R-ϕ) 580 (z)	100	50	12
Disks	17 (R-ϕ) 580 (R)	50	200	12
TRT	130			30

Table 2.2: Intrinsic measurement accuracies and mechanical alignment tolerances for the ID sub-systems, as defined by the performance requirements of the ATLAS experiment.

grows with time in a radiation dose-dependent way. To contain the long term annealing and to reduce the leakage current, the sensors are operated in a temperature range of -5 °C to -10 °C. The sensors must further meet significant geometrical constraints on their thickness, granularity and charge-collection efficiency.

2.4.1 Pixel detector

2.4.1.1 Pixel sensors

The pixel sensors required the most leading-edge technology to meet the specifications on radiation hardness, resolution and occupancy in the innermost layers. The sensors are 250 μm thick wafers. These were produced from oxygenated n-type ingots with readout pixels on the n^+-implanted side of the detector. There are 1744 identical pixel sensors with a size of 19×63 mm^2. The sensors operated initially at 150 V bias voltage, but operating voltages of up to 600 V will be required for good charge collection efficiency after ten years of operation. The nominal pixel size is 50×400 μm^2 (90 % of the pixels). The size of the remaining pixels is 50×600 μm^2 in the edge regions at the front-end chips on a module. There are 47232 pixels on each sensor, but there are four ganged pixels in each column of the front-end chip, thus leading to a total of 46080 readout channels.

2.4.1.2 Pixel modules

The 1744 pixel modules are arranged in three barrel layers and two end-caps, each with three disk layers as shown in Figure 2.16. The detector parameters are listed in the table 2.3. The barrel is formed of 112 barrel staves arranged in three layers and the end-caps are composed of 48 end-cap sectors (8 sectors per disk).

A schematic view of a pixel module is shown in the Figure 2.12. A pixel module consists of a stack of the components (from the bottom up):

- 16 front-end electronic chips, each with 2880 electronic channels.

Barrel	**Radius (mm)**	**Staves**	**Modules**	**Pixels**
Layer-0	50.5	22	286	13.2×10^6
Layer-1	88.5	38	494	22.8×10^6
Layer-2	122.5	52	676	31.2×10^6
End-cap (one side)	**z (mm)**	**Sectors**	**Modules**	**Pixels**
Disk 1	495	8	48	2.2×10^6
Disk 2	580	8	48	2.8×10^6
Disk 3	650	8	48	2.2×10^6
Barrel and both end-caps			1744	80.4×10^6

Table 2.3: Parameters of the pixel detector, position of the layers/disks, number of modules per structure and pixels.

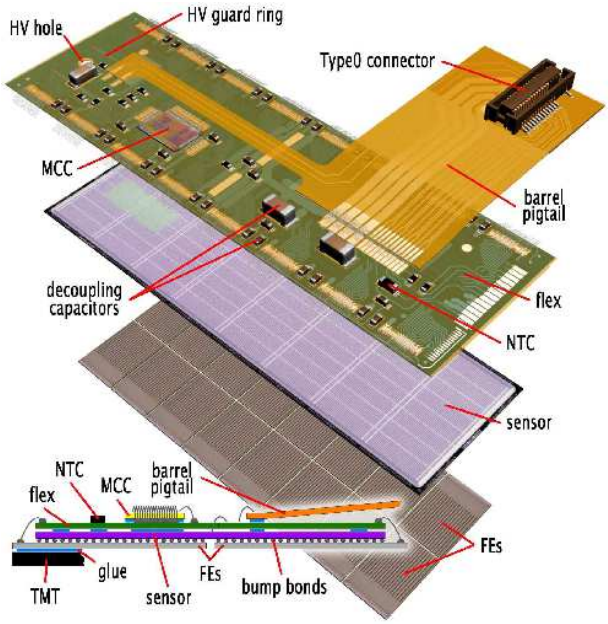

Figure 2.12: Schematic view of a pixel module.

- Bump bonds which connect the electronics channels to pixel sensor elements.
- The sensor tile.
- A flexible polyimide circuit board (flex-hybrid) with a module-control chip glued to the (flex-hybrid).
- A polyimide pig-tail with Cu lines and a connector (barrel modules) or a wire micro-cable (end-cap modules) bonded to the flex-hybrid.

In the barrel all the modules are facing the beam-pipe, while the end-cap disks have modules facing both ways. In the barrel region, 13 pixel modules were mounted on each stave using robotic tools and then glued. The staves were themselves mounted on carbon-fibre structures. As the pixel staves overlap they were mounted with a tilt angle of -20° in three layers. The end-cap equivalent of the stave is a sector. The two pixel end-caps have three identical disks. Each disk is composed of eight sectors and each sector has six pixel modules.

The spatial resolution of individual pixel modules has been measured in a test beam, for both non-irradiated and fully irradiated modules. At normal incidence, a spatial resolution of 12 μm is measured and approximately 80% of the tracks have a single pixel hit. The Figure 2.13 shows the number of measured clusters per track in the pixel barrel and end-cap. The resolution is not significantly degraded after irradiation.

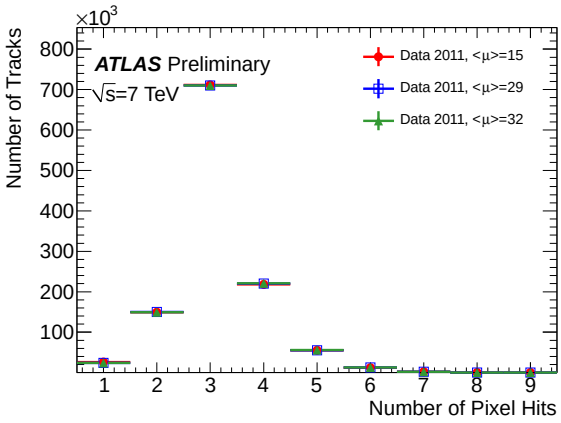

Figure 2.13: Number of pixel hits by track for different pile-up conditions in real data collected during 2011 run at 7 /tev[25].

2.4.2 SCT

2.4.2.1 SCT sensors

The sensors of the SCT use a classic single-sided p-on-n technology with AC-coupled readout strips. The sensors operate initially at 150 V bias voltage, but operating voltages of between 350 and 500 V would be required for good charge collection efficiency after ten years of operation. The sensor thickness of 285 ± 15 μm is a compromise between the required operating voltage, the primary signal ionisation and the simplicity of fabrication. The strip pitch was determined by the required digitising precision, granularity, particle occupancy and noise performance. A strip pitch of 80 μm with two 6 cm-long sensors daisy-chained was chosen for the rectangular barrel sensors and radial strips of constant azimuth with mean pitch of 80 μm were chosen for the trapezoidal end-cap sensors. There are thus a total of 768 active strips of 12 cm length per sensor

Module type	Sensor type	Cut length (mm)	Outer Width (mm)	Inner width (mm)	Strip pitch μm	Inter-strip angle μrad
Barrel	Barrel	63.960	63.560	63.560	80.0	0
End-cap inner	W12	61.060	55.488	47.735	56.9-69.2	207.0
End-cap middle	W21	65.085	66.130	55.734	69.9-83.0	207.0
	W22	54.435	74.847	66.152	83.4-94.2	207.0
End-cap outer	W31	65.540	64.635	56.475	70.9-81.1	161.5
	W32	57.515	71.814	64.653	81.5-90.4	161.5

Table 2.4: External cut dimensions of the SCT barrel and end-cap sensors

plus two strips at bias potential to define the sensor edge. The sensor dimensions are summarised in table 2.4.

2.4.2.2 SCT modules

The SCT consists of 4088 modules mounted in four coaxial cylindrical layers in the barrel region and in two end-caps each containing nine disk layers, shown in Figure 2.11, The modules cover a surface of 63 m^2 of silicon and provide almost hermetic coverage with at least four precision space-point measurements. The table 2.5 shows the SCT detector parameters. The 2112 barrel SCT modules use 80 μm pitch micro-strip sensors. The sensors are connected to binary signal readout chips. The barrel module is shown in figure 2.14 (left). The four sensors, two each on the top and bottom side are rotated with their hybrids by $\pm$20 mrad around the geometrical centre of the sensors. They are glued on a 380 μm thick thermal pyrolytic graphite (TPG) base-board, which provides thermal and mechanical structure. A polyimide hybrid with a carbon-fibre substrate bridges the sensors on each side. An end-cap module is shown in the figure 2.14 (right). In the end-caps there are three module types, inner, middle and outer. Each of the 1976 modules has two sets of sensors glued back-to-back around a central TPG spine with a rotation of $\pm$20 mrad to give the required space-point resolution in $R-\phi$ and R.

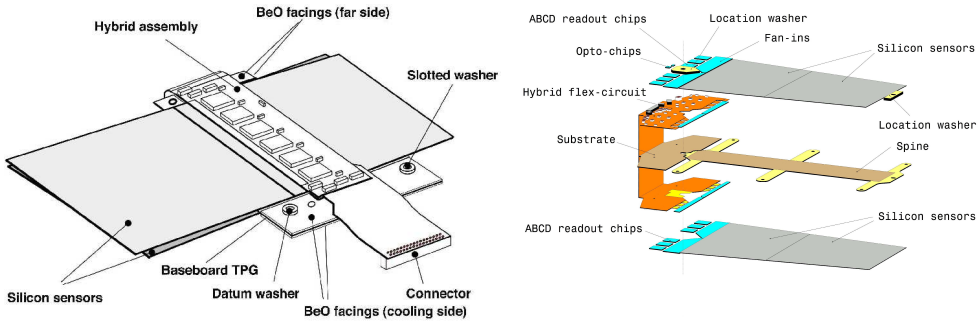

Figure 2.14: Schematic view of a barrel SCT module (left) and an end-cap SCT outer module (right).

Barrel	**Radius (mm)**	**Rows**	**Modules**	**Channels**
Layer-0	284	32	384	294×10^3
Layer-1	355	40	480	368×10^3
Layer-2	427	48	576	442×10^3
Layer-3	498	56	672	516×10^3
Total Barrel			2112	1622×10^3
End-cap (one side)	**z (mm)**	**Rings**	**Modules**	**Channels**
Disk-1	854	2	92	70×10^3
Disk-2	934	3	132	101×10^3
Disk-3	1091	3	132	101×10^3
Disk-4	1300	3	132	101×10^3
Disk-5	1400	3	132	101×10^3
Disk-6	1771	3	132	101×10^3
Disk-7	2115	2	92	70×10^3
Disk-8	2505	2	92	70×10^3
Disk-9	2729	1	52	40×10^3
Total both end-caps			1976	1517×10^3
Total			4088	313910^3

Table 2.5: Parameters of the SCT, position of the layers/disks, number of modules per structure and channels.

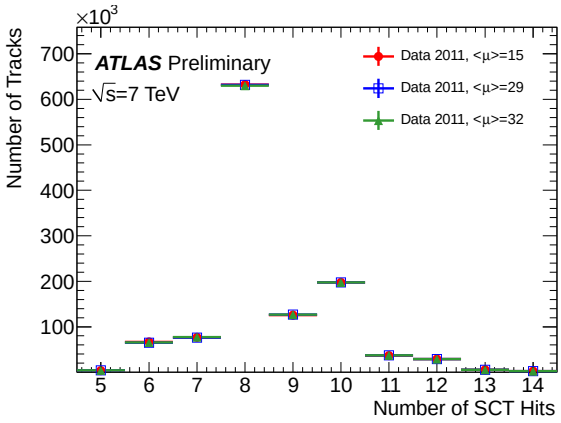

Figure 2.15: Number of SCT hits by track for different pile-up conditions in real data collected during 2011 run at 7 /tev[25].

In Instituto de Fisica Corpuscular (IFIC) a total of 282 modules (125 outer and 157 long-middle) were built [26]. In order to carry out the module production according to the quality criteria set by the ATLAS collaboration, dedicated machinery and tooling

was constructed and installed in a clean room (class 1000) where temperature (21°C) was controlled within 0.5°C and relative humidity (40%) within 5%.

2.4.3 TRT

2.4.3.1 TRT straw tubes

Polyamide drift tubes of 4 mm diameter are the basic TRT detector elements. The straw tube wall is made of two 35 μm thick multi-layer films bonded back to back. After fabrication, the straws were cut to length (144 cm for the barrel and 37 cm for the end-caps). The anodes are 31 μm diameter tungsten wires plated with gold, supported at the straw end by and end-plug.

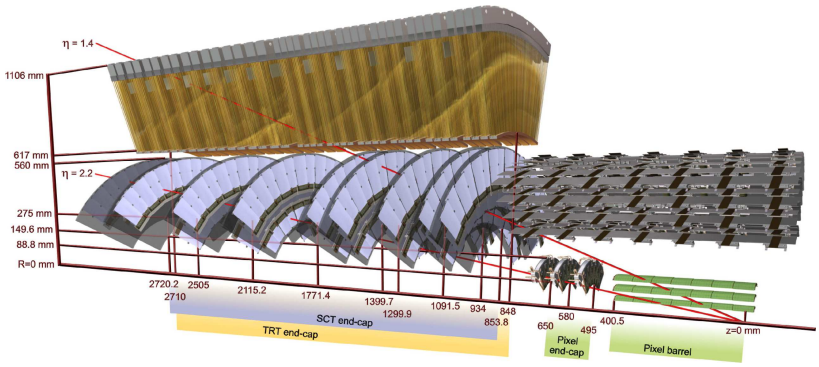

Figure 2.16: Drawing showing the sensors and structural elements.

2.4.3.2 TRT modules

The TRT contains up to 73 layers of straws interleaved with fibres (barrel) and 160 straw planes interleaved with foils (end-cap), which provide transition radiation for electron identification. All charges tracks with $p_T > 0.5$ GeV and $|\eta| < 2.0$ will traverse at least 36 straws, except in the barrel-end-cap transition region, where this number decreases to a minimum of 22 crossed straws. The TRT barrel is divided into three rings of 32 modules each, supported at each end by a space frame, which is the main component of the barrel support structure. Each module consists of a carbon-fibre laminate shell and an internal array of straws embedded in a matrix of polypropylene fibres serving as the transition radiation material. The straws form a uniform axial array with a mean spacing of 7 mm. The module shell also serves as a gas manifold for CO_2 which circulates outside the straws to prevent high-voltage discharges and the accumulation of xenon due to possible gas leaks. Each of the TRT end-caps consists of two sets of independent wheels. The set closer to the interaction point contains 12 wheels, each with eight successive layers spaced 8 mm apart. The outer set of wheels contains eight wheels, also with eight straw layers but spaced 15 mm apart. Each layer contains 768 radially oriented straws of 37 cm length with uniform azimuthal spacing.

	$\|z\|_{\min}$ **mm**	$\|z\|_{\max}$ **mm**	$R_{\max}$ **mm**	$R_{\min}$ **mm**	**Number of modules**	**Number of layers**	**Straws per module**
Barrel (both sides)	0	780	554	1082	96	73	52544
Type-1 module (inner)	400	712.1	563	624	32	9	329
Type-1 module (outer)	7.5	712.1	625	694		10	
Type-2 module	7.5	712.1	697	860	32	24	520
Type-3 module	7.5	712.1	863	1066	32	30	793
End-cap (one side)	827	2744	615	1106	20	160	122880
Type A wheels	848	1705	644	1004	12	8	6144
Type B wheels	1740	2710	644	1004	8	8	6144

Table 2.6: Parameters of the TRT, position of the structures, number of modules, layers and straws.

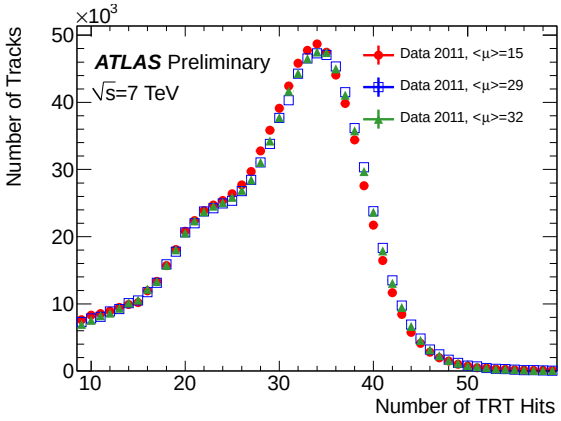

Figure 2.17: Number of TRT hits by track for different pile-up conditions in real data collected during 2011 run at 7 /tev[25].

2.4.4 The solenoid magnet

The CS is designed to provide an axial magnetic field of 2 T (current of 7730 A) at the centre of the Inner Detector in a warm bore volume of 2.5 of diameter and 5.3 of length. The position of the CS in front of the electromagnetic calorimeter requires the minimisation of the material in order to achieve the best calorimeter performance. For this reason, the solenoid coil is installed in a common vacuum vessel shared with the LAr calorimeter. The coil design also features high strength aluminium superconducting cable to make the solenoid thinnest while keeping its electrical stability. Before the insertion of the different ID sub-detectors, the solenoid field has been measured by means of a mapping machine using an array of Hall probes in combination with a small number of Nuclear Magnetic Response (NMR) probes. The three components of the field were measured as a function of Z, R and ϕ. The relative error on track sagittas due to the field uncertainty varies from 0.7×10^{-4} in the centre of the solenoid to 12×10^{-4}

at the highest rapidity value. From the solenoid modelling, a 3-D grid in cylindrical coordinates is created to determine by interpolation the field value at any point of the ID with an r.m.s. error of 1 Gauss. Figure 2.18 shows the magnetic field map.

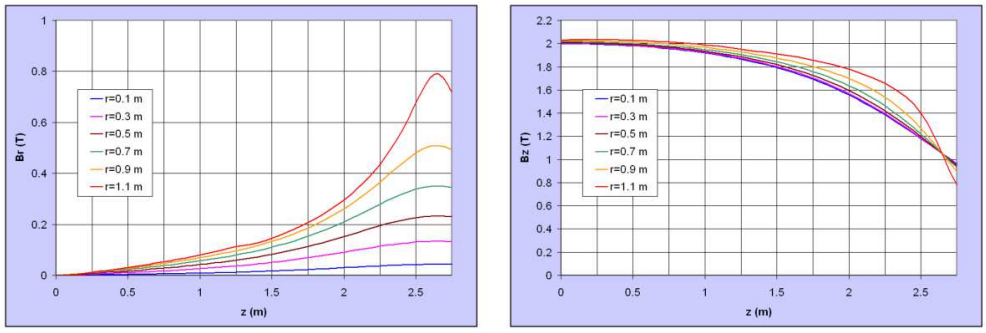

Figure 2.18: B_R as a function of Z and R (right) and B_Z and a function of Z and R (left). It is estimated to be accurate to 5 Gauss and the extra error added by the interpolation procedure is 1 Gauss [27].

2.4.5 Material distribution of the ID

The performance requirements of the ATLAS ID are more stringent than any tracking detector built so far for operation at a hadron collider. The harsh environment and the pile-up from multiple interactions per bunch crossing make a high detector granularity mandatory with good mechanical stability. The overall weight of 4.5 tonnes and material budget of the ID (in terms of radiation length X_0 and interaction length λ) are much larger than previous detectors. The consequences of this are:

1. Many electrons lose most of their energy through bremsstrahlung before reaching the electromagnetic calorimeter.

2. 40% of photons convert into an electron-positron pair before reaching the LAr.

3. Even in the case of low-energy charged pions, a significant fraction will have an inelastic hadronic interaction inside the ID volume.

A detailed modelling of the ID material has been implemented in the simulation. The detector description and the real geometry has a very good agreement as shown in Figure Figure 2.21. A map of generated photon-conversion vertices in the ID volume, integrated over azimuth shows the internal structure of the detector (Figure 2.19). Figure 2.20 shows the integrated radiation length, X_0, and interaction length, λ, traversed by a straight track as function of $|\eta|$. The most striking feature is the effect of non-active service and structural material. A large fraction of the service and structural material is external to the active ID envelope, deteriorating the calorimeter resolution but not the tracking performance.

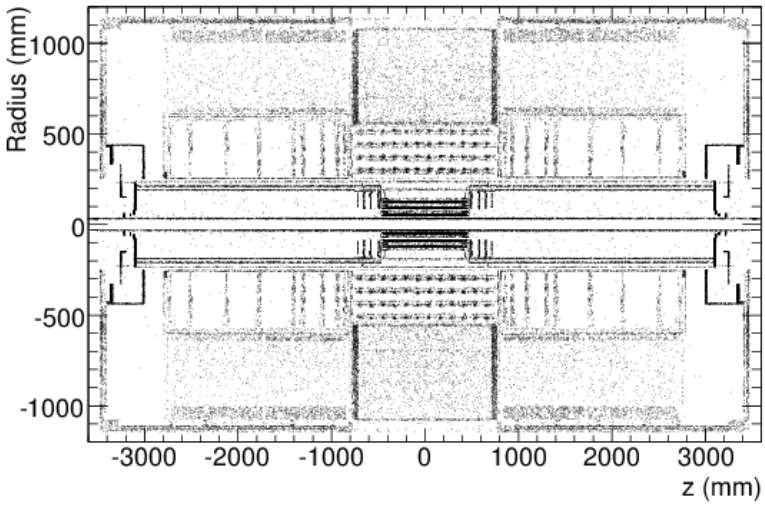

Figure 2.19: Mapping of photon conversions as a function of z and radius, integrated over ϕ. The mapping has been done with 500,000 simulated minimum bias events.

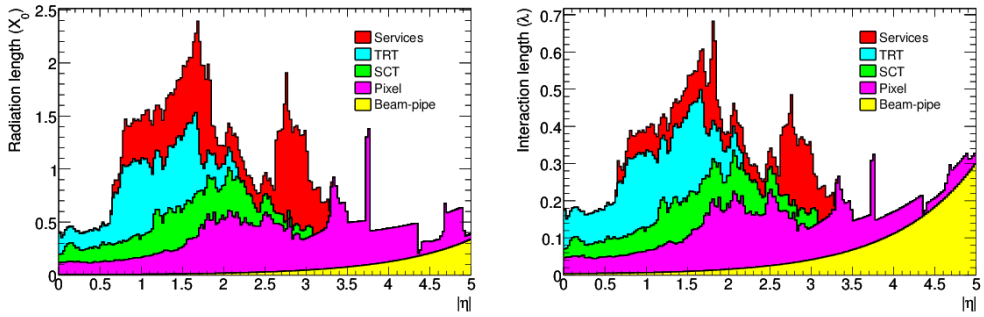

Figure 2.20: Material distribution (X_0 and λ) at the exit of the ID envelope averaged over ϕ.

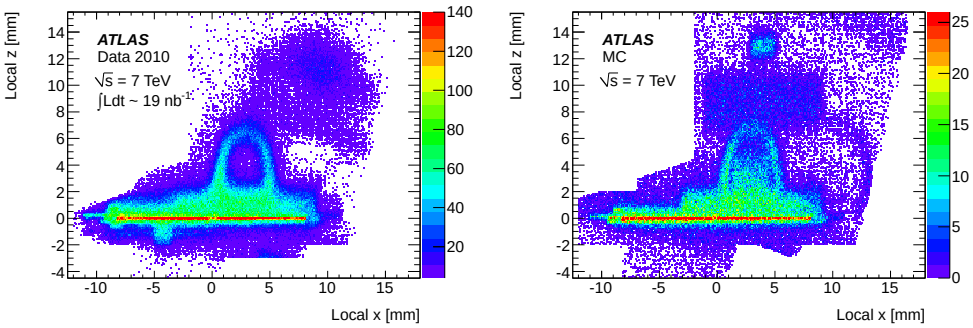

Figure 2.21: z vs x in the local coordinate system for the first pixel detector layer using data (left) and MC (right).

Chapter 3

Inner Detector Alignment Basics

The knowledge of the position of sensitive detector elements is crucial for the optimal operation and performance of a tracking device. A precise way to determine this information is by using a track-based alignment algorithm. These kind of algorithms are based on the minimisation of the distance between the recorded sensor hits and the corresponding reconstructed tracks. The characterisation of the tracks is needed to obtain the parameters used to align the system. The ATLAS tracking model is used to reconstruct these tracks.

3.1 Tracking

3.1.1 ATLAS tracking model

The ATLAS track reconstruction model is based on the Event Data Model (EDM) [28] that uses a common track object, which is suited to describe the trajectory of the particles in the innermost tracking sub-detectors and in the muon detectors. The aim of this framework is to make the reconstruction software flexible and easily maintainable, by delegating each reconstruction step to a dedicated software module. This provides a very customisable tracking software for each reconstruction step. There is also the possibility of store the event information at every stage of the reconstruction process. The ID tracking model is composed by:

- Data Preparation.
- Pattern recognition and track fitting.
- Post-processing.

3.1.2 Track reconstruction

Track reconstruction in the ID uses the measurements of the pixel, SCT and TRT detectors. Tracks are reconstructed in the ID using a sequence of algorithms [29]. The inside-out algorithm starts from three-point seeds in the silicon detectors and adds hits moving away from the interaction point using a combinatorial Kalman filter [30]. Ambiguities in the track candidates found in the silicon detectors are resolved, and tracks are extended into the TRT. The inside-out algorithm is the baseline algorithm designed for the efficient reconstruction of primary charged particles. Primary particles are defined as particles with a mean lifetime greater than 3×10^{-11}s directly produced in a pp interaction or from the subsequent decays or interaction of particles with a lifetime shorter than 3×10^{-11}s. The tracks reconstructed by the inside-out algorithms are required to have transverse momentum $P_T > 400$ MeV.

In a second stage, a track search starts from segments reconstructed in the TRT and extends them inwards by adding silicon hits, which is referred to as back-tracking. Back-tracking is designed to reconstruct secondaries, which are particles produced in the interactions of primaries, mainly with detector and services material. Finally tracks with a TRT segment but no extension into the silicon detectors are referred to as TRT-standalone tracks.

3.1.3 Track parameters

The trajectory of a charged particle in a uniform magnetic field (B) is a helix that can be parametrised by a set of five parameters. The chosen representation for the alignment is given by the parameters $\boldsymbol{\tau} = \{d_0, z_0, \phi_0, \cot\theta, q/p\}$. The d_0 is the transverse impact parameter, which is the signed distance to the XY plane with the sign defined to be positive when the direction of the track is clockwise with respect to the origin and negative otherwise. z_0 is the longitudinal impact parameter that corresponds to the Z-coordinate of the perigee. ϕ_0 is the azimutal angle in the XY plane at the perigee and θ corresponds with the polar angle. Finally, q/p is the charge of the particle over its momentum. The geometrical interpretation of the track parameters are shown in the Figure 3.1.

The expected performance of the tracking system for reconstructing single particles and particles in jets is determined using a precise modelling of the individual detector response, geometry and passive material in the simulation [31]. The resolution of a track parameter X can be expressed as a function of p_T as:

$$\sigma_X(p_T) = \sigma_X(\infty)(1 \oplus p_X/p_T) \tag{3.1}$$

where $\sigma_X(\infty)$ is the asymptotic resolution expected at infinite momentum and p_X is a constant representing the value of p_T for which the intrinsic and multiple-scattering therms in the equation are equal for the parameter X under consideration. Table 3.1 shows the values of $\sigma_X(\infty)$ and p_X for tracks in two η-regions, corresponding to the barrel and end-caps. Figure 3.2 shows the momentum resolution for isolated muons and transverse impact parameter resolution for isolated pions.

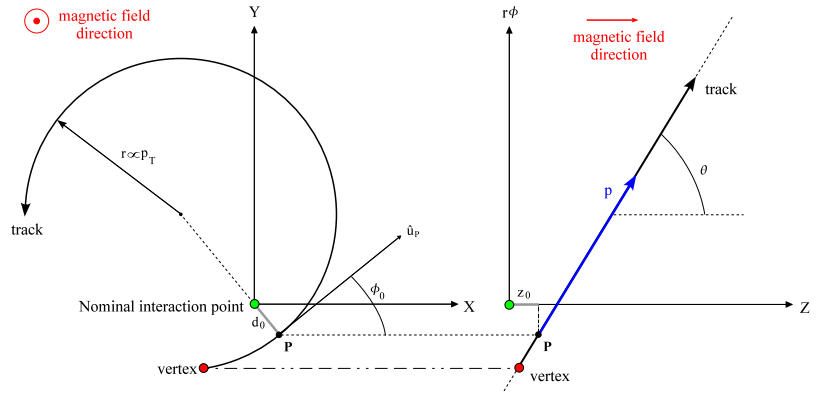

Figure 3.1: Graphical interpretation of track parameters at perigee.

Track parameter	$0.25 < \|\eta\| < 0.50$		$1.55 < \|\eta\| < 1.75$	
	$\sigma_X(\infty)$	p_X(GeV)	$\sigma_X(\infty)$	p_X(GeV)
Transverse impact parameter (d_0)	10 μm	14	12 μm	20
Longitudinal impact parameter ($z_0 \times \sin\theta$)	91 μm	2.3	71 μm	3.7
Azimuthal angle (ϕ)	70 μrad	39	92 μrad	49
Polar angle ($\cot\theta$)	0.7×10^{-3}	5.0	0.7×10^{-3}	10
Inverse transverse momentum (q/p_T)	0.34 TeV^{-1}	44	0.41 TeV^{-1}	80

Table 3.1: Expected track parameter resolutions at infinite transverse momentum, $\sigma_X(\infty)$, and transverse momentum, p_X, at which multiple-scattering contribution equals that from the detector resolution [31]. The values are shown for two η-regions, one in the barrel inner detector and one in the end-cap.

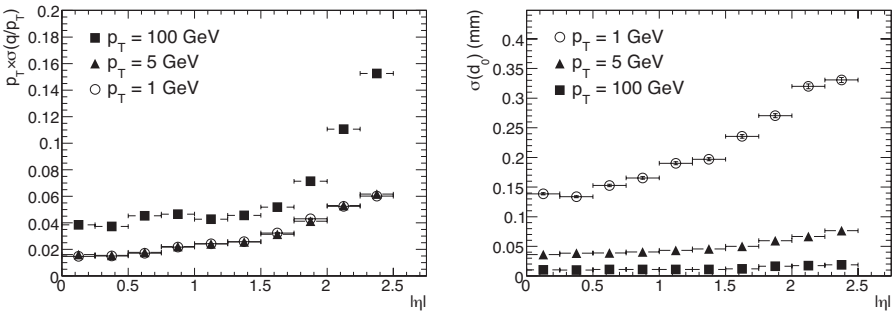

Figure 3.2: Relative transverse momentum resolution (left) and transverse impact parameter (d_0) resolution (right) as function of $|\eta|$.

3.1.4 Residuals

Track fitting and detector alignment make extensive use of the track-hit residual. That is, every detector element may contribute to the track with a measurement (or hit) of that track. On the other hand, it is possible for each track to predict where the sensor measurement should appear. The distance between these two points is known as residual. Two different residuals can be defined in the ID:

- distance of closest approach (DOCA) residuals (3-D). Defined as distance between the measurement and the trajectory of the reconstructed track.
- Within plane residuals (2-D). Defined as distance along the sensitive coordinate within the measurement plane of the strip or cluster with the extrapolated point to that surface of the reconstructed track.

In the local reference system of the element, $\mathbf{m}$ can be considered as the vector that represents the measurement of the sensor and $\mathbf{e}(\boldsymbol{\tau}, \mathbf{a})$ as the vector to the predicted point that depends of the track parameters ($\boldsymbol{\tau}$) and the alignment parameters ($\mathbf{a}$). Then the residual vector $\mathbf{r}$ (in the generic case as 3-dimensional) is defined as:

$$\mathbf{r} = (\mathbf{m} - \mathbf{e}(\boldsymbol{\tau}, \mathbf{a})) \tag{3.2}$$

To calculate the within plane residuals, $\mathbf{r}$ is projected to the sensitive direction of the sensor under test. As the pixel sensor has two sensitive directions, two residual components will be measured, called r_x and r_y. The SCT provides only one sensitive direction which is perpendicular to the strips, so there will be only one residual component per SCT plane. The TRT residuals also provide only one residual component (the distance with respect to reconstructed drift circle). A representation of both residual types in a SCT module is shown in Figure 3.3

In addition, two different kind of residuals can be defined:

- Biased residuals: the residual of every hit is calculated using the reconstructed track fitted with all of the available hits. In general these kind of residuals are used for tracking and alignment.
- Unbiased residuals: the residual is calculated with the track fitted excluding the hit under test. This means that in order to calculate every residual of the hits of a track, the track has to be refitted many times (one for every hit under study). These residuals are used mainly for monitoring.

3.2 Alignment algorithm implementation

The main goal of the alignment is to determine the position and orientation of each detector element. As shown in the Figure 3.4, the real position of the modules differs with respect the aparent position. Therefore the determination of the actual location of each one is required. This can be achieved using track-based alignment algorithms.

Each alignable structure has 6 degrees of freedom (DoF). These correspond to the three translations (T_x,T_y,T_z) that determine the position and three rotations (R_x,R_y,R_z)

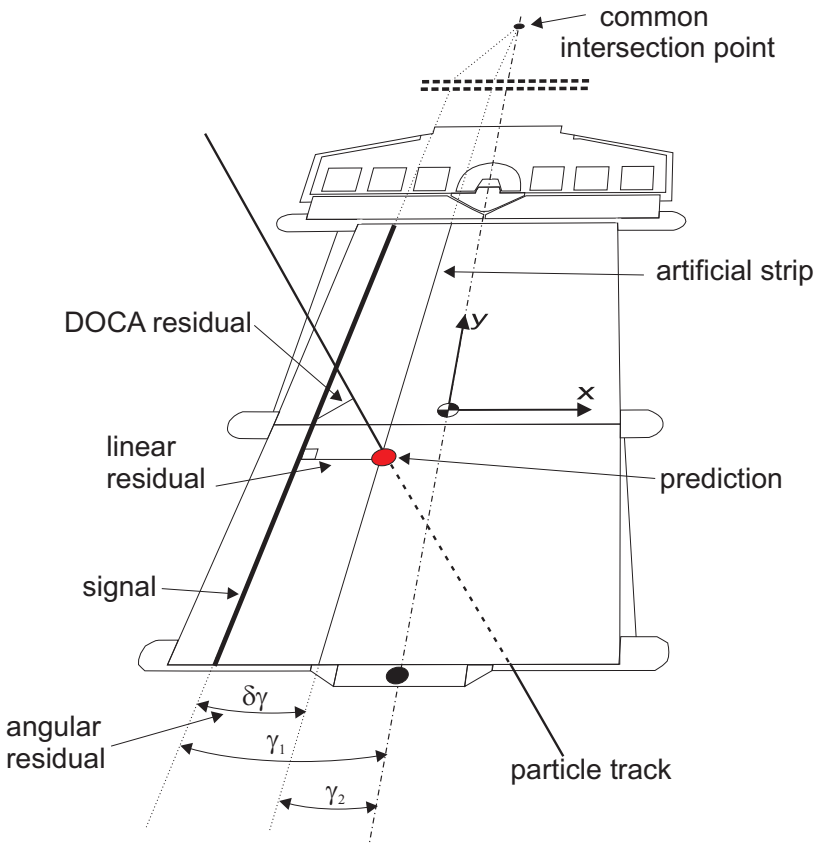

Figure 3.3: Representation of the both residual types for a planar detector, linear or within plane residual (2D) and DOCA (3D) in a SCT end-cap module. The artificial strip is an imaginary line that passes through the extrapolated point.

that provide the orientation of the structure [1]. Several different alignable structures can be defined, like a single silicon module, a TRT wire, a full layer or disk or even a full subdetector.

The alignment of the individual detectors uses a local Cartesian right-handed reference frame with the origin in the geometrical centre of the alignable structure. The axes are defined depending of the detector type:

- In the Pixel and SCT, the X and Y axes are in the detector plane with the X-axis pointing along the most precise measurement direction, i.e in the SCT module the X-axis is perpendicular to the to the strips.

[1] The 3 translations and 3 rotations are the basic DoF. It is possible to consider the deformation of the basic structures. For instance, the bending and/or bowing of a planar sensor. The deformation can also be fitted by the alignment software. But this case is beyond the scope of this work.

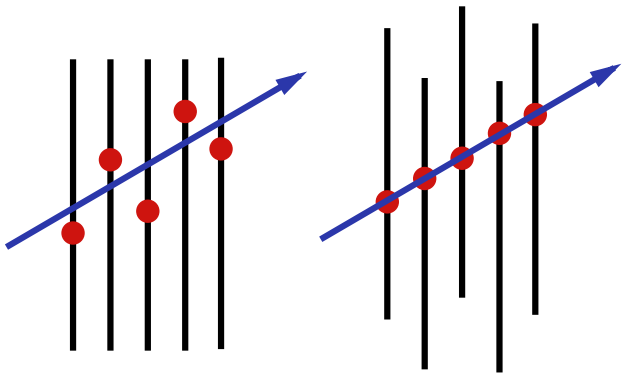

Figure 3.4: Schematic showing a track reconstructed in a misaligned detector. The figure on the right represents the real position and the one on the left represents the observed track

- In the TRT modules and wires the Z-axis points along the wire. The X-axis is perpendicular to both the wire direction and the radial direction from the origin of the global frame to the straw centre.

The alignment can be performed using different combination of alignable structures. The most important configurations of structures are called levels. There are three main levels that are included in the alignment constants database:

- Level 1: The Pixel is considered as one structure, the barrel and end-caps of the SCT and TRT are considered as independent structures.
- Level 2: The Pixel and SCT are splitted in layers and end-cap disks. The TRT is splitted in barrel modules and end-cap wheels.
- Level 3: The Pixel and SCT modules and the TRT wires are considered as alignable structures.

These levels are summarized in the Table 3.2. Different sub-structures can be considered to define new software alignment levels:

- Pixel half-shells: Each layer of the Pixel is considered as two half-shells or the full Pixel barrel is considered as two half-shells.
- Barrel ladders: In the Pixel and SCT barrels the modules can be grouped in ladders (along the z-axis)
- Barrel rings: In the Pixel and SCT barrels the modules can be grouped in rings (modules in the same z-plane)-

- SCT Endcap rings: the modules of the SCT end-cap can be grouped in rings (modules placed in the same radius)

These sub-structures can be combined with the main levels to implement additional levels:

- Level 1.5: 2 Pixel half-shells, 2 Pixel end-caps, SCT barrel and 2 SCT end-caps.
- Level 1.8: 3×2 Pixel half-shels, 2 Pixel end-caps, SCT barrel and 2 SCT end-caps.
- Level 2.7: 112 Pixel ladders, 2 Pixel end-caps, 176 SCT ladders and 2 SCT end-caps.

The alignment corrections of the intermediate levels are written in the database transforming them to the three main levels.

Although every structure has the 6 nominal DoF, it may happen that not all of them are actually aligned or computed. It is further possible to consider certain detector

Alignment level	Detector	Structures	degrees of freedom
Level 1	Pixel: whole detector	1	6
	SCT: barrel and 2 end-caps	3	18
	TRT: barrel	1	6
	TRT: 2 end-caps	2	12
	Total	**7**	**42**
Level 2	Pixel barrel: layers	3	18
	Pixel end-caps: disks	6	36
	SCT barrel: layers	4	24
	SCT end-caps: disks	18	108
	TRT barrel: modules	96	576
	TRT end-caps: wheels	80	480
	Total	**210**	**1236**
Level 3	Pixel: barrel modules	1456	8736
	Pixel: end-cap modules	288	1782
	SCT: barrel modules	2112	12672
	SCT: end-cap modules	1976	11856
	TRT: barrel wires	105088	210176
	TRT: end-cap wires	245760	491520
	Total	**356680**	**736742**

Table 3.2: Summary of the main alignment levels and the number of structures for each ID subdetector. Each structure has 6 DoF, except the TRT wires where only two DoF have been defined: the T_ϕ as the translation along the ϕ direction and R_r as the rotation around the radial direction.

module or structure deformations. For example, a silicon module may be modelled as a perfectly flat surface, or as a plane that may be twisted or bent. In addition to the

track-based alignment algorithms, the ID alignment can use several additional types of information. For example, it is possible to use the survey data obtained during the assembly of the detector [32]. Information of the calorimeters and muon spectrometer can be used as well, as the momentum of the particles as a constraint. Online information from the Frequency Scanning Interferometry (FSI) system [33], an optical alignment system installed in the SCT, is also available, though currently is not used yet.

3.2.1 Track-based alignment algorithms

Several track-based algorithms have been implemented over the years in the ATLAS software framework. All of them use the track-hit residuals. The alignment constants are those that minimize the residuals. There are two different approaches to calculate the alignment corrections, Localχ^2 and Globalχ^2. Both of them are based on the minimization of χ^2 function. The Localχ^2 can be regarded as a particular case of the Globalχ^2 case.

3.2.2 Globalχ^2 formalism

This algorithm consists on the minimization of the χ^2 built from the track-hit residuals with respect the alignment parameters [34, 35] defined as:

$$\chi^2 = \sum_t \sum_{h \in t} \left(\frac{r_{th}}{\sigma_{th}} \right)^2 \tag{3.3}$$

where t are the tracks used to perform the alignment and h the hits of each track. r_{th} is the residual of the hit and σ_{th} is the uncertainty associated to the hit. Is convenient to rewrite this definition using the matrix and vector algebra. Therefore, the vector $\mathbf{r}$ can be defined as a vector with all the residuals that the system can provide, being N_{RES} the number of possible residuals. These consists of the residuals associated to the track

hits in the Pixel, SCT and TRT.

$$\mathbf{r} = \begin{pmatrix} r_1 \\ \vdots \\ r_{N_{\mathrm{RES}}} \end{pmatrix} = \begin{pmatrix} r_{\mathrm{PIX}x_1} \\ \vdots \\ r_{\mathrm{PIX}x_{N_{\mathrm{PIX}}}} \\ r_{\mathrm{PIX}y_1} \\ \vdots \\ r_{\mathrm{PIX}y_{N_{\mathrm{PIX}}}} \\ r_{\mathrm{SCT}r\phi_1} \\ \vdots \\ r_{\mathrm{SCT}r\phi_{N_{\mathrm{SCT}}}} \\ r_{\mathrm{SCT}st_1} \\ \vdots \\ r_{\mathrm{SCT}st_{N_{\mathrm{SCT}}}} \\ r_{\mathrm{TRT}_1} \\ \vdots \\ r_{\mathrm{TRT}_{N_{\mathrm{TRT}}}} \end{pmatrix} \tag{3.4}$$

where $r_{\mathrm{PIX}x_1}$ and $r_{\mathrm{PIX}yi}$ are the x and y residuals of the i-th pixel module respectively. $r_{\mathrm{SCT}r\phi_i}$ and $r_{\mathrm{SCT}st_i}$ are the $r\phi$ side and stereo side residuals of the i-th SCT module. Finally, r_{TRT_i} is the residual of the i-th TRT straw. Similarly he covariance matrix V can be defined as:

$$V = \begin{pmatrix} \ddots & & & & & & & & & & \\ & \sigma^2_{\mathrm{PIX}\phi_i} & & & & & & & & & \\ & & \ddots & & & & & & & & \\ & & & \sigma^2_{\mathrm{PIX}\eta_i} & & & & 0 & & & \\ & & & & \ddots & & & & & & \\ & & & & & \sigma^2_{\mathrm{SCT}r\phi_i} & & & & & \\ & & & & & & \ddots & & & & \\ & & & 0 & & & & \sigma^2_{\mathrm{SCT}st_i} & & & \\ & & & & & & & & \ddots & & \\ & & & & & & & & & \sigma^2_{\mathrm{TRT}_i} & \\ & & & & & & & & & & \ddots \end{pmatrix} \tag{3.5}$$

where each σ is the associated uncertainty of the measurement. In principle, the covariance matrix is diagonal, which in practical terms means that what a sensor measure is independent of the other measurements[2]. But generally V is not diagonal due to contribution from the Multiple Coulomb Scattering ($V = V_{\mathrm{meas}} + V_{MCS}$) what actually

[2]Which is a sound approximation. However, in a general case V is not diagonal.

means that the measurement in one plane is affected by the scattering in the previous surface.

The vector **a** can be defined as a vector with all the alignment parameters that describe the geometry of the system. In a general case this vector can be written as a vector with $N_{\mathrm{DoF}} \times N_{\mathrm{ALI}}$ components that corresponds with the number of degrees of freedom being aligned:

$$a = \begin{pmatrix} T_{x1} \\ T_{y1} \\ T_{z1} \\ R_{x1} \\ R_{y2} \\ R_{z1} \\ \vdots \\ T_{xN_{\mathrm{ALI}}} \\ T_{yN_{\mathrm{ALI}}} \\ T_{zN_{\mathrm{ALI}}} \\ R_{xN_{\mathrm{ALI}}} \\ R_{yN_{\mathrm{ALI}}} \\ R_{zN_{\mathrm{ALI}}} \end{pmatrix} \tag{3.6}$$

Using the matrix and vector notation, χ^2 can be rewritten as:

$$\chi^2 = \sum_{\text{tracks}} \mathbf{r}^T V^{-1} \mathbf{r} \tag{3.7}$$

Obviously the track-hit residual distributions will be centered around zero for a system which is well aligned, and biased or browder for a system in which the real location of the sensors is not precisely known. Therefore the alignment of the system requires the minimization of the χ^2 with respect to the alignment parameters:

$$\frac{d\chi^2}{d\mathbf{a}} = 0 \tag{3.8}$$

Combining the definition of the χ^2 with the condition of minimum:

$$\frac{d\chi^2}{d\mathbf{a}} = \frac{d}{d\mathbf{a}} \left[\sum_{\text{tracks}} \mathbf{r}^T V^{-1} \mathbf{r} \right] = \sum_{\text{tracks}} \left[\left(\frac{d\mathbf{r}}{d\mathbf{a}} \right)^T V^{-1} \mathbf{r} \right]^T + \sum_{\text{tracks}} \left[\mathbf{r}^T V^{-1} \left(\frac{d\mathbf{r}}{d\mathbf{a}} \right) \right] = 0 \tag{3.9}$$

where $\frac{d\mathbf{r}}{d\mathbf{a}}$ represents the matrix with the derivative of each residual with respect each alignment correction. Using the fact that V^{-1} is a symmetric matrix, the previous equation can be simplified to:

$$\frac{d\chi^2}{d\mathbf{a}} = 2 \sum_{\text{tracks}} \left[\mathbf{r}^T V^{-1} \left(\frac{d\mathbf{r}}{d\mathbf{a}} \right) \right] = 0 \tag{3.10}$$

For convenience, it is useful to transpose the above equation, which of course reads as:

$$\sum_{\text{tracks}} \left(\frac{d\mathbf{r}}{d\mathbf{a}}\right)^T V^{-1}\mathbf{r} = 0 \tag{3.11}$$

Now, the goal is to find the correction of the alignment parameters ($\delta\mathbf{a}$) that will satisfy this equation. Therefore, the total derivative of $\mathbf{r}$ with respect to $\mathbf{a}$ has to be evaluated as shown in the next section.

3.2.2.1 Residual derivatives

From equation 3.2, it is obvious that the residuals depend on both: the track and alignment parameters. Accordingly, its differential is:

$$d\mathbf{r} = \frac{\partial \mathbf{r}}{\partial \boldsymbol{\tau}} d\boldsymbol{\tau} + \frac{\partial \mathbf{r}}{\partial \mathbf{a}} d\mathbf{a} \tag{3.12}$$

and $d\mathbf{r}/d\boldsymbol{\tau}$ and $d\mathbf{r}/d\mathbf{a}$ can be calculated as:

$$\frac{d\mathbf{r}}{d\boldsymbol{\tau}} = \frac{\partial \mathbf{r}}{\partial \boldsymbol{\tau}}\frac{d\boldsymbol{\tau}}{d\boldsymbol{\tau}} + \frac{\partial \mathbf{r}}{\partial \mathbf{a}}\frac{d\mathbf{a}}{d\boldsymbol{\tau}} = \frac{\partial \mathbf{r}}{\partial \boldsymbol{\tau}} + \frac{\partial \mathbf{r}}{\partial \mathbf{a}}\frac{d\mathbf{a}}{d\boldsymbol{\tau}} = \frac{\partial \mathbf{r}}{\partial \boldsymbol{\tau}} \tag{3.13}$$

$$\frac{d\mathbf{r}}{d\mathbf{a}} = \frac{\partial \mathbf{r}}{\partial \boldsymbol{\tau}}\frac{d\boldsymbol{\tau}}{d\mathbf{a}} + \frac{\partial \mathbf{r}}{\partial \mathbf{a}}\frac{d\mathbf{a}}{d\mathbf{a}} = \frac{\partial \mathbf{r}}{\partial \boldsymbol{\tau}}\frac{d\boldsymbol{\tau}}{d\mathbf{a}} + \frac{\partial \mathbf{r}}{\partial \mathbf{a}} \tag{3.14}$$

Where in equation 3.13 it has already considered that the alignment parameters ($\mathbf{a}$) do not depend on the track parameters ($\boldsymbol{\tau}$). Inserting the expression (3.14) in the equation (6.11):

$$\sum_{\text{tracks}} \left(\frac{d\mathbf{r}}{d\mathbf{a}}\right)^T V^{-1}\mathbf{r} = \sum_{\text{tracks}} \left(\frac{\partial \mathbf{r}}{\partial \boldsymbol{\tau}}\frac{d\boldsymbol{\tau}}{d\mathbf{a}} + \frac{\partial \mathbf{r}}{\partial \mathbf{a}}\right)^T V^{-1}\mathbf{r} = 0 \tag{3.15}$$

then, the next step is to compute $d\boldsymbol{\tau}/d\mathbf{a}$. This requires a previous step: finding the track parameters. This is shown in the next section.

3.2.2.2 Track fitting

The solution for the track parameters for any arbitrary alignment and for every independent track has to been found. So the minimization of the χ^2 function with respect the track parameters ($\boldsymbol{\tau}$) for a given track is needed:

$$\chi^2 = \mathbf{r}^T V^{-1}\mathbf{r} \rightarrow \frac{d\chi^2}{d\boldsymbol{\tau}} = 0 \tag{3.16}$$

Again, the minimization condition is applied:

$$\frac{d\chi^2}{d\boldsymbol{\tau}} = 0 \tag{3.17}$$

This is the minimum condition, which with repeating the algebra can be expresed as:

$$\left(\frac{\partial \mathbf{r}}{\partial \boldsymbol{\tau}}\right)^T V^{-1}\mathbf{r} = 0 \tag{3.18}$$

Now, the goal is to find the track parameter corrections $\delta\boldsymbol{\tau}$ which have to be applied to the initial values ($\boldsymbol{\tau}_0$) to get the final track parameters $\boldsymbol{\tau} = \boldsymbol{\tau}_0 + \delta\boldsymbol{\tau}$. It can be assumed that the initial values $\boldsymbol{\tau}_0$ are close to the solution $\boldsymbol{\tau}$, so the residuals can be expanded around $\boldsymbol{\tau}_0$ with a first order Taylor expansion. High order derivatives are neglected since small changes to the track parameters are being considered. If the initial parameters are still far from the solution, iterations will be required in order to obtain the final corrections. Using this approximation, the residuals will change linearly around the initial track parameters as follows:

$$\mathbf{r}(\boldsymbol{\tau}, \mathbf{a}) = \mathbf{r}(\boldsymbol{\tau}_0, \mathbf{a}) + \left.\frac{\partial \mathbf{r}}{\partial \boldsymbol{\tau}}\right|_{\boldsymbol{\tau}=\boldsymbol{\tau}_0} \delta\boldsymbol{\tau} \tag{3.19}$$

And the matrix E can be defined as:

$$E \equiv \left.\frac{\partial \mathbf{r}}{\partial \boldsymbol{\tau}}\right|_{\boldsymbol{\tau}=\boldsymbol{\tau}_0} \tag{3.20}$$

Using the equation (3.19) the minimization condition (3.18) can be developed:

$$\begin{aligned}\left(\frac{\partial \mathbf{r}}{\partial \boldsymbol{\tau}}\right)^T V^{-1}\mathbf{r} = 0 \rightarrow \left(\left.\frac{\partial \mathbf{r}}{\partial \boldsymbol{\tau}}\right|_{\boldsymbol{\tau}=\boldsymbol{\tau}_0}\right)^T V^{-1}\left[\mathbf{r}(\boldsymbol{\tau}_0, \mathbf{a}) + \left.\frac{\partial \mathbf{r}}{\partial \boldsymbol{\tau}}\right|_{\boldsymbol{\tau}=\boldsymbol{\tau}_0}\delta\boldsymbol{\tau}\right] = \\ = E^T V^{-1}\left[\mathbf{r}(\boldsymbol{\tau}_0, \mathbf{a}) + E\delta\boldsymbol{\tau}\right] = E^T V^{-1}\mathbf{r}(\boldsymbol{\tau}_0, \mathbf{a}) + E^T V^{-1} E\delta\boldsymbol{\tau} = 0\end{aligned} \tag{3.21}$$

which allows to obtain the track parameters corrections $\delta\boldsymbol{\tau}$ as:

$$\delta\boldsymbol{\tau} = -(E^T V^{-1} E)^{-1} E^T V^{-1}\mathbf{r}(\boldsymbol{\tau}_0, \mathbf{a}) \tag{3.22}$$

In order to use a compact notation, the matrix $\mathcal{M}_t$ and vector v_t can be defined as:

$$\begin{aligned}\mathcal{M}_t &\equiv E^T V^{-1} E \\ v_t &\equiv E^T V^{-1}\mathbf{r}\end{aligned} \tag{3.23}$$

$\mathcal{M}_t$ is a $N_{\text{Trk}} \times N_{\text{Trk}}$ dimension matrix and v_t is a N_{Trk} dimension vector. The expression (3.22) which gives the corrections to the track parameters for an arbitrary track becomes:

$$\delta\boldsymbol{\tau} = -\mathcal{M}_t^{-1} v_t \tag{3.24}$$

and the final solution of the track parameters can be written as:

$$\boldsymbol{\tau} = \boldsymbol{\tau}_0 - \mathcal{M}_t^{-1} v_t \tag{3.25}$$

Once the track parameters are known, it is possible to compute $d\boldsymbol{\tau}/d\mathbf{a}$ differentiating the previous expression and considering that $d\boldsymbol{\tau}_0/d\mathbf{a}$, $dV/d\mathbf{a}$ and $dE/\mathbf{a} = \partial^2\mathbf{r}/\delta\mathbf{a}\delta\boldsymbol{\tau}$ are null or neglected:

$$\frac{d\boldsymbol{\tau}}{d\mathbf{a}} = \frac{d\boldsymbol{\tau}_0}{d\mathbf{a}} - \frac{d}{d\mathbf{a}}\left[(E^T V^{-1} E)^{-1} E^T V^{-1}\mathbf{r}(\boldsymbol{\tau}_0, \mathbf{a})\right] = -\mathcal{M}_t^{-1} E^T V^{-1} \left.\frac{d\mathbf{r}}{d\mathbf{a}}\right|_{\boldsymbol{\tau}=\boldsymbol{\tau}_0} \tag{3.26}$$

and assuming that $d\mathbf{r}/d\mathbf{a}|_{\boldsymbol{\tau}=\boldsymbol{\tau}_0} = \partial\mathbf{r}/\partial\mathbf{a}|_{\boldsymbol{\tau}=\boldsymbol{\tau}_0}$ because $\boldsymbol{\tau}_0$ is a fixed value so variations are only with respect to $\mathbf{a}$.

$$\frac{d\boldsymbol{\tau}}{d\mathbf{a}} = -\mathcal{M}_t^{-1} E^T V^{-1} \left.\frac{\partial \mathbf{r}}{\partial \mathbf{a}}\right|_{\boldsymbol{\tau}=\boldsymbol{\tau}_0} \tag{3.27}$$

Covariance matrix

After determining the track parameters, their error and correlations have to be estimated. The covariance matrix of the track parameter corrections ($\mathcal{C}$) is therefore needed. In this notation, $\mathbf{E}$ represents the expected value. The matrix is computed as:

$$\begin{aligned}
\mathcal{C} &= \mathbf{E}[(\delta\boldsymbol{\tau})(\delta\boldsymbol{\tau})^T] = \\
&= \mathbf{E}[\left((E^T V^{-1} E)^{-1} E^T V^{-1} \mathbf{r}(\boldsymbol{\tau}, \mathbf{a})\right) \left((E^T V^{-1} E)^{-1} E^T V^{-1} \mathbf{r}(\boldsymbol{\tau}, \mathbf{a})\right)^T] = \\
&= \mathbf{E}[\mathcal{M}_t^{-1} (E^T V^{-1} \mathbf{r})(\mathbf{r}^T V^{-1} E) \mathcal{M}_t^{-1} = \mathcal{M}_t^{-1} (E^T V^{-1} \mathbf{E}[\mathbf{r}\mathbf{r}^T] V^{-1} E) \mathcal{M}_t^{-1} = \\
&= \mathcal{M}_t^{-1} (E^T V^{-1} V V^{-1} E) \mathcal{M}_t^{-1}] = \mathcal{M}_t^{-1} \mathcal{M}_t \mathcal{M}_t^{-1} = \mathcal{M}_t^{-1}
\end{aligned} \tag{3.28}$$

where the equivalence $\mathbf{E}[\mathbf{r}\mathbf{r}^T] = V$ has been used. Therefore, the covariance matrix of the track parameters is:

$$\mathcal{C} = \mathcal{M}_t^{-1} = (E^T V^{-1} E)^{-1} \tag{3.29}$$

coinciding with the matrix of the χ^2 track parameters fit.

3.2.2.3 Alignment corrections fit

The corrections to the track parameters for any alignment parameter set and $d\boldsymbol{\tau}/d\mathbf{a}$ have been calculated in the previous section. Those tracks and their residuals will be used to find the alignment parameters by minimizing the χ^2. Considering that the solution is calculated for the initial parameters $\boldsymbol{\tau}_0$. Substituting the expressions (3.20) and (3.27) in (3.15):

$$\begin{aligned}
&\sum_{\text{tracks}} \left(\frac{\partial \mathbf{r}}{\partial \boldsymbol{\tau}} \frac{d\boldsymbol{\tau}}{d\mathbf{a}} + \frac{\partial \mathbf{r}}{\partial \mathbf{a}} \right)^T V^{-1} \mathbf{r} = \sum_{\text{tracks}} \left(-E \mathcal{M}_t^{-1} E^T V^{-1} \frac{\partial \mathbf{r}}{\partial \mathbf{a}} + \frac{\partial \mathbf{r}}{\partial \mathbf{a}} \right)^T V^{-1} \mathbf{r} = \\
&\sum_{\text{tracks}} \left((I - E \mathcal{M}_t^{-1} E^T V^{-1}) \frac{\partial \mathbf{r}}{\partial \mathbf{a}} \right)^T V^{-1} \mathbf{r} = \sum_{\text{tracks}} \left((I - \mathcal{G}_E) \frac{\partial \mathbf{r}}{\partial \mathbf{a}} \right)^T V^{-1} \mathbf{r} = 0
\end{aligned} \tag{3.30}$$

where the matrix $\mathcal{G}_E$ has been defined to pack the notation:

$$\mathcal{G}_E = E \mathcal{M}_t^{-1} E^T V^{-1} \tag{3.31}$$

Note that the matrix $\mathcal{G}_E$ has dimension $N_{\text{RES}} \times N_{\text{RES}}$. The matrix E is the core of the Globalχ^2 method because this matrix correlates the modules that enter in the reconstruction of the same track. For each track, the derivatives of the residuals from different modules will be computed with respect the same track parameters. If E is neglected or

discarded, then $\mathcal{G}_E$ will be consequently null and the module correlations will be lost (this is actually the case of Localχ^2 method). A weight matrix W can be defined as:

$$W \equiv (I - \mathcal{G}_E)^T V^{-1} = (I - \mathcal{G}_E^T) V^{-1} \tag{3.32}$$

and then the equation (3.30) becomes:

$$\sum_{\text{tracks}} \left(\frac{d\mathbf{r}}{d\mathbf{a}} \right)^T V^{-1} \mathbf{r} = \sum_{\text{tracks}} \left(\frac{\partial \mathbf{r}}{\partial \mathbf{a}} \right)^T W \mathbf{r} \tag{3.33}$$

When module correlations are not considered (E is taken as 0) then $W = V^{-1}$, the weight matrix becomes just the hit covariance matrix.

Now in order to compute the alignment corrections, one applies almost the same idea that in the previous section. Let be $\mathbf{a}$ the set of alignment parameters and $\mathbf{a}_0$ the set of initial alignment parameters. The goal is to find the corrections ($\delta\mathbf{a}$) such that $\mathbf{a} = \mathbf{a}_0 + \delta\mathbf{a}$ minimizes the χ^2. As in the expression (3.19), the residuals will be assumed to change linearly with $\delta\mathbf{a}$ around the initial values. Using a series expansion of the residuals the next expression can be obtained:

$$\mathbf{r} = \mathbf{r}(\boldsymbol{\tau}_0, \mathbf{a}_0) + \left. \frac{\partial \mathbf{r}}{\partial \mathbf{a}} \right|_{\mathbf{a}=\mathbf{a}_0} \delta\mathbf{a} \tag{3.34}$$

The $\boldsymbol{\tau}_0$ is used as it represents the track parameters fitted with the initial set of alignment constants. Then inserting (3.34) in (3.33):

$$\sum_{\text{tracks}} \left(\frac{\partial \mathbf{r}}{\partial \mathbf{a}} \right)^T W \mathbf{r} + \sum_{\text{tracks}} \left(\frac{\partial \mathbf{r}}{\partial \mathbf{a}} \right)^T W \left(\frac{\partial \mathbf{r}}{\partial \mathbf{a}} \right) \delta\mathbf{a} = 0 \tag{3.35}$$

where $\mathbf{r}$ means $\mathbf{r}(\boldsymbol{\tau}_0, \mathbf{a}_0)$ and $\partial\mathbf{r}/\partial\mathbf{a}$ means $\partial\mathbf{r}/\partial\mathbf{a}|_{\boldsymbol{\tau}=\boldsymbol{\tau}_0, \mathbf{a}=\mathbf{a}_0}$ to simplify the notation. Proceeding as in equation (3.22):

$$\delta\mathbf{a} = -\left[\sum_{\text{tracks}} \left(\frac{\partial \mathbf{r}}{\partial \mathbf{a}} \right)^T W \left(\frac{\partial \mathbf{r}}{\partial \mathbf{a}} \right) \right]^{-1} \sum_{\text{tracks}} \left(\frac{\partial \mathbf{r}}{\partial \mathbf{a}} \right)^T W \mathbf{r} \tag{3.36}$$

This would provide a solution for $\delta\mathbf{a}$ which is a column vector of dimension $N_{\text{ALI}} \times 1$. The previous expression represents a set of N_{ALI} equations, one for each DoF of each module being aligned. This equation can be written in a more compact form defining a new matrix and a vector:

$$\mathcal{M} = \left[\sum_{\text{tracks}} \left(\frac{\partial \mathbf{r}}{\partial \mathbf{a}} \right)^T W \left(\frac{\partial \mathbf{r}}{\partial \mathbf{a}} \right) \right] = \left[\sum_{\text{tracks}} \left(\frac{\partial \mathbf{r}}{\partial \mathbf{a}} \right)^T (I - \mathcal{G}_E^T) V^{-1} \left(\frac{\partial \mathbf{r}}{\partial \mathbf{a}} \right) \right] \tag{3.37}$$

$$v = \sum_{\text{tracks}} \left(\frac{\partial \mathbf{r}}{\partial \mathbf{a}} \right)^T W \mathbf{r} = \sum_{\text{tracks}} \left(\frac{\partial \mathbf{r}}{\partial \mathbf{a}} \right)^T (I - \mathcal{G}_E^T) V^{-1} \mathbf{r} \tag{3.38}$$

The matrix $\mathcal{M}$ is called *big-matrix* and has a dimension of $N_{\text{ALI}} \times N_{\text{ALI}}$. The vector v is the *big-vector* with N_{ALI} components. Using these two new definitions, the expression (3.36) can be represented as:

$$\delta\mathbf{a} = -\mathcal{M}^{-1} v \tag{3.39}$$

The matrix $\mathcal{M}^{-1}$ is in fact the covariance matrix of the alignment parameter corrections as it was demonstrated with the track parameters and the matrix $\mathcal{M}_t^{-1}$. So inverting $\mathcal{M}$ the corrections to the alignment parameters can be obtained as well their errors and correlations. Finally, the new alignment parameters can be obtained:

$$\mathbf{a} = \mathbf{a}_0 + \delta\mathbf{a} = \mathbf{a}_0 - \mathcal{M}^{-1}v \tag{3.40}$$

This method can be iterative repeating this procedure as many times as needed changing the initial alignment parameters:

$$\mathbf{a}_{\text{IterN}} = \mathbf{a}_{\text{IterN-1}} + \delta\mathbf{a}_{\text{IterN}} \tag{3.41}$$

The determination of a solution to the alignment problem involves two steps:

- Filling the Globalχ^2 alignment matrix ($\mathcal{M}$) and the alignment vector (v) from all the reconstructed tracks considered for the alignment.
- Solving the system of linear equations.

The size of the alignment matrix may vary by several orders of magnitude. A few tens of degrees of freedom are considered when aligning large structures like barrels and/or end-caps, and many thousands when aligning all modules of the system. In the case of the Globalχ^2 algorithm the alignment matrix is usually dense. This is because the Globalχ^2 method correlates the alignable structures that participate in the reconstruction of the same track. The matrix may become highly dense when filled with cosmic-rays tracks, because these tracks correlate detector regions different that the collision tracks that are pointing to the detector centre Figure 3.5.

Inverting small matrices is not a major issue, even for dense matrices. However if the matrix is not sparse and its size is large, then solving the linear system in the equation (3.39) is quite challenging from the computational point of view.

3.2.3 Localχ^2 formalism

A very practical way of making the alignment matrix sparse is by performing a Localχ^2 alignment [36, 37]. In this case the correlation between alignable structures is discarded and the tracks are not refitted. The correlation between structures is implicitly included. So in the Localχ^2 case, each structure is aligned locally with respect to the others. In the Localχ^2 approach the alignment matrix ($\mathcal{M}'$) and the alignment vector (v') from equation (3.39) are reduced to:

$$\begin{aligned} \mathcal{M}' &= \sum_{\text{tracks}} \left[\left(\frac{\partial \mathbf{r}}{\partial \mathbf{a}} \right)^T V^{-1} \left(\frac{\partial \mathbf{r}}{\partial \mathbf{a}} \right) \right] \\ v' &= \sum_{\text{tracks}} \left(\frac{\partial \mathbf{r}}{\partial \mathbf{a}} \right)^T V^{-1}\mathbf{r} \end{aligned} \tag{3.42}$$

The crucial point in the Localχ^2 approach is that $\mathcal{M}'$ becomes 6×6 block diagonal. Hence, the Localχ^2 method is less demanding in computer resources because the matrix inversion is much less CPU time consuming than the full Globalχ^2 matrix. On the other hand, in the Localχ^2 method, the correlation between alignable structures is just recovered by successive iterations, and more of those are needed to reach convergence.

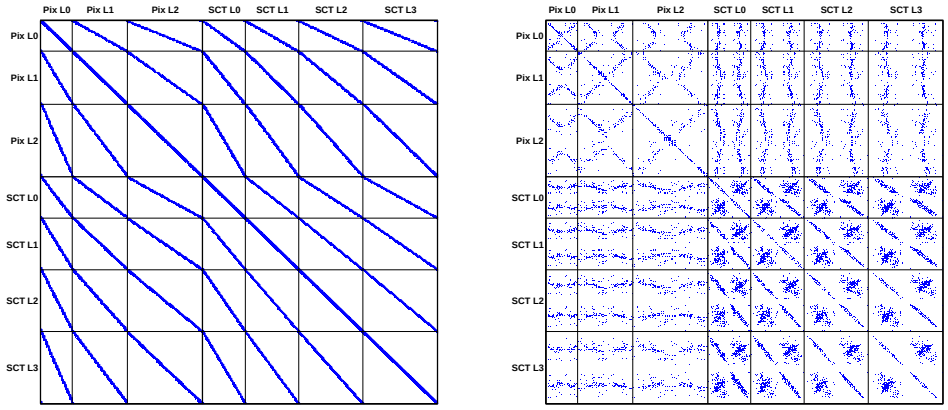

Figure 3.5: Plots showing the alignment matrix at module level for two different kind of data: collision tracks in the left and cosmic rays in the right. The correlation between different modules are showed as the matrix is populated in a different manner.

3.2.4 Derivatives of the residuals

Through the previous section, the derivatives of the residuals whit respect track and alignment parameters have been used. These derivatives are used to compute the *big-vector* and *big-matrix*. This section deals with the algebraic computation of the mentioned derivatives.

3.2.4.1 Derivatives with respect to the alignment parameters

The derivatives in this section are given for planar sensors which can measure either 1 (SCT module sides) or 2 (pixels) coordinates. The Z axis is considered to be out of the plane. The measurements are recorded in the sensor XY plane whilst no measurement is given in the Z direction. The coordinates of any point in the sensing plane can be expressed:

$$\mathbf{v} = \begin{pmatrix} v_x \\ v_y \\ 0 \end{pmatrix} \tag{3.43}$$

Obviously, the components of $\mathbf{v}$ can be extracted via:

$$\begin{aligned} v_x &= \hat{\mathbf{X}}^T \cdot \mathbf{v} \\ v_y &= \hat{\mathbf{Y}}^T \cdot \mathbf{v} \\ v_z &= \hat{\mathbf{Z}}^T \cdot \mathbf{v} \end{aligned} \tag{3.44}$$

being $\hat{\mathbf{X}}$,$\hat{\mathbf{Y}}$ and $\hat{\mathbf{Z}}$ the unit vectors of the sensor surface: X,Y and Z axis.

Then, for a given coordinate (e.g. x), the derivatives with respect the alignment parameters are:

$$\begin{aligned}\frac{\partial v_x}{\partial t_x} &= \hat{\mathbf{X}}_S^T \frac{\partial \mathbf{v}}{\partial t_x} \\ \frac{\partial v_x}{\partial t_y} &= \hat{\mathbf{X}}_S^T \frac{\partial \mathbf{v}}{\partial t_y} \\ \frac{\partial v_x}{\partial t_z} &= \hat{\mathbf{X}}_S^T \frac{\partial \mathbf{v}}{\partial t_z}\end{aligned} \tag{3.45}$$

Other components ar computed in a similar manner. In the next section the calculation of the within plane residuals will be computed.

3.2.4.2 Computing $\partial r/\partial a$: residuals on the sensing plane

This section will focus on how the within plane residuals change as function of the local frame movements: translations and rotations. Two main cases can be distinguished:

- Within plane motions. The XY plane remains the same, then the extrapolated point remains physically the same point, only the reference frame changes and so do the coordinates of the point.
- Out of plane motions. In this case the XY plane changes, then the extrapolated point also changes, as its coordinates in the new frame.

Lets consider first the derivatives with respect to the three translations. Obviously t_x and t_y are within plane, whilst t_z are out plane. Derivating analytically, the derivatives for the within plane translations are:

$$\begin{aligned}\frac{\partial v_x}{\partial t_x} &= \lim_{t_x \to 0} \frac{v_x^{'} - v_x}{t_x} = \lim_{t_x \to 0} \frac{v_x - t_x - v_x}{t_x} = -1 \\ \frac{\partial v_y}{\partial t_x} &= 0 \\ \frac{\partial v_z}{\partial t_x} &= 0 \\ \frac{\partial v_x}{\partial t_y} &= 0 \\ \frac{\partial v_y}{\partial t_y} &= \lim_{t_y \to 0} \frac{v_y^{'} - v_y}{t_y} = \lim_{t_y \to 0} \frac{v_y - t_y - v_y}{t_y} = -1 \\ \frac{\partial v_z}{\partial t_y} &= 0\end{aligned} \tag{3.46}$$

For derivatives with respect to the movements along the Z axis, the angles Θ and Φ need to be defined. These are defined as the angles of the trajectory in the local axis system at the intersection point. The relations $L = t_z / \cos\Theta$, $v_x^{'} = v_x + L \sin\Theta \cos\Phi$ and $v_y^{'} = v_y + L \sin\Theta \sin\Phi$ are also defined as seen in the Figure 3.6:

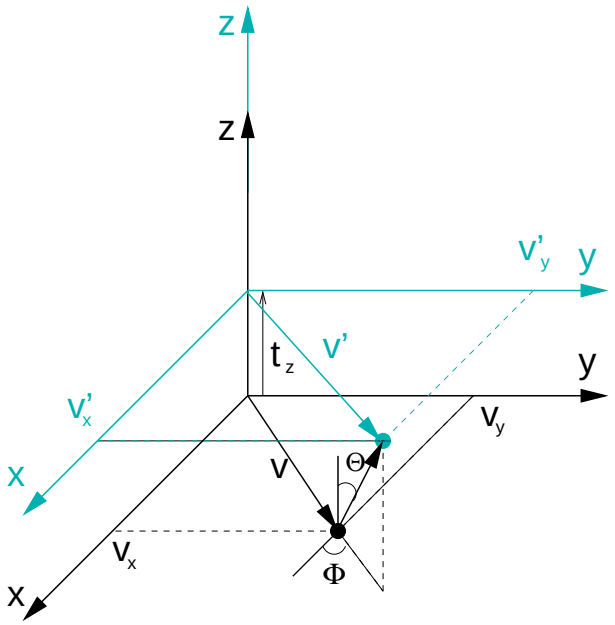

Figure 3.6: Effect of a translation along the local Z direction on the coordinates of a given vector **v** which is in the XY plane. Now the extrapolated point physically changes according to the incidence angles at the extrapolated point in the original frame.

$$\begin{aligned}\frac{\partial v_x}{\partial t_z} &= \lim_{t_z\to 0}\frac{v_x' - v_x}{t_z} = \lim_{t_z\to 0}\frac{v_x + t_z\sin\Theta\cos\Phi/\cos\Theta - v_x}{t_z} = \tan\Theta\cos\Phi \\ \frac{\partial v_y}{\partial t_z} &= \lim_{t_z\to 0}\frac{v_y' - v_y}{t_z} = \lim_{t_z\to 0}\frac{v_y + t_z\sin\Theta\sin\Phi/\cos\Theta - v_y}{t_z} = \tan\Theta\sin\Phi\end{aligned} \tag{3.47}$$

and as v is a vector in the XY plane:

$$\frac{\partial v_z}{\partial t_z} = 0 \tag{3.48}$$

3.2.5 Globalχ^2 algorithm with track parameter constraints

The solution of the alignment parameters presented in section 3.2.2 does not contain any external constraint imposed in the solution. This kind of constraints can be introduced in the algorithm. The external constraints can be implemented in two ways: extra χ^2 terms with different dependencies for the residuals and Lagrange multipliers. In this section the inclusion of extra χ^2 constraints with linear dependence on the reconstructed track parameters will be explained. A general new residual-like vector can be defined as $\mathbf{R}_{\boldsymbol{\tau}} = \mathbf{R}_{\boldsymbol{\tau}}(\boldsymbol{\tau})$. The size of the vector is N_{TRP}, being N_{TRP} the number of track

parameters. Adding a new term to the original χ^2 has the following form:

$$\chi^2 = \chi^2_{\text{basic}} + \chi^2_{\text{trkConst}} = \sum_{\text{tracks}} \mathbf{r}^T(\boldsymbol{\tau}, \mathbf{a}) V^{-1} \mathbf{r}(\boldsymbol{\tau}, \mathbf{a}) + \sum_{\text{tracks}} \mathbf{R}^T_{\boldsymbol{\tau}}(\boldsymbol{\tau}) S^{-1} \mathbf{R}_{\boldsymbol{\tau}}(\boldsymbol{\tau}) \tag{3.49}$$

where the second term is the contribution to the χ^2 from the track constraints. S is a matrix that defines the tolerances of the track constraints. The track constraints only depend on the track parameters and not on the alignment ones. This has the consequence:

$$d\mathbf{R}_{\boldsymbol{\tau}} = \frac{\partial \mathbf{R}_{\boldsymbol{\tau}}}{\partial \boldsymbol{\tau}} d\boldsymbol{\tau} \tag{3.50}$$

and therefore:

$$\begin{aligned} \frac{d\mathbf{R}_{\boldsymbol{\tau}}}{d\mathbf{a}} &= \frac{\partial \mathbf{R}_{\boldsymbol{\tau}}}{\partial \boldsymbol{\tau}} \frac{d\boldsymbol{\tau}}{d\mathbf{a}} \\ \frac{d\mathbf{R}_{\boldsymbol{\tau}}}{d\boldsymbol{\tau}} &= \frac{\partial \mathbf{R}_{\boldsymbol{\tau}}}{\partial \boldsymbol{\tau}} \end{aligned} \tag{3.51}$$

R_τ can represent constraints in the impact parameter to force the track to came from the primary vertex or beamspot. It can also represent the momentum to match it to the measurement provided by other subsystem as the calorimeters, etc. The goal still is to minimize the χ^2 with respect to the alignment parameters requiring:

$$\frac{d\chi^2}{d\mathbf{a}} = 0 \tag{3.52}$$

Therefore differentiating the expression 3.49 with respect to the alignment parameters and requiring the previous condition of minimum leads to:

$$\sum_{\text{tracks}} \left(\frac{d\mathbf{r}}{d\mathbf{a}} \right)^T V^{-1} \mathbf{r} + \sum_{\text{tracks}} \left(\frac{d\mathbf{R}_{\boldsymbol{\tau}}}{d\mathbf{a}} \right)^T S^{-1} \mathbf{R}_{\boldsymbol{\tau}} = 0 \tag{3.53}$$

And bringing the derivatives $d\mathbf{r}/d\mathbf{a}$ and $d\mathbf{R}_{\boldsymbol{\tau}}/d\mathbf{a}$ into the previous equation, it becomes:

$$\sum_{\text{tracks}} \left(\frac{\partial \mathbf{r}}{\partial \boldsymbol{\tau}} \frac{d\boldsymbol{\tau}}{d\mathbf{a}} + \frac{\partial \mathbf{r}}{\partial \mathbf{a}} \right)^T V^{-1} \mathbf{r} + \sum_{\text{tracks}} \left(\frac{\partial \mathbf{R}_{\boldsymbol{\tau}}}{\partial \boldsymbol{\tau}} \frac{d\boldsymbol{\tau}}{d\mathbf{a}} \right)^T S^{-1} \mathbf{R}_{\boldsymbol{\tau}} = 0 \tag{3.54}$$

Now the derivative $d\boldsymbol{\tau}/d\mathbf{a}$ is needed to be determined. The way to proceed is through the track fitting as seen in section 3.2.2.2, which means determining the correction to the track parameters ($\delta\boldsymbol{\tau}$) for an arbitrary alignment to calculate $\boldsymbol{\tau} = \boldsymbol{\tau}_0 + \delta\boldsymbol{\tau}$ and then the derivative $d\boldsymbol{\tau}/d\mathbf{a}$ as done before in section 3.2.2.3. Only this time the track parameter constraints have to be included in the track fit.

3.2.5.1 Track fitting with track parameter constraints

The track fitting is very similar to the one explained in section 3.2.2.2 but now with the new χ^2 (3.49) as input. For a given track:

$$\frac{d\chi^2}{d\boldsymbol{\tau}} = \frac{\partial \chi^2}{\partial \boldsymbol{\tau}} = 0 \rightarrow \left(\frac{\partial \mathbf{r}}{\partial \boldsymbol{\tau}} \right)^T V^{-1} \mathbf{r} + \left(\frac{\partial \mathbf{R}_{\boldsymbol{\tau}}}{\partial \boldsymbol{\tau}} \right)^T S^{-1} \mathbf{R}_{\boldsymbol{\tau}} = 0 \tag{3.55}$$

Using Taylor series expansion around the initial values $\boldsymbol{\tau}_0$ and neglecting second and higher order derivatives:

$$\begin{aligned}\mathbf{r}(\boldsymbol{\tau},\mathbf{a}) &= \mathbf{r}(\boldsymbol{\tau}_0,\mathbf{a}) + \left.\frac{\partial \mathbf{r}}{\partial \boldsymbol{\tau}}\right|_{\boldsymbol{\tau}=\boldsymbol{\tau}_0} \delta\boldsymbol{\tau} \\ \mathbf{R}_{\boldsymbol{\tau}}(\boldsymbol{\tau}) &= \mathbf{R}_{\boldsymbol{\tau}}(\boldsymbol{\tau}_0) + \left.\frac{\partial \mathbf{R}_{\boldsymbol{\tau}}}{\partial \boldsymbol{\tau}}\right|_{\boldsymbol{\tau}=\boldsymbol{\tau}_0} \delta\boldsymbol{\tau}\end{aligned} \tag{3.56}$$

and here F can be defined in a form similar to E:

$$F_{\boldsymbol{\tau}} \equiv \left.\frac{\mathbf{R}_{\boldsymbol{\tau}}}{\partial \boldsymbol{\tau}}\right|_{\boldsymbol{\tau}=\boldsymbol{\tau}_0} \tag{3.57}$$

and now including in the equation 3.55 the series expansion with $F_{\boldsymbol{\tau}}$ and E:

$$\begin{aligned}\frac{\partial \chi^2}{\partial \boldsymbol{\tau}} &= E^T V^{-1}[\mathbf{r}(\boldsymbol{\tau}_0,\mathbf{a}) + E\delta\boldsymbol{\tau}] + F_{\boldsymbol{\tau}}^T S^{-1}[\mathbf{R}_{\boldsymbol{\tau}}(\boldsymbol{\tau}_0) + F_{\boldsymbol{\tau}}\delta\boldsymbol{\tau}] = \\ &= E^T V^{-1}\mathbf{r}(\boldsymbol{\tau}_0,\mathbf{a}) + F_{\boldsymbol{\tau}}^T S^{-1}\mathbf{R}_{\boldsymbol{\tau}}(\boldsymbol{\tau}_0) + E^T V^{-1} E\delta\boldsymbol{\tau} + F_{\boldsymbol{\tau}}^T S^{-1} F_{\boldsymbol{\tau}}\delta\boldsymbol{\tau} = \\ &= (E^T V^{-1} E + F_{\boldsymbol{\tau}}^T S^{-1} F_{\boldsymbol{\tau}})\delta\boldsymbol{\tau} + (E^T V^{-1}\mathbf{r}(\boldsymbol{\tau}_0,\mathbf{a}) + F_{\boldsymbol{\tau}} S^{-1}\mathbf{R}_{\boldsymbol{\tau}}(\boldsymbol{\tau}_0)) = 0\end{aligned} \tag{3.58}$$

and then, the corrections to the track parameters fitted with the constraints are:

$$\delta\boldsymbol{\tau} = -(E^T V^{-1} E + F_{\boldsymbol{\tau}}^T S^{-1} F_{\boldsymbol{\tau}})^{-1}(E^T V^{-1}\mathbf{r}(\boldsymbol{\tau}_0,\mathbf{a}) + F_{\boldsymbol{\tau}} S^{-1}\mathbf{R}_{\boldsymbol{\tau}}(\boldsymbol{\tau}_0)) \tag{3.59}$$

The previous expression can be rewritten defining:

$$\begin{aligned}\mathcal{M}_t &\equiv E^T V^{-1} E \\ \mathcal{M}_{t_\tau} &\equiv F_\tau^T S^{-1} F_\tau \\ \tilde{\mathcal{M}}_t &\equiv \mathcal{M}_t + \mathcal{M}_{t_\tau} \\ v_t &\equiv E^T V^{-1}\mathbf{r}(\boldsymbol{\tau}_0,\mathbf{a}) \\ v_{t_\tau} &\equiv F_\tau^T S^{-1}\mathbf{R}_{\boldsymbol{\tau}}(\boldsymbol{\tau}_0)\end{aligned} \tag{3.60}$$

And finally:

$$\delta\boldsymbol{\tau} = -(\mathcal{M}_t + \mathcal{M}_{t_\tau})^{-1}(v_t + v_{t_\tau}) = -\tilde{\mathcal{M}}_t{}^{-1}(v_t + v_{t_\tau}) \tag{3.61}$$

It is clear that introducing an extra term to the χ^2 with only track parameters dependence, the new solution in the track fitting has the same structure but adding a new matrix $\mathcal{M}_{t_\tau}$) and vector v_{t_τ}. The solution of the track parameters is: $d\boldsymbol{\tau} = \boldsymbol{\tau}_0 + \delta\boldsymbol{\tau}$ and evaluating $d\boldsymbol{\tau}/d\mathbf{a}$ differentiating this solution:

$$\frac{d\boldsymbol{\tau}}{d\mathbf{a}} = -\tilde{\mathcal{M}}_t{}^{-1} E^T V^{-1}\frac{\partial \mathbf{r}(\boldsymbol{\tau}_0,\mathbf{a})}{\partial \mathbf{a}} \tag{3.62}$$

because $\partial \mathbf{R}_{\boldsymbol{\tau}}(\boldsymbol{\tau}_0)/\partial\boldsymbol{\tau} = 0$. The difference with respect the case without track constraint is that now the track tolerance matrix (S) and F_τ play also an important role in the derivative of the track parameters with respect to the alignment ones.

3.2.5.2 Alignment corrections fit with track constraints

After the calculation of $d\boldsymbol{\tau}/d\mathbf{a}$ (equation (3.62)) the fit of the alignment corrections can be done. Assuming $\mathbf{r}(\boldsymbol{\tau}_0, \mathbf{a})$ and $\mathbf{R}_{\boldsymbol{\tau}}(\boldsymbol{\tau}_0)$ and including 3.62, the expression 3.54 becomes:

$$\sum_{\text{tracks}} \left(-E\tilde{\mathcal{M}_t}^{-1} E^T V^{-1} \frac{\partial \mathbf{r}}{\partial \mathbf{a}} + \frac{\partial \mathbf{r}}{\partial \mathbf{a}} \right)^T V^{-1}\mathbf{r} + \sum_{\text{tracks}} \left(-F_\tau \tilde{\mathcal{M}_t}^{-1} E^T V^{-1} \frac{\partial \mathbf{r}}{\partial \mathbf{a}} \right)^T S^{-1}\mathbf{R}_{\boldsymbol{\tau}} = 0 \tag{3.63}$$

A new term can be defined to simplify the expression:

$$\mathcal{G}_{\text{EF}_\tau} \equiv \tilde{\mathcal{M}_t}^{-1} E^T V^{-1} \tag{3.64}$$

and the previous expression becomes:

$$\begin{aligned} &\sum_{\text{tracks}} \left(-E\mathcal{G}_{\text{EF}_\tau} \frac{\partial \mathbf{r}}{\partial \mathbf{a}} + \frac{\partial \mathbf{r}}{\partial \mathbf{a}} \right)^T V^{-1}\mathbf{r} - \sum_{\text{tracks}} \left(F_\tau \mathcal{G}_{\text{EF}_\tau} \frac{\partial \mathbf{r}}{\partial \mathbf{a}} \right)^T S^{-1}\mathbf{R}_{\boldsymbol{\tau}} = \\ &= \sum_{\text{tracks}} \left(\frac{\partial \mathbf{r}}{\partial \mathbf{a}} \right)^T \left(I - E\mathcal{G}_{\text{EF}_\tau}\right)^T V^{-1}\mathbf{r} - \sum_{\text{tracks}} \left(\frac{\partial \mathbf{r}}{\partial \mathbf{a}} \right)^T \left(F_\tau \mathcal{G}_{\text{EF}_\tau}\right)^T S^{-1}\mathbf{R}_{\boldsymbol{\tau}} = 0 \end{aligned} \tag{3.65}$$

Defining a new weight matrix $W' \equiv (I - E\mathcal{G}_{\text{EF}_\tau})^T V^{-1}$:

$$\sum_{\text{tracks}} \left(\frac{\partial \mathbf{r}}{\partial \mathbf{a}} \right)^T W'\mathbf{r} - \sum_{\text{tracks}} \left(\frac{\partial \mathbf{r}}{\partial \mathbf{a}} \right)^T \left(F_\tau \mathcal{G}_{\text{EF}_\tau}\right)^T \mathbf{R}_{\boldsymbol{\tau}} = 0 \tag{3.66}$$

And again, a series expansion is needed to solve the problem. In this case the expansion of for $\mathbf{R}_{\boldsymbol{\tau}}(\boldsymbol{\tau}_0)$ is not needed as it does not depend on $\mathbf{a}$ and the $\mathbf{r}(\boldsymbol{\tau}_0, \mathbf{a})$ expansion around $\mathbf{a}_0$ is just:

$$\mathbf{r}(\boldsymbol{\tau}_0, \mathbf{a}) = \mathbf{r}(\boldsymbol{\tau}_0, \mathbf{a}_0) + \left.\frac{\partial \mathbf{r}}{\partial \mathbf{a}}\right|_{\mathbf{a}=\mathbf{a}_0} \delta\mathbf{a} \tag{3.67}$$

Using this in the previous expression:

$$\begin{aligned} &\sum_{\text{tracks}} \left(\frac{\partial \mathbf{r}}{\partial \mathbf{a}} \right)^T W'\mathbf{r}(\boldsymbol{\tau}_0, \mathbf{a}_0) + \sum_{\text{tracks}} \left(\frac{\partial \mathbf{r}}{\partial \mathbf{a}} \right)^T W' \left(\frac{\partial \mathbf{r}}{\partial \mathbf{a}} \right) \delta\mathbf{a} \\ &- \sum_{\text{tracks}} \left(\frac{\partial \mathbf{r}}{\partial \mathbf{a}} \right)^T \left(F_\tau \mathcal{G}_{\text{EF}_\tau}\right)^T S^{-1}\mathbf{R}_{\boldsymbol{\tau}} = 0 \end{aligned} \tag{3.68}$$

and isolating $\delta\mathbf{a}$, it is obtained:

$$\delta\mathbf{a} = -\left(\sum_{\text{tracks}} \left(\frac{\partial \mathbf{r}}{\partial \mathbf{a}} \right)^T W' \frac{\partial \mathbf{r}}{\partial \mathbf{a}} \right)^{-1} \sum_{\text{tracks}} \left(\left(\frac{\partial \mathbf{r}}{\partial \mathbf{a}} \right)^T W'\mathbf{r} - \left(\frac{\partial \mathbf{r}}{\partial \mathbf{a}} \right)^T \left(F_\tau \mathcal{G}_{\text{EF}_\tau}\right)^T S^{-1}\mathbf{R}_{\boldsymbol{\tau}} \right) \tag{3.69}$$

where $\mathbf{r} \equiv \mathbf{r}(\boldsymbol{\tau}_0, \mathbf{a}_0)$ and $\mathbf{R}_{\boldsymbol{\tau}} \equiv \mathbf{R}_{\boldsymbol{\tau}}(\boldsymbol{\tau}_0)$. To write the previous equation in a compact way a new *big-matrix*($\mathcal{M}_\tau$) and *big-vector*(v_τ) plus an extra *big-vector*(w_τ) can be defined:

$$\begin{aligned} \mathcal{M}_\tau &\equiv \sum_{\text{tracks}} \left(\frac{\partial \mathbf{r}}{\partial \mathbf{a}}\right)^T W' \left(\frac{\partial \mathbf{r}}{\partial \mathbf{a}}\right) \\ v_\tau &\equiv \sum_{\text{tracks}} \left(\frac{\partial \mathbf{r}}{\partial \mathbf{a}}\right)^T W' \mathbf{r} \\ w_\tau &\equiv -\sum_{\text{tracks}} \left(\frac{\partial \mathbf{r}}{\partial \mathbf{a}}\right)^T (F_\tau \mathcal{G}_{\text{EF}_\tau})^T S^{-1} \mathbf{R}_{\boldsymbol{\tau}} \end{aligned} \tag{3.70}$$

Using this definitions a compact way for $\delta\mathbf{a}$ is obtained:

$$\delta\mathbf{a} = -\mathcal{M}_\tau^{-1}(v_\tau + w_\tau) \tag{3.71}$$

being the final solution:

$$\mathbf{a} = \mathbf{a}_0 - \mathcal{M}_\tau^{-1}(v_\tau + w_\tau) \tag{3.72}$$

which is the general solution for $\mathbf{a}$ when the χ^2 contains the constraints of the track parameters. The differences between the solution without constraint are an additional big-vector and W'.

3.2.6 Application of track parameter constraints

3.2.6.1 External track parameters constraint

The simplest case is to consider a residual like $\mathbf{R}_{\boldsymbol{\tau}}(\boldsymbol{\tau}) = (\boldsymbol{\tau} - \hat{\boldsymbol{\tau}})$ where $\hat{\tau}$ would be the external track parameters and $\boldsymbol{\tau}$ the original track parameters. Considering the helix parameters representations, $\mathbf{R}_{\boldsymbol{\tau}}$ is:

$$\mathbf{R}_{\boldsymbol{\tau}}(\boldsymbol{\tau}) = \begin{pmatrix} d_0 - \widehat{d_0} \\ z_0 - \widehat{z_0} \\ \phi_0 - \widehat{\phi_0} \\ \cot(\theta) - \widehat{\cot(\theta)} \\ q/p - \widehat{q/p} \end{pmatrix} \tag{3.73}$$

where the track parameters are considered independent. The covariance matrix will be:

$$S^{-1} = \begin{pmatrix} 1/\sigma^2_{d_0} & 0 & 0 & 0 & 0 \\ 0 & 1/\sigma^2_{dz0} & 0 & 0 & 0 \\ 0 & 0 & 1/\sigma^2_{\phi_0} & 0 & 0 \\ 0 & 0 & 0 & 1/\sigma^2_{\cot\theta} & 0 \\ 0 & 0 & 0 & 0 & 1/\sigma^2_{q/p} \end{pmatrix} \tag{3.74}$$

where each σ is the tolerance on the determination of the corresponding track parameter. In this case F_τ is the identity matrix because there are no correlations between track parameters.

$$F_\tau = \frac{\partial \mathbf{R}_\tau}{\partial \pi} = \frac{\partial(\boldsymbol{\tau} - \hat{\boldsymbol{\tau}})}{\partial \boldsymbol{\tau}} = \frac{\partial \boldsymbol{\tau}}{\partial \boldsymbol{\tau}} = I \tag{3.75}$$

Using this, $\tilde{\mathcal{M}}_t$ becomes:

$$\tilde{\mathcal{M}}_t = E^T V^{-1} E + S^{-1} \tag{3.76}$$

and the term $\mathcal{G}_{\mathrm{EF}_\tau}$:

$$\mathcal{G}_{\mathrm{EF}_\tau} = (E^T V^{-1} E + S^{-1})^{-1} E^T V^{-1} \tag{3.77}$$

Finally the new *big-vector* is:

$$w_\tau = \sum_{\text{tracks}} \left(\frac{\partial \mathbf{r}}{\partial \mathbf{a}} \right)^T {\mathcal{G}_{\mathrm{EF}_\tau}}^T S^{-1} \mathbf{R}_{\boldsymbol{\tau}} \tag{3.78}$$

Therefore, the implementation of this constraints is straightforward. There are several kind of constraints that can be applied:

- The truth Monte Carlo (MC) information can be used to constrain the track parameters when running over simulated data as testing purposes. In this case $\hat{\tau}$ are simply the truth track parameters.

- The Beam Spot (BS) information can be used to constrain the track parameters if the impact parameter (specially d_0) is considered as a function of the beam spot parameters. This dependence is:

$$d_0 = -(x_{\mathrm{BS}} + z_0 \alpha_{\mathrm{BS}}) \sin\phi_0 + (y_{\mathrm{BS}} - z_0 \beta_{\mathrm{BS}}) \cos\phi_0 \tag{3.79}$$

  where x_{BS} and y_{BS} are the two global coordinates of the BS and α_{BS} and β_{BS} are the tilts with respect the X and Y axis in the global coordinates system of the BS. In this case d_0 is correlated to z_0 and ϕ_0 and $\partial \mathbf{R}_\tau / \partial \boldsymbol{\tau}$ is not the identity matrix anymore:

$$F_\tau = \frac{\partial \mathbf{R}_\tau}{\partial \boldsymbol{\tau}} = \begin{pmatrix} 1 & \frac{\partial d_0}{\partial z_0} & \frac{\partial d_0}{\partial \phi_0} & 0 & 0 \\ 0 & 1 & 0 & 0 & 0 \\ 0 & 0 & 1 & 0 & 0 \\ 0 & 0 & 0 & 1 & 0 \\ 0 & 0 & 0 & 0 & 1 \end{pmatrix} \tag{3.80}$$

  where these off-diagonal derivatives can be calculated:

$$\begin{aligned} \frac{\partial d_0}{\partial z_0} &= -\alpha_{\mathrm{BS}} \sin\phi_0 - \alpha_{\mathrm{BS}} \cos\phi_0 \\ \frac{\partial d_0}{\partial \phi_0} &= -(x_{\mathrm{BS}} + z_0) \cos\phi_0 - (y_{\mathrm{BS}} - z_0 \beta_{\mathrm{BS}}) \sin\phi_0 \end{aligned} \tag{3.81}$$

- It is also possible to use the calorimetry information. In particular the E/p measurement can be used to constraint the momentum of the reconstructed electron tracks.

3.2.6.2 Physical observable constraint

Some physical samples can be used to apply constraints on track parameters thanks to its event observables. The main idea is to constrain the mass of a known resonance. For example, the Z resonances can be used through its decay $Z \to \mu^+\mu^-$. The reconstructed muons will be the ones used to define the extra χ^2_{trkConst} term. This means that the event constraint requires that the invariant mass of the muon pairs has to be compatible with the Z mass. In general, this extra term is:

$$\chi^2_{\text{trkConst}} = \sum_{\text{evt}} \left(\frac{m_{\text{reco}} - M_{\text{reso}}}{\sigma_{\text{reso}}} \right)^2 \tag{3.82}$$

where M_{reso} and σ_{reso} are the experimental mass and resolution of the mass of this resonance, respectively, and m_{reco} is the invariant mass of the reconstructed products in each event. The next expression can be obtained using the matrix notation where S^{-1} is the covariance matrix as $1/\sigma^2_{\text{reso}}$:

$$\chi^2_{\text{trkConst}} = \sum_{\text{evt}} \mathbf{R}^T_{\boldsymbol{\tau}}(\boldsymbol{\tau}) S^{-1} \mathbf{R}_{\boldsymbol{\tau}}(\boldsymbol{\tau}) = \sum_{\text{evt}} (m_{\text{reco}} - M_{\text{reso}})^T S^{-1} (m_{\text{reco}} - M_{\text{reso}}) \tag{3.83}$$

where, generally, $\mathbf{R}_{\boldsymbol{\tau}} = (m_{\text{reco}} - M_{\text{reso}})$ will be a vector of size N_{PHYS} and S will be diagonal matrix of dimension $N_{\text{PHYS}} \times N_{\text{PHYS}}$, being N_{PHYS} the number of physical observables used. Additional constraints can be introduced as for instance that both muons in the event should be generated in the same space point, and due the extremely short life of the resonance it must be the collision point where the primary vertex is. Therefore, both impact parameters d_0 and z_0 of both muons should be distributed accordingly to the intrinsic resolution in each parameter (σ_{d_0} and σ_{z_0}). A new residual vector can be defined:

$$\mathbf{R}_{\boldsymbol{\tau}} = \begin{pmatrix} m_{\mu\mu} - M_Z \\ d_0(\mu^+) - d_0(\mu^-) \\ z_0(\mu^+) - z_0(\mu^-) \end{pmatrix} \equiv \begin{pmatrix} m_{\mu\mu} - M_Z \\ \delta d_0 \\ \delta z_0 \end{pmatrix} \tag{3.84}$$

and a covariance matrix S:

$$S = \begin{pmatrix} \sigma^2_Z & 0 & \\ 0 & \sigma^2_{d_0} & 0 \\ 0 & 0 & \sigma^2_{z_0} \end{pmatrix} \tag{3.85}$$

And finally F_τ will be:

$$F_\tau \equiv \left. \frac{\partial \mathbf{R}_\tau}{\partial \boldsymbol{\tau}} \right|_{\boldsymbol{\tau}_0} = \begin{pmatrix} \left. \frac{\partial m_{\mu\mu}}{\partial \boldsymbol{\tau}} \right|_{\boldsymbol{\tau}_0} \\ \left. \frac{\partial \delta d_0}{\partial \boldsymbol{\tau}} \right|_{\boldsymbol{\tau}_0} \\ \left. \frac{\partial \delta z_0}{\partial \boldsymbol{\tau}} \right|_{\boldsymbol{\tau}_0} \end{pmatrix} \tag{3.86}$$

And using this expression in the final expression of the alignment with constrained tracks a solution can be calculated.

3.2.7 Globalχ^2 algorithm with alignment parameter constraints

In analogy to the previous section, a generic residual-like vector with a dependence on the alignment parameters can be considered. The vector will be $\mathbf{R_a} = \mathbf{R_a}(\mathbf{a})$ and its generic covariance the matrix G. Here, $\mathbf{R_a}$ is a N_{ALI} column vector and G is a $N_{\text{ALI}} \times N_{\text{ALI}}$ symmetric matrix. An important point in this case is that the related χ^2 term will be evaluated only per data sample instead of per event or track because the alignment parameters must be constant. The χ^2 definition is extended to:

$$\chi^2 = \chi^2_{\text{basic}} + \chi^2_{\text{alignConst}} = \sum_{\text{tracks}} \mathbf{r}^T(\boldsymbol{\tau}, \mathbf{a}) V^{-1} \mathbf{r}(\boldsymbol{\tau}, \mathbf{a}) + \mathbf{R_a}(\mathbf{a})^T G^{-1} \mathbf{R_a}(\mathbf{a}) \tag{3.87}$$

The vector $\mathbf{R_a}(\mathbf{a})$ has an explicit dependence on the alignment parameter which has the following consequences:

$$\frac{d\mathbf{R_a}}{d\mathbf{a}} = \frac{\partial \mathbf{R_a}}{\partial \mathbf{a}} \quad \text{and} \quad \frac{d\mathbf{R_a}}{d\boldsymbol{\tau}} = \frac{\partial \mathbf{R_a}}{\partial \mathbf{a}} \frac{d\mathbf{a}}{d\boldsymbol{\tau}} = 0 \tag{3.88}$$

Again, the goal is the minimization of the χ^2 with respect to the alignment parameters which requires:

$$\frac{d\chi^2}{d\mathbf{a}} = 0 \tag{3.89}$$

Differentiating the expression 3.87 with respect to the alignment parameters leads to:

$$\frac{d\chi^2}{d\mathbf{a}} = 2 \left(\sum_{\text{tracks}} \left[\mathbf{r}^T V^{-1} \left(\frac{d\mathbf{r}}{d\mathbf{a}} \right) \right] + \mathbf{R_a}^T G^{-1} \left(\frac{d\mathbf{R_a}}{d\mathbf{a}} \right) \right) = 0 \tag{3.90}$$

Then, using the transposed of the previous expression and applying the equations 3.88 to the minimum condition:

$$\begin{gathered} \sum_{\text{tracks}} \left[\left(\frac{d\mathbf{r}}{d\mathbf{a}} \right)^T V^{-1} \mathbf{r} \right] + \left(\frac{d\mathbf{R_a}}{d\mathbf{a}} \right)^T G^{-1} \mathbf{R_a} = \\ \sum_{\text{tracks}} \left[\left(\frac{\partial \mathbf{r}}{\partial \boldsymbol{\tau}} \frac{d\boldsymbol{\tau}}{d\mathbf{a}} + \frac{\partial \mathbf{r}}{\partial \mathbf{a}} \right)^T V^{-1} \mathbf{r} \right] + \left(\frac{\partial \mathbf{R_a}}{\partial \mathbf{a}} \right)^T G^{-1} \mathbf{R_a} = 0 \end{gathered} \tag{3.91}$$

where now $\partial \mathbf{R_a} / \partial \mathbf{a}$ is a $N_{\text{ALI}} \times N_{\text{ALI}}$ matrix. Like in the previous section, $d\boldsymbol{\tau}/d\mathbf{a}$ has to be estimated within the track fitting section.

3.2.7.1 Track fitting with alignment parameter constraints

This time, as $\mathbf{R_a} = \mathbf{R_a}(\mathbf{a})$ and therefore $d\mathbf{R_a}/d\boldsymbol{\tau} = 0$, there is no extra contribution to the track fitting, so the results will be the same that in the case without constraint (equation 3.27).

3.2.7.2 Alignment corrections fit with alignment parameter constraints

The equation 3.91 can be rewritten using the equation 3.33:

$$\sum_{\text{tracks}} \left(\frac{\partial \mathbf{r}}{\partial \mathbf{a}} \right)^T W \mathbf{r} + \left(\frac{\partial \mathbf{R_a}}{\partial \mathbf{a}} \right)^T G^{-1} \mathbf{R_a} = 0 \tag{3.92}$$

To solve this equation, again an expansion in series is needed for $\mathbf{r}(\boldsymbol{\pi}_0, \mathbf{a})$ and $\mathbf{R}_\mathbf{a}(\mathbf{a})$ around $\mathbf{a}_0$. The first one was already calculated in equation 3.34. The second one is:

$$\mathbf{R}_\mathbf{a}(\mathbf{a}) = \mathbf{R}_\mathbf{a}(\mathbf{a}_0) + \left.\frac{\partial \mathbf{R}}{\partial \mathbf{a}}\right|_{\mathbf{a}_0} \delta\mathbf{a} = \mathbf{R}_\mathbf{a}(\mathbf{a}_0) + F_\mathbf{a}\delta\mathbf{a} \tag{3.93}$$

where second and higher order derivatives are neglected and $F_\mathbf{a}$ has been defined as:

$$F_\mathbf{a} \equiv \left.\frac{\partial \mathbf{R}}{\partial \mathbf{a}}\right|_{\mathbf{a}_0} \tag{3.94}$$

Inserting both expansions in the expression 3.92 and assuming $\mathbf{r}$ and $\mathbf{R}_\mathbf{a}$ mean $\mathbf{r}(\boldsymbol{\tau}_0, \mathbf{a}_0)$ and $\mathbf{R}_\mathbf{a}(\mathbf{a}_0)$ to simplify the notation:

$$\begin{aligned} &\sum_{\text{tracks}} \left(\frac{\partial \mathbf{r}}{\partial \mathbf{a}}\right)^T W\mathbf{r} + \sum_{\text{tracks}} \left(\frac{\partial \mathbf{r}}{\partial \mathbf{a}}\right)^T W\frac{\partial \mathbf{r}}{\partial \mathbf{a}}\delta\mathbf{a} + F_\mathbf{a}^T G^{-1}\mathbf{R}_\mathbf{a} + F_\mathbf{a}^T G^{-1}F_\mathbf{a}\delta\mathbf{a} = \\ = &\left[\sum_{\text{tracks}} \left(\frac{\partial \mathbf{r}}{\partial \mathbf{a}}\right)^T W\frac{\partial \mathbf{r}}{\partial \mathbf{a}} + F_\mathbf{a}^T G^{-1}F_\mathbf{a}\right]\delta\mathbf{a} + \sum_{\text{tracks}} \left(\frac{\partial \mathbf{r}}{\partial \mathbf{a}}\right)^T W\mathbf{r} + F_\mathbf{a}^T G^{-1}\mathbf{R}_\mathbf{a} = 0 \end{aligned} \tag{3.95}$$

Using the definitions of the standard *big-matrix* and *big-vector* plus an new vector and matrix:

$$\begin{aligned} \mathcal{M} &= \sum_{\text{tracks}} \left(\frac{\partial \mathbf{r}}{\partial \mathbf{a}}\right)^T W\frac{\partial \mathbf{r}}{\partial \mathbf{a}} \\ v &= \sum_{\text{tracks}} \left(\frac{\partial \mathbf{r}}{\partial \mathbf{a}}\right)^T W\mathbf{r} \\ \mathcal{M}_\mathbf{a} &= F_\mathbf{a}^T G^{-1}F_\mathbf{a} \\ v_\mathbf{a} &= F_\mathbf{a}^T G^{-1}\mathbf{R}_\mathbf{a} \end{aligned} \tag{3.96}$$

Using this definitions the equation 3.92 can compacted as:

$$(\mathcal{M} + \mathcal{M}_\mathbf{a})\delta\mathbf{a} + (v + v_\mathbf{a}) = 0 \tag{3.97}$$

and solving for $\delta\mathbf{a}$:

$$\delta\mathbf{a} = -(\mathcal{M} + \mathcal{M}_\mathbf{a})^{-1}(v + v_\mathbf{a}) \tag{3.98}$$

Finally, the solution of the alignment parameters is:

$$\mathbf{a} = \mathbf{a}_0 + \delta\mathbf{a} = \mathbf{a}_0 - (\mathcal{M} + \mathcal{M}_\mathbf{a})^{-1}(v + v_\mathbf{a}) \tag{3.99}$$

Taking a look to the final expression, the conclusion is that adding a constraints which just depends on the alignment parameters, the results from the general formalism can be used directly adding two extra terms.

3.2.8 Application of alignment parameter constraints

The applications of the alignment parameter constraints are basically used to impose constraints according the survey data and introduce penalty terms to large shifts of the alignment parameters.

3.2.8.1 Survey measurements as constraints

The information from the detector survey can be used to constraint the alignment parameters. If the survey measurements are done at module levels, the constraints can be added straightforward with the following extra χ^2 term:

$$\chi^2_{\text{survey}} = (\mathbf{a} - \hat{\mathbf{a}})^T G^{-1}_{\text{survey}} (\mathbf{a} - \hat{\mathbf{a}}) \tag{3.100}$$

where $\mathbf{R}_a = (\mathbf{a} - \hat{\mathbf{a}})$ is the residual, $\hat{\mathbf{a}}$ represents the survey measurement and $\mathbf{a}$ is the alignment parameter to be determined. In this situation:

$$\frac{d\mathbf{R}_a}{d\mathbf{a}} = \frac{\partial \mathbf{R}_a}{\partial \mathbf{a}} = I \tag{3.101}$$

The covariance matrix G accounts the uncertainties in the survey measurements, considering all the measurement correlations due to common physical anchors between modules. Therefore $\mathcal{M}_{\mathbf{a}}$ and $v_{\mathbf{a}}$ from the expressions in 3.96 become:

$$\mathcal{M}_{\mathbf{a}} = G^{-1}_{\text{survey}} \quad \text{and} \quad v_{\mathbf{a}} = G^{-1}_{\text{survey}} (\mathbf{a} - \hat{\mathbf{a}}) \tag{3.102}$$

Sometimes, the survey measurements are expressed as linear combination of the modules or structures DoF. In this case $\mathbf{R}_a(\mathcal{C}\mathbf{a})$, where $\mathcal{C}$ is a $[N_{\text{ALI}} \times N_{\text{ALI}}]$ matrix which introduces the correlations. In this case the χ^2 is:

$$\chi^2_{\text{survey}} = \mathbf{R}_a(\mathcal{C}\mathbf{a})^T G^{-1}_{\text{survey}} \mathbf{R}_a(\mathcal{C}\mathbf{a}) \tag{3.103}$$

where, generally, G^{-1}_{survey} will not be diagonal anymore, and $d\mathbf{R}_a/d\mathbf{a}$ will not be the identity matrix:

$$\frac{d\mathbf{R}_a}{d\mathbf{a}} = \frac{\partial \mathbf{R}_a}{\partial \mathbf{a}} = \frac{\partial \mathcal{C}\mathbf{a}}{\partial \mathbf{a}} = \mathcal{C} \tag{3.104}$$

And the *big-matrix* and *big-vector* read as:

$$\mathcal{M}_{\mathbf{a}} = \mathcal{C}^T G^{-1}_{\text{survey}} \mathcal{C} \quad \text{and} \quad v_{\mathbf{a}} = \mathcal{C}^T G^{-1}_{\text{survey}} (\mathbf{a} - \hat{\mathbf{a}}) \tag{3.105}$$

Obviously, when $\mathcal{C} = I$ the previous results are recovered. This formalism is equivalent to start from the survey values without this extra χ^2 therm instead of starting from the nominal positions using the constraint. Anyhow, the problem is not as simple since the survey measurements involve combinations of alignment parameters where relative positions and a mixture of structures are measured, such as relative position differences between modules, staves, barrels or discs. In this case, the problem is to translate these complex measurements to individual DoF of each module. In the ATLAS Silicon Tracker case, survey data exists for the SCT End-Cap and for the Pixel although only the Pixel position information was used to align the detector.

3.2.8.2 Alignment parameters constrained using penalty terms

It is possible to add constraints to the alignment parameters in such a way that they represent χ^2-penalties, also known as *softmode cut (SMC)*. In this case the residuals are

$\mathbf{R}_a = (\mathbf{a} - \mathbf{a}_0)$ and the covariance matrix $G_{\text{SMC}}^{-1} = 1/\sigma_{\text{SMC}}^2$ which is diagonal. With these residuals:

$$\frac{d\mathbf{R}_a}{d\mathbf{a}} = \frac{\partial \mathbf{R}_a}{\partial \mathbf{a}} = \mathbf{I} \tag{3.106}$$

therefore, $\mathcal{M}_{\mathbf{a}}$ and $v_{\mathbf{a}}$ from the expressions in 3.96 can be written as:

$$\mathcal{M}_{\mathbf{a}} = G_{\text{SMC}}^{-1} \quad \text{and} \quad v_{\mathbf{a}} = 0 \tag{3.107}$$

where $v_{\mathbf{a}} = 0$ because $\mathbf{R}_a(\mathbf{a}_0) = (\mathbf{a}_0 - \mathbf{a}_0) = 0$. This means that the implementation is trivial and the solution is just the same as without constraint but adding an additional diagonal matrix to $\mathcal{M}$:

$$\mathbf{a} = \mathbf{a}_0 + \delta\mathbf{a} = \mathbf{a}_0 - (\mathcal{M} + G_{\text{SMC}}^{-1})^{-1} v \tag{3.108}$$

These kind of constraints are very useful and where used to avoid big detector movements as will be explained in the next chapter.

3.3 Centre-of-Gravity Correction

In the current scheme of the Inner Detector alignment the only external constraint comes from the transverse position of the luminous region, leaving the remaining four degrees of freedom of the global transformation (translation in z and the three rotations) unconstrained. In order to undo any effective global transformation of the detector system, understood as the average translation and rotation in space, the Centre-of-Gravity (CoG) algorithm is applied at the very end of the alignment sequence. This step is required because in ATLAS the ID provides the reference frame for the rest of the detector (calorimeters, muon system). The CoG algorithm is based on the least squares minimization of all detector element distances between their actual positions and positions of their reference counterparts. The χ^2 is defined as:

$$\chi^2 = \sum_i \sum_{\kappa=x,y,z} (\Delta\kappa_i)^2 \qquad \text{and} \qquad \Delta\kappa = \kappa_{\text{cur}} - \kappa_{\text{ref}} \tag{3.109}$$

where the displacement is given in the local frame of the module and the index i goes over all detector elements. The Δ's from Equation 3.109 can be linearly expanded with respect to the six global transformations of the entire detector system (G_l):

$$\Delta\kappa = \Delta\kappa_0 + \sum_l \frac{\partial \kappa}{\partial G_l} \qquad \text{with} \qquad G_l \in \{T_x, T_y, T_z, R_x, R_y, R_z\} \tag{3.110}$$

where $\frac{\partial \kappa}{\partial G_l}$ is the Jacobian transformation from the global to the local frame of a module. The χ^2 minimization condition leads to six linear equations with six parameters (T_x,T_y,T_z,R_x,R_y,R_z) which are trivially solvable to yield the required CoG transformation of the ID.

3.4 Alignment systematics

The alignment algorithm is capable of producing a description of the detector geometry which provides an efficient and good-quality track fit. But it is difficult to guarantee that the track parameter reconstruction is free from systematic biases. It is possible to find geometry descriptions which satisfy the assumed track model but lead to biased physics measurements. These are called the *weak modes* of the alignment as they correspond to near-singular modes of the solution to the alignment problem. The *weak modes* can be also defined as the geometry deformations to which track-hit residuals or the χ^2 of the track fit remain invariant. They can arise from deformations of the real detector (which are not correlated) or as artifact of the alignment procedure itself. The track parameters for which it is easiest to introduce significant distortions and which consequently have most significant influence on physics measurements are the measured particle momentum and the track impact parameter. The *weak modes* deformations cannot be identified just by studying the quality of individual track fits. In order to identify these deformations, additional information or measurements that are dependent on the track parameters are needed [38]. An example of such an observable is provided by the reconstructed invariant mass of known particles (eg. $Z \to \mu^+\mu^-$, $J/\psi \to \mu^+\mu^-$, $K^0_S \to \mu^+\mu^-$). For the study, the electromagnetic calorimeter of ATLAS have been used to provide an independent measure of electron energy, thus enabling the E/p analysis for electrons.

3.4.1 Charge-antisymmetric deformations

The *sagitta* deformations consist of detector movements orthogonal to the track trajectory that affect the reconstructed track curvature oppositely for positively and negatively charged particles. In the plane transverse to the uniform magnetic field, the circular trajectory of a high-p_T charged particle with radius R can be approximated by a second order polynomial:

$$R^2 = \rho^2 + (t - R)^2 \to t = R - \sqrt{R^2 - \rho^2} \approx \frac{1}{2R}\rho^2 \tag{3.111}$$

Where ρ is the coordinate along the initial particle direction (at the point of production), t is the coordinate in the perpendicular direction and R is the curvature radius of the trajectory. In the 2 T magnetic field of the ATLAS ID, R is related to the transverse momentum via: $p_T[\text{GeV}] = 0.3B(T)\rho(m) = 0.6 \times 10^{-3}R[\text{mm}]$. In order to maintain the helical trajectory, the *sagitta* distortion has to take the form:

$$t \to t + \epsilon_{\text{sagitta}}\rho^2 \tag{3.112}$$

Such a parabolic displacement of reconstructed hits in the detector results in a charge-anti-symmetric alteration of the track's curvature (R), which translates in a shift of the measured transverse momentum according to:

$$q/p_T \to q/p_T + \delta_{sagitta} \tag{3.113}$$

or

$$p_T \to p_T(1 + qp_T\delta_{sagitta})^{-1} \tag{3.114}$$

The $\delta_{sagitta}$ is a universal bias parameter for all measured momenta and uniquely defines the deformation. A parabolic distortion is only consistent with a helical trajectory in the limit of small distortions or high-p_T. Nevertheless in many cases, this is a good approximation. Because the reconstructed polar angle does not change, the longitudinal component of the momentum scales identically along with the transverse component, leading to:

$$p \to p(1 + qp_T\delta_{sagitta})^{-1} \tag{3.115}$$

From Equations 3.111, 3.112 and the relationship between the curvature radius and the transverse momentum in the ID solenoidal fields, one gets:

$$\epsilon_{sagitta}[1/\text{mm}] = 0.3 \times 10^{-3}\delta_{sagitta}[1/\text{GeV}] \tag{3.116}$$

The absolute momentum bias due to a *sagitta* deformation is proportional to the square of the transverse momentum and for that reason high-p_T tracks are more suitable to detect them. The simplest example of the charge-anti-symmetric deformation is the *curl* distortion typical for systems with a concentric cylindrical layout. It consists of azimuthal rotation of detector layers proportional to their radius: $\Delta\phi \sim r$, as shown in Figure 3.7b. The rotation is characterized by the parameter $\delta_{curl} \equiv \delta_{sagitta}$ as:

$$\delta\phi[\text{mrad}] = 0.3\delta_{curl}[1/\text{ GeV}]r[\text{mm}] \tag{3.117}$$

and results in a uniform momentum bias in the entire detector volume.

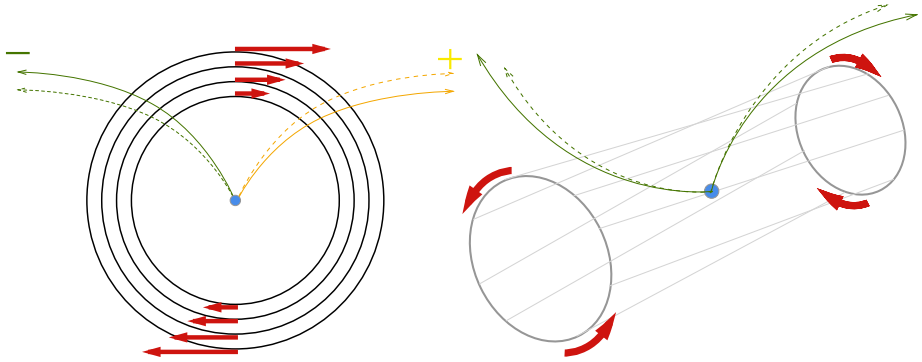

(a) *curl* (b) *twist*

Figure 3.7: Example of basic distortions affecting the measured particle momentum in a charge-asymmetric way: *curl*(a) and *twist*(b). The detector deformation as well as the impact on the reconstructed particle momenta are shown schematically. The true particle trajectories are shown as dashed lines, and the reconstructed trajectories as continuous lines.

Another example is the *twist* distortion depicted in Figure 3.7a. Physically it corresponds to a linear twist of the detector around the z-axis: $\Delta\phi \propto z$ and as such is likely to occur in the disk detector layout found in forward regions of the tracking systems.

For all tracks emerging from the center of the detector, the twist appears as a *sagitta* distortion with a magnitude proportional to $\cot\theta$ of the track direction:

$$\begin{aligned} q/p_T &\rightarrow q/p_T + \delta_{twist}\cot\theta \\ p &\rightarrow p(1 + qp_T\delta_{twist}\cot\theta)^{-1} \end{aligned} \tag{3.118}$$

3.4.2 Charge-symmetric deformations

An example of charge-symmetric deformations comes from *radial* distortions. These affect the measured momentum via the radial expansion/contraction of the measured trajectory. An example of a ϕ -dependent distortion is shown schematically in Figure 3.8. It does not have to take the particular form displayed in the figure and can be generally described as the direction-dependent radial scaling $r \rightarrow (1 + f(\phi,\eta)\epsilon_{radial})r$. The lowest-order mode is a homogeneous radial expansion/contraction and does not usually occur due other constraints on the geometry. This is just as well since it is difficult to disentangle from other deficiencies in the detector description. As it was in the case of the *sagitta* distortion, the generic radial expansion is not an exact weak mode but it approximates to one for large momenta. Radial scaling affects particles of both charges symmetrically. The geometrical transformation in the transverse plane leads to an approximate change of the measured transverse momentum according to:

$$p_T \rightarrow p_T(1 + \epsilon_{radial})^{-1} \equiv p_T \rightarrow p_T(1 + 2\epsilon_{radial}) \text{ for small } \epsilon_{radial} \tag{3.119}$$

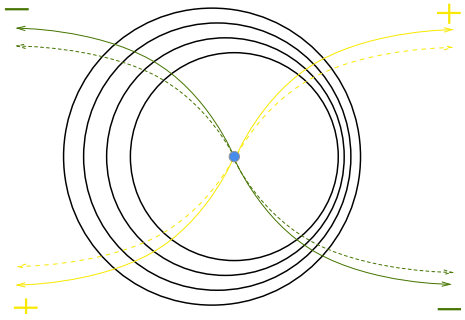

Figure 3.8: Example of a basic distortion affecting the measured particle momentum in a charge-symmetric way. The detector deformation as well as the impact on the reconstructed particle momenta are schematically shown. The true particle trajectories are shown as dashed lines, and the reconstructed trajectories as continuous lines.

The polar angle is not maintained and it results in the following scaling of the longitudinal component of the reconstructed momentum:

$$\cot\theta \rightarrow \cot\theta(1 + \epsilon_{radial})^{-1} \text{ hence } p_z \rightarrow p_z(1 + \epsilon_{radial}) \tag{3.120}$$

In contrast to the sagitta distortions described earlier, the momentum bias is proportional to the change in the radial scale, and independent of the momentum. For this reason, low-momentum tracks are just sensitive to radial deformations as high-momentum ones.

3.4.3 The B-field orientation

There is a special case of *radial* distortion which originates not from the deformation of the tracker but its relative misalignment with respect to the direction of the solenoidal B-field. To a good approximation the solenoidal field is uniform over the volume of the tracking system and hence its 3D position is of no concern to alignment. However, the orientation of the B vector has a fundamental consequence for tracking, as illustrated in Figures 3.9-3.10. The upper plot in Figure 3.9 shows how the rotation affects tracks in the $r-z$ plane. The discrepancy between the real tracks and the fitted ones is shown in the lower plot of Figure 3.9. This causes the track hits in the $x-y$ plane to be displaced in such a way that the track curvature is altered (Figure 3.10). Here again, the dashed lines represent real tracks and the solid lines the reconstructed ones. As can be seen,the measured curvature is changed exactly the same way as for the radial deformation. The bias on the measured p_T has an oscillatory ϕ dependence with the amplitude proportional to $\cot\theta$. The effect can be easily quantified considering the rotation of the B-field relative to the stationary tracking system. The magnitude of the Lorentz bending force is modified by the field rotation:

$$\begin{aligned} |\mathbf{B}\times\mathbf{p}| = Bp\sin\theta \rightarrow Bp\sin(\theta-\sin\phi\alpha_{\rm rot}) &\overset{\alpha_{\rm rot}<<1}{\cong} Bp(\sin\theta-\cos\theta\sin\phi\alpha_{\rm rot}) = \\ &= Bp_T(1-\cot\theta\sin\phi\alpha_{\rm rot}) \end{aligned} \quad (3.121)$$

where it is assumed the vertical rotation of the magnetic field by a small angle $\alpha_{\rm rot}$ around the x-axis. The previous equation leads to the same scaling of the reconstructed momentum:

$$p \rightarrow p(1-\cot\theta\sin\phi\alpha_{\rm rot}) \quad (3.122)$$

This directly affects the reconstructed invariant mass of a particle for which the decay products are close to each other. Thus the measurement of the reconstructed invariant mass as function of the production angle allows for a precise measurement of the magnetic field alignment relative to the tracking system.

3.4.4 Bias on the transverse impact parameter

Bias on the impact parameter of the reconstructed charged track can occur from various deformations of the detector geometry and can be associated with biases on other track parameters, e.g. *sagitta* distortions. Nonetheless, a pure local d_0 bias can be generically described by:

$$t \rightarrow t + \delta d_0 \quad (3.123)$$

where t is the measured track position in the tangential direction as defined in Equation 3.111. It can also be expressed in terms of rotations of the subsequent layers of the

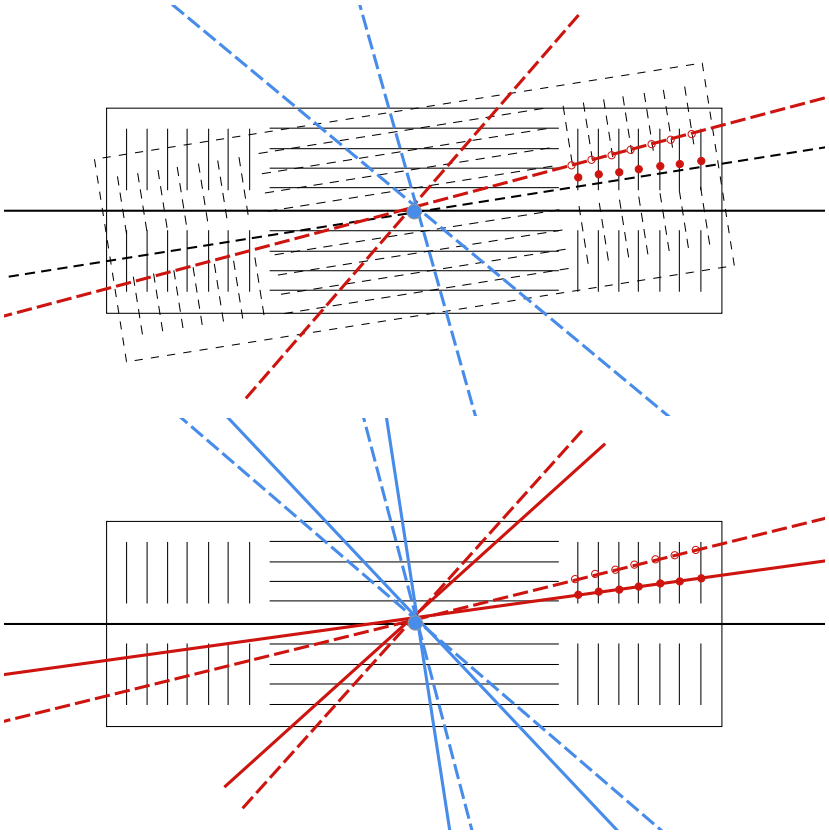

Figure 3.9: Result of the tracking system rotation around the x axis with respect to the magnetic field (aligned with the z axis) shown in the $r - z$ view.

detector according to:

$$\Delta\phi[\text{rad}] = \frac{\delta d_0}{r} \tag{3.124}$$

In general, the δd_0 parameter may have an arbitrary dependence on the track direction (ϕ, η).

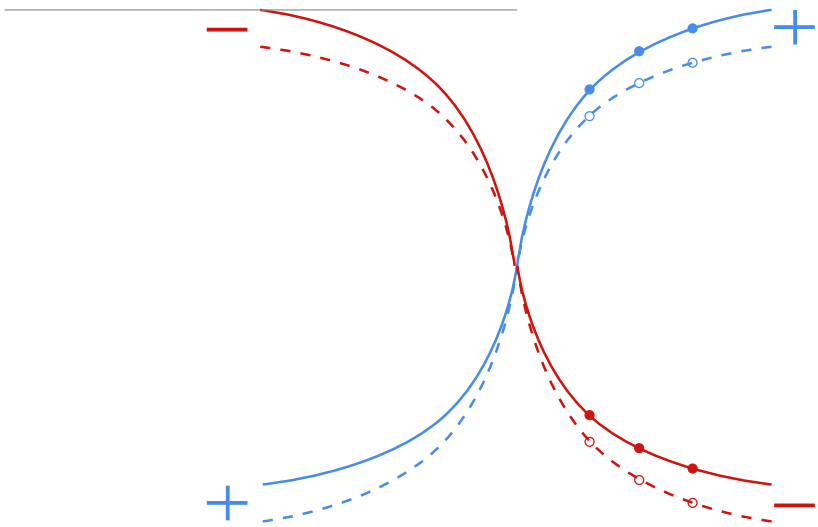

Figure 3.10: Result of the tracking system rotation around the x axis with respect to the magnetic field (aligned with the z axis) shown in the $x - y$ view.

Chapter 4

Inner Detector Alignment performance

4.1 Implementation

4.1.1 Athena

The alignment Globalχ^2 algorithm has been implemented within the *Athena* framework [39]. Athena is the ATLAS software framework based on C++ language. It provides several tools for various purposes like event generation, reconstruction and detector description. It is composed by several algorithms organised in packages. It ensures that the algorithms are run in the correct order, that the data is correctly loaded from local or remote disc server, the histograms and ntuples are filled, etc.

The handling of the input and output as well the required services and packages is done using files written in Python called *jobOptions*. Each ATLAS package contains services and algorithms where each one has dependencies on other packages. All these packages are managed in a version control repository (SVN). Each package has a tag number and a project consists of a complete collection of tagged packages and it is identified with a release number.

The off-line software contains also a complete description of the ATLAS detector which is used by the EDM for simulation and reconstruction. This part has the information about the geometry and material of the detector, as well as the position and orientation of each detector element.

Another important part are the databases. Several databases are needed in the *Athena* framework. For example, the numbers that define the size and position of each volume are stored in an Oracle database. Also, the alignment constants are stored in a database which is used by the detector description to modify the nominal positions of the sensors. It also contains the calibration constants to transform pulse sizes in energy deposition measurement, and also a list of dead or noisy silicon channels. An important feature of the condition database is that it implements intervals of validity (IOV) services. This allows to have different calibrations and alignment constants for different sets of

data.

4.1.2 Alignment script runner

In order to obtain a set of alignment constants, the algorithm has to run over a big amount of data. It is also required to perform several iterations with different alignment configurations. All the different configurations can be managed using a python script *RunIterator.py*. This script selects the input data and split them in different jobs. Each job is run in a different CPU and all the outputs are collected. The outputs are merged in a simple file and the solving part of the alignment is run and the constants are obtained. This constants will be the input constants for the next iteration. This procedure is repeated n iterations. For each iteration the different options can be modified. The cycle is summarised in the Figure 4.1.

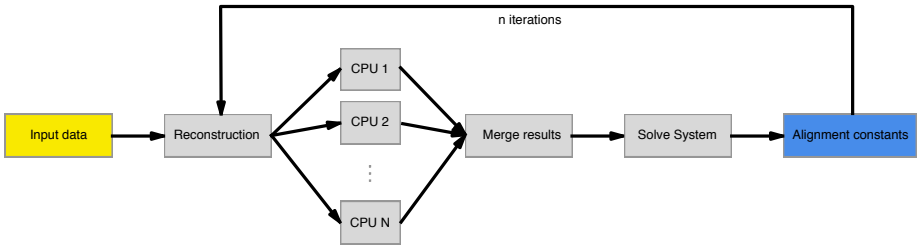

Figure 4.1: Schematic of the alignment procedure as performed by the alignment script runner.

The options of the alignment script runner are:

- Number of iterations.
- Number of CPU's to use.
- Run in local or batch machine.
- Data to use: cosmic ray data, collision data, ...
- Number of events.
- Alignment level for each iteration.
- Sub-detectors to align at each iteration.

4.2 Alignment studies

4.2.1 Initial Cosmic alignment

Since 2008, before the first beams were circulating in the LHC, the detector was ready and taking data. These data was obtained from cosmic rays. With this first data, many tests were done in ATLAS to check the system status:

- ATLAS operation with all of the subsystems.
- Testing of the Trigger and Data Acquisition (TDAQ) and Detector Control Systems (DCS) systems.
- Data processing and re-processing at Tier-0 and Tier-1.
- Obtain the first track-based alignment and calibration constants.

There were two big periods of cosmic data taking in 2008 and 2009. Two different sets of alignment constants were produced for both cosmic ray data taking periods, denoted as *Cosmic08 alignment* and *Cosmic09 alignment*. In both cases a combination of the data taken with and without the presence of the solenoid magnetic field was used. The starting geometry used the Pixel module survey [32] whilst SCT modules were assumed to be at their nominal values. The Pixel modules were surveyed once assembled in the staves. This information was used and translated to obtain the individual module positions, being these positions the starting geometry for the alignment.

4.2.1.1 Cosmic08 alignment

On fall 2008, more than 200 million events of cosmic ray were registered, reconstructed and processed during this period with different detector and magnet configurations. There were almost 7 million events with tracks traversing the ID volume, of which 2.6 million tracks were obtained with the ID solenoid on and ∼5 millions tracks with the solenoid off. The number of tracks are shown in the Figure 4.2. There were about 240 thousands of tracks crossing the pixel detector. Both kind of tracks (with and without

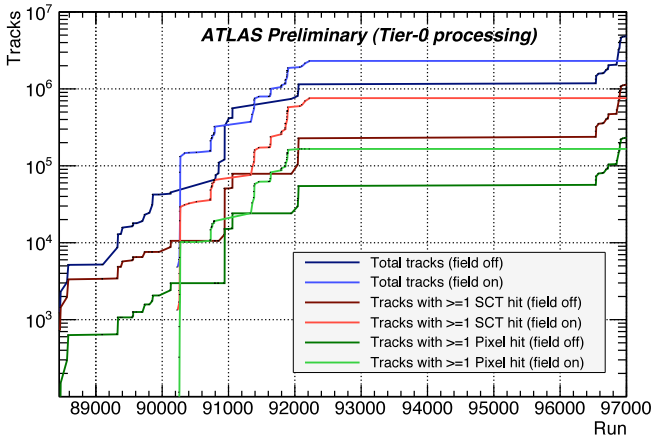

Figure 4.2: Integrated cosmic data rate in the Inner Detector versus the run number in fall 2008. The number of tracks with and without solenoid field are shown as well the tracks with at least one hit in the SCT and one hit in the Pixel detector.

magnetic field) were used to align the parts of the tracking system. A simple track quality selection was applied based on a transverse momentum cut, $p_T < 2$ GeV, for events with magnetic field. For events without magnetic field, straight tracks were reconstructed and the material effects were not taken into account in the track fit as no momentum estimation was available. Tracks with less than 10 SCT hits were rejected. This track and hit selection cuts will be denoted as a standard quality in this subsection. In addition, when the alignment was done at stave level, the requirement was strengthen by asking for at least one overlap in some of the layers. This way enhances the stave correlation. The alignment strategy used was proposed to cover all the real assembled units: full structures, Pixel half-shells, staves, barrel layers and end-cap disks and modules. In the first step the detector was aligned using cosmic rays without the presence of the magnetic field. A series of four iterations for each level was realised, comprising alignment at level of big structures, pixel half-shells and pixel and SCT staves. Then as a second step several iterations combining both kind of data, with and without magnetic field, were performed. These iterations were done at module level, using only two degrees of freedom (T_x and R_z). As last step, the first step was repeated using both kind of data to ensure convergence.

The improvement in the residuals in the Pixel barrel is shown in the Figure 4.3. It is shown the starting residual distributions for the nominal geometry (with the Pixel survey) and with the aligned geometry. For comparison, the MC with perfect geometry is also shown. In the Figure 4.4 the same distribution is shown but for the SCT barrel. A big improvement can be seen in the width of the distributions, from 128 μm and 282 μm to 24 μm and 131 μm for the Pixel barrel x and y residuals. In the SCT the width of the residuals goes from 123 μm to 30 μm in both x and y.

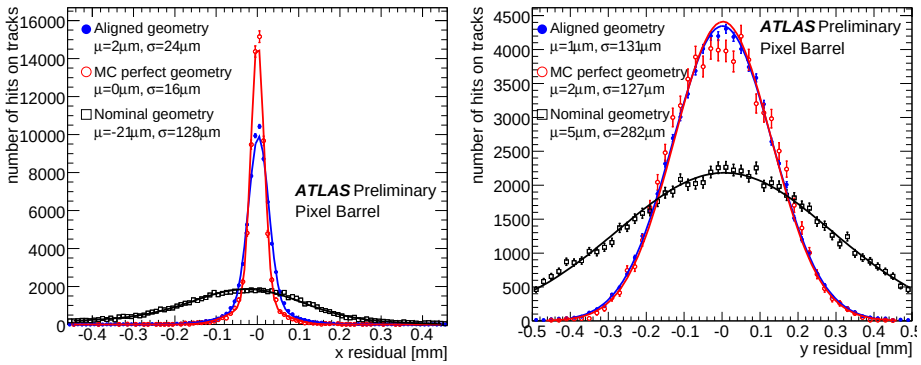

Figure 4.3: Unbiased residual distributions in the pixel barrel showing the nominal geometry with the Pixel survey, the aligned geometry using the *Cosmic08* constants and MC perfect geometry.

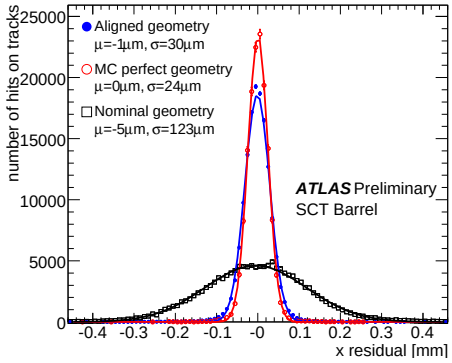

Figure 4.4: Unbiased residual distributions in the SCT barrel showing the nominal geometry, the aligned geometry using the *Cosmic08* constants and MC perfect geometry.

4.2.1.2 Cosmic09 alignment

In Summer 2009 another run of cosmic events was done. More than 90 million of events were collected with different detector and magnet configuration. There were about 20 million events with tracks traversing the ID. The strategy followed to produce the *Cosmic09 alignment* benefited from the experience gained with the previous 2008 cosmic ray data campaign. A mixture of ∼1.7 million of events without magnetic field and ∼1.5 million of events with the ID solenoid switched on were used to obtain the new set of constants. Translated to tracks, it means about 440k and 52k useful cosmic tracks, respectively. The starting geometry was the Pixel module survey as in the previous alignment. In addition, an *error scaling*[1] was introduced in some iterations. The idea is to account for initial misalignment errors which are beyond the intrinsic error of the hits. A track quality selection was applied, denoted in this subsection as *standard* quality cut. It is based in a transverse momentum cut, $p_T > 2$ GeV for events with magnetic field. In this case, for events without magnetic field, the material effects were estimated inside the tracking code assuming that the tracks had a momentum of 2 GeV. An additional requirement of at least 12 hits in the SCT was used. In some iterations the InDetAlignHitQualSelTol (HQST)[40] package was used. This package allows to reject hits in edge channels, ganged pixels and hits where the incidence angle is too big. It allows also to cut on the maximum track incidence angle with respect the local z axis of a module in the local xz plane or on the cluster size of the hit. The alignment strategy was similar to the one used to obtain the *Cosmic09* alignment, but using the new implementations.

[1] The intrinsic error of the hit (σ) is scaled using two parameters a and c following the equation $\sigma_{\text{scaled}} = a\sigma \otimes c$

4.2.2 900 GeV collision alignment

The first proton-proton collisions events recorded by ATLAS were produced in November 23rd during the beam commissioning of the LHC. The tracks were reconstructed using the silicon alignment constants derived from the *Cosmic08 alignment*. Since the first collisions until early December, collision data was being recorded by all the LHC experiments. The first LHC run allowed to ATLAS to record almost 1 million collision candidates at 900 GeV. This collisions were used to improve the alignment and calibration of the different ATLAS sub-detectors. At the end, a new set of alignment constants called *Collision09 alignment* in this thesis was obtained. In this alignment the goal was mainly to fix the end-caps because the cosmic rays does not correlate them. The standard selection is defined as a cut of $p_T > 1$ GeV/c and tracks with more than 6 silicon hits. The alignment procedure comprised an initial iteration at level 1 ad 8 iterations at disk level considering only the end-caps with three degrees of freedom (T_x, T_y and R_z).

In the next sections this alignment set will be referred as *Autumn 2010 Alignment*.

4.2.3 7 TeV collision alignment

On March 30th 2010, ATLAS recorded collisions at 7 TeV centre-of-mass energy for the first time. During the years 2010 and 2011, the LHC was operated at this energy and ATLAS recorded about 4.5 fb^{-1}. For 7 TeV alignment collision and cosmic-ray samples were used. The initial knowledge of the ATLAS ID detector geometry was taken from the results of the previous alignment with 900 GeV data (Subsection 4.2.2, *Autumn 2010 Alignment*). The alignment at *Level 1* was performed using the degrees of freedom given in Table 3.2, aligning pixels, SCT and TRT simultaneously. The size of the corrections were of the order of micrometers. This implies that the change in position of the ID subsystems during the 2009-2011 winter shutdown and the spring 2010 data taking was of that order of magnitude. This is an important indication of the level of detector stability.

The alignment was then performed at *level 2*. During initial iterations the TRT structures were kept fixed whilst the silicon substructures were aligned. The corrections in the barrel layers were small, as in the level 1 case. However, the corrections of some SCT disks were up to 100 μm. The extent of these corrections was expected as this was the first time that the end-cap disks were aligned with large track statistics and high momentum tracks (hence reduced multiple Coulomb scattering effects).

In the second stage of the *Level 2* alignment, all three sub detectors were aligned simultaneously. Some readjustment of the SCT and TRT end-cap wheels was observed as corrections of several tens of micrometers were obtained. Convergence was found after just three iterations. In order to verify that no structure movements were introduced by the alignment of the layers and disk, the alignment stage was complemented with an extra level 1 iteration. In this last iteration, the magnitude of the alignment corrections was sub-micrometer.

In the final step the alignment was performed at *Level 3*. In this step the silicon modules and TRT wires were aligned separately. Due to the very large number of degrees of freedom involved, the Localχ^2 algorithm was used. Subsection 4.2.3.1 describes the silicon modules alignment, and Subsection 4.2.3.2 describes the wire-by-wire alignment

in the TRT. An overall correction of the centre-of-gravity (CoG) of the entire Inner Detector was applied at the very end of the alignment sequence, as described in Subsection 4.2.3.3.

4.2.3.1 Alignment of the Silicon System at Module Level

The alignment of the individual silicon modules was performed in two stages. In both stages the TRT was fixed and only the silicon modules were aligned. The alignment technique applied was the Localχ^2 method, described in Section 3.2.3. The main characteristics of the first stage of the silicon module alignment are the following:

- All the silicon modules (pixel and SCT, barrel and end-cap) were aligned.
- Only the most sensitive degrees of freedom (namely T_x, T_y and R_z) were considered.
- In order to increase the correlation between modules, the track selection was tightened. Only tracks intersecting two adjacent overlapping modules in at least one silicon layer (either in the pixel or the SCT) were retained.
- Pixel modules were modelled as a perfect flat surface

Several iterations of the Localχ^2 alignment were carried out at this stage. The overall corrections for the translation along the precise coordinate (T_x) were at a maximum 30 μm. Once this stage was completed, the TRT wire-by-wire alignment was executed. After the completion of the TRT wire-by-wire alignment the second stage of the silicon module alignment was carried out. The main features of this stage were:

- Only the pixel barrel modules were aligned. The rest of silicon modules were fixed along with the TRT.
- All the degrees of freedom (except T_z) were used.
- Pixel modules were no longer modelled as a perfectly flat surface. Instead a distorted module geometry was used, according to the survey measurements of twist and/or bend of the detector wafers. It corresponds to out of plane corrections of the order of few tens of micrometers [32].

By including the measured pixel module distortions into the reconstruction the 3D coordinates of the measured hit position are corrected. The impact of the module distortions on the pixel residuals was sizeable and was visible before any realignment was applied. Alignment of the pixel modules while enabling the pixel module distortions resulted in further improvements of the alignment results of the pixel modules. Further iterations were performed at this stage and resulted in corrections of a maximum 10 μm along the precise pixel coordinate. The effect of the alignment and the use of the distortions can be seen in Figure 4.5. For the sake of clarity, the figure only shows a subset of the intermediate pixel barrel layer. It is possible to observe that some modules had internal variations of the average residual of up to 15 μm (Figure 4.5 (left)). These internal variations are reduced after the module distortions correction and the subsequent module level alignment (Figure 4.5 (right)).

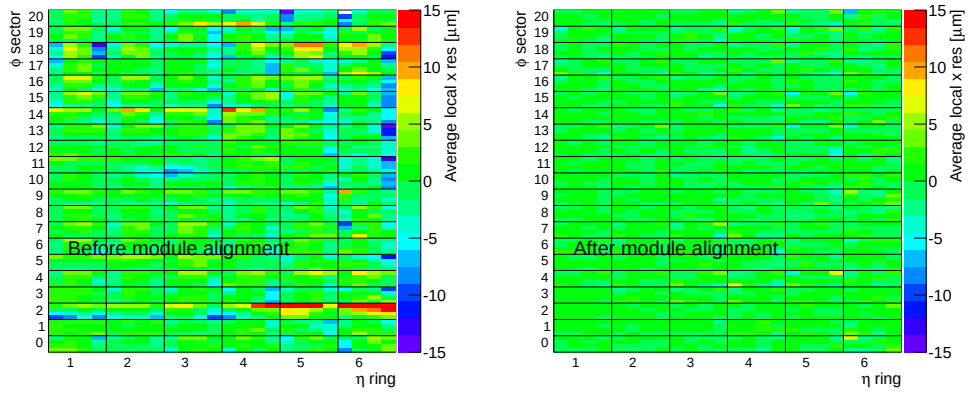

Figure 4.5: Detailed residual maps of the barrel pixel modules. Each pixel module has been split into a 4×4 grid and the average residual in each cell is plotted. Each module is identified by its position in the layer. This is given by its η ring and ϕ sector indices. The left figure shows the average local x residual before the module level alignment. The right figure shows the average local x residual after module level alignment (including pixel module distortions). Only a subset of the pixel modules of the intermediate pixel barrel layer is shown.

4.2.3.2 TRT Wire-By-Wire Alignment Method

After the alignment of the TRT modules at *Level 2* an overall improvement in the track-hit residuals for the TRT modules was observed. Nevertheless, detailed maps of the mean of the residual distributions of the barrel and end-cap modules revealed internal structures that could not be removed by a level 2 alignment. Therefore a wire-by-wire alignment was performed in both barrel and end-cap TRT detectors. Figure 4.6(left) displays the mean of the TRT track-hit residuals as a function of ϕ-sector and z (along the wires) for the innermost TRT barrel layer. One can observe biases in the residuals of up to 80 μm that vary along the wires. This residual structure in z can only be removed by aligning the wires. A similar internal structure of the track-hit residuals was also observed in the end-cap wires. Figure 4.7(left) shows the fitted mean of the TRT residual as a function of ϕ and end-cap wheel identifier. Within an end-cap wheel, there are regions with internal variations of the residual means of up to 150 μm. These regions vary continuously within the end-cap wheels and discontinuously across wheel boundaries. The residual variation in ϕ is oscillatory with two full periods over 2π. This pattern in the residual structure was thought to be the result of elliptical deformations of the end-cap wheels. Such deformations would be expected to be uncorrelated wheel-to-wheel given their independent construction, and cannot be described by either a translation or rotation of the whole wheel (*Level 2* alignment) as the internal wire alignment in each wheel is preserved at this level. The internal structure of the TRT end-cap module residuals can also be observed in a different view. Figure 4.7(left) shows

the fitted mean of the TRT residual as a function of radius and end-cap wheel. Within an end-cap wheel, the residual mean varies (up to 150 μm) continuously along the radius (r), and tends to oscillate in neighbouring wheels. This pattern in the residual structure is consistent with a ϕ rotation of the inner radius of the wheel with respect to the outer radius. The wheel-to-wheel oscillations can be explained by the way in which the wheels were assembled. Neighbouring wheels were constructed independently on the same assembly table, and pairs of end-cap wheels were then combined back-to- back and stacked to form the end-caps. A deformation in the machining table, giving rise to a twisting of the end-cap rings, would give rise to the observed wheel-to-wheel oscillatory pattern. A wire-by-wire alignment was performed in order to correct the systematic variations shown in the left plot of the Figures 4.6-4.8. All of the TRT barrel and end-cap wires were aligned using just two degrees of freedom per wire. In the barrel, the translations along $\hat{\phi}$ (T_ϕ) and rotations about $\hat{r}$ (R_r) were aligned. $\hat{\phi}$ represents the unit vector in the plane transverse to the beam direction at the wire position, whilst $\hat{r}$ denotes the radial direction in the transverse plane at the wire position. The end-cap degrees of freedom used were the translations along $\hat{\phi}$ (T_ϕ) and rotations about z (R_z). These degrees of freedom are those that correspond to movements of the wire in the sensitive direction, perpendicular to the track trajectory of tracks coming from the interaction point. The resulting alignment corrections correspond to wire movements of up to hundreds of micrometers.

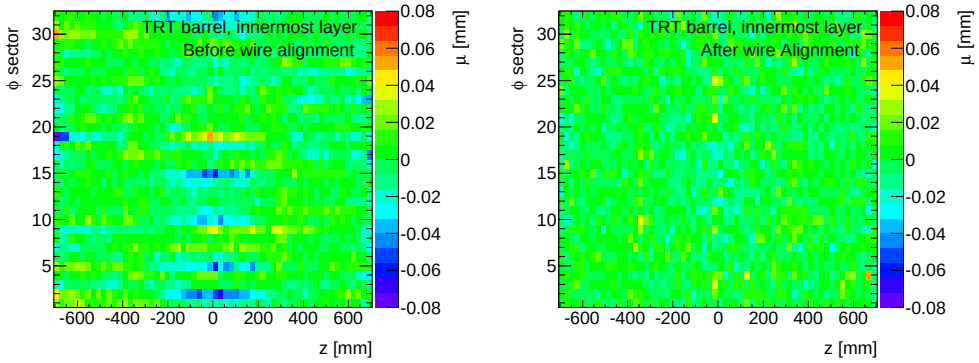

Figure 4.6: Mean of a Gaussian fit to TRT residuals vs ϕ-sector and z for the first TRT barrel layer before (left) and after (right) the wire-by-wire alignment.

4.2.3.3 Centre-of-Gravity Correction

The CoG algorithm (Section 3.3) was applied at the very end of the complete alignment sequence. Due to the beam spot constraint used during alignment, only four corrections were actually applied: T_z, R_x, R_y and R_z. Such a scheme results in an unchanged position of the apparent luminous region after the alignment procedure. The typical values found for the rotations is of the order of 0.1 mrad. This alignment set it will be indicated as *Spring 2010 Alignment*.

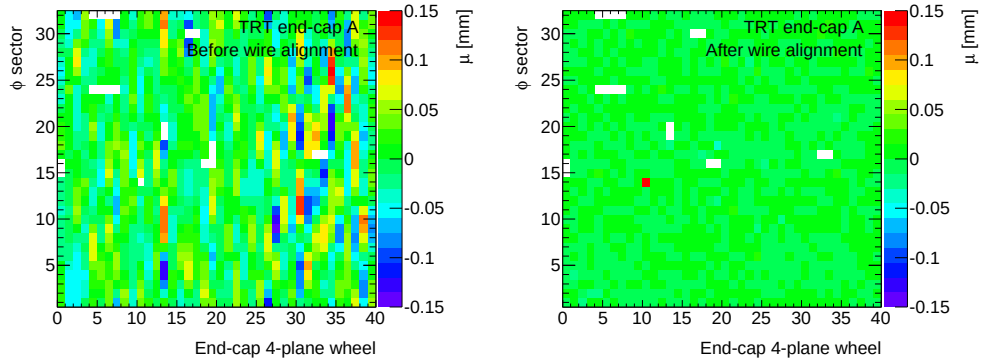

Figure 4.7: Mean of a Gaussian fit to TRT residuals versus ϕ-sector and wheel before (left) and after (right) the wire-by-wire alignment. The plots illustrate the end-cap A results. The white bins are due to dead channels.

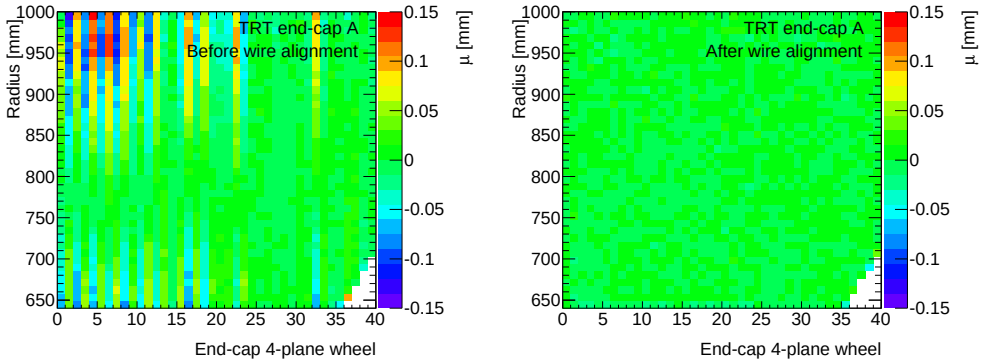

Figure 4.8: Mean of a Gaussian fit to TRT residuals versus radius and wheel before (left) and after (right) the wire-by-wire alignment. The plots illustrate the end-cap A results. The white area in the lower right corner is due to acceptance effects.

4.2.3.4 Error Scaling Determination

If the detector intrinsic errors ($\sigma_{0\text{hit}}$) describe exhaustively the uncertainties on hit positions, then the pull of the track-hit residual distributions should follow a Gaussian distribution with mean $\mu = 0$ and standard deviation $\sigma = 1$. If there are some other unaccounted effects, e.g. residual detector misalignments, the observed pull distributions will generally have $\sigma > 1$. It must be noted that the intrinsic hit errors depend strongly on the detector type and on their calibration. Thus, the final stage of the alignment procedure is to determine corrections to the intrinsic detector hit error to restore the track-hit residual pull distributions to unit-width Gaussians. In order to account for possible extra contributions, the assumed hit error may be altered according to the

following expression:

$$\sigma_{\text{scaled}} = a\sigma \otimes c \tag{4.1}$$

where a is a multiplicative factor that may account for internal resolution details, and c is a constant, which can be interpreted as a measure of the module random misalignments. The two terms are added in quadrature. The determination of the error scaling terms allows an appropriate description of the measurement errors. Consequently, the resulting errors on reconstructed track parameters and vertices are more accurate. In order to obtain the error scaling terms, an iterative method was applied on the *collision* track data set. The tuning was performed by fixing $a = 1$ and only altering c. So the main extra contributors to the hit errors are thus the module random misalignments. The error scaling tuning was conducted using *unbiased* residuals in the pixel, SCT and TRT detectors, and in particular the hits on both sides of the respective SCT modules were dropped from the reference track (so-called *fully unbiased* residuals) Starting with $c = 0$, the residual pull distributions were fitted to a Gaussian distribution. The c value was then computed such that the residual pull distributions became unit-width Gaussians. In the next iteration, the tracks were refitted, but this time, the hits on the track used the new hit error (which employs the new c value as given in Equation 4.1). New residual pull distributions were obtained and a new correction c calculated. This procedure was iterated several times. A different set of error scaling values was determined for each ID sub-detector.

The c values give an estimation of each sub-detector resolution. The residual pull distributions of each sub-detector barrel, before and after the error scaling determination, are given in Figure 4.9, whilst the final c values are given in Table 4.1. These pull distributions are produced using data collected with a minimum-bias trigger [41] from $\sqrt{s} = 7$ TeV LHC proton-proton collisions. It must be noted that the c terms for the TRT are zero for both barrel and end-cap. This is because the TRT residual pulls already have $\sigma < 1$. This is a sign that the TRT hit errors are currently being overestimated.

Detector type	Coordinate	Barrel	End-caps
		$c[\mu\text{m}]$	
Pixel	local x	4	7
	local y	18	35
SCT	local x	10	11
TRT		0	0

Table 4.1: Error-scaling constant term (c) for the barrel and end-cap part of the ID subsystems as derived using real data at 7 TeV.

4.3 Alignment performance

4.3.1 Residuals

In this section the results which demonstrate the quality and performance of the ID alignment are presented. For this purpose two 7 TeV proton-proton collision datasets

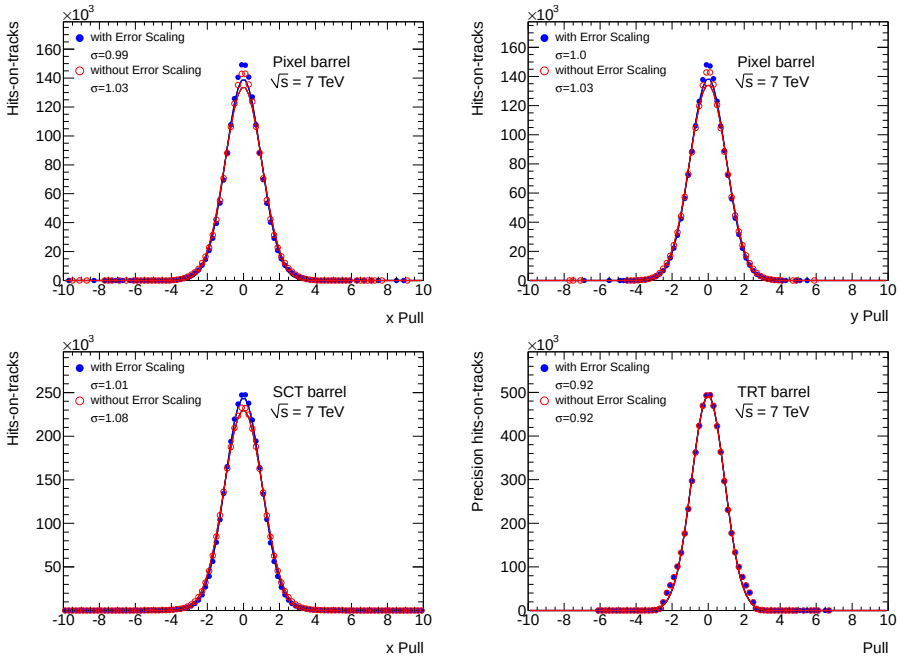

Figure 4.9: Pulls of the Pixel barrel modules (top), SCT barrel modules (bottom left) and TRT barrel modules (bottom right) before and after error scaling is applied for $\sqrt{s}$ = 7 TeVLHC proton-proton collisions.

are used and are reconstructed using the ID alignment geometry that results from the **??**, although there are more recent results at present. The first dataset comprises events collected using a minimum-bias[41] trigger from proton-proton collision runs corresponding to run period E (runs taken between 29th July 2010 and 18th August 2010). The second dataset comprises events collected using a jet trigger, again using runs from run period E. In both datasets only data collected during stable beam periods in which the silicon systems were operated at full bias voltage is used. Each event used is required to have a primary vertex reconstructed with at least 3 tracks.

4.3.1.1 Comparison between alignment sets

In this section the improvement in the 7 TeV alignment with respect to the previous alignment is investigated. The minimum bias data sample is reconstructed using the new ID alignment and error scaling described in section 4.2.3 (labelled *Autumn 2010 Alignment*), and this is compared to the same data sample reconstructed with the previous ID alignment and error scaling described in section 4.2.2(labelled *Spring 2010 alignment*). Figure 4.10 compares the hit-on-track residual distributions obtained with the two different ID alignment setups for the Pixel, SCT and TRT barrel and end-cap modules. In the case of the Pixel and SCT the residual shown is that in the local x

direction. Shown is the full width half maximum (FWHM) of each distribution, divided by a factor 2.35 (for a Gaussian distribution the FWHM and standard deviation, σ, are related by $\sigma = \mathrm{FWHM}/2.35$).

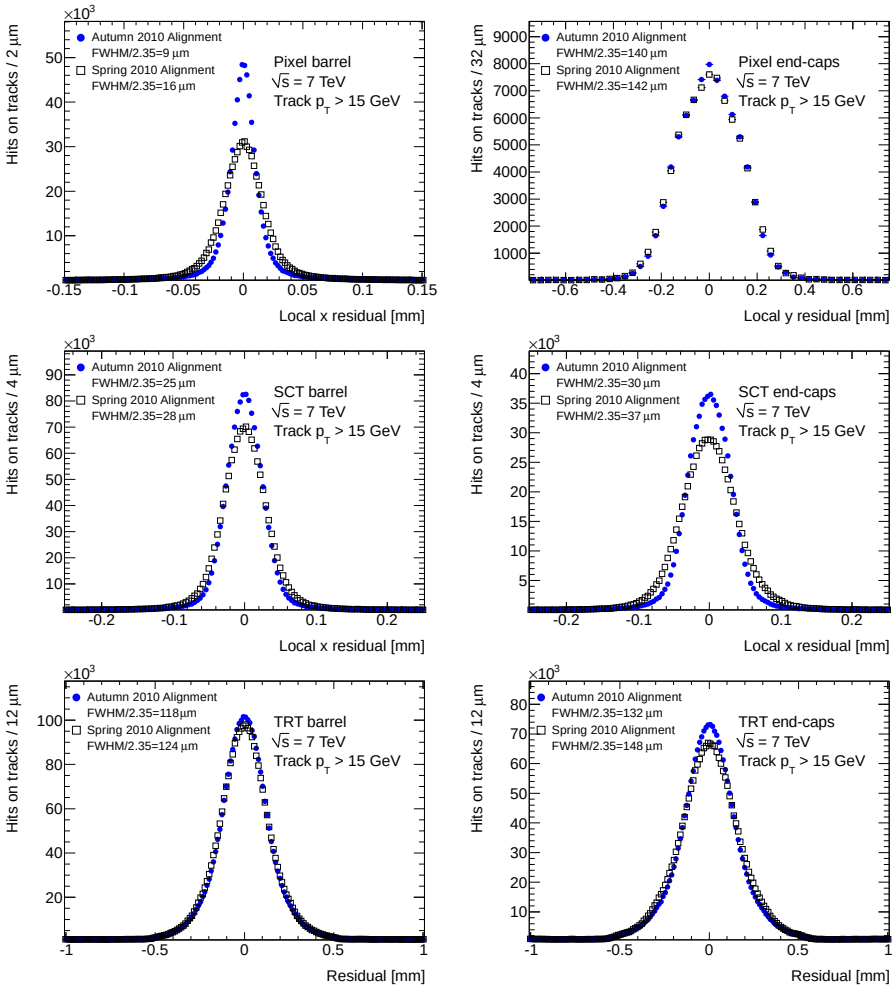

Figure 4.10: Tracking local x unbiased residual distributions obtained by reconstructing the jet trigger data sample with the *Spring 2010 Alignment* (open squares) and *Autumn 2010 Alignment* (solid circles). The distributions are integrated over all hits-on-tracks in the Pixel barrel and end-cap modules (top), SCT barrel and end-cap modules (middle), and TRT barrel and end-cap modules (bottom).

In this comparison, the narrower residual distributions observed when using the *Autumn 2010 Alignment* relates directly to the overall improvement in the hit resolution for those modules. In order to more quantitatively assess the improvement in the alignment,

one can perform a simple calculation to determine the additional resolution component (σ_{diff}) that would have to be added in quadrature to the *Autumn 2010 Alignment* width (σ_{Autumn}) in order to reproduce the *Spring 2010 Alignment* width (σSpring). Thus: $\sigma_{\text{diff}} = \sqrt{\sigma^2_{\text{Spring}} - \sigma^2_{\text{Autumn}}}$. These results are reported in Table 4.2.

type	Coordinate	σ_{Spring} μm	σ_{Autumn} μm	σ_{diff} μm
Pixel barrel	local x	25	19	16
Pixel end-caps	local x	20	19	6
SCT barrel	local x	41	36	19
SCT end-caps	local x	44	38	22
TRT barrel		127	122	35
TRT end-caps		150	136	63

Table 4.2: The additional resolution component (σ_{diff}) that would have to be added in quadrature to the Autumn 2010 Alignment width (σAutumn) in order to reproduce the Spring 2010 Alignment width (σSpring).

As expected, the internal wire-by-wire alignment of the TRT barrel and end-caps (Section 4.2.3.2) resulted in a substantial reduction of the contribution of misalignment to the effective TRT hut resolutions. Large improvements in the alignment of the Pixel barrel, SCT barrel and SCT end-caps are also observed. These improvements are of course expected since the number of hits per module and momenta of the tracks used to perform the module-to-module alignment are both much larger in the last alignment. In the case of the Pixel barrel modules, the modelling of the pixel module distortions in the reconstructions had a large impact. In the case of the SCT end-caps, al large component of the improvements derives from the significant corrections applied to the individual end-cap disks.

4.3.1.2 Comparison to Monte Carlo Simulation

In this section the data samples are compared with the corresponding Monte Carlo simulation samples. These MC samples are simulated using a detector model where the ID modules are in their nominal positions and orientations, and subsequently with *perfect* ID alignment. The same track reconstruction setup is used in the MC as was used in the data, and exactly the same track selection requirements are applied. Many of the observables are dependent on the p_T and η distributions of the input tracks. Due the impact of multiple scattering, the width if hit-on-track residual distributions is strongly dependent on the p_T spectra of the tracks. The residual distributions are also strongly dependent on η due to the differing intrinsic resolutions of ID modules traversed by the tracks at different rapidity regions. In order to have a good ID alignment performance, comparing the data and MC, they should have a reasonable agreement.

Figure 4.11 shows the local x residual distribution for all hits-on-tracks in Pixel barrel modules(left) and Pixel end-cap modules (right). Similarly, Figure 4.12 shows the local y residual distributions for Pixel barrel and end-cap modules while Figure 4.13 shows the

local x residual distributions for SCT barrel and end-cap modules. Figure 4.14 shows the residual distributions for TRT barrel and end-caps. Under the assumption that the MC simulation models perfectly the intrinsic hit resolution and the contribution of Multiple Coulomb Scattering (MCS), the difference in the observed residual width between the MC simulation and the data can be related directly to the contribution of residual mis-alignments in the data. In the case of the Pixel end-cap, SCT end-cap and TRT barrel modules, it can be seen that the data and MC simulation residual distributions agree very well, implying that the contribution of mis-alignments to the effective hit resolution in these modules is negligible. In the case of the Pixel barrel, SCT barrel and TRT end-cap modules, the slightly larger residual widths observed in the data imply relatively small residual mis-alignments that continue to degrade the hit resolution in these areas of the detector.

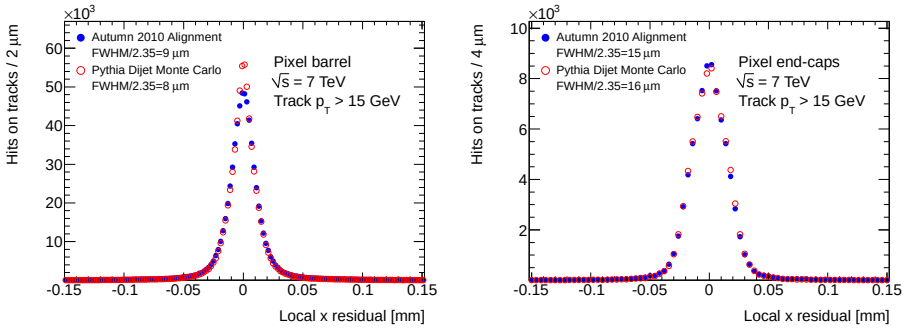

Figure 4.11: The Pixel local x residual distributions for the jet trigger data sample reconstructed with the *Autumn 2010 Alignment* (full circles), compared with the dijet MC simulation sample (open circles). The distributions are integrated over all hits-on-tracks in barrel modules (left) and end-cap modules (right). Tracks are required to have $p_T > 15$ GeV.

In order to investigate further the impact of MCS effects on these conclusions, the FWHM/2.35 of the residual distributions are plotted as a function of track p_T for $p_T > 2$ GeV (Figure 4.15). In can be observed that the residual width decreases as track p_T increases, until it reaches an asymptotic limit, where the residual width is determined by the contributions of the intrinsic resolution and, in the data, module mis-alignments. Above $p_T > 15$ GeV, the MCS contribution is strongly suppressed and the data-simulation discrepancy likely due to remaining module-to-module misalignments.

If a module layer in the barrel or a disk in the end-caps is mis-aligned with respect to the others the hits in that layer/disk will be systematically displaced from their true position, and the mean of the residual distribution for that layer or disk will be significantly different from zero. Figure 4.16 shows the mean of the residual distributions as a function of the module layer in the Pixel and SCT barrels, and as a function of the module disk in the Pixel and SCT end-caps. Figure 4.17 shows the mean of the residual distributions as a function of the straw layer in the TRT barrel, and Figure 4.18 shows the residual mean as a function of the end-cap wheel in the TRT end-caps. Since the

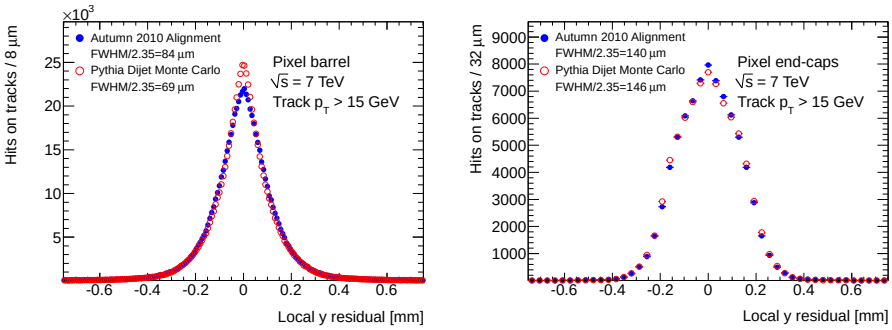

Figure 4.12: The Pixel local y residual distributions for the jet trigger data sample reconstructed with the *Autumn 2010 Alignment* (full circles), compared with the dijet MC simulation sample (open circles). The distributions are integrated over all hits-on-tracks in barrel modules (left) and end-cap modules (right). Tracks are required to have $p_T > 15$ GeV.

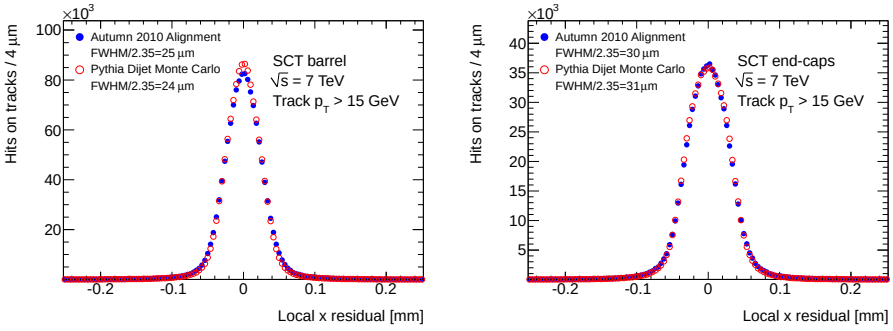

Figure 4.13: The SCT local x residual distributions for the jet trigger data sample reconstructed with the *Autumn 2010 Alignment* (full circles), compared with the dijet MC simulation sample (open circles). The distributions are integrated over all hits-on-tracks in barrel modules (left) and end-cap modules (right). Tracks are required to have $p_T > 15$ GeV.

mean of the residual distribution is not dependent on the track p_T, for these distributions the tracks are required to have $p_T > 2$ GeV. In the case of the Pixel and SCT barrel and end-cap layers, very small biases at the sub-micron level can be observed. In the TRT barrel layers and end-cap wheels, the biases are below 3 micrometers. The origin of this small biases may be related with relative movements of the ID layers and disks of the level of 5μm between different run periods. In this case, the runs used to analyse the alignment performance differ from the runs used to derive the alignment constants.

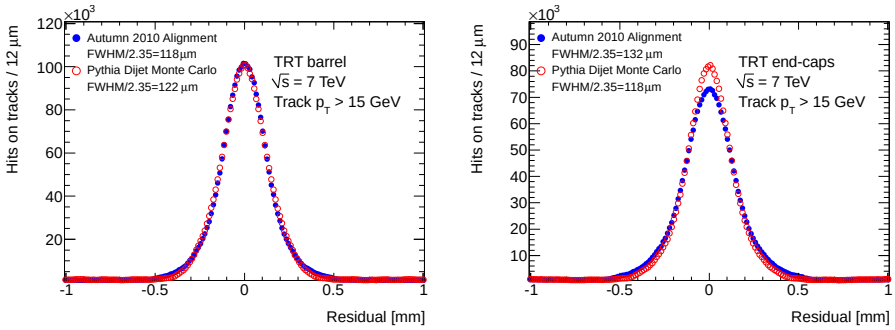

Figure 4.14: The TRT residual distributions for the jet trigger data sample reconstructed with the *Autumn 2010 Alignment* (full circles), compared with the dijet MC simulation sample (open circles). The distributions are integrated over all hits-on-tracks in barrel modules (left) and end-cap modules (right). Both precision and non-precision (tube) hits are used. Tracks are required to have $p_T > 15$ GeV.

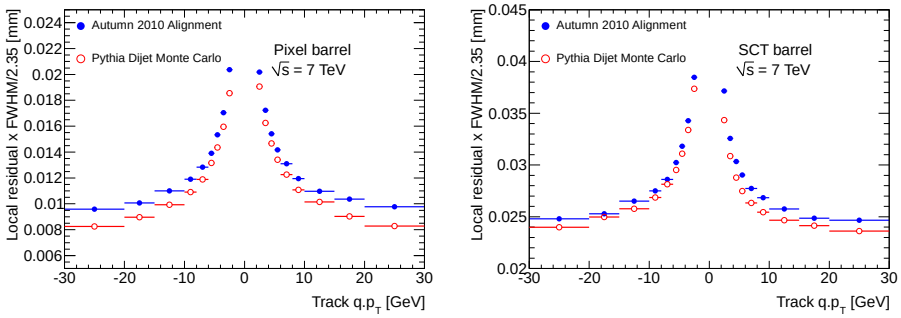

Figure 4.15: The FWHM/2.35 width of the residual distributions for modules in the Pixel and SCT barrels as a function of track p_T. The residual distributions for the jet trigger data sample reconstructed with the *Autumn 2010 Alignment* (full circles) are compared with the dijet MC simulation sample (open circles).

4.3.2 Study of alignment-related systematic effects

The ID has been aligned as presented in previous sections. However, any generic track-based alignment is confronted with some modes to which fitted tracks have very low or no sensitivity. These so called *weak modes* of alignment are detector deformations that preserve a helical trajectory of the tracks and hence of not affect the χ^2 of the track fit (see Section 3.4).Weak modes are the principal source of systematic effects related to the alignment procedure. Among the possible biases on the reconstructed track parameters, the most important biases are those which affect the measured momentum and impact parameter. The biases on the momentum have an impact on many observables: the invariant mass of resonances, charge symmetries [42], etc. The biases in the impact

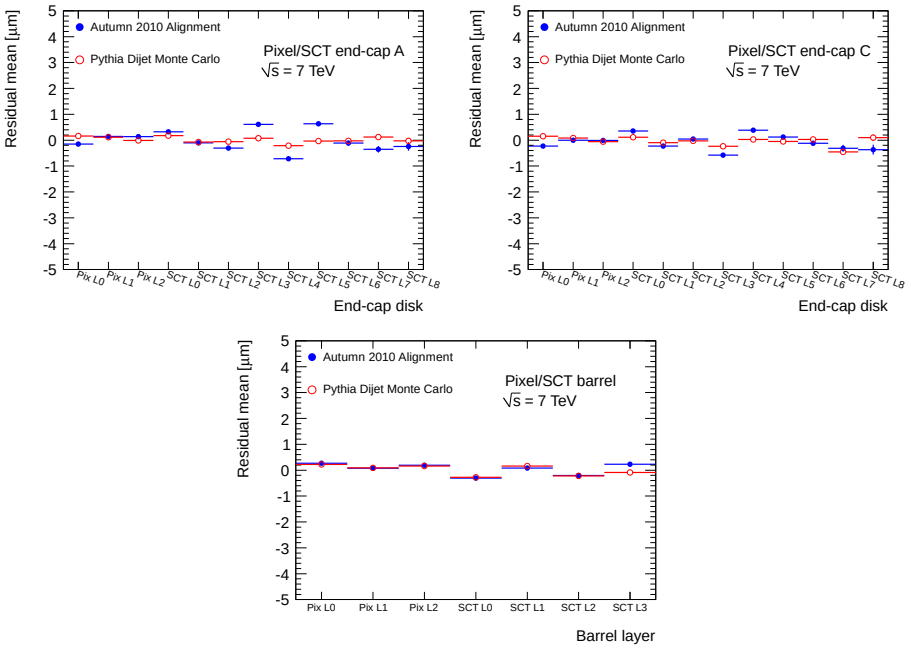

Figure 4.16: Mean of the residual distributions as a function of the module layer in the Pixel and SCT barrels, and as a function of the module disk in the Pixel and SCT end-caps. The residual distributions for the jet trigger data sample reconstructed with the *Autumn 2010 Alignment* (full circles) are compared with the dijet MC simulation sample (open circles). Tracks are required to have $p_T > 2$ GeV.

parameter affect many measurements related to the beam-spot reconstruction [43], primary and secondary vertex fitting [44, 45], and the b-tagging performance [46, 47]. This section documents experimental techniques developed and applied to detect, assess and eventually eliminate various systematics present in the ID alignment. Two different set of alignment sets will be compared. The corrections obtained in the Section 4.2.3 are hereafter referred to as *Release 16*. Correction of the charge anti-symmetric momentum bias based on the asymmetry of the measured E/p ratio for electrons and positrons was introduced during summer 2011 reprocessing campaign. Data from this reprocessing are hereafter referred to as *Release 17*

4.3.2.1 Detector distortions as observed using reconstructed invariant masses

The invariant mass of a particle in its two-body decay can be used to constrain certains systematics biases on the reconstructed momenta of charged particles. This subsection describes the basic principle of the techniques used to extract information on the momentum biases present in the detector by studying invariant masses of the K^0_S and J/ψ mesons and the Z boson. Violations of expected symmetries in the reconstructed masses

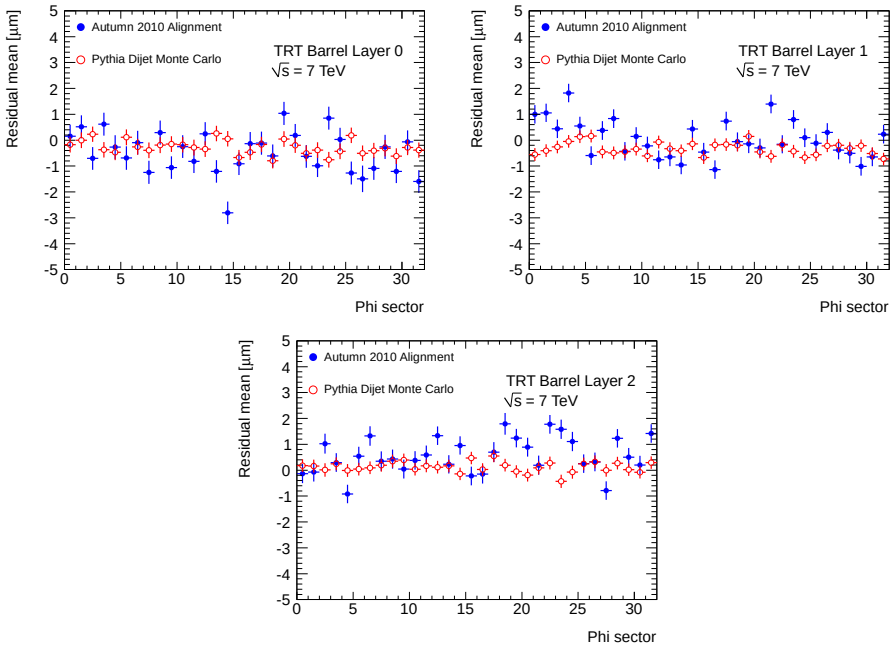

Figure 4.17: Mean of the residual distributions as a function of phi sector for the three layers of the TRT barrel. The residual distributions for the jet trigger data sample reconstructed with the *Autumn 2010 Alignment* (full circles) are compared with the dijet MC simulation sample (open circles). Tracks are required to have $p_T > 2$ GeV.

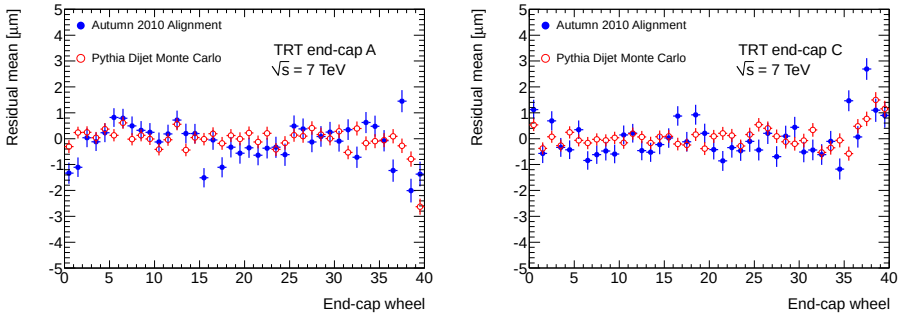

Figure 4.18: Mean of the residual distributions as a function of end-cap wheel in the TRT end-cap A and end-cap C. The residual distributions for the jet trigger data sample reconstructed with the *Autumn 2010 Alignment* (full circles) are compared with the dijet MC simulation sample (open circles). Tracks are required to have $p_T > 2$ GeV.

of known particles can be converted into a measurement of the assumed deformation. Particles decaying into one positively and one negatively charged particles will be considered. In the case of a perfect detector, the reconstructed mass should not depend on the particular kinematics of the decay. As seen in Section 3.4.1, the charge-antisymmetric deformations result in biases which are quadratic in the transverse momentum. This leads to an expected mass shift which also depends quadratically on the momenta of the decay products. Therefore, high-mass particles are favoured for their detection. In contrast to the charge-antisymmetric momentum bias, the charge symmetric bias has a linear impact on the measured momentum as seen in Section 3.4.2. Low-mass particles such as K_S^0 and J/ψ are adequate for the study.

4.3.2.2 Probing systematic misalignments using the $Z \to \mu^+\mu^-$ decays.

The Z boson, with its decay to two oppositely charged muons, provides a clean signature and a powerful tool for studying alignment performance and probing systematic effects. With a well-known intrinsic resolution, the estimated resolution of the di-muon invariant mass is a measure of detector effects. Muons from Z decays tend to have considerably higher p_T and are less sensitive to systematic effects in the material description compared to lower-mass particle decays. The distributions of the reconstructed invariant mass of the Z boson for 2011 data before charge-antisymmetric alignment corrections (*Release 16*), and Monte Caro simulation of a perfectly aligned detector will be shown. The systematic misalignment effects are probed by searching for biases of the invariant mass as function of various kinematic quantities.

Figure 4.19 shows he distributions of the reconstructed Z invariant mass for data in *Release 16*, and perfectly aligned Monte Carlo. It shows the Z mass for all the detector and for different detector regions. The mass distributions in data are wider than in the Monte Carlo for all regions of the detector.

Systematic misalignment effects are probed by searching for shifts of the invariant mass as functions of various kinematic quantities. The invariant mass distribution is fitted using a Breit-Wigner convolved with a Crystal-Ball function. The Breit-Wigner distribution is used for describing the intrinsic Z-mass distribution, keeping the width fixed to its PDG value at 2.495 GeV[2]. For the resolution function, a Crystal-Ball function is used. The Crystal-Ball consists of a Gaussian core with a polynomial tail to take the energy-loss into account. The fitted mean of the Z invariant-mass distribution and corresponding mass resolution are shown as functions of muon η, shown in Figure 4.20. The mass resolution is degraded in data, especially in the End-cap regions.

Figure 4.21 shows the curvature difference, probing the curl misalignment, and Figure **??** shows the mass as a function of the difference in η between the two muons, probing the twist misalignment. There is not suggestion of a significant curl of the detector, while there is some indication of a twist like deformation of end-cap A.

Figure **??** shows the mean invariant mass as function of ϕ of the positive and negative muons. Large deviations of the reconstructed mass can be seen as function of ϕ, especialy in the end-cap regions of the detector. End-cap A, which shows signs of a twist as seen in Figure 4.22 has the largest mass biases when viewed as function of ϕ. However, the magnitude of the distortion is a factor three to four times larger when comparing the mass shifts as a function of ϕ and $(\eta^+ - \eta^-)$. This strongly suggests that a large degree

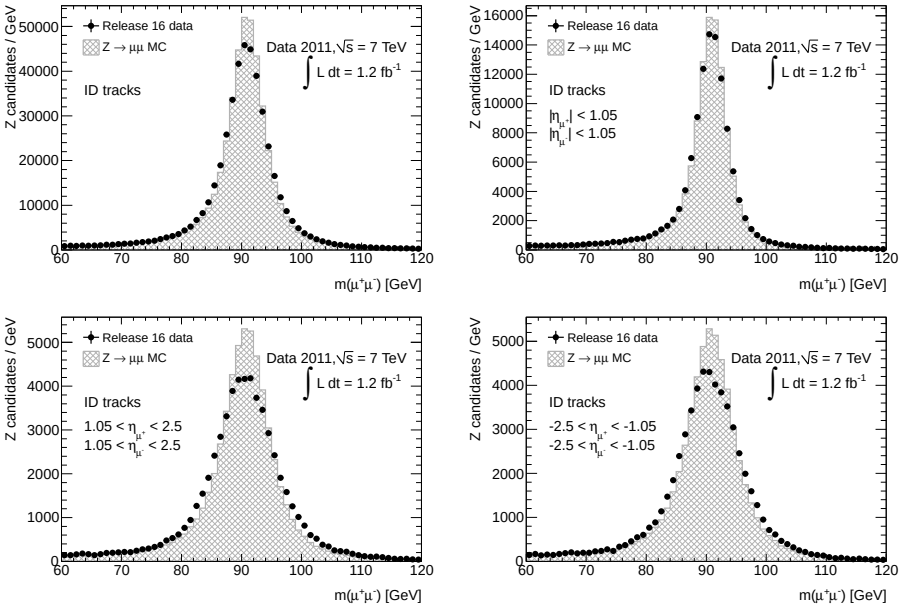

Figure 4.19: Reconstructed Z mass distributions showing data before charge-antisymmetric alignment corrections and perfectly aligned Monte Carlo for the entire detector (top left), when both muons are in the barrel of the detector(top right), when both muons are in end-cap A (bottom left) and when both muons are in end-cap C (bottom right).

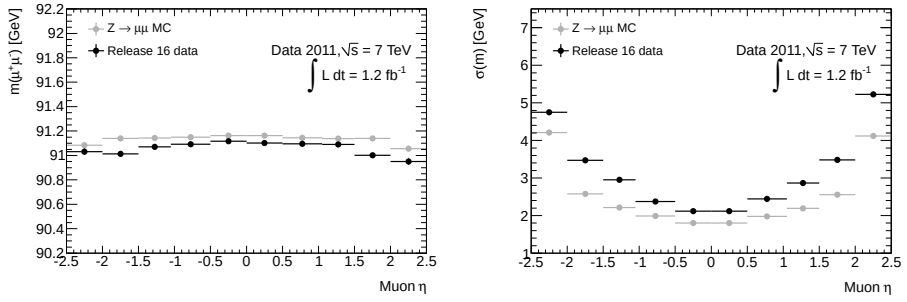

Figure 4.20: Fitted mean Z mass (right) and resolution (left) as a function of muon η and , for collision data before charge- antisymmetric alignment corrections and perfectly aligned Monte Carlo. Both muons from the Z are used.

of cancellation is occurring when looking at data more inclusively.

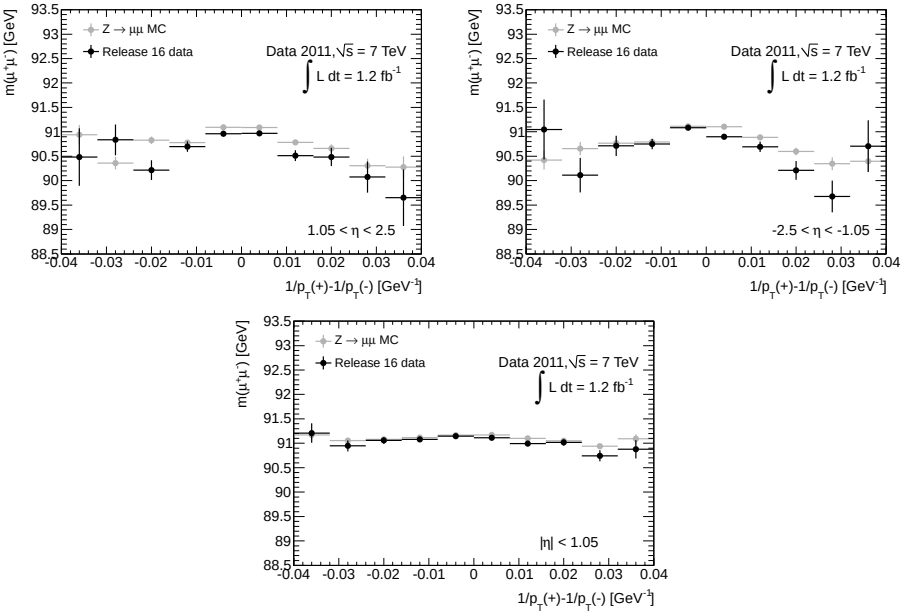

Figure 4.21: Fitted mean Z mass as a function of curvature difference in the barrel (bottom), end-cap A (top left) and end-cap C (top right), for collision data before charge-antisymmetric alignment corrections and perfectly aligned Monte Carlo.

4.3.2.3 Iterative method to extract momentum biases using $Z \to \mu^+\mu^-$

In general, the systematic deformations of the detector will not be as simple as those described in earlier sections. Due to the limited correlation between the modules during the alignment procedure, higher-order deformations are foreseen and would result in localised distortions to the track parameters which may be missed when inspecting inclusive distributions. As deformations manifest as biases in the reconstructed track parameters, in particular the momentum, this will in turn bias the reconstructed Z mass. It is then possible to extract the magnitude of the individual track momentum biases by characterising the shifts in the reconstructed Z mass throughout the different detector regions. This method is able to provide local systematic momentum bias information at a much higher granularity than the differential method presented in previous section. In addition, this method is complementary to the E/p method of determining momentum biases which will be presented in a later section. The invariant mass m of two low-mass and highly relativistic particles is given approximately by:

$$m^2 = 2p_1p_2(1 - \cos\theta) \tag{4.2}$$

where p_1 and p_2 are the momenta of the particles and θ is the angle between the momentum vectors. If we assume a sagitta deformation (Section 3.4.1), then the momentum

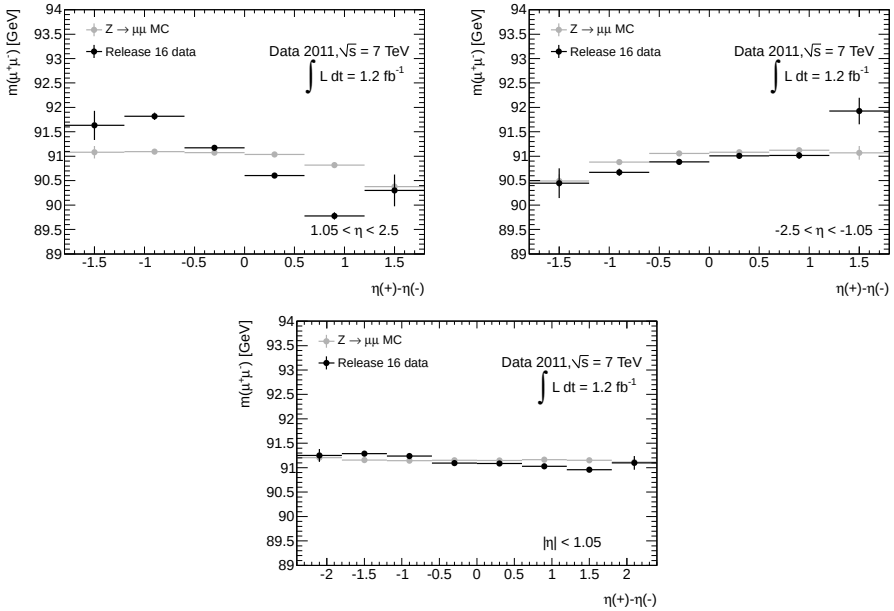

Figure 4.22: Fitted mean Z mass as a function of difference in *eta* in the barrel (bottom), end-cap A (top left) and end-cap C (top right), for collision data before charge-antisymmetric alignment corrections and perfectly aligned Monte Carlo.

will scale charge-anti-symmetrically as:

$$q/p \to q/p(1 + qp_T\delta_{sagitta}) \tag{4.3}$$

Ignoring the uncertainties on the angular variables, the reconstructed mass m_{rec} can be expressed in therms of the momentum biases:

$$\Delta(m^2) \equiv \frac{m^2_{\text{rec}} - m^2_{\text{Z}}}{m^2_{\text{Z}}} \approx q_1 p_{T1}\delta_1 + q_2 p_{T2}\delta_2 \tag{4.4}$$

where we have used $\delta \equiv \delta_{\text{sagitta}}$ for brevity. Likewise, we could also assume a radial misalignment (Section 3.4.2) which biases the momenta symmetrically for opposite-sign tracks:

$$p \to p(1 + \delta_r) \tag{4.5}$$

In this case:

$$\Delta(m^2) \equiv \frac{m^2_{\text{rec}} - m^2_{\text{Z}}}{m^2_{\text{Z}}} \approx \delta_{r1} + \delta_{r2} \tag{4.6}$$

In either parametrisation, there is no a reason to assign the momentum bias to one mount or the other. To handle this ambiguity properly, $\frac{1}{2}\Delta(m^2)$ is assigned to the δ of each muon. As the momentum systematics are expected to vary in η and ϕ due to

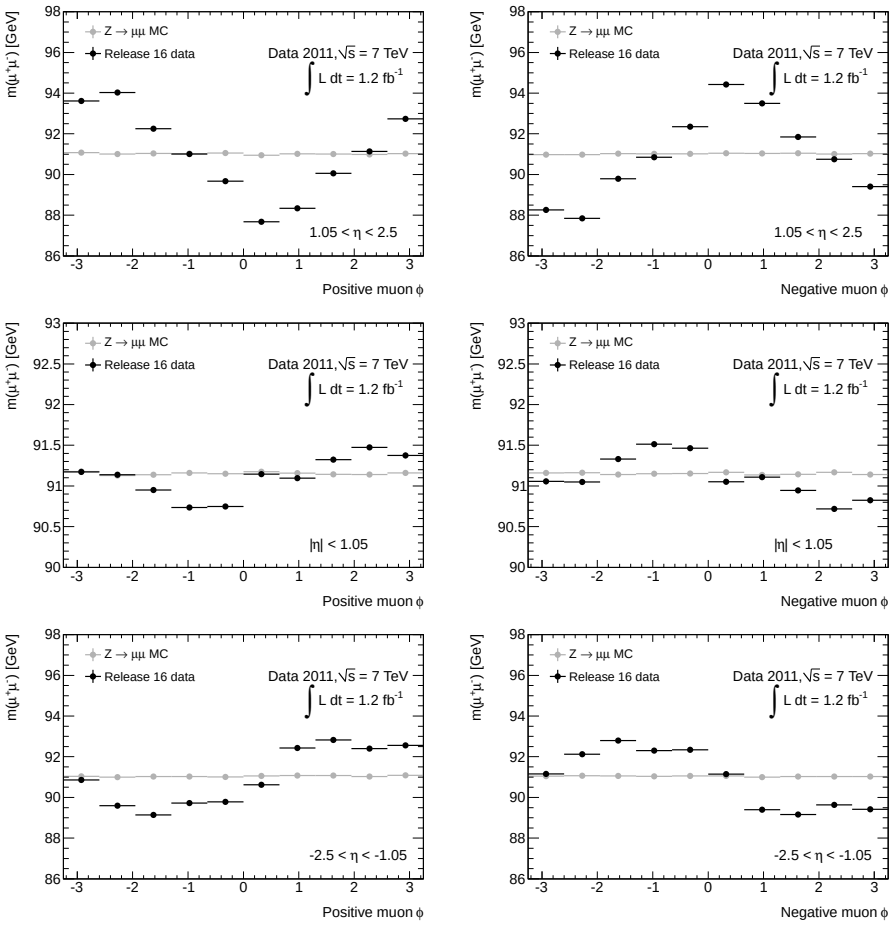

Figure 4.23: Fitted mean Z mass as a function of phi of the indicated muon in the barrel (middle), end-cap A (top) and end-cap C (bottom) for collision data before charge-antisymmetric alignment corrections and perfectly aligned Monte Carlo.

detector deformations, the δ parameters are binned as a function of them. For each bin in η and ϕ, the measured δ distribution is fitted with a Gaussian function using an iterative fir procedure in which the range of the fit is restricted to 1.4σ of the previous iteration fit. This procedure fins the peak position of the δ distribution and is not sensitive to the tails of the distribution. The fitted value of μ is assigned as the systematic momentum bias δ in each η and ϕ bin. Because this ambiguity in assigning the momentum bias to either moun, an iterative procedure is then applied to ensure that derived momentum biases are estimated correctly. In each iteration, the measured biases from the previous iteration are used to correct the muon momenta before calculating the Z mass and re-calculating the δ parameters. This procedure is then iterated until the δ parameters

have converged and the Z mass is a flat function of η and ϕ, within the uncertainties.

Figure 4.24 shows the derived δ_{sagitta} (left) and δ_{r}(right) parameters for *Release 16* data as function of η and ϕ. Biases up to 8% at 40 GeV can be seen in the forward positive η region. These biases are the result of weak modes in the detector (resolved by the E/p constrained alignment procedure) and time-dependent movements of large detector structures. The barrel region of the detector shows significantly smaller biases than the regions where $|\eta| > 1$. Results of this analysis show that the dominating systematic effects are charge-antisymmetric and have highly non-uniform nature.

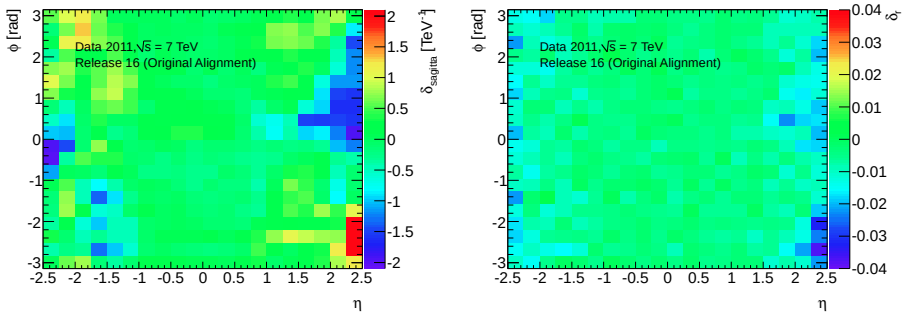

Figure 4.24: Derived momentum bias parameters for the charge-antisymmetric parametrisation (left) and the charge-symmetric parametrisation (right) in *Release 16* data, using the iterative $Z \to \mu\mu$ method.

4.3.2.4 Measurement of detector distortions using the electron E/p method

By using the electromagnetic calorimeter as a reference system, it is possible to probe the systematics present in the ID. I can be done using the ratio of the measured energy deposited calorimeter (E) and of momentum as measured by the ID (p) of electrons.

Under the assumption that the calorimeter response is independent of the charge of the incoming particle, charge-dependent momentum biases introduced by the alignment procedure in the ID are expected to be seen as differences in the E/p ratio for electrons and positrons. There are some deformations, such as radial expansions, which will affect both positive and negative particles in a similar manner and as such can not be disentangled from potential calorimeter energy-scale problems. A sagitta deformation in the ID would bias the reconstructed momentum according to Equation 4.3. As a result, them measured $\langle E/p \rangle$ should be modified as:

$$\langle E/p \rangle^{\pm} \to \langle E/p \rangle^{\pm} \pm \langle E_T \rangle \delta_{\text{sagitta}} \tag{4.7}$$

If it is assumed that $\langle E/p \rangle^{+}_{\text{true}} = \langle E/p \rangle^{-}_{\text{true}}$, then it is possible to extract the momentum biases present in the detector. This is a valid assumption if the kinematic properties of the selected electrons and positrions are similar. Under this assumption the momentum

bias in terms of $\langle E/p \rangle$ can be shown to be:

$$\delta_{\text{sagitta}} = \frac{\langle E/p \rangle^{+}_{\text{rec}} - \langle E/p \rangle^{-}_{\text{rec}}}{2\langle E_T \rangle} \tag{4.8}$$

If the kinematics for electrons and positrons used are the same, the energy scale of the calorimeter will not affect the difference between $\langle E/p \rangle^{+}$ and $\langle E/p \rangle^{-}$. However, the energy scale will affect the $\langle E_T \rangle$ which will act as scaling factor in the measured δ. At present, the energy scale is known to better that 1% across the entire calorimeter[48]. To perform the E/p studies, it is desirable to have a high-purity collection of high-p_T electrons and positrons. A study of the systematic uncertainties affecting the value of $\langle E/p \rangle$ can be found in [49]. As we are only interested in the difference between $\langle E/p \rangle^{+}$ and $\langle E/p \rangle^{-}$, the majority of these effects will cancel (material effects, energy and momentum resolution, and fit model). However, if background levels differ significantly for electrons and positrons, then this may bias the momentum measurement. Consequently electrons from W and Z boson decays have been used to obtain a high purity sample of electron candidates. To reduce the effects of background contamination, which may differ for electrons and positrons given our signal selection, a fit to the E/p distribution is performed to extract the mean value. The fit of the E/p distribution is performed using an unbinned maximum-likelihood fit with a Crystal-Ball function, which allows the non-Gaussian bremsstrahlung tail to be fitted accurately. To fit the Crystal-Ball function to the data an iterative fit procedure was used.

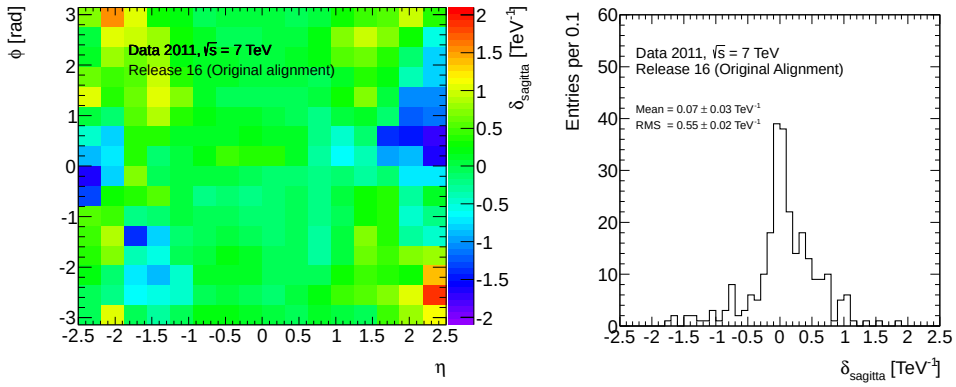

Figure 4.25: Momentum biases (δ_{sagitta}) as measured using E/p in *Release 16* ATLAS data using electrons from W and Z boson decays and represented in a 2D map(left) and 1D projection(right).

Figure 4.25 shows the calculated δ in the various regions of the detector as well the spread of therse values. Significant deviations from the ideal situation can be seen: up to 2 TeV^{-1} which corresponds to $\approx 8\%$ at 40 GeV. The largest deviations are concentrated at the outer edges of the detector's acceptance. These results are in good agreement with what has been shown using muons from Z decays as seen in Section 4.3.2.3.

4.3.2.5 Removing sagitta deformations

It is possible to remove the systematic deformations present in the detector alignment using the information obtained from studies that have been performed. The small charge-symmetric effects that have been observed using $Z \to \mu\mu$ could be caused by a number of non-alignment related factors, as such no attempt to further correct them has been made. The charge anti-symmetric sagitta deformations are best corrected using the high-granularity studies of electron E/p and $Z \to \mu\mu$ as it will be described now. Just as systematic distortions of the detector bias the reconstructed track parameters, the geometry can be efficiently corrected by biasing and constraining track parameters input into the alignment. In particular the momenta of tracks used for alignment can be corrected using the information from the momentum bias measurements to correct for the momentum biases. To correct the momentum using the results from both E/p and the charge anti-symmetric $Z \to \mu\mu$ studies requires that:

$$q/p_{\text{corrected}} = q/p_{\text{reconstructed}}(1 - qp_T\delta_{\text{sagitta}}) \tag{4.9}$$

Tracks tightly constrained to the corrected momentum were used as the input of the alignment algorithm and new alignment constants were calculated to reduce momentum deformations present in the detector. In addition, the impact parameter was contained to the collider luminous region in order to minimise impact parameter distortions [50]. Multiple iterations of the alignment were performed. Between each iteration, the momentum biases were recalculated. Using only E/p for the corrections allowed $Z \to \mu\mu$ event to be used as an independent probe of the alignment performance. Initially three iterations were performed on the entire detector at Level 2 using the Globalχ^2 algorithm. This removed the bulk of the momentum distortions. This was then followed by seven iterations at Level 3 for the silicon part of the detector again using the Globalχ^2 algorithm. Only the silicon detector was aligned at this stage as it was found that the TRT had momentum biases present at the wire-alignment level. The Globalχ^2 solution would not be possible for the entire system due to computational limitations that arise due the large number of degrees of freedom (in excess of 700k). After producing a silicon detector alignment that was free from biases, the TRT was realigned to the silicon utilizing two iterations of the Globalχ^2 algorithm at the module level followed by thirty iterations of the TRT Level 3 wire alignment with the Localχ^2 algorithm and keeping the silicon positions fixed. This ensured that TRT momentum biases were corrected by using the silicon detector as a reference. The results of using such a procedure on data will be shown now.

4.3.2.6 Momentum bias measurement with the updated alignment

In this section, the momentum bias measurements presented in Sections 4.3.2.2 and 4.3.2.4 are repeated on 2011 data after the charge-antisymmetric alignment corrections have been applied (*Release 17*). The $Z \to \mu\mu$ reconstructed mass studies show a significant improvement of the Z-boson mass resolution as a result of the updates to the detector geometry. Figure 4.26 shows the distribution of the reconstructed Z invariant mass, for *Release 17* data and perfectly aligned Monte Carlo. The plots should be compared with analogous ones obtained with *Release 17* data, shown in Figure 4.19. The

agreement between data and Monte Carlo is significantly improved, although not quite perfect. For all regions, the resolution in data is still slightly worse than predicted by the Monte Carlo (Table 4.3).

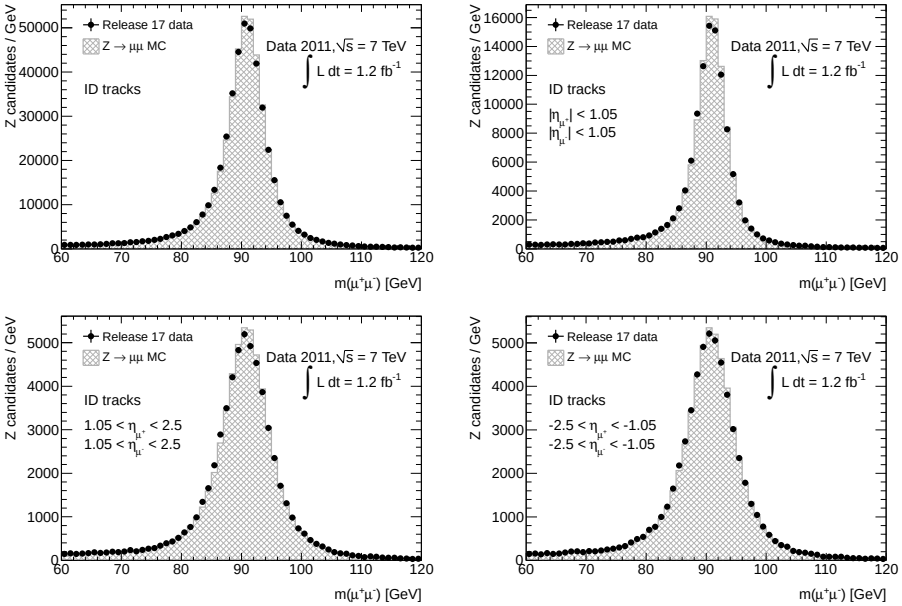

Figure 4.26: Reconstructed Z mass distributions showing data after charge-antisymmetric alignment corrections and perfectly aligned Monte Carlo for the entire detector (top left), when both muons are in the barrel of the detector(top right), when both muons are in end-cap A (bottom left) and when both muons are in end-cap C (bottom right).

	Z mass resolution		
Detector region	Data *Release 16*	Data *Release 17*	Monte Carlo
Full detector	2.90 ± 0.01	2.46 ± 0.01	2.34 ± 0.00
Barrel, Barrel	1.86 ± 0.01	1.75 ± 0.01	1.65 ± 0.00
End-cap A, End-cap A	4.70 ± 0.03	3.63 ± 0.03	3.42 ± 0.01
End-cap C, End-cap C	4.51 ± 0.03	3.60 ± 0.03	3.43 ± 0.01

Table 4.3: Resolution of the fitted Z invariant mass distribution, shown both for the full detector and separately for when both muons are in the barrel region, both in end-cap A or both in end-cap C. Results from data using *Release 16* or *Release 17* are compared to the fitted resolution from perfectly aligned Monte Carlo

The fitted mean of the Z invariant mass and corresponding mass are plotted as

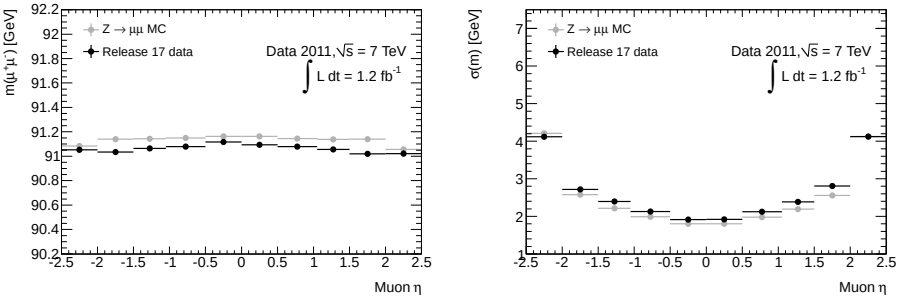

Figure 4.27: Fitted mean Z mass (left) and resolution (right) as a function of muon eta, for collision data after charge- antisymmetric alignment corrections, and perfectly aligned Monte Carlo.

functions of muon μ, shown in Figure 4.27. A clear improvement in the resolution can be observed when it is compared to results from *Release 16*(Figure 4.20). Figure 4.28 shows the curvature difference, probing the curl misalignment, and Figure 4.29 shows the difference in η between the two muons, probing the twist misalignment. Previously, in *Release 16* there was an indication of a twist in end-cap A (see Figure 4.22) which appears to have been removed during the updates to detector geometry for *Release 17*. The most significant improvements can be seen in Figure 4.30, which shows the mean invariant mass as function of ϕ of the positive and negative muons. The results of the iterative $Z \rightarrow \mu\mu$ studies (Section 4.3.2.2) repeated using *Release 17* data are shown in Figure 4.31. The measured biases are flat and nearly zero over much of the detector. Biases of up to 1% at 40 GeV can be seen in the most forward positive η region. After correcting the detector geometry using information from E/p, the resulting biases as measured by E/p are virtually zero (see Figure 4.32) and in good agreement with the results observed in the iterative $Z \rightarrow \mu\mu$ study.

4.4 Run by run alignment

Starting from a fixed set of reference constants a *Level 1* alignment is performed for each ATLAS run prior to data reconstruction to determine if the detector has moved significantly between runs. The results obtained are monitored [2] and it a significant displacement is observed, the detector alignment is corrected before to the bulk data processing (reconstruction of the full dataset). For example, Figure 4.33 displays the T_x corrections for each detector sub-system during April - May 2011 period with respect to the baseline constants. Changes to the environmental conditions of the detector (temperature, magnetic field strength, etc.) occurring during breaks in data-taking often lead to significant movements of the detector. In addition to these relative movements of the detector, slow gradual drifts of the sub-detectors were observed. In the period show in the Figure 4.33 the significant movements were produced due:

[2] https://atlas-alignment.cern.ch/

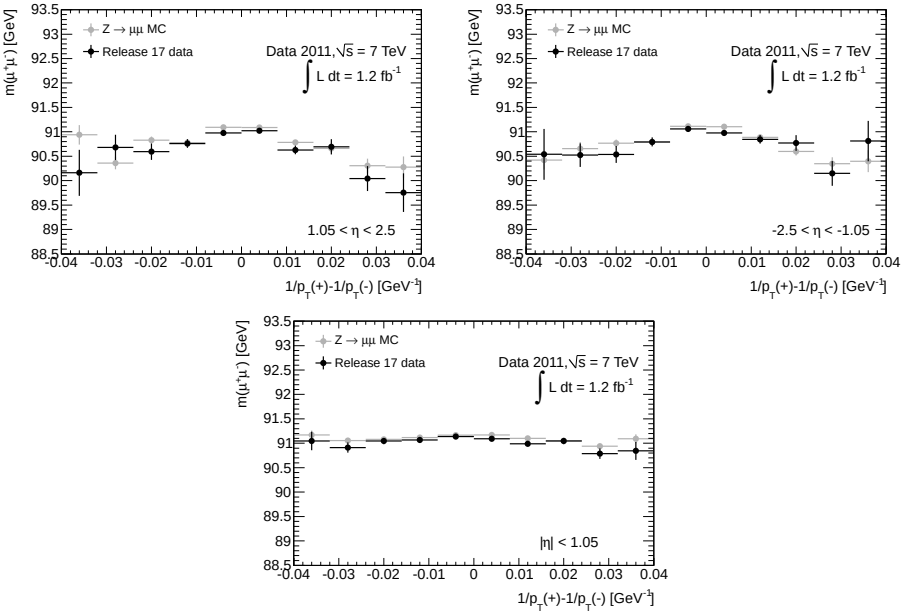

Figure 4.28: Fitted mean Z mass as a function of curvature difference in the barrel (bottom), end-cap A (top left) and end-cap C (top right), for collision data after charge-antisymmetric alignment corrections and perfectly aligned Monte Carlo.

- 179939 - 180149: cooling system failure.
- 180481 - 180614: power cut.
- 180710 - 182284: LHC technical stop where the cooling and power was turned off.
- 182519 - 182726: a fire alarm went off and as a result the cooling system was required to be shut down.
- 182787 - 183003: the toroidal magnetic field was dumped

In the plot show in the Figure 4.34 the T_x corrections during 2012 are shown for each sub-system. In this case, by convention, the alignment corrections are defined relative to the Pixel detector, hence corrections for the latter are not displayed.

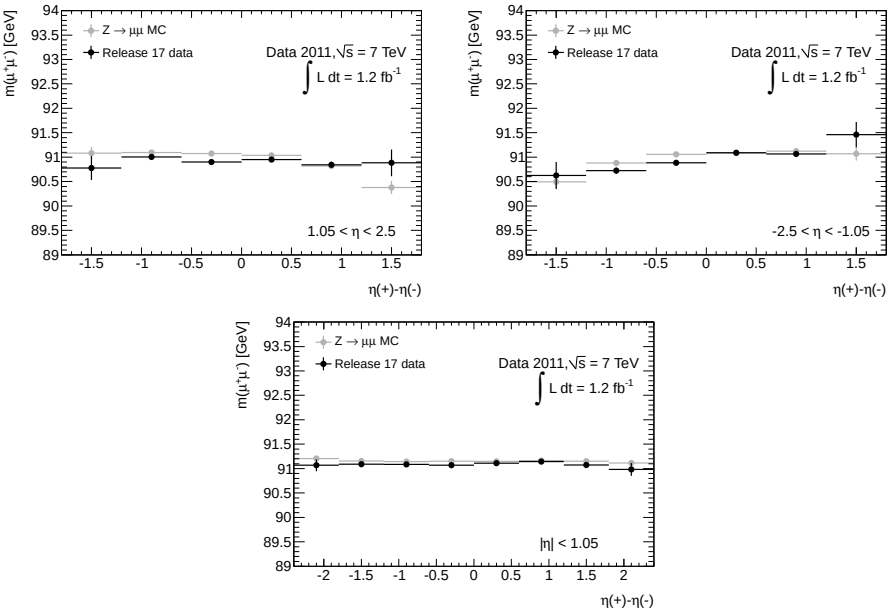

Figure 4.29: Fitted mean Z mass as a function of difference in *eta* in the barrel (bottom), end-cap A (top left) and end-cap C (top right), for collision data after charge-antisymmetric alignment corrections and perfectly aligned Monte Carlo.

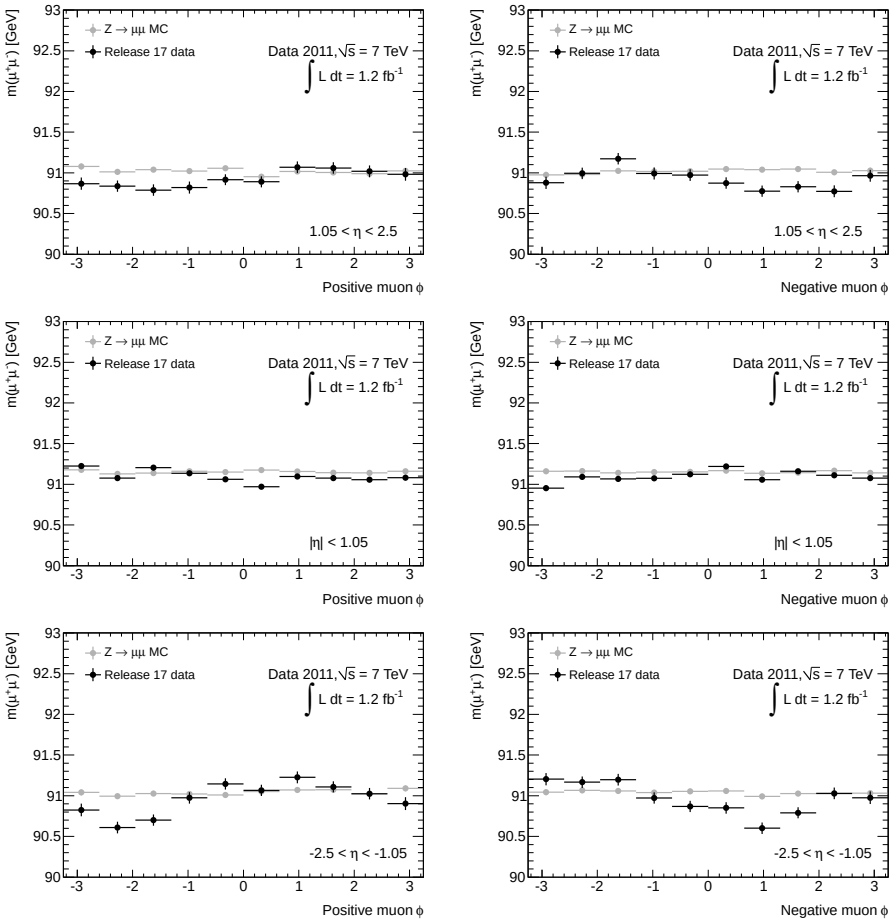

Figure 4.30: Fitted mean Z mass as a function of phi of the indicated muon in the barrel (middle), end-cap A (top) and end-cap C (bottom) for collision data after charge-antisymmetric alignment corrections and perfectly aligned Monte Carlo.

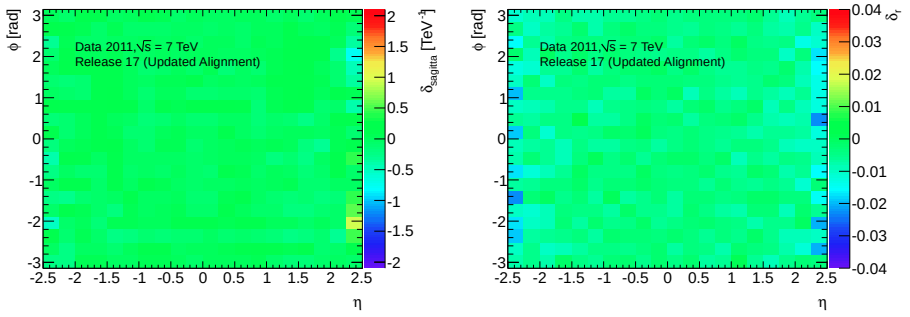

Figure 4.31: Derived momentum bias parameters for the charge-antisymmetric parametrisation (left) and the charge-symmetric parametrisation (right) in *Release 17* data, using the iterative $Z \to \mu\mu$ method.

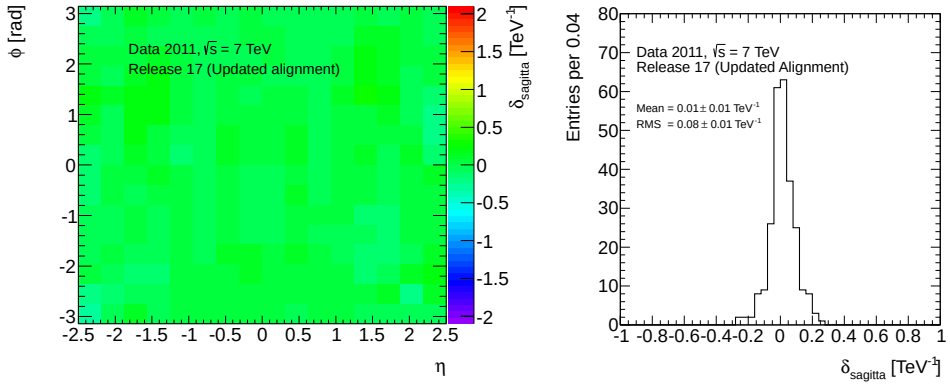

Figure 4.32: Momentum biases (δ_{sagitta}) as measured using E/p in *Release 17* ATLAS data using electrons from W and Z boson decays and represented in a 2D map(left) and 1D projection(right).

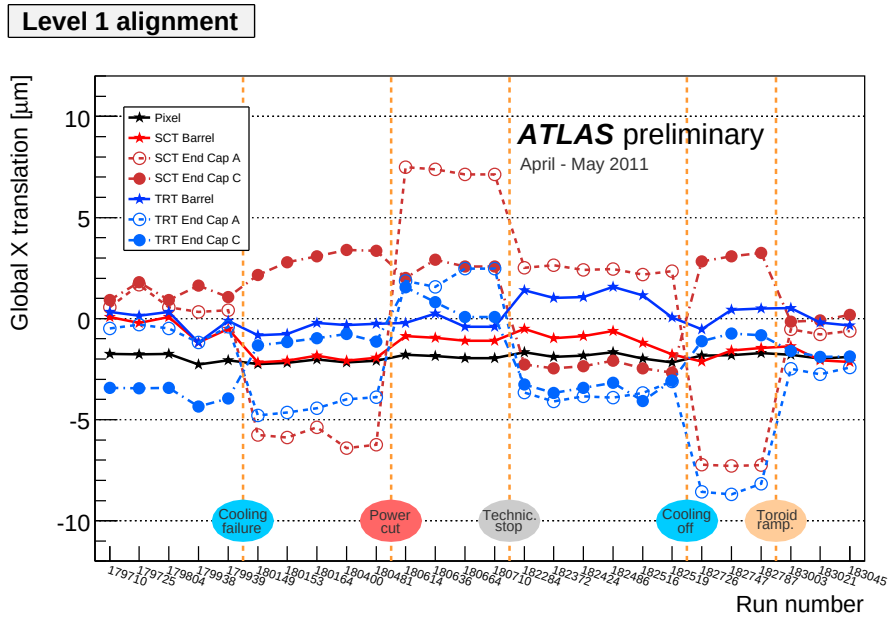

Figure 4.33: The corrections to the global X position (T_x) of all ID sub-detectors during April - May 2011 period. The big changes in the constants are related to changes in the detector conditions.

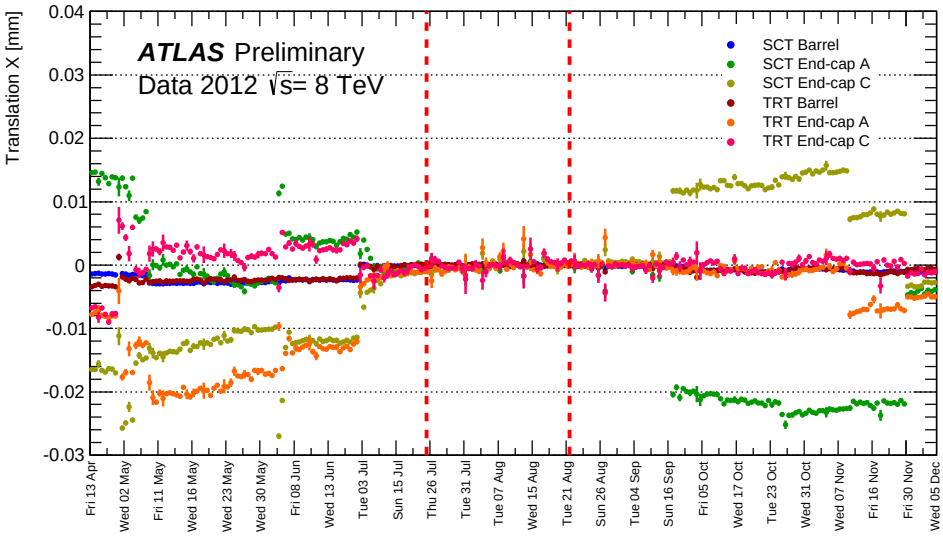

Figure 4.34: The corrections to the global X position (T_x) of all ID sub-detectors with respect to the Pixel detector during 2012. The vertical dashed lines indicate the data-taking periods in which the baseline constants were determined. Errors show are statistical uncertainties on determined alignment parameter and crucially depend on the statistics of data recorded in a given run.

Chapter 5

AFBT measurement

This chapter presents the determination of g_{R} at the ATLAS experiment at the LHC. The analysis is based on the measurement of an asymmetry in the angular distribution of the charged lepton from the W decay in single top quark events from the t-channel production (see Figure 1.3). As seen in section 1.3 the asymmetry AFBT is measured in order to obtain the coupling constant g_{R}.

5.1 Data and simulated samples

The data used in the analysis are from proton-proton (pp) collisions delivered by the LHC in 2011 at $\sqrt{s} = 7$ TeV and collected by the ATLAS detector requiring a single lepton trigger (electron or muon). With the increasing instantaneous luminosity of the LHC, the average number of simultaneous pp interactions per beam crossing (pile-up) at the beginning of a given fill of the LHC increased from about 6 to 17 during the 2011 data-taking period. Due to these changing pile-up conditions, different triggers were used to select events for different data periods. These pile-up conditions are included in the MC simulation. The amount of data used by this analysis corresponds to an integrated luminosity of 4656 ± 84 pb^{-1} [51]. Table 5.1 gives an overview of the different data periods of 2011 along with their respective integrated luminosities and the triggers applied.

MC simulated event samples were produced using different event generators interfaced to various parton shower (PS) generators. The single top quark t-channel process was produced with the AcerMC multi-leg LO generator [52] using MRST LO** [53] as parton distribution function (PDF). The computation of this channel in AcerMC incorporates both the $q + b \to q' + t$ and $q + g \to q' + t + \overline{b}$ subprocesses (see Figure 1.3) and features an automated procedure to remove the overlap in phase space between them [54]. The other two single top quark processes (s-channel and Wt-channel) were produced using the Powheg NLO generator [55] coupled with the CT10 [56] set of PDFs. The factorisation and renormalisation scales were set to $\mu_{\mathrm{F}} = \mu_{\mathrm{R}} = \sqrt{\hat{s}}$, the center-of-mass energy of the partonic system. Samples for the different $t\overline{t}$ processes were generated using Powheg with the CT10 set of parton distribution functions (PDFs).

Run Period	Run numbers	Integrated luminosity (pb^{-1})	Electron trigger	Muon trigger
B–D	177986 – 180481	176 ± 3	e_20_medium	mu_18
E–H	180614 – 184169	938 ± 17	e_20_medium	mu_18
I	185353 – 186493	333 ± 6	e_20_medium	mu_18
J	186516 – 186755	224 ± 4	e_20_medium	mu_18_medium
K	186873 – 187815	583 ± 11	e_22_medium	mu_18_medium
L–M	188902 – 191933	2402 ± 43	e_22vh_medium1	mu_18_medium

Table 5.1: Recorded luminosity per run period considering a relative systematic uncertainty of 1.8%. In addition, the trigger requirements for each period are shown. The name of the lepton trigger items are encoded in the following way: "e" and "mu" denote electron and muon trigger items. The next value denotes the threshold of the transverse momentum given in GeV and the last is the lepton identification quality.

For these processes involving top quarks, additional samples with varied parameters for initial and final state radiation (ISR/FSR) were generated using AcerMC to study their effect on the analysis. For the evaluation of the systematic uncertainties due to the $t\bar{t}$ generator modelling, parton shower (PS) and hadronisation uncertainty, samples were produced with the Alpgen LO generator [57]. To evaluate t-channel generator modelling and to cross check the unfolding procedure, samples using the Protos [58] LO generator were produced. All top quark samples produced with Pythia, Powheg and Protos were interfaced with Pythia [59] for showering and hadronisation using the AUET2 tune [60] except for $t\bar{t}$ that used the Perugia2011 tune [61]. The samples produced with Alpgen were interfaced to Herwig [62] together with the Jimmy underlying event model [63]. All these samples were produced assuming a top quark mass of 172.5 GeV. Vector boson (W/Z) production in association with jets was simulated using the Alpgen generator interfaced to Herwig+Jimmy, where a jet is defined as a cone of hadrons and other particles produced by the hadronisation of a quark (with the exception of the top quark) or gluon. Since the fraction of W+jets events containing heavy flavour jets is not well established, the contributions of W+light and W+heavy flavour jets ($Wb\bar{b}, Wc\bar{c}, Wc$) were simulated separately. To remove overlaps between the n and $n+1$ parton samples the MLM matching scheme [57] was used. The double counting between the inclusive $W+n$ parton samples and samples with associated heavy quark pair production was removed using an overlap-removal algorithm based on parton-jet ΔR matching [64]. The di-boson processes WW, WZ and ZZ were generated using Herwig. The multijet background was generated using an inclusive Pythia sample with a filter for di-jet events. After the event generation step, all samples were passed through the full simulation of the ATLAS detector [65] based on GEANT4 [66] and were then reconstructed using the same procedure as for collision data.

The simulated samples were generated within the MC11c production [70], which includes much of the knowledge gained from the ATLAS data collected in 2011 about alignment, material distribution or underlying event and minimum bias tunings. Tables 5.2-5.4 list all the simulated samples which are used within this analysis. These tables show all the relevant information for each sample: identification sample numbers, event generator and used PS scheme, their corresponding theoretical cross-section and

Process	Channel	Sample ID	Generator	σ [pb]	k-factors	N_{evt}^{MC}
t-channel	inclusive lepton decay	110101	AcerMC+Pythia	19.24	1.087	24000000
s-channel	inclusive lepton decay	110119	Powheg+Pythia	1.35	1.112	900000
Wt-channel	all inclusive	110140	Powheg+Pythia	14.34	1.097	500000

Table 5.2: Simulated samples for the different single top quark channels used in this analysis. NNLO theoretical cross-sections are used for these samples [7, 8, 9].

Process	Sample ID	Generator	σ [pb]	k-factors	N_{evt}^{MC}
Multijet	105802	Pythia	-	-	9999419
top quark pair (no fully had)	117050	Powheg+Pythia	80.07	1.2	9994443
top quark pair (fully had)	117049		67.36	1.23	3998998
WW	105985	Herwig	11.50	1.48	2489242
ZZ	105986		0.97	1.30	249999
WZ	105987		3.46	1.60	999896
Z (electron ch) + Np0	107650	Alpgen+Jimmy	668.32	1.25	6618284
Z (electron ch) + Np1	107651		134.36	1.25	1334897
Z (electron ch) + Np2	107652		40.54	1.25	2004195
Z (electron ch) + Np3	107653		11.16	1.25	549949
Z (electron ch) + Np4	107654		2.88	1.25	149948
Z (electron ch) + Np5	107655		0.83	1.25	50000
Z (muon ch) + Np0	107660	Alpgen+Jimmy	668.68	1.25	6615230
Z (muon ch) + Np1	107661		134.14	1.25	1334296
Z (muon ch) + Np2	107662		40.33	1.25	1999727
Z (muon ch) + Np3	107663		11.19	1.25	549896
Z (muon ch) + Np4	107664		2.75	1.25	150000
Z (muon ch) + Np5	107665		0.77	1.25	50000
Z (tau ch) + Np1	107670	Alpgen+Jimmy	668.40	1.25	10613179
Z (tau ch) + Np1	107671		134.81	1.25	3334137
Z (tau ch) + Np2	107672		40.36	1.25	1004847
Z (tau ch) + Np3	107673		11.25	1.25	509847
Z (tau ch) + Np4	107674		2.79	1.25	144999
Z (tau ch) + Np5	107675		0.77	1.25	45000

Table 5.3: Some of the simulated samples used in this analysis. The $t\bar{t}$ cross-section is normalised to the NNLO predicted value using HATHOR [67]. For Z+jets background the inclusive cross-sections are calculated to NNLO with FEWZ [68]. The diboson cross-sections are normalised to NLO theoretical calculations [69]. For multijet background its normalisation is determined in-situ using a control region (see Section 5.3.1). The cross-sections and k-factors (ratio of the NLO to LO cross-section for a given process) quoted are the ones used to normalise these MC samples to an integrated luminosity of $4.66\,\text{fb}^{-1}$.

k-factors (ratio of the NLO to LO cross-section for a given process) and the number of events in each simulated sample (N_{evt}^{MC}). Total cross-sections (cross-section times k-factor) are used to normalise each simulated sample to the integrated luminosity of

Process	Sample ID	Generator	σ [pb]	k-factors	N_{evt}^{MC}
$Wb\bar{b}$ + Np0	107280	Alpgen+Jimmy	47.35	1.20	474997
$Wb\bar{b}$ + Np1	107281		35.76	1.20	205000
$Wb\bar{b}$ + Np2	107282		17.33	1.20	174499
$Wb\bar{b}$ + Np3	107283		7.61	1.20	69999
$Wc\bar{c}$ + Np0	117284	Alpgen	127.53	1.20	1274846
$Wc\bar{c}$ + Np1	117285		104.68	1.20	1049847
$Wc\bar{c}$ + Np2	117286		52.08	1.20	524947
$Wc\bar{c}$ + Np3	117287		16.96	1.20	170000
Wc + Np0	117293	Alpgen	644.40	1.52	6427837
Wc + Np1	117294		205.00	1.52	2069646
Wc + Np2	117295		50.80	1.52	519974
Wc + Np3	117296		11.40	1.52	115000
Wc + Np4	117297		2.80	1.52	30000
W (electron ch) + Np0	107680	Alpgen+Jimmy	6930.50	1.20	6952874
W (electron ch) + Np1	107681		1305.30	1.20	4998487
W (electron ch) + Np2	107682		378.13	1.20	3768632
W (electron ch) + Np3	107683		101.86	1.20	1008947
W (electron ch) + Np4	107684		25.68	1.20	250000
W (electron ch) + Np5	107685		6.99	1.20	69999
W (muon ch) + Np0	107690	Alpgen+Jimmy	6932.40	1.20	6962239
W (muon ch) + Np1	107691		1305.90	1.20	4988236
W (muon ch) + Np2	107692		378.07	1.20	3768737
W (muon ch) + Np3	107693		101.85	1.20	1008446
W (muon ch) + Np4	107694		25.72	1.20	254950
W (muon ch) + Np5	107695		7.00	1.20	70000
W (tau ch) + Np0	117700	Alpgen+Jimmy	6931.80	1.20	3418296
W (tau ch) + Np1	117701		1304.90	1.20	2499194
W (tau ch) + Np2	117702		377.93	1.20	3750928
W (tau ch) + Np3	117703		101.96	1.20	1009946
W (tau ch) + Np4	117704		25.71	1.20	249998
W (tau ch) + Np5	117705		7.00	1.20	65000

Table 5.4: Simulated samples for W+jets used in this analysis. Their normalisation is determined in-situ using a control region (see Section 5.3.2). The cross-sections and k-factors (ratio of the NLO to LO cross-section for a given process) quoted are the ones used to normalise these simulated samples to an integrated luminosity of $4.66\,\text{fb}^{-1}$.

$4.66\,\text{fb}^{-1}$. Table 5.2 summarises the relevant information for the single top quark t-channel (i.e. the signal) and the other single top quark processes.

For a better understanding of the plots and in most tables the background and signal processes are grouped together as follows:

- ***t*-channel**: single top quark t-channel production process (i.e. the signal).
- ***s*-channel**, ***Wt*-channel** and **top quark pair**: background processes that include

the production of top quarks, i.e. the s and Wt single top quark channels and top quark pair ($t\bar{t}$) production.

- ***W*+HF jets**: production of a real W boson in association with heavy flavour quark jets. The simulated samples grouped together are $W{+}b\bar{b}$, $W{+}c\bar{c}$ and $W{+}c$.
- ***W*+light jets**: production of a real W boson in association with light quark jets.
- ***Z*+jets** and **diboson**: production of a Z boson and the diboson production WW, ZZ and WZ.
- **Multijet**: events with a misidentified lepton originating from multijet production.

5.2 Object definition and event selection

The object definition of all physics objects (electron, muon, jet, missing energy) follows the recommendations given by the ATLAS top physics working group [71]. The event selection follows the basic selection of the ATLAS single top physics group for the leptonic t-channel signal where the lepton can be either an electron or muon originating from the W boson decay. This analysis also takes into account events involving $W^+ \to \tau^+\nu_\tau$ decays if the τ's subsequently decay into either $e^+\nu_e\overline{\nu}_\tau$ or $\mu^+\nu_\mu\overline{\nu}_\tau$ and their charge conjugates. This selection applies general event quality/cleaning cuts and cuts derived from the t-channel topology on the level of the basic physics objects. It is described in detail in [72] although for convenience is summarised below. In addition to the basic single top quark selection, which is denoted as *pre-selection* in this analysis, a few more additional cuts on combined quantities are applied in order to further reject background events.

5.2.1 Event pre-selection

All events for the data stream have to pass the quality criteria defined in the Good Run List[1] (GRL) defined by the ATLAS top physics working group. In addition, each event needs to pass a single lepton trigger (see Table 5.1), to have a primary vertex with at least five tracks, have a good jet with $p_{\mathrm{T}} > 20$ GeV and there must not have been any noise burst in the liquid argon calorimeter.

Selected events are required to contain exactly one lepton (electron or muon) passing the tight selection [73] and these requirements: $p_{\mathrm{T}} > 25$ GeV and $0 < |\eta| < 1.37$ and $1.52 < |\eta| < 2.47$ for electrons and $|\eta| < 2.5$ for muons. Exactly two good jets with $p_{\mathrm{T}} > 30$ GeV, $|\eta| < 4.5$ and a jet vertex fraction (probability that a jet originated from a particular vertex) greater than 0.75 are required. In the region where $2.75 < |\eta| < 3.5$, the p_{T} cut for jets is increased to up to 35 GeV. Exactly one jet is required to be b-tagged by the JetFitterCOMBNNc algorithm [74] [75] at a working point of 55% b-tagging efficiency and with $|\eta| < 2.5$. In order to reject multijet events, $E_{\mathrm{T}}^{\mathrm{miss}} > 30$ GeV is required and the transverse W mass, defined as:

$$m_{\mathrm{T}}(W) = \sqrt{2p_{\mathrm{T}}(\mathrm{lepton})E_{\mathrm{T}}^{\mathrm{miss}}\left(1 - \cos\left(\phi(\mathrm{lepton}) - \phi(E_{\mathrm{T}}^{\mathrm{miss}})\right)\right)} \tag{5.1}$$

[1] The GRL is defined in the following XML file: *data11_7TeV.periodAllYear_DetStatus-v36-pro10_CoolRunQuery-00-04-08_Top_allchannels.xml*

to be greater than 30 GeV. Finally, an extra isolation cut is required in order to remove discrepancies in the modelling of transverse momentum of muons as shown in [76]. Low p_{T} muons show a significant deficit in the model relative to the data in the region where the multijet contribution is significant. In order to reduce this mismodeling, the lepton p_{T} is required to satisfy:

$$p_{\mathrm{T}}(lepton) > 40 \mp (40/\pi - 1)(\Delta\phi(\text{leading-jet}, \text{lepton}) \pm \pi) \tag{5.2}$$

This isolation cut is applied to both lepton flavours in order to maintain symmetry between the treatment of electrons and muons.

Figures 5.1-5.2 show the comparison between data and expectation for $E_{\mathrm{T}}^{\mathrm{miss}}$, $m_{\mathrm{T}}(W)$, η of the light jet (i.e. spectator quark), $\Delta\eta$(light-jet, b-jet), mass of the reconstructed top quark and the sum of the transverse energy of all final objects involved, denoted by H_{T} and defined as

$$H_{\mathrm{T}} = p_{\mathrm{T}}(\text{lepton}) + p_{\mathrm{T}}(\text{light-jet}) + p_{\mathrm{T}}(b\text{-jet}) + E_{\mathrm{T}}^{\mathrm{miss}}, \tag{5.3}$$

in the t-channel *pre-selection* region for both channels in the tagged sample. In addition, Figure 5.3 shows the angular distributions in the transversal direction for the electron and muon channels in the tagged sample. More comparisons between data and expectation on kinematic distributions of final state objects and angular distributions for both channels can be found in the Appendix B (see Figures B.1-B.4). A good agreement between data and prediction is observed. Uncertainties on the prediction are the statistical plus the multijet normalisation. The multijet and W+jets background contribution have been estimated using data driven methods in both channels. For details, see Section 5.3. At this level, the sample is dominated by W+jets and $t\bar{t}$ backgrounds.

5.2.2 Event selection

On top of the basic single top quark t-channel event *pre-selection*, additional selection criteria is used in this analysis to further separate the signal from background (these selection was used already in previous analysis [72]):

- The $|\eta|$ of the light jet (i.e. spectator quark) has to be larger than 2.
- H_{T} must be larger than 210 GeV.
- The mass of the reconstructed top quark (m_t) (see Appendix A for a detailed description on how the top quark mass has been reconstructed) needs to be within the mass range 150 GeV to 190 GeV.
- The distance in η between the light jet and the b-jet, $\Delta\eta$(light-jet, b-jet), must be larger than 1.

Figures 5.4-5.5 show the comparison between data and expectation for $E_{\mathrm{T}}^{\mathrm{miss}}$, $m_{\mathrm{T}}(W)$, $|\eta|$ of the light jet (i.e. spectator quark), $\Delta\eta$(light-jet, b-jet), mass of the reconstructed top quark and H_{T} at selection level for both channels in the tagged sample. Uncertainties on the prediction are the statistical plus the multijet normalisation. As commented above and explained in Section 5.3, the multijet and W+jets background contribution have

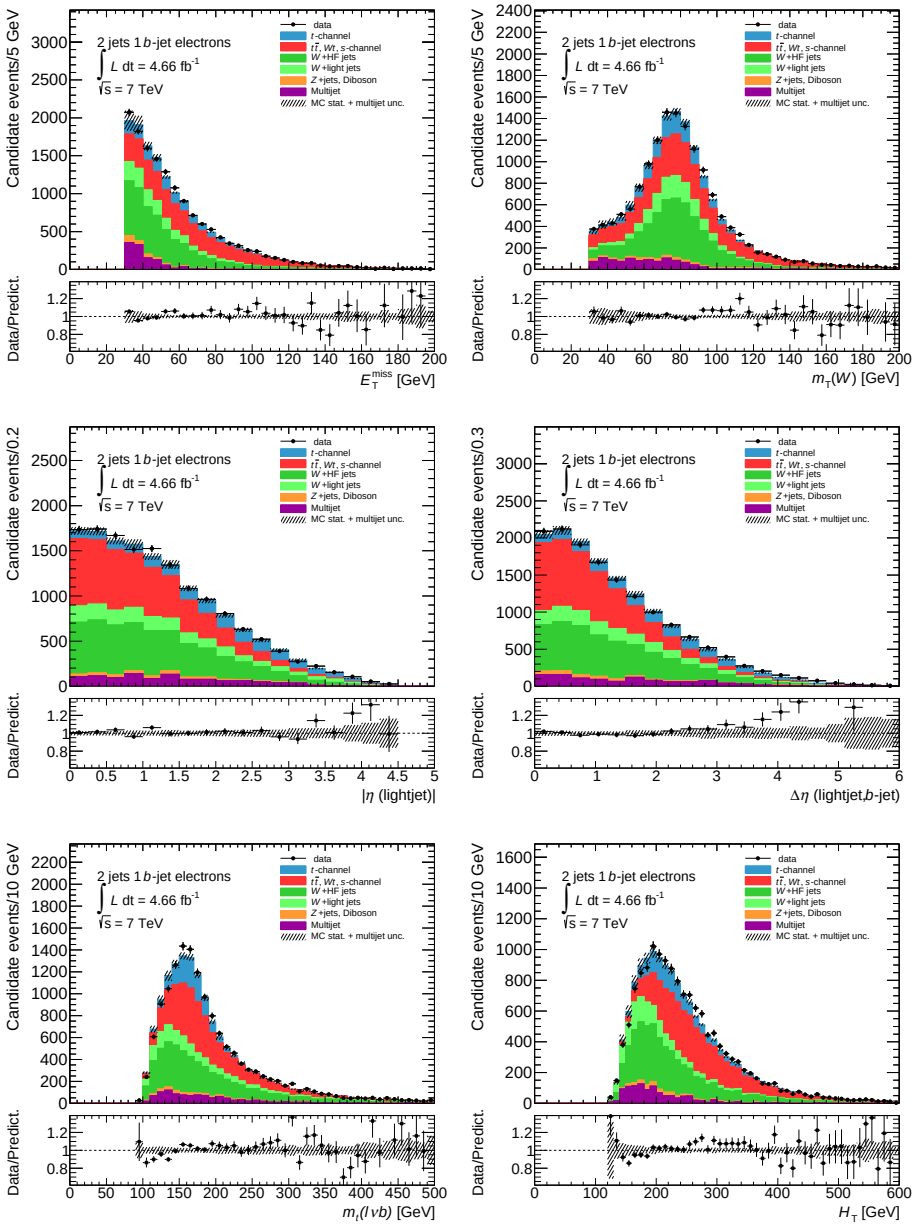

Figure 5.1: Comparison between data and expectation from MC at Preselection level for the electron channel in the Tagged sample. From top left to bottom right: $E_{\mathrm{T}}^{\mathrm{miss}}$, $m_{\mathrm{T}}(W)$, η of the light jet (i.e. spectator quark), $\Delta\eta$(light-jet, b-jet), mass of the reconstructed top quark and H_{T}.

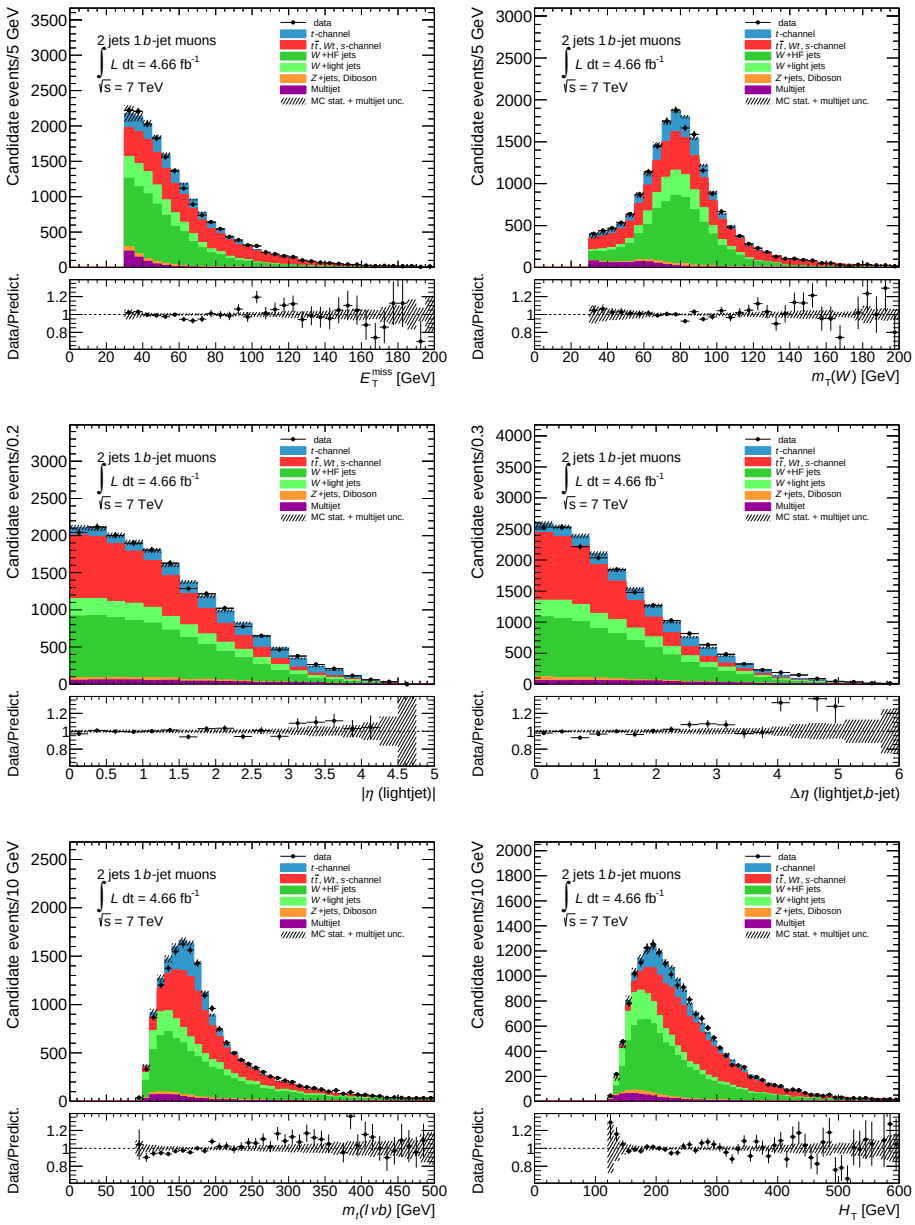

Figure 5.2: Comparison between data and expectation from MC at *pre-selection* level for the muon channel in the tagged sample. From top left to bottom right: $E_{\mathrm{T}}^{\mathrm{miss}}$, $m_{\mathrm{T}}(W)$, η of the light jet (i.e. spectator quark), $\Delta\eta$(light-jet, b-jet), mass of the reconstructed top quark and H_{T}.

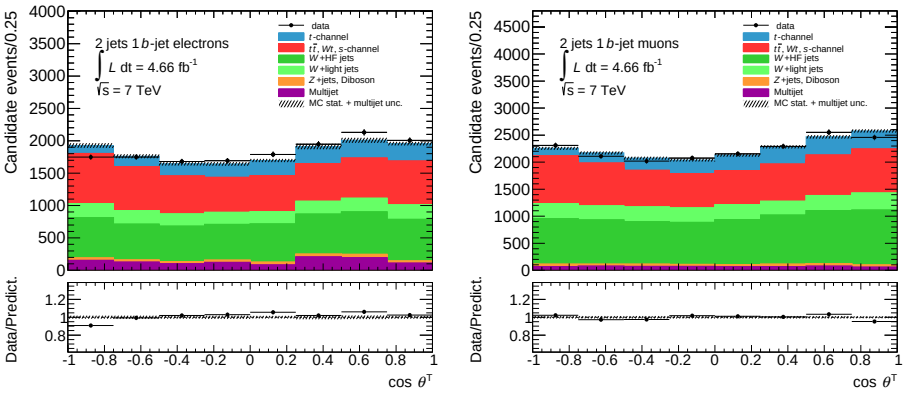

Figure 5.3: Angular distributions in the transversal direction at *pre-selection* level for electron (left) and muon (right) channels in the tagged sample.

been estimated using data driven methods in both channels. At this level, the statistics of multijet and W+light jets is low, for both templates are used in order to model the shape. For multijet a template with events from di-bosons, Z+jets and multijet itself is built and then normalised to the yields obtained for multijet in the data driven techniques (di-bosons and Z+jets are not changed). For W+light jets, the shape from W+heavy flavour is used.

5.3 Background estimation and event yields

The main backgrounds to the single top quark t-channel final state come from W boson production in association with jets, multijet or QCD events and top quark pair production. Smaller backgrounds originate from Z+jets, single top quark Wt-channel and s-channel and diboson production. These smaller backgrounds and the top quark pair background are modelled using MC simulation and normalised to the corresponding theory predictions. For multijet and W+jets backgrounds, the normalisation is obtained from data driven methods while the shape is taken from MC samples.

5.3.1 Estimation of the multijet background

Multijet events can pass the event selection if one of the jets is mis-identified as an electron or muon. Even though the probability for this to happens is very low, due to the extremely large production cross-section of multijet events, which is several orders of magnitude higher than the t-channel signal cross-section, it is still a significant background. Because this probability depends on the detector configuration and geometry, methods based on data are the most appropriate estimate for the multijet background.

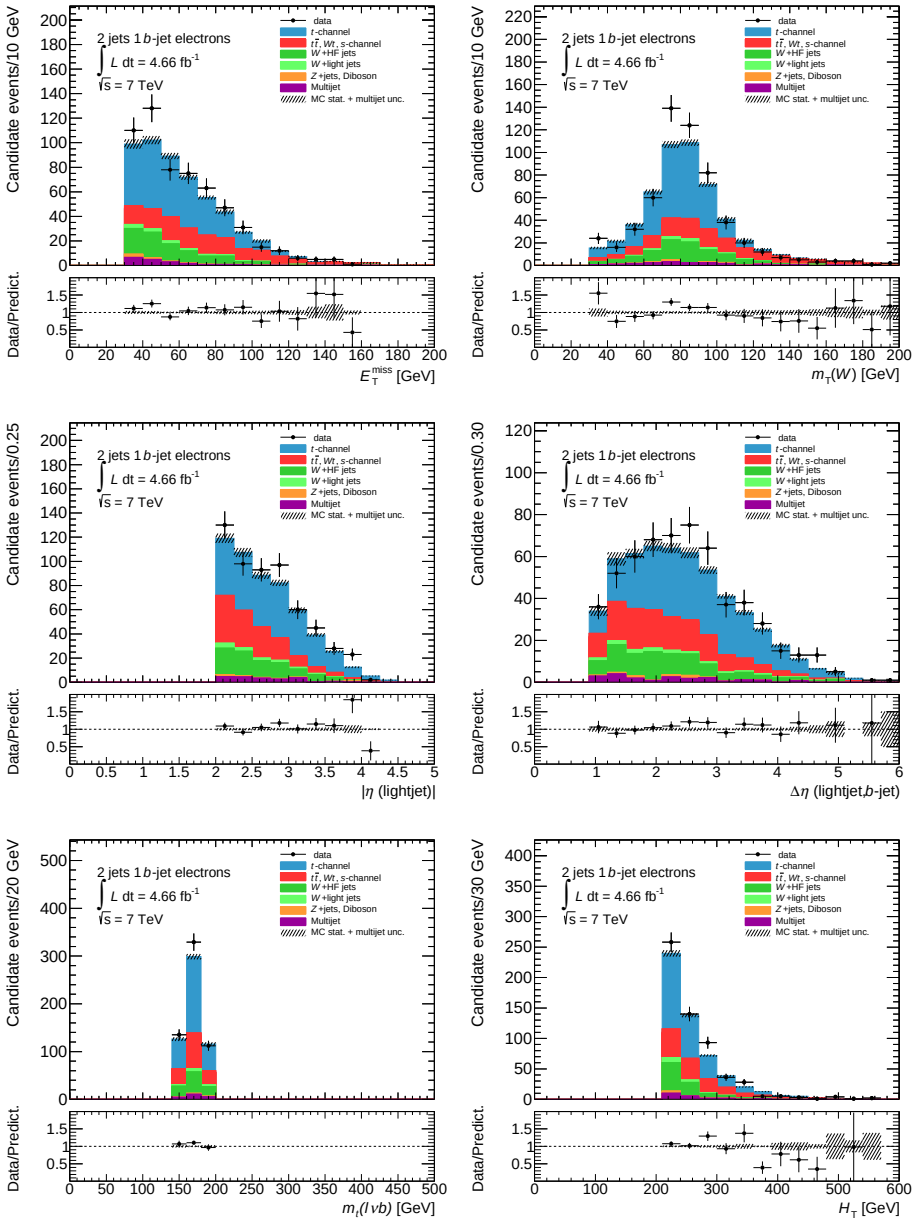

Figure 5.4: Comparison between data and expectation from MC at selection level for the electron channel in the tagged sample. From top left to bottom right: $E_{\mathrm{T}}^{\mathrm{miss}}$, $m_{\mathrm{T}}(W)$, η of the light jet (i.e. spectator quark), $\Delta\eta$(light-jet, b-jet), mass of the reconstructed top quark and H_{T}.

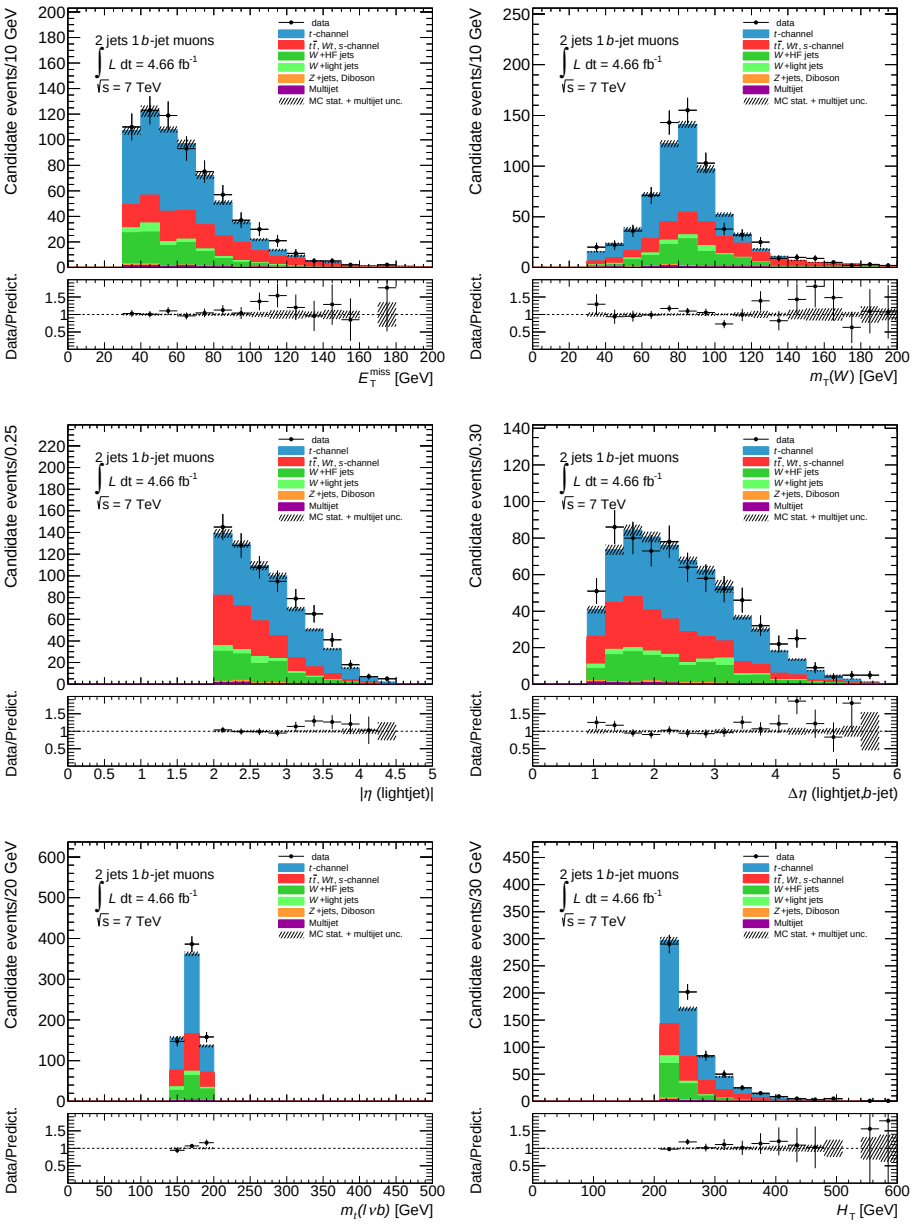

Figure 5.5: Comparison between data and expectation from MC at selection level for the muon channel in the tagged sample. From top left to bottom right: $E_{\mathrm{T}}^{\mathrm{miss}}$, $m_{\mathrm{T}}(W)$, η of the light jet (i.e. spectator quark), $\Delta\eta$(light-jet, b-jet), mass of the reconstructed top quark and H_{T}.

5.3.1.1 The jet-electron model for the electron channel

For the electron channel a di-jet sample simulated with PYTHIA is used to model the shape of the multijet background, together with templates derived from MC simulation for all other processes (top quark, W/Z+jets, diboson). The multijet template consists of events where the electron requirement in the selection is replaced by a jet requirement. This method is called jet-electron model and it is described in detail in [77]. The basic concept is to accept a reconstructed jet as a lepton if it has a lepton like signature. The selection cuts for the fake leptons, i.e. the jets, are $E_{\mathrm{T}}^{\mathrm{miss}} > 25$ GeV, $|\eta| < 2.47$, an electromagnetic fraction between 0.8 and 0.95 and at least three reconstructed tracks.

A fit is performed after applying the single top quark t-channel event *pre-selection* cuts (see Section 5.2.1), including the $m_{\mathrm{T}}(W) > 30$ GeV cut, but leaving out the $E_{\mathrm{T}}^{\mathrm{miss}}$ cut. From this fit, the multijet fraction in the selected region $E_{\mathrm{T}}^{\mathrm{miss}} > 30$ GeV is determined. The result of the fitting method is used as the primary background estimate for the analysis for the electron channel as explained in [71] and [72]. Table 5.5 provides the estimate of multijet background at *pre-selection* level for the electron channel which is fitted in two separate electron η regions: forward ($1.52 < |\eta| < 2.47$) and central ($|\eta| < 1.37$). The JetFitterCOMBNNc algorithm at a working point of 55% b-tagging efficiency is used to computed the tagged normalisation. The normalisation at selection is estimated from these numbers and considering the selection cut efficiency.

	Electron	
η region	Multijet events	Multijet fraction
Central	664 ± 332	6.0%
Forward	426 ± 213	11.5%

Table 5.5: Estimated normalised number of events given by the jet-electron model for the multijet background in the selected region $E_{\mathrm{T}}^{\mathrm{miss}} > 30$ GeV at *pre-selection* level in the tagged sample (using the JetFitterCOMBNNc@55%) for the electron channel. A systematic uncertainty of 50% is assumed on the multijet rate (see Section 5.3.1.3).

5.3.1.2 The matrix method for the muon channel

For the muon channel the matrix method using the muon impact parameter (d_0) significance is used (for a detailed description see [71]). In this method the signal efficiency is determined directly from the MC sample following the t-channel analysis selection and it is not parametrised to any observables since the value is nearly a constant in the phase space. Additionally the fake efficiency is extrapolated from the ratio between loose and tight muons (the loose-to-tight efficiency) with high d_0 significance using the data sample and assuming that the fake muons are dominated by the heavy flavour decay in the muon+jets channel. The measurement of the fake efficiency is done within a multijet enriched region by using the following cuts: $E_{\mathrm{T}}^{\mathrm{miss}} < 20$ GeV and $E_{\mathrm{T}}^{\mathrm{miss}} + m_{\mathrm{T}}(W) < 60$ GeV. Dependency on muon η is taken into account by applying the fake efficiency measurement individually in a subset of the data sample divided by muon η. Table 5.6 provides the estimate of multijet background for the muon channel.

Muon	
PreSelection	Selection
550 ± 275	6 ± 3

Table 5.6: Estimated normalised values given by the matrix method for the multijet background in the tagged sample (using the JetFitterCOMBNNc@55%) for the muon channel. A systematic uncertainty of 50% is assumed (see Section 5.3.1.3).

5.3.1.3 Systematic uncertainties of the multijet background

In the electron channel, for the jet-electron method the systematic uncertainty for the normalisation is evaluated by dividing the jet-electron data sample into a high pile-up sample and a low pile-up sample based on the number of primary vertices. The method is applied to both subsamples separately to gauge the effect of pile-up on the procedure. A systematic uncertainty on the multijet rate of 50% is assigned from studies already done in the context of the single top quark cross-section measurement and detailed in [78]. In the muon channel, for the matrix method the systematic uncertainty for the normalisation was estimated to be 50%. This uncertainty was computed by varying the real/fake efficiencies within their uncertainties covering the data/MC disagreement.

5.3.2 Estimation of the W+jets background

Production of W together with jets (either light or heavy flavour jets) has a large production cross-section at LHC (see Table 5.4). W+jets events with final states including leptons, jets and $E_{\mathrm{T}}^{\mathrm{miss}}$are important since they are a dominant background in single top quark channels.

For this background, the shape of the distributions is obtained from simulated samples using ALPGEN. The predictions are multiplied by k-factors to correct the cross-sections to the NLO predictions provided by theory. The k-factor for the W+$b\bar{b}$, W+$c\bar{c}$ and W+light jet samples is 1.20, and for the Wc+jets process is scaled by a factor of 1.52 obtained from MCFM [79]. The cross-sections and k-factors for all simulated samples are given in Table 5.4.

In addition, data driven techniques are used to estimate the different flavour composition and the overall normalisation, as done in $t\bar{t}$ analyses [80]. This is done in a control region dominated by W+jets events, with less than 5% contamination of signal events. In order to get this signal free sample, events are required to pass the *pre-selection* cuts (see Section 5.2) but to fail the top quark mass cut, i.e. the mass of the reconstructed top quark is required to be outside the expected value (that is $m_t < 150.0$ GeV or $m_t > 190.0$ GeV). Then the normalisation and flavour fractions are obtained as follows:

- Overall normalisation is obtained by computing the ratio of data with all the background subtracted but W+jets over MC W+jets.
- Flavour fractions (W+$b\bar{b}$, W+$c\bar{c}$, W+c and W+light jets) are derived using total event yields in 1 and 2 jet bin. A numerical fit, using MINUIT, is performed to obtain them.

A detailed explanation on the method used to estimate this background can be found in Appendix C. Both the overall normalisation and flavour fraction scale factors (denoted by K_i being i the flavour) are determined simultaneously and for different jet multiplicities. The total W+jets scale factor for each flavour component is the product of the overall normalisation and the corresponding flavour fraction scale factors. Values obtained for events with 2 jets are shown in Tables 5.7-5.8 with their respective statistical and systematic uncertainties. The difference between the flavour fractions between electrons and muons is due to a slightly different selection and backgrounds. The multijet contribution is very different and its systematic is the biggest. These fractions are compensated because the method assumes that the sum of the four fractions for each channel is equal to 1.

Electron	Muon
0.990 ± 0.004 (stat.) ± 0.170 (syst.)	1.029 ± 0.003 (stat.) ± 0.155 (syst.)

Table 5.7: Overall W+jets normalisation factors in the 2-jet exclusive bin for the electron and muon channel individually with the statistical and systematic uncertainties.

	Electron	Muon
$K_{bb} = K_{cc}$	1.173 ± 0.115 (stat.) ± 0.591 (syst.)	1.463 ± 0.089 (stat.) ± 0.574 (syst.)
K_c	1.162 ± 0.071 (stat.) ± 0.235 (syst.)	0.880 ± 0.068 (stat.) ± 0.185 (syst.)
K_{light}	0.938 ± 0.002 (stat.) ± 0.037 (syst.)	0.956 ± 0.002 (stat.) ± 0.045 (syst.)

Table 5.8: W+jets flavour fraction scale factors (so-called K factors) in the 2-jet exclusive bin for the electron and muon channel individually with the statistical and systematic uncertainties.

The dissimilarity observed between flavour fractions for electrons and muons is understood as coming from the different selection requirements and the different multijet background contribution for each channel. The latter is quite different between channels, and it is one of the largest systematic to this method. Despite discrepancies in the flavour fractions, the scale factors are still compatible.

To evaluate the uncertainty of the method, samples which include each of the systematic sources (described in Section 5.5) are used to recompute the overall normalization and flavour fractions (e.g. for the uncertainty on jet energy scale, samples with jet energy up and down are used). In this way a different set of values for the overall normalization and flavour fraction scale factors are obtained for each systematics.

5.3.3 Event Yields

Table 5.9 lists the event yields at each analysis step for the electron and the muon channels in the tagged (exactly one b-jet is required) samples. As mentioned in subsection 5.2.1 only events with two jets are considered within this analysis. The predictions

are derived from simulated samples together with their theoretical cross-sections (see Table 5.2 and Tables 5.4-5.3). W+jets are scaled by a factor determined from data driven techniques and multijet is estimated using the jet-electron model for the electron channel and the matrix method for the muon channel. The uncertainties correspond to the statistical uncertainty from the size of the simulated samples, while for multijet the uncertainty is exclusively from the jet-electron method and the matrix method (as already discussed in Section 5.3.1.3). Both channels show a good agreement between data and predictions from *pre-selection* level.

	Electron		Muon	
	Preselection	Selection	Preselection	Selection
t-channel	1717 ± 5	278 ± 2	2076 ± 6	341 ± 2
s-channel	117 ± 1	4 ± 0	151 ± 1	6 ± 0
Wt-channel	585 ± 7	13 ± 1	682 ± 8	16 ± 1
Top quark pair	4320 ± 14	121 ± 2	5038 ± 15	149 ± 3
Diboson	121 ± 2	1 ± 0	142 ± 2	2 ± 0
Z+jets	196 ± 9	4 ± 1	190 ± 7	3 ± 1
W+HF jets	4773 ± 31	86 ± 4	6953 ± 37	109 ± 4
W+light jets	1624 ± 28	15 ± 0	2215 ± 31	23 ± 3
Multijet	1090 ± 545	20 ± 10	550 ± 275	6 ± 3
Total expected	14544 ± 640	541 ± 15	17997 ± 280	654 ± 7
S/B	0.13	0.95	0.13	0.96
ATLAS data	14738	576	17966	691

Table 5.9: Event yields for the electron and muon channels at *pre-selection* and selection level in the tagged samples. The predictions are derived from simulated samples together with their theoretical cross-section. W+jets are scaled by a factor determined from data and multijet is estimated using the jet-electron model for the electron channel and the matrix method for the muon channel. The uncertainties correspond to the statistical one except for multijet sample that corresponds to the systematic uncertainty.

5.4 Measurement of the forward-backward asymmetry $A_{\mathrm{FB}}^{\mathrm{T}}$

The scope of this chapter is to probe the anomalous coupling g_{R} of the Wtb vertex. As described in Section 1.3, the forward-backward asymmetry $A_{\mathrm{FB}}^{\mathrm{T}}$ is sensitive to the real part of the coupling g_{R}. This asymmetry $A_{\mathrm{FB}}^{\mathrm{T}}$ is computed from the angular distribution $\cos\theta^{\mathrm{T}}$, where θ^{T} is the angle between the transversal direction T (as defined in Equation 6.4) and the lepton (in the W boson rest frame), as shown in Figure 1.4. The spin direction of the top quark $\vec{s}_t$ in the single top quark t-channel is assumed to be in the direction of the momentum of the spectator quark. To measure θ^{T}, the reconstructed momentum of the lepton is boosted into the rest frame of the W boson

and the momentum of the W boson is boosted back to the top quark rest frame.

Figure 5.3 shows the angular distribution of $\cos\theta^{\mathrm{T}}$ at *pre-selection* level for the electron and muon channel for those events with two jets and exactly one of them b-tagged. At this level, the distributions are dominated by background events. This allows to check the data to MC agreement in the signal region. Actually the agreement is good. The equivalent plots at selection level are shown in Figure 5.6. One can clearly see the enhancement of the signal over background due to the additional selection cuts. The latter distributions are used to compute the forward-backward asymmetry $A_{\mathrm{FB}}^{\mathrm{T}}$. Since this is obtained by counting the number of events in the *forward* ($\cos\theta^{\mathrm{T}} > 0$) and *backward* ($\cos\theta^{\mathrm{T}} < 0$) regions, a two-binned distribution is used (this binning choice avoids problems due to the limited statistics in the simulated samples). The corresponding distributions are shown in Figure 5.7 for the electron and muon channel.

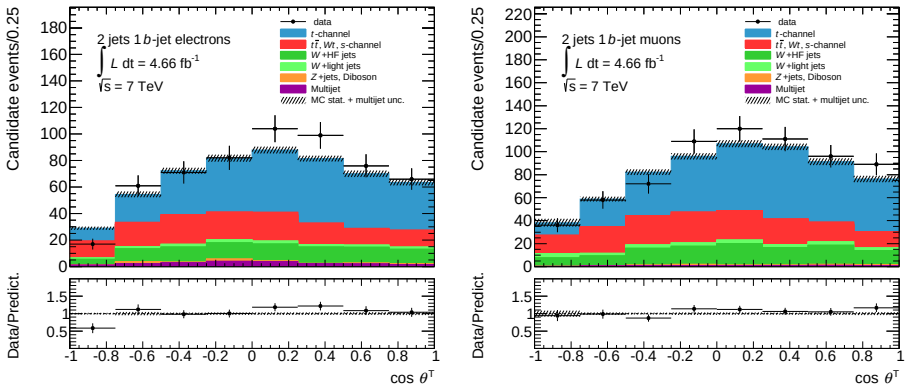

Figure 5.6: Reconstructed $\cos\theta^{\mathrm{T}}$ angular distribution obtained at selection level for electron (left) and muon (right) channel in the tagged sample. ATLAS data, simulated signal and different background contributions are shown. Uncertainties are statistical except for multijet which uses the systematic uncertainty on normalisation.

The measurement of the asymmetry $A_{\mathrm{FB}}^{\mathrm{T}}$ is given in this thesis for the combined electron and muon channel. This means that all the results shown from now on are for the combination though in Appendix C.1 all the results obtained in the electron and muon channel individually are shown. Figure 5.8 shows the angular distribution for events with two jets for the combined electron and muon channel.

5.4.1 Distortions of the angular distribution $\cos\theta^{\mathrm{T}}$

Since the angle θ^{T} is measured using the reconstructed momenta of the charged lepton and W boson, the shape of the distribution of $\cos\theta^{\mathrm{T}}$ is convoluted by detector reconstruction and selection effects. Before the asymmetry can be deduced from Figure 5.7, it has to be de-convoluted from distortions (due to experimental limitations) to parton level (i.e. to parton from hard process). The different effects are described below and their impact is shown in Figure 5.9.

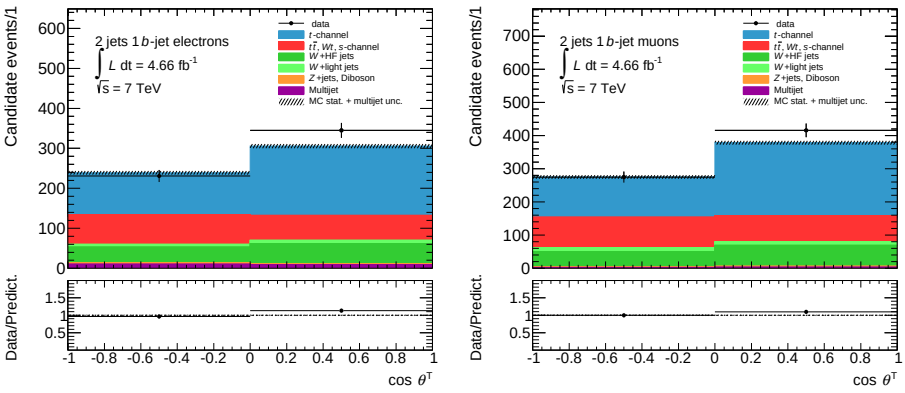

Figure 5.7: Reconstructed $\cos\theta^{\mathrm{T}}$ angular two-bin distribution obtained at selection level for electron (left) and muon (right) channel in the tagged sample. ATLAS data, simulated signal and different background contributions are shown. Uncertainties are statistical but for multijet which shows the systematic uncertainty on normalization.

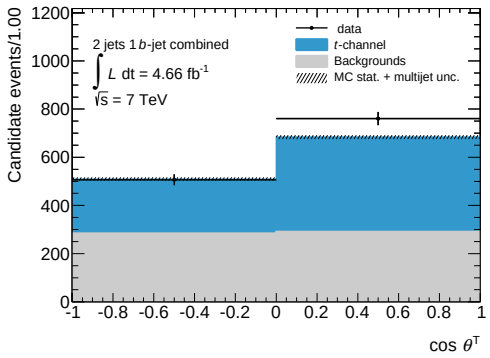

Figure 5.8: Angular distribution for the combined electron and muon channel. ATLAS data, MC signal and the merged backgrounds (grey) are shown. Uncertainties are statistical and for multijet include also the 50% systematic uncertainty on normalization.

- **Impact of the event selection:** Tenim que parlar d'aço. Comparing the $\cos\theta^{\mathrm{T}}$ distribution obtained at parton level from the generated objects before and after applying the event selection, one can observe a strong suppression of events with $\cos\theta^{\mathrm{T}}$ values in the central region. This is due to the requirement of an isolated lepton. In fact, $\cos\theta^{\mathrm{T}} \simeq 0$ means that the angle θ^{T} between the lepton and the tangential direction is $\sim \pi/2$; that is, the lepton is in the plane formed by the W momentum and the top quark spin direction (see Figure 1.4). Then, since the W momentum is back-to-back to the b quark, and the top quark spin direction is the spectator jet momentum direction, the lepton and the two jets (coming from the b and spectator quarks) in the event are all in the same plane. Therefore, the

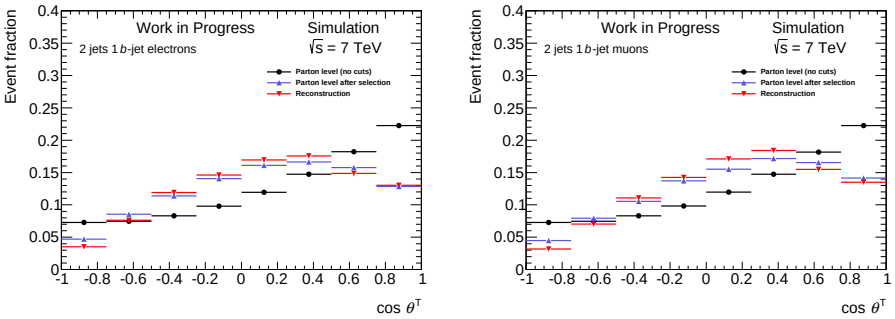

Figure 5.9: Comparison of the angular distribution $\cos\theta^{\mathrm{T}}$ from simulated single top quark t-channel events at different stages of the analysis: from the generated objects before and after the event selection and the distribution obtained from the reconstructed objects for all selected events for electrons (left) and muons (right).

efficiency is lower when one requires lepton isolation. Due to this effect the event selection efficiency (A_j) is not flat as a function of $\cos\theta^{\mathrm{T}}$, as it can be seen in Figure 5.10 which shows the event selection efficiency for the combined electron and muon channel.

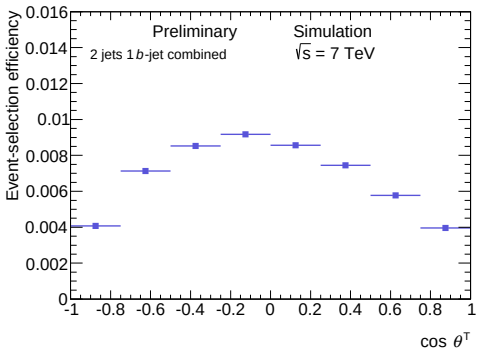

Figure 5.10: Event selection efficiency as a function of $\cos\theta^{\mathrm{T}}$ for the combined electron and muon channel.

- **Impact of the event reconstruction:** The shape of the simulated $\cos\theta^{\mathrm{T}}$ distribution is also affected by the reconstruction. Several effects contribute to this distortion: imperfect measurement of physics objects quantities due to detector acceptance or inefficiencies, as well as resolution effects due to the neutrino and the reconstruction of the top quark. All these smearing effects lead to the migration of events between different bins in the $\cos\theta^{\mathrm{T}}$ distribution. These migrations can be described by a migration matrix M_{ji} that translates reconstructed $\cos\theta^{\mathrm{T}}$ values in bin i into the corresponding generated values in bin j, and that it is equivalent to a detector resolution function.

A transfer matrix T_{ji} is calculated using simulated t-channel events filling one entry for each event passing the acceptance cuts. The migration matrix M_{ji} is obtained from this transfer matrix, by normalising the sum of the entries in a bin of the truth physical quantity (each row) to unity. In this way, the migration matrix M_{ji} gives the probability for a value of the truth (bin j) physical quantity to be reconstructed at another value (bin i).

$$T_{ji} \Rightarrow M_{ji} \; ; \text{by construction} \sum_{i} M_{ji} = 1 \; .$$

In order to minimise the reconstruction distortion, the optimal strategy has been to choose the smallest bin size without substantially deteriorating the total uncertainty after unfolding. This means to check the condition number[2] since it is an indicative measurement of how much the matrix inversion inflates the error propagation. Since the aim is to measure a forward-backward asymmetry, the choice is two bins. The obtained 2x2 transfer T_{ji} and migration M_{ji} matrices for the combined electron and muon channel is illustrated in Figure 5.11.

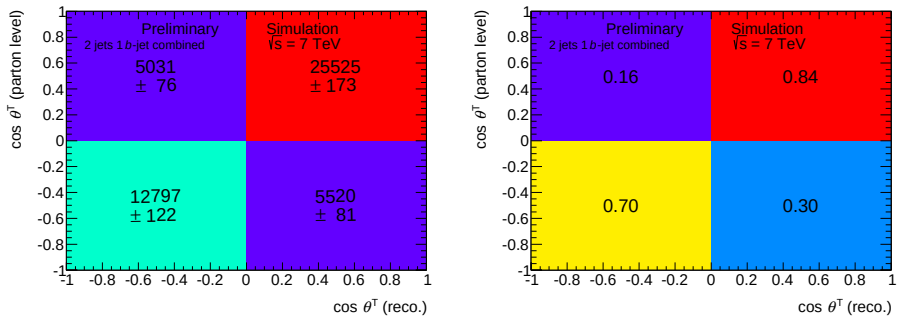

Figure 5.11: Transfer matrix T_{ji} (left) and migration matrix M_{ji} (right) for the combined electron and muon channel. The latter is obtained from the former by normalising the sum of the entries in each row.

5.4.2 Unfolding to parton level

In high-energy physics, measurements of physical observables are typically distorted from experimental limitations (i.e. detector resolution, geometric acceptance of the detector, analysis event selection, limited event statistics). This makes direct comparison with theoretical predictions a complex process. One approach is to use MC simulations to model these effects and therefore be able to correct them. This procedure is called *unfolding* since it allows to unfold the experimental results accounting for resolution and acceptance effects. There are several procedures to perform this unfolding; here, a fit has been used to recover the truth $\cos\theta^{\mathrm{T}}$ distribution. The observed data distribution

[2] The condition number of a matrix, k, is defined as $k = ||M||||M^{-1}||$

has to be corrected for acceptance, detector and reconstruction effects using the following formula:

$$N_i^{\text{data}} = M_{ji} A_j N_j^{\text{MC signal truth}} + N_i^{\text{bkg}} \tag{5.4}$$

where N_i^{data} is the number of events in data for bin i, N_i^{bkg} is the sum of all backgrounds obtained from MC, $N_j^{\text{MC signal truth}}$ is the computed signal events corrected at parton level, A_j is the event selection efficiency (i.e. acceptance correction) and M_{ji} the migration matrix (i.e. detector resolution correction). In the case of two bin distributions, to recover the truth $\cos\theta^{\text{T}}$ 2-bin distribution, the $N_i^{\text{data}} - N_i^{bkg}$ 2-bin distribution is fitted with the equation system:

$$\begin{pmatrix} N_-^{\text{data}} - N_-^{bkg} \\ N_+^{\text{data}} - N_+^{bkg} \end{pmatrix} = M \times \begin{pmatrix} A_- N_-^{\text{MC signal truth}} \\ A_+ N_+^{\text{MC signal truth}} \end{pmatrix} \tag{5.5}$$

where $A_- N_-^{\text{MC signal truth}}$ and $A_+ N_+^{\text{MC signal truth}}$ are the fitting parameters. Once this parameters are extracted from the fit, the distribution $N_j^{\text{MC signal truth}}$ is straightforward obtained.

In order to validate the unfolding procedure, one check have been performed using simulated samples: a closure test.

5.4.2.1 Closure test

A closure test has been performed to check that the procedure is able to reproduce the distribution at generator level. It consists basically in a folding followed by an unfolding on simulated signal events and checking the deviation of the unfolded A_{FB}^{T} value to be consistent with the input asymmetry value. The values obtained for the MC signal at reconstructed level can be seen in Table 5.10. The resulting unfolded distribution and calculated A_{FB}^{T} are compatible with generated values (parton level) within statistical uncertainties.

combined	A_{FB}^{T}
MC signal (raw)	0.271 ± 0.005 (stat.)
MC signal (unfolded)	0.344 ± 0.016 (stat.)

Table 5.10: Measured value of A_{FB}^{T} for the closure test, obtained for the reconstructed t-channel signal events for the combined electron and muon channel. The uncertainty is statistical only.

5.4.3 Unfolded data distribution

Once the unfolding procedure has been validated, it can be used to unfold the measured data distribution after background subtraction. The obtained values of A_{FB}^{T} are given

in Table 5.11 before and after background subtraction and after the unfolding for the combined electron and muon channel. The unfolded value for the $A_{\mathrm{FB}}^{\mathrm{T}}$ is compared with the SM prediction in Figure 5.12.

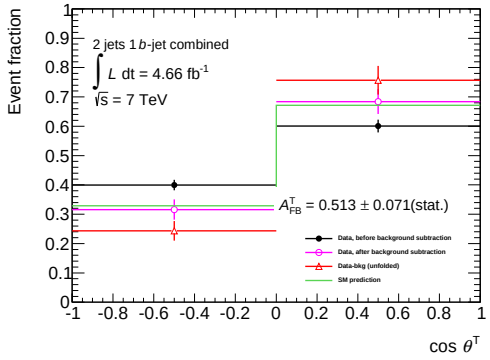

Figure 5.12: Unfolded angular distribution for the combination of electron and muon channels. The uncertainties are statistical only.

combined	$A_{\mathrm{FB}}^{\mathrm{T}}$
Data (raw)	0.201 ± 0.028 (data stat.)
Data (raw, bkg. subtracted)	0.357 ± 0.051 (data stat.) ± 0.015 (bkg. MC stat.) = 0.375 ± 0.038 (total stat.)
Data unfolded	0.495 ± 0.090 (data stat.) ± 0.030 (bkg. MC stat.) ± 0.013 (signal MC stat.) = 0.495 ± 0.071 (total stat.)

Table 5.11: Measurement of $A_{\mathrm{FB}}^{\mathrm{T}}$ for events with two jets in the combined electron and muon channel. Only the statistical uncertainty is shown.

5.5 Systematic uncertainties

There are multiple systematic effects that can have an impact on the $A_{\mathrm{FB}}^{\mathrm{N}}$ measurement. These systematic uncertainties are evaluated using the common prescriptions from the ATLAS top physics working group and the standard ATLAS procedures [71] and [81]). For each systematic, the W+jets overall normalisation and flavour fractions computed for the given systematic shift is used. The following systematics have been considered in this analysis:

- **Lepton trigger, reconstruction and identification efficiency scale factors:** Scale factors are applied to MC lepton trigger and identification efficiencies in order to reproduce the trigger, reconstruction and selection efficiencies obtained in data. $Z \to \ell\ell$ decays were used to obtain these scale factors as functions of the lepton

kinematics. The uncertainties on the derived factors were evaluated by varying the lepton and signal selections and from the uncertainty in the evaluation of backgrounds. Systematic uncertainties of the level of few % were found. Their impact on the $A_{\rm FB}^{\rm N}$ asymmetry measurement is evaluated by re-computing the predicted MC event yields and signal acceptance using the shifted (up and down) scale factors.

- **Lepton momentum/energy scale/resolution:** In order to take into account discrepancies between data and MC in the momentum/energy scale and resolutions, electrons and muons are modified on the MC to reflect data. $Z \to \ell\ell$ processes were used to derive correction factors and the associated uncertainties. A systematic uncertainty is assigned by shifting up and down the momentum/energy scaling and smearing by 1σ and re-applying the event selection. The $E_{\rm T}^{\rm miss}$ of the event is re-calculated accordingly.

- **Jet energy scale (JES):** The JES was derived using data from the full 2011 dataset and simulations. Its uncertainty is estimated with the MultijetJESUncertaintyProvider tool and depends on the $p_{\rm T}$ and η of the reconstructed jet. The tool is used to scale the energy of each jet up or down by 1σ, propagate this change to the $E_{\rm T}^{\rm miss}$ calculation, then re-apply the object and event selection. The tool also provides the additional uncertainty to the JES due to pile-up events. An additional uncertainty is applied to b-jets. The b-jets are identified by their truth-flavour. This uncertainty is provided in five $p_{\rm T}$bins ranging from 2.5% to 0.80% for low and high $p_{\rm T}$jets and added in quadrature to provide the final uncertainty.

- **Jet energy resolution (JER):** The JER measured with the di-jet balance and the bi-sector techniques in data and MC agrees within uncertainty. For this reason, no systematic smearing is applied to jets in MC simulation for the nominal measurement but an uncertainty on the JER is evaluated by smearing the jets according to the systematic uncertainties of the resolution measurement in the full 2011 dataset.

- **Jet reconstruction efficiency:** The jet reconstruction efficiency is defined as the fraction of probe track-jets matched to a calorimeter jet and it was estimated using minimum bias events and multijet events. The observed difference between data and MC efficiencies was applied to MC by randomly dropping jets from events.

- ***b*-tag scale factors/efficiency:** Since the b-tagging efficiencies and fake rates are not identical in data and MC, all jets are assigned a specific weight factor to account for this difference. The obtained weights for each jet are combined into an event weight by multiplying the weights. The provided b-tagging data/MC scale factors have an associated uncertainty which is evaluated separately for heavy flavour (i.e. b and c quarks) and light flavour quark jets in the MC.

- **JVF scale factors:** The application of a cut on the JVF to reduce contamination by pile-up jets introduces an uncertainty related to the efficiency with which this cut successfully selects hard scattered jets. Scale factors provided by the jet calibration group are applied to determine this uncertainty.

- $\boldsymbol{E_{\mathrm{T}}^{\mathrm{miss}}}$: The uncertainties from the energy scale and resolution corrections on leptons and jets are propagated into the calculation of the $E_{\mathrm{T}}^{\mathrm{miss}}$. Additional uncertainties are added from contributions of calorimeter cells not associated to any jets (cell-out term) and due to soft-jets. The cell-out and soft-jet uncertainties are treated as fully correlated.

- **Pile-up $\boldsymbol{E_{\mathrm{T}}^{\mathrm{miss}}}$**: The uncertainty in the description of extra energy deposited due to pile-up interactions is treated as a separate $E_{\mathrm{T}}^{\mathrm{miss}}$ scale uncertainty.

- **Multijet background normalisation and shape:** For the electron channel, the shape of this background is estimated using simulated events and the normalisation is estimated from data using the jet-electron model as discussed in Section 5.3.1. For the muon channel, both the normalisation and shape are estimated using the matrix method. A global normalisation and shape uncertainty on this background is obtained by taking the largest variation between considering a change of 50% in the normalisation and removing completely the multijet background. It is found that in both channels the latter is more conservative.

- ***W*+jets background normalisation and shape:** The normalisation is estimated using the method outlined in Section 5.3.2 and the shape is obtained directly from the MC samples. To compute the uncertainty of the normalisation method, the overall normalisation and flavour fractions are recalculated for each systematic source (JES, etc.) using the corresponding MC samples that include these systematic variations, i.e. a set of normalisation values is obtained for each of the systematics. To compute the total uncertainty of the method and avoid double counting each set of normalisation values is applied when computing each of the systematics. In this way the systematics on the W+jets normalisation is already included in the systematic evaluation of the different sources listed. On the other hand, systematic uncertainties on the shape of the W+jets distributions are assigned based on differences in simulated events generated with different simulation parameters: functional forms of the factorisation scale (*iqopt3*) and minimum ALPGEN parton p_T (*ptjmin10*).

- **Theoretical cross-section:** In this analysis, the event yields from the $t\bar{t}$, Z+jets and diboson background processes are estimated using the acceptance from MC and the theoretically predicted cross-sections. The cross-section uncertainty on the $t\bar{t}$ cross-section is $\sigma_{t\bar{t}} = 167^{+17}_{-18}$ pb [67]. An uncertainty of 5% is assigned to the diboson background and an uncertainty of 60% to the Z+jets background. For the single top quark s and Wt channels, a 10% uncertainty is used. These uncertainties account for scale variations, PDFs, and the uncertainty in α_S value.

- **Initial and final state radiation (ISR/FSR):** The dependence of the signal acceptance and the other top quark background processes uncertainty on the ISR/FSR model is estimated from a set of ACERMC+PYTHIA samples for the top quark processes generated with various ISR/FSR tunes which explore the full experimentally allowed parameter space. The uncertainty is assigned as half of the difference between the up/down variations.

- **MC generator:** The dependence on the MC generator is estimated for the top quark processes comparing different generators. The resulting uncertainty is symmetrized. For single top quark t-channel the AcerMC is compared with Protos (both of them interfaced with Pythia). Since there are no τ samples available with Protos, just the electron and muon channels are considered to compute this systematic uncertainty.

  In case of the $t\bar{t}$ sample, Powheg+Pythia (default) and Alpgen+Jimmy are compared and the difference is taken as a combined MC generator and PS systematic uncertainties.

- **PDFs:** The PDF uncertainty of an observable is evaluated following the recommendations of the PDF4LHC [82] as explained in [83]. The total uncertainty is the result of two factors:

  - **Intra-PDF uncertainty**: This is the uncertainty within a given PDF set. Usually a certain PDF is accompanied by a set of error PDFs and there is a PDF-dependent prescription how to evaluate the PDF uncertainty using these error PDFs.

  - **Inter-PDF uncertainty**: This is the variation when switching from one PDF (set) to another PDF. The comparison is made using the best fit PDF (or central value) for each PDF and comparing the variation on the observable.

    The full PDF uncertainty is the combination of these inter and intra-PDF uncertainty. The procedure outlined by the PDF4LHC working group is used to combine both. An event re-weighting is used where each event obtains a new weight w, which is calculated as:

    $$w = \frac{\mathrm{PDF}(x_1, f_1, Q) \times \mathrm{PDF}(x_2, f_2, Q)}{\mathrm{PDF}_0(x_1, f_1, Q) \times \mathrm{PDF}_0(x_2, f_2, Q)} \ , \tag{5.6}$$

    where $\mathrm{PDF}_0(x_i, f_i, Q)$ is the PDF used for the sample generation and $\mathrm{PDF}(x_i, f_i, Q)$ represents each of the variations for each of the PDF sets. This computed for all the PDF flavours. The signal and all background MC samples are re-weighted according to each of the PDF uncertainty eigenvectors and the largest variation is taken as the uncertainty. The PDF sets taken into account are CT10, MSTW2008nlo and NNPDF. All the uncertainties are combined using the *envelope* to compute the final uncertainty.

- **Unfolding method:** This uncertainty is estimated from the closure test (see Section 5.4.2.1). The unfolded MC signal $A_{\mathrm{FB}}^{\mathrm{T}}$ value (shown in Table 5.10 and Table C.3) is compared with the generated $A_{\mathrm{FB}}^{\mathrm{T}}$ value in the MC sample, in this case the SM value ($A_{\mathrm{FB}}^{\mathrm{T}}$=0.341) and the difference is taken as systematic uncertainty due to the unfolding method.

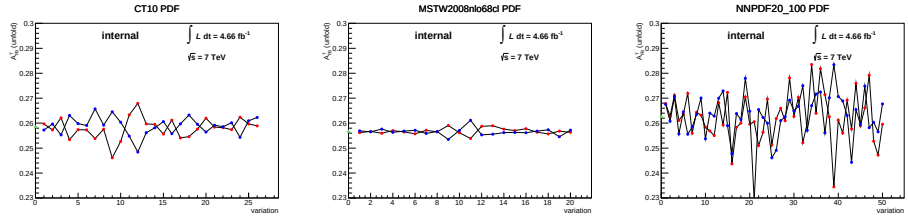

Figure 5.13: Effect of the PDF variations for three different sets in the $A_{\mathrm{FB}}^{\mathrm{T}}$ measurement.

- **Luminosity:** The relative luminosity uncertainty for 2011 data is 1.8%, based on dedicated *van der Meer* scans [51].

To compute the different systematic uncertainties for the $A_{\mathrm{FB}}^{\mathrm{T}}$ measurement the angular distribution $\cos\theta^{\mathrm{T}}$ is varied for each source of uncertainty. The impact of these uncertainties in the asymmetry is evaluated using 15k pseudo-experiments. In each pseudo-experiment, the measurement is repeated on a simulated data sample using the same statistics as in the original dataset. The difference of the estimated asymmetry with and without variation is quoted as systematic uncertainty. Since the ensembles of pseudo-data are built from simulated data, the expected uncertainty is given as systematic uncertainty. The procedure is to scale the pseudo-data and keep the estimator (background, migration matrix and event selection efficiency) not varied, as seen in Equation 5.8.

The procedure is the following

- Vary the source of systematic uncertainty (e.g., JES) up and down and create new pseudo-data sets.
- Re-do the ensemble tests with the scaled inputs and estimate the expectation of the asymmetry value leaving the background, migration matrix and event selection efficiency unchanged.
- Quote the difference of the expectation values of the estimator for the scaled and unscaled ensemble tests as systematic uncertainty.

$$N_i^{\text{pseudo-data}}(d_k) = N_i^{\text{MC signal reco}}(d_k) + N_i^{\text{bkg}}(d_k) \ , \tag{5.7}$$

where the notation d_k refers to the different pseudo-experiments and d_k to the unvaried elements.

$$\begin{pmatrix} N_-^{\text{pseudo-data}}(d_k) - N_-^{\text{bkg}}(d_0) \\ N_+^{\text{pseudo-data}}(d_k) - N_+^{\text{bkg}}(d_0) \end{pmatrix} = M(d_0) \times \begin{pmatrix} A_-(d_0) N_j^{\text{MC signal truth}}(d_k)_- \\ A_+(d_0) N_j^{\text{MC signal truth}}(d_k)_+ \end{pmatrix} \tag{5.8}$$

Table 5.12 shows a breakdown of the systematic uncertainties and their contribution to the $A_{\mathrm{FB}}^{\mathrm{T}}$ measurement for the combined electron and muon channel.

Systematic	$\Delta A_{\mathrm{FB}}^{\mathrm{T}}$
Lepton reco. eff.	0.008 / -0.009
Lepton energy reso.: no scale	0.003 / -0.03
Lepton energy reso.: ID	0.003 / -0.005
Lepton energy reso.: MS	0.003 / -0.010
Jet energy scale	0.08 / -0.06
E_T^{miss} (cellout)	0.010 / -0.07
E_T^{miss} (pileup)	0.04 / -0.014
SF b-tag	0.015 / -0.014
SF c-tag	0.0013 / -0.003
SF mistag	0.02 / -0.002
JVF SF	0.003 / -0.005
Jet reconstruction efficiency	0.008 / -0.008
Jet energy resolution	0.04 / -0.04
Luminosity	0.024 / -0.015
Z+jets norm.	0.005 / -0.005
$t\bar{t}$ norm.	0.02 / -0.02
s-ch. norm.	<0.001 / <0.001
Wt-ch. norm.	0.002 / -0.002
dibosons norm.	<0.001 / <0.001
W+jets shape (iqopt3)	0.001 / -0.001
W+jets shape (ptjmin10)	0.001 / -0.001
QCD shape and norm.	0.02 / -0.02
ISR/FSR	<0.001 / <0.001
t-ch. MC generator	0.015 / -0.015
$t\bar{t}$ MC gen. and PS	0.003 / -0.003
PDF	0.017 / -0.017
Unfolding	0.013 / -0.013
Total	+0.11 / -0.11

Table 5.12: Detailed breakdown of the contribution of each source of systematic uncertainty ($\Delta A_{\mathrm{FB}}^{\mathrm{T}}$) for the 2 jets tagged events for electrons and muons combined.

5.6 Results

The final value of the forward-backward asymmetry $A_{\mathrm{FB}}^{\mathrm{T}}$ and its statistic and systematic uncertainties are quoted in Table 5.13 for the combined electron and muon channel. The individual measurements for the electron and muon channels are shown in Appendix C.1. The unfolded value of $A_{\mathrm{FB}}^{\mathrm{T}}$ is extracted from the distribution shown in Figure 5.12 and all systematics shown in Section 5.5 have been combined to give the final systematic uncertainty.

Once the forward-backward asymmetry $A_{\mathrm{FB}}^{\mathrm{T}}$ has been measured, the Equation 1.33 can be used (taking V_{L} =1, $V_{\mathrm{R}} = g_{\mathrm{L}} = 0$ and assuming that g_{R} is close to 0) to constrain the real part of the anomalous coupling g_{R}. Figure 5.14 shows the top quark

combined	$A_{\mathrm{FB}}^{\mathrm{T}}$
Data (raw)	0.20 ± 0.03 (stat.)
Data (raw, bkg. subtracted)	0.36 ± 0.04 (stat.)
Data unfolded	0.51 ± 0.09 (stat.) ± 0.11 (syst.)
Expected S.M.	0.341

Table 5.13: $A_{\mathrm{FB}}^{\mathrm{T}}$ measurement for events with two jets for the combined electron and muon channel. Both the statistic and systematic uncertainties are shown for the unfolded result.

polarisation dependence with $\mathbb{R}(g_{\mathrm{R}})$ given by the $A_{\mathrm{FB}}^{\mathrm{T}}$ measurement (see Table 5.13) showing the allowed region at 68% and 95% confidence level (CL) for $\mathbb{R}(g_{\mathrm{R}})$ which is defined by the total uncertainty of this measurement.

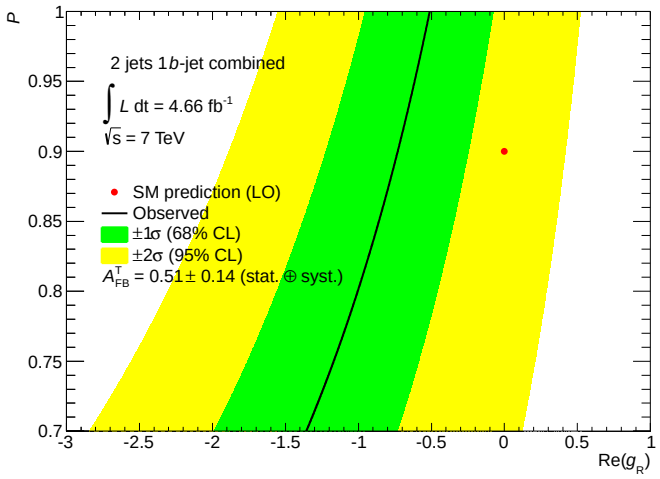

Figure 5.14: Top quark polarisation dependence with $\mathbb{R}(g_{\mathrm{R}})$ given by the current $A_{\mathrm{FB}}^{\mathrm{T}}$ measurement, showing the allowed region at 68% and 95% CL for $\mathbb{I}(g_{\mathrm{R}})$ which is defined by the total uncertainty of this measurement. The SM prediction at tree level ($P = 0.9$) is also shown.

Additionaly, the limits to the value of g_{R} can be computed using the value of $A_{\mathrm{FB}}^{\mathrm{N}}$ measured in ATLAS at 7 TeV collisions [84] and the value of $A_{\mathrm{FB}}^{\mathrm{T}}$ obtained in this thesis. These computations have been performed using the **TopFit** software, a program to fit the Wtb vertex [85]. That limits are shown in the Figure 5.15 where the green color indicates the constraint to g_{R} using only the values of the helicity of W and the value of $A_{\mathrm{FB}}^{\mathrm{N}}$. The red color indicates the constrainig using the previous information and a value of P between 0.7 and 1.0. Finally the blue dots indicate the limits when the value of $A_{\mathrm{FB}}^{\mathrm{T}}$ is added.

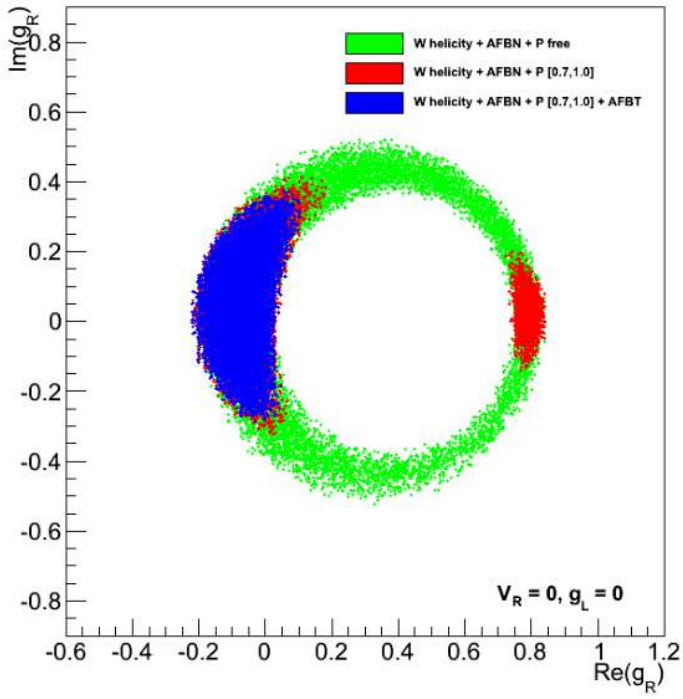

Figure 5.15: Constraints to the value of g_{R} using information of W helicity and $A_{\mathrm{FB}}^{\mathrm{N}}$ (green), W helicity, $A_{\mathrm{FB}}^{\mathrm{N}}$ and a value of polarisation P between 0.7 and 1.0 (red) and W helicity, $A_{\mathrm{FB}}^{\mathrm{N}}$, a value of polarisation P between 0.7 and 1.0 and $A_{\mathrm{FB}}^{\mathrm{T}}$ (blue))

5.7 Conclusions

The final ABFT measurement is:

$$A_{\mathrm{FB}}^{\mathrm{T}} = 0.51 \pm 0.09\,(\mathrm{stat.}) \pm 0.11\,(\mathrm{syst.})\ .$$

This measurement and the results for the electron and muon channel individually, which can be found in Appendix C.1, are found a bit more than a sigma awat from away the SM prediction ($A_{\mathrm{FB}}^{\mathrm{T}} = 0.341$) within the total uncertainties of the measurements.

Chapter 6

Resumen

6.1 Motivaciones teóricas

6.1.1 El modelo estándar

El Modelo Estándar (SM) una teoría que describe la descripción más exacta de las interacciones entre partículas elementales hasta la fecha[1]. Durante las últimas décadas, sus predicciones han sido confirmadas por un alto número de medidas experimentales, incluyendo la existencia del bosón de Higgs, una de los principales motivos de la construcción del Gran Colisionador de Hadrones (LHC). Según el SM, toda la materia está compuesta por un pequeño número de partículas elementales de espín 1/2 llamadas fermiones: seis *quarks* y seis leptones. De los seis leptones existen tres cargados con carga negativa: el electrón, el muón y el tau. Los otros tres leptones no tienen carga y son conocidos como neutrinos y cada uno esta emparejado con su correspondiente leptón. Los *quarks* tienen carga fraccionaria de $+\frac{2}{3}$ o $-\frac{1}{3}$. Todas las partículas tienen asociada una antipartícula con carga de signo diferente. Como los leptones, los *quarks* están agrupados en parejas que difieren en una unidad de carga eléctrica. Los tipo de *quark*, llamado también sabor, son: *u* o *quark* up, *d* o *quark down*, *s* o *quark strange*, *c* o *quark charm*, *b* o *quark bottom* y *t* o *quark top*. En la tabla 6.1 se muestran el símbolo y carga de cada fermión ordenados de menor a mayor según su masa.

Mientras que los leptones existen como partículas libres, los *quarks* solo aparecen en estados ligados. Los protones y neutrones están formados por tres de los *quarks* más ligeros, *uud* el protón y *udd* el neutrón. El material más común del universo son las partículas estables, electrones, *quarks u* y *d*. Los *quarks* más pesados también se combinan para formar partículas pero mucho más pesadas que el protón y neutrón. Estas partículas son inestables y decaen rápidamente a combinaciones de *u* y *d*. Las variedades pesadas son observadas solo en colisiones de altas energías en aceleradores de partículas o naturalmente en los rayos cósmicos.

El Modelo Estándar también es capaz de explicar las interacciones de las partículas. Estas interacciones se explican en términos de intercambio de bosones (partículas con espín entero) entre los constituyentes. Estos mediadores se muestran en la tabla 6.2. Las cuatro interacciones fundamentales son:

Partícula	Sabor			Q/|e|
leptones	e^-	μ^-	τ^-	-1
	ν_e	ν_μ	ν_μ	0
quarks	u	c	t	$+\frac{2}{3}$
	d	s	b	$-\frac{1}{3}$

Table 6.1: Tabla de los fermiones fundamentales según el Modelo Estándar.

Interacción	Teoría	Mediador	Constante de acoplamiento	Alcance (m)
fuerte	QCD	gluón, g	$\alpha_S = 1$	10^{-15}
electromagnética	QED	fotón, γ	$\alpha = 1/137$	∞
débil	EW	$W^\pm$, Z^0	$\alpha_W = 10^{-1}$	10^{-18}
gravitatoria	GR	gravitón, G	$\alpha_g = 6 \times 10^{-39}$	∞

Table 6.2: Interacciones fundamentales.

- La interacción fuerte. Es la responsable de la unión de los *quarks* en protones, neutrones y otros hadrones. También es la responsable de la unión de los protones y neutrones dentro del núcleo. De las cuatro interacciones, es la más fuerte pero de corto alcance. Esta mediada por una partícula sin masa, el gluón.

- La interacción electromagnética. Es la responsable de casi todos los fenómenos fuera de la física nuclear, en particular de los enlaces entre el electrón y el núcleo, así como las fuerzas entre moléculas. Es una interacción muy débil pero de alcance infinito. Está mediada por los fotones (γ), partículas sin masa.

- Interacción débil. Es responsable de la desintegración radiactiva y de la fusión nuclear de partículas subatómicas. Los mediadores de esta interacción son los bosones $W^\pm$ y Z^0, con masas de casi 100 veces la masa del protón.

- Interacción gravitatoria. Actúa sobre todos los tipos de partículas con masas. Es de lejos la más débil de todas las interacciones fundamentales, aunque es la más dominante a escalas universales. Aunque no detectada, se teoriza que está mediada por el intercambio de un bosón de espín 2, el gravitón.

El Modelo Estándar además predice el bosón de Higgs, una partícula elemental con masa y espín 0. El bosón de Higgs desempeña un papel único en el Modelo Estándar, y un papel dominante en explicar los orígenes de la masa de otras partículas elementales, particularmente la diferencia entre el fotón sin masa y los bosones pesados W y Z.

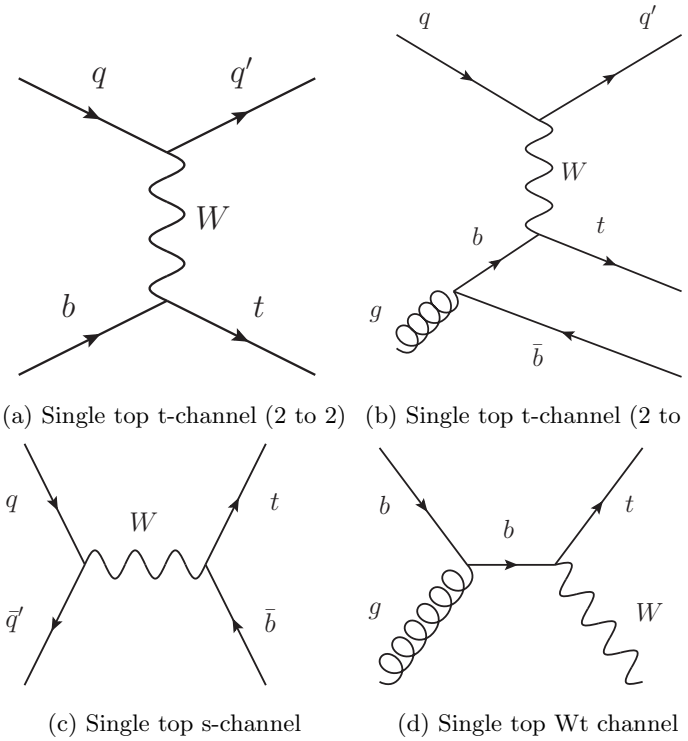

(a) Single top t-channel (2 to 2) (b) Single top t-channel (2 to 3)

(c) Single top s-channel (d) Single top Wt channel

Figure 6.1: Diagramas de Feynman para la producción del single top.

6.1.2 Single Top

Uno de los objetivos de esta tesis es el estudio de la física del *quark top* aislado. En los colisionadores hadronicos los *quarks*, incluido el *quark top*, se producen básicamente a pares mediante interacción fuerte. Pero además, el *quark top* tiene un modo alternativo de producción, el single top, mediante la interacción débil, involucrando un vértice *Wtb*, es decir un vértice compuesto por un bosón W, un *quark b* y un *quark top*. Los diferentes procesos de producción se detallan en la figura 6.1

Al ser el *quark top* una partícula muy pesada y debido a su corta vida media, este decae antes de hadronizar (formar hadrones junto con otros *quarks*) y en el SM, decae casi exclusivamente a un bosón W y un *quark b*. La medida de los acoplamientos del vértice *Wtb* ofrece una interesante ventana a nueva física. En el marco efectivo más general, el lagrangiano del vértice *Wtb* se puede expresar de la siguiente forma:

$$\mathcal{L}_{Wtb} = -\frac{g}{\sqrt{2}}\bar{b}\gamma^{\mu}(V_L P_L + V_R P_R)tW_{\mu}^{-} - \frac{g}{\sqrt{2}}\bar{b}\frac{i\sigma^{\mu\nu}q_{\nu}}{M_W}(g_L P_L + g_R P_R)tW_{\mu}^{-} + \text{h.c} \quad (6.1)$$

En esta formula, g es la constante de acoplamiento débil, m_W es la masa y q_ν el cuadrimomento del bosón W. $P_{LR} \equiv (1 \mp \gamma^5)/2$ son los proyectores levógiro y dextrógiro y

$\sigma^{\mu\nu} = [\gamma^\mu, \gamma^\nu]/2$. $V_{\mathrm{L,R}}$ y $g_{\mathrm{L,R}}$ son los acoplamientos vectoriales y tensoriales levógiros y dextrógiros. En el Modelo Estándar a nivel árbol, el acoplamiento V_{L} es cercano a 1 y es idéntico a V_{tb} que es uno de los elementos de mezclado de *quarks* en la matriz Cabibbo–Kobayashi–Maskawa (CKM)[2], mientras que los acoplamientos anómalos V_{R} y $g_{\mathrm{L,R}}$ son todos nulos. Las desviaciones de esos valores pueden ser medidas midiendo las fracciones de polarización del bosón W o las asimetrías angulares en los productos resultantes del decaimiento del single top. Las asimetrías angulares se definen como:

$$A_z \equiv \frac{N_{\mathrm{evt}}(\cos\theta > z) - N_{\mathrm{evt}}(\cos\theta < z)}{N_{\mathrm{evt}}(\cos\theta > z) + N_{\mathrm{evt}}(\cos\theta < z)} \ , \tag{6.2}$$

donde z es un valor arbitrario fijado en la distribución angular, θ es el ángulo de desintegración y N_{evt} el numero de eventos donde el $\cos\theta$ está por encima o debajo de z. Para la elección de $z = 0$, la asimetría se llama asimetría adelante-atrás (A_{FB}) y es la usada para el análisis mostrado en esta tesis. En las desintegraciones del *quark top*, θ está definido como el ángulo entre la dirección del leptón proveniente de la desintegración del bosón W, en el sistema de referencia en reposo del bosón W, respecto a otra dirección de referencia. Para la producción del quark top no polarizado, la única dirección de referencia significativa es el momento del bosón W en el sistema de referencia en reposo del *quark top* (base de helicidad) y el ángulo correspondiente se denomina θ^* como se puede observar en el esquema de la figura 6.2

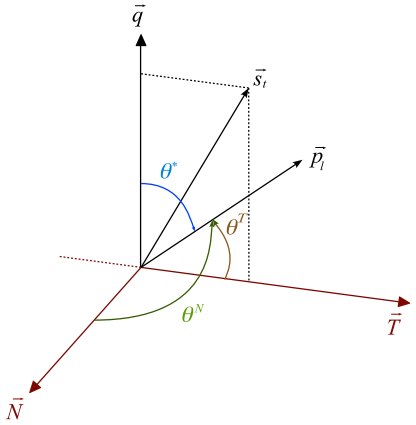

Figure 6.2: Definición de las dos direcciones $\vec{N}$ y $\vec{T}$ dada la dirección de polarización del quark top, $\vec{s}_t$, y el momento del bosón W, $\vec{q}$ en la base de helicidad. Los ángulos mostrados están definidos como los ángulos entre sus direcciones de referencia y la dirección del momento del leptón cargado, $\vec{p}_l$.

En el canal t del *quark top* aislado 6.1a, los *quark top* se esperan altamente polarizados en la dirección del quark espectador com un grado pe polarización de $P \approx 0.9$ para $\sqrt{s} = 7$ TeV como se muestra en Ref. [14, 15]. Con esta dirección de polarización ($\vec{s}_t$)

se pueden definir dos nuevas direcciones en la base de helicidad:

$$\vec{N} = \vec{s}_t \times \vec{q}\,, \tag{6.3}$$

$$\vec{T} = \vec{q} \times \vec{N}\,, \tag{6.4}$$

donde $\vec{N}$ es la dirección normal y $\vec{T}$ la transversal (Figura 6.2), $\vec{s}_t$ es la dirección del espín (dirección del *quark* espectador en el sistema de referencia en reposo del *quark top*) y $\vec{q}$ es el momento del bosón en este mismo sistema. Los ángulos θ^N y θ^T pueden ser definidos como los ángulos entre el leptón en el sistema de referencia en reposo del bosón W y las nuevas direcciones $\vec{N}$ y $\vec{T}$, respectivamente. En la referencia [6] se muestra que la asimetría adelante-atrás en la dirección normal, $A_{\rm FB}^{\rm T}$, es sensible a la parte real del acoplamiento $g_{\rm R}$. Después de varios cálculos la asimetría viene dada por la ecuación:

$$A_{\rm FB}^{\rm T} = \frac{1.98P\mathbb{R}(g_{\rm R})^2 - 5.19P\mathbb{R}(g_{\rm R})V_L + 1.99PV_L^2}{8.03\mathbb{R}(g_{\rm R})^2 - 10.11\mathbb{R}(g_{\rm R})V_L + 5.19V_L^2} \tag{6.5}$$

Para pequeños valores de $g_{\rm R}$ y tomando $V_{\rm L} = 1$ y $V_{\rm R} = g_{\rm L} = 0$, la relación se puede aproximar por:

$$A_{\rm FB}^{\rm T} \approx 0.38P - 0.26 * P\mathbb{R}(g_{\rm R}) \tag{6.6}$$

La medida de la asimetría $A_{\rm FB}^{\rm T}$ y de la parte real del acoplamiento anómalo $g_{\rm R}$ será presentada más adelante.

6.2 El CERN, LHC y los experimentos

6.2.1 El Gran Colisionador de Hadrones

La Organización Europea para la Investigación Nuclear (CERN) es el mayor laboratorio científico en el mundo. Fundado en 1954 para la investigación del núcleo atómico, esta situado en la frontera entre Francia y Suiza. Más adelante sus objetivos se dirigieron hacia la física de altas energías, alcanzando varios logros como el descubrimiento de los bosones W y Z o el más reciente descubrimiento del bosón de Higgs. Hay varios aceleradores situados en el CERN, de los cuales el más grande es el gran colisionador de hadrones (LHC).

El LHC es el acelerador de partículas más grande y de mayor energía del mundo. Consiste en un túnel de 27 kilómetros donde se sitúa el acelerador con unos imanes superconductores y cavidades de radio frecuencia que acelera dos haces de partículas en sentidos opuestos y los hace colisionar en cuatro puntos de la circunferencia. El objetivo del LHC es permitir comprobar las predicciones de distintas teorías de física de partículas y física de altas energías. En particular, su principal objetivo es comprobar la existencia del bosón de Higgs o nuevos fenómenos físicos más allá del modelo estándar. El modelo estándar ha sido comprobado por muchos experimentos pero deja muchas respuestas sin resolver, algunas de las cuales el LHC esta ayudando a resolver.

6.2.2 Experimentos del LHC

Los mayores experimentos del LHC son ALICE, ATLAS, CMS y LHCb, situados en los cuatro puntos donde colisionan los haces como se muestra en la figura 6.3

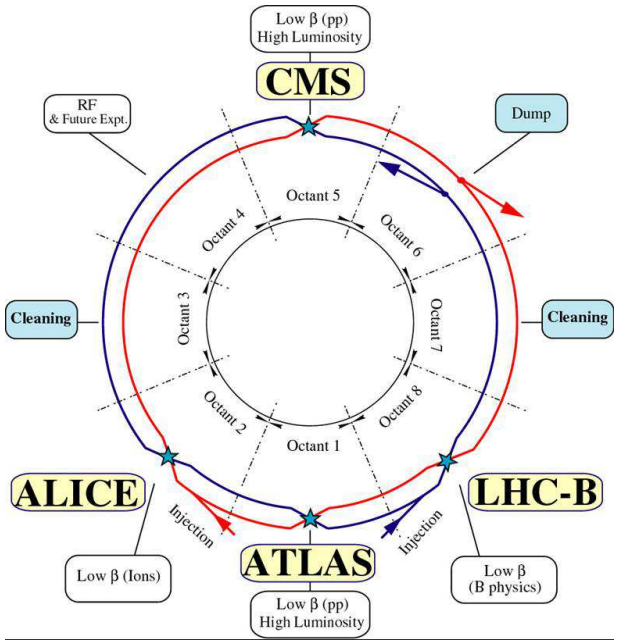

Figure 6.3: Esquema que muestra los cuatro grandes experimentos y la estructura de doble anillo del LHC

ALICE es un experimento que investiga iones pesados. Está diseñado para estudiar la física de la materia a altas densidad, donde se forma una fase de la materia llamada plasma de *quark*-gluón. Durante una parte de cada año, una parte de las colisiones se realizan con iones de plomo, recreando en las colisiones las condiciones similares a aquellas en breves momentos después del big-bang. El detector tiene un peso de 10.000 toneladas, una longitud de 26 m y una altura y anchura de 16 m.

ATLAS es un detector de propósito general. Este experimento se diseñó para aprovechar la alta energía disponible en el LHC y observar fenómenos de física a muy altas energías. Como esta tesis se ha realizado en el experimento ATLAS, este detector será explicado con más detalle más adelante.

CMS es el otro detector de propósito general. Al igual que ATLAS, está diseñado para investigar un amplio abanico de física, incluyendo la búsqueda del bosón de Higgs, dimensiones extra y partículas que pudieran ser materia oscura. CMS está rodeado por un inmenso imán solenoidal que genera un campo de hasta 4 T. El detector tiene un tamaño de 21 m de largo y 15 m de ancho y alto, con un peso total de 15000 toneladas.

El experimento LHCb esta especializado en investigar la pequeña diferencia entre materia y antimateria estudiando las propiedades de los hadrones B (hadrones que contienen el *quark* b) y sus antipartículas. LHCb utiliza una serie de sub-detectores para observar partículas producidas en la dirección hacia adelante. El detector LHCb mide 21 metros de largo, 10 metros de alto y 13 metros de ancho con un peso de 5600 toneladas.

Además de estos cuatro grandes experimentos, existen otros experimentos más pequeños como LHCf, TOTEM o MoEDAL.

6.2.3 El experimento ATLAS

El detector ATLAS tiene una longitud de 45 m, un diámetro de 25 m y un peso de unas 7000 toneladas. La colaboración ATLAS tiene más de 3000 integrantes repartidos entre 175 institutos en 38 países. El experimento ATLAS está compuesto de diversas partes (sub-detectores o sistemas) como se puede ver en la figura 6.4:

- El Detector Interno o de Trazas ID.
- Los calorímetros electromagnético y hadrónicos.
- El espectrómetro de muones (MS).
- Imanes solenoidales y toroidales (Sistema de imanes de ATLAS).
- *Trigger* y adquisición sistema de adquisición de datos (DAQ).
- Software de reconstrucción.
- Computación GRID.

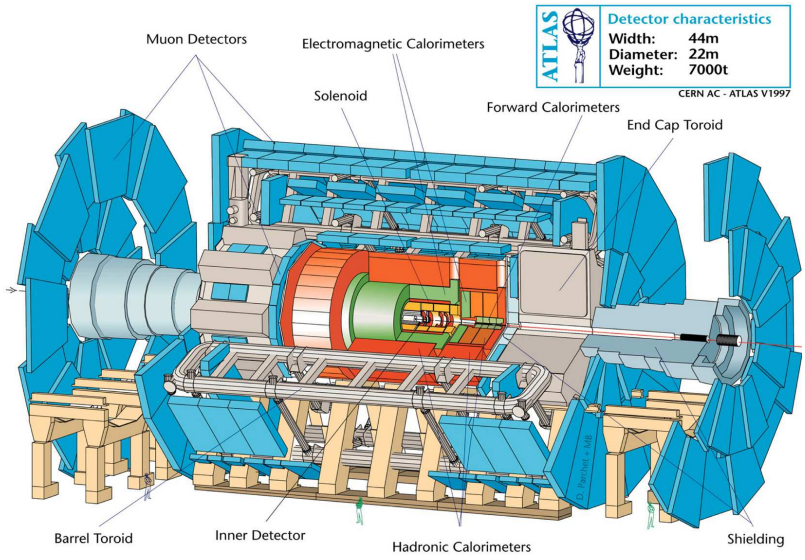

Figure 6.4: Ilustración de detector ATLAS. Se muestran todos los sub-detectores de ATLAS.

El ID es el sistema de detección más interno de ATLAS. Es capaz de detectar las trazas de cientos de partículas cargadas que se producen en cada colisión. Está formado

por capas concéntricas de detectores de trazas, con los detectores de más alta precisión cerca del punto de colisión. El ID esta compuesto por tres sub-sistemas situados dentro de un solenoide que produce un campo magnético de 2 T. El campo magnético hace que la trayectoria de las partículas cargadas se curve, proporcionando información para determinar el momento y carga de cada partícula. Los tres sub-sistemas son: el detector Pixel, el SCT y el TRT. La figura 6.5 muestra una ilustración del ID con sus tres sub-detectores.

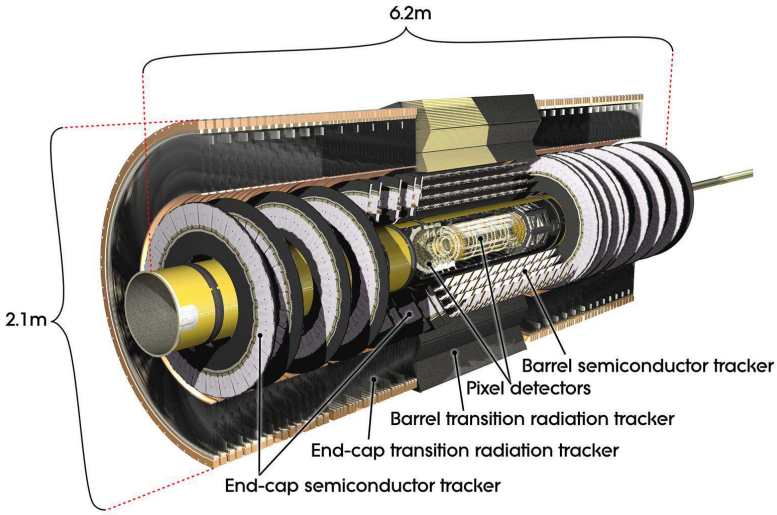

Figure 6.5: Ilustración del ID de ATLAS. Se muestran el detector Pixel, el SCT y el TRT. También se puede distinguir las capas concéntricas del barril y los discos de los end-caps.

Los calorímetros, que rodean el ID y el solenoide, absorben y miden la energía de la mayor parte de partículas cargadas y neutras producidas en las colisiones. La energía depositada en el calorímetro es detectada y convertida a señales eléctricas que son leídas por la electrónica. Los calorímetros están compuestos por varias capas de placas densas que absorben las partículas incidentes y transforman su energía en grandes cascadas de partículas de baja energía. Entre estas placas hay unas finas capas de detectores sensibles a las partículas que registran las cascadas de partículas y producen señales proporcionales a la energía. En ATLAS existen dos tipos de calorímetros, el electromagnético y el hadrónico. El calorímetro electromagnético absorbe y mide principalmente la energía de electrones y fotones mientras que el hadrónico mide las partículas que no han sido frenadas por el electromagnético.

El espectrómetro de muones (MS) es un gran sistema de detección de trazas diseñado para detectar y reconstruir las trazas de los muones. Está compuesto por tres partes, un campo magnético, cámaras para medir con alta precisión espacial las trazas y un conjunto de cámaras para tener una gran resolución temporal.

El sistema de *Trigger* junto con el sistema de adquisición de datos (DAQ) proporcionan el hardware y software necesario para ser capaces de filtrar y almacenar los datos de las colisiones, ya que las estas se producen con una frecuencia de hasta 40 MHz.

6.2.4 El Detector Interno de trazas

El ID es el sub-detector más interno de ATLAS. Combina detectores discretos de alta resolución en la parte más interna con detectores de medida continua en la parte más externa. Tiene un diámetro de 2.1 m y una longitud de 6.2 m. Se ha diseñado para que proporcione un buen reconocimiento de patrones, una resolución de momento excelente y buena medida de los vértices de partículas cargadas. En la figura 6.6 se muestra un esquema transversal de un cuadrante del detector interno.

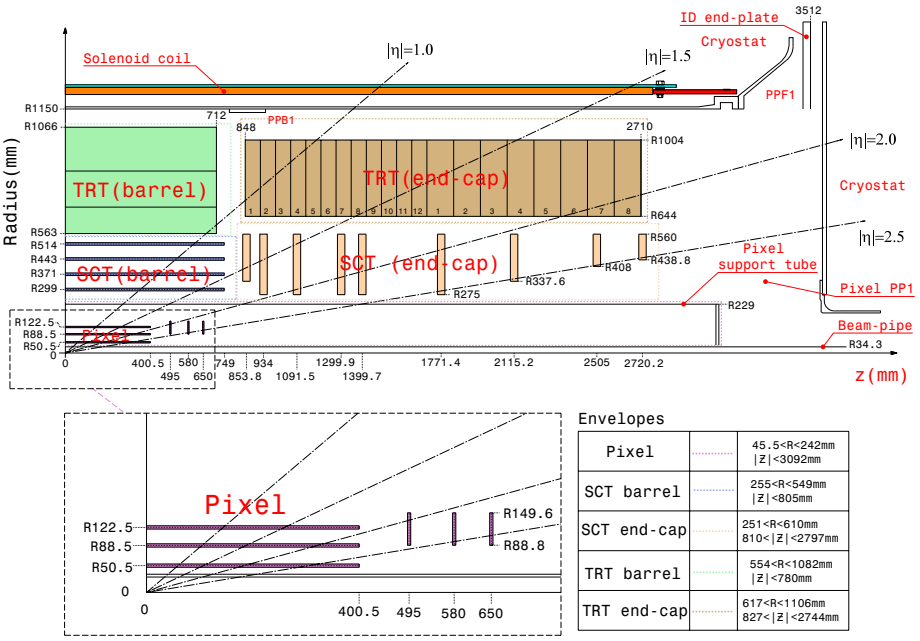

Figure 6.6: Esquema transversal de un cuadrante del ID de ATLAS.

Los sensores del Pixel requieren de tecnología punta para llegar a las especificaciones en resistencia a la radiación, resolución y ocupancia en las capas más internas. Para ello se usaron sensores pixel tipo n oxigenados con pixels de lectura en la cara implantada n+ del detector. Hay 1744 sensores pixel idénticos con un tamaño de $19 \times 63 \text{mm}^2$. Cada sensor esta montado en uno de los 1744 módulos. Estos módulos están organizados en tres capas en el barril y dos tapas en los extremos (*end-caps*), cada uno con tres discos. El barril esta formado por 112 *staves* con 13 módulos organizados en tres capas. Cada disco del *end-cap* esta formado por 8 sectores.

Los sensores del SCT utilizan la tecnología p-on-n a una cara con bandas de lectura. El SCT consta de 4088 módulos montados en cuatro cilindros coaxiales en la región del

barril y dos *end-caps*, cada uno de los cuales contiene nueve discos. Los módulos cubren una superficie de 63 m^2 de silicio y proporcionan una cobertura casi hermética con al menos cuatro medidas espaciales de precisión. 282 de los modulos fueron construidos en el Instituto de Fisica Corpuscular (IFIC).

El TRT está formado por tubos de deriva de poliamida de 4 mm de diámetro. El TRT contiene hasta 73 capas de tubos entrelazados con fibras en el barril y 160 planos de tubos intercalados con hojas en el *end-cap*, que proporcionan radiación de transición para la identificación de electrones. Todas las trazas con $p_T > 0.5$ GeV y $|\eta| < 2.0$ atraviesan al menos 36 tubos, excepto en la región de transición barril-*end-cap*, donde este número disminuye hasta un valor mínimo de 22. El barril del TRT esta dividido en tres anillos de 32 módulos cada uno. Cada *end-cap* del TRT esta formado por dos conjuntos de ruedas independientes.

6.3 Alineamiento del detector interno de trazas

El conocimiento de la posición de los elementos sensores del detector de trazas es crucial para tener una operación y rendimiento óptimos. Una forma precisa de determinar esta información es usando un algoritmo de alineamiento basado en trazas. Este tipo de algoritmos se basan en la minimización de la distancia entre los hits registrados en el sensor y las correspondientes trazas reconstruidas. La caracterización de las trazas es necesaria para obtener los parámetros utilizados para alinear el sistema. La trayectoria de una partícula cargada en un campo magnético uniforme es una hélice que puede ser parametrizada por un conjunto de cinco parámetros. La representación elegida para el alineamiento viene dada por los parámetros $\boldsymbol{\tau} = \{d_0, z_0, \phi_0, \cot\theta, q/p\}$ como se muestra en la figura 6.7. d_0 es el parámetro transversal de impacto, que esta definido como la distancia al plano XY con el signo definido positivo cuando la dirección de la traza es en el sentido de las agujas de un reloj. z_0 es el parámetro de impacto longitudinal que corresponde a la coordenada Z del perigeo. ϕ_0 es el ángulo azimutal en el plano XY en el perigeo y θ corresponde con el ángulo polar. Finalmente, q/p es la carga de la partícula partido por el momento.

El rendimiento esperado del sistema para reconstruir partículas se ha determinando utilizando un modelado preciso de la respuesta individual de los detectores, la geometría y el material pasivo en la simulación. Así la resolución esperada de una parámetro de la traza X puede ser expresada en función de p_T por la ecuación:

$$\sigma_X(p_T) = \sigma_X(\infty)(1 \oplus p_X/p_T) \tag{6.7}$$

donde $\sigma_X(\infty)$ es la resolución asintótica esperada para una partícula con momento infinito y p_X es una constante representando el valor de p_T para el cual los términos intrínseco y de *multiple-scattering* son iguales para el parámetro X bajo consideración. La tabla 6.3 muestra estos dos parámetros para trazas en dos regiones de η, correspondiendo a la zona del barril y los end-caps.

El ajuste de las trazas y el alineamiento del detector utilizan continuamente los residuos traza-hit. Esto es, cada elemento del detector puede contribuir a la traza con una medida de esa traza. Además, es posible predecir donde va a aparecer una medida en el sensor para cada traza. La distancia entre esos dos puntos es lo que se conoce como

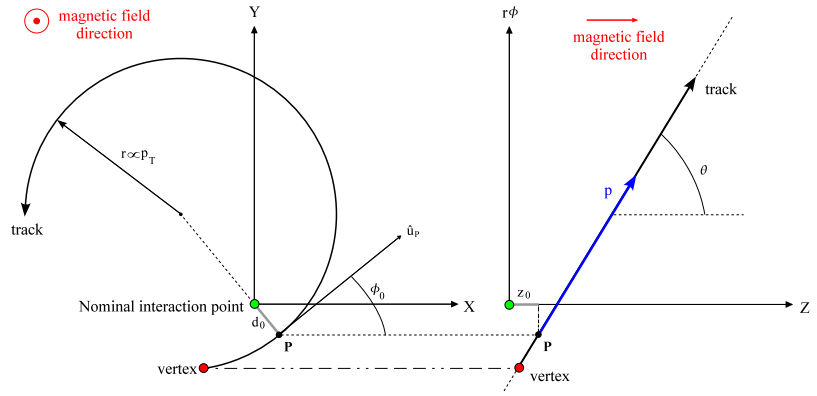

Figure 6.7: Interpretación gráfica de los parámetros de las trazas en el perigeo.

Parámetro de la traza	$0.25 < \|\eta\| < 0.50$		$1.55 < \|\eta\| < 1.75$	
	$\sigma_X(\infty)$	p_X(GeV)	$\sigma_X(\infty)$	p_X(GeV)
Parámetro de impacto transversal (d_0)	10 μm	14	12 μm	20
Parámetro de impacto longitudinal ($z_0 \times \sin\theta$)	91 μm	2.3	71 μm	3.7
Angulo azimutal (ϕ)	70 μrad	39	92 μrad	49
Angulo polar ($\cot\theta$)	0.7×10^{-3}	5.0	0.7×10^{-3}	10
Momento transversal inverso (q/p_T)	0.34 TeV^{-1}	44	0.41 TeV^{-1}	80

Table 6.3: Resoluciones esperadas de los parámetros de las trazas para un momento infinito, $\sigma_X(\infty)$, y para momento transverso, p_X en el cual la contribución de *multiple-scattering* es igual a la de la resolución intrínseca del detector [31]. Los valores se muestran para dos regiones η, una en el barril y otra en los *end-caps*.

residuo. En un sistema de referencia local de un elemento, $\mathbf{m}$ puede ser considerado como el vector que representa la medida del sensor y $\mathbf{e}(\boldsymbol{\tau}, \mathbf{a})$ como el vector al punto predicho que depende de los parámetros de la traza ($\boldsymbol{\tau}$) y de los parámetros de alineamiento ($\mathbf{a}$). Entonces, el vector de residuos puede ser definido como:

$$\mathbf{r} = (\mathbf{m} - \mathbf{e}(\boldsymbol{\tau}, \mathbf{a})) \tag{6.8}$$

Además, se pueden definir dos tipos distintos de residuos:

- Residuos *biased*: el residuo de cada hit se calcula usando la traza ajustada con todos los hits disponibles. Estos residuos se utilizan básicamente para reconstrucción de trazas y alineamiento.

- Residuos *unbiased*: el residuo se calcula con el ajuste de la traza ajustada excluyendo el hit bajo estudio. Esto significa que para calcular cada residuo de los hits de una traza, la traza tiene que ser reconstruida tantas veces como hits bajo estudio. Estos residuos se usan principalmente para monitorización.

Como se ha dicho anteriormente, el principal objetivo del alineamiento es determinar la posición y orientación de cada elemento del detector. Como la posición real de los modelos no es la misma que la posición aparente, la determinación de la situación actual de cada elemento es necesaria. Cada estructura alienable tienes seis grados de libertad. Estos corresponden a tres traslaciones (T_x, T_y, T_z) y tres rotaciones (R_x, R_y, R_z) que determinan la posición y orientación de la estructura. Las diferentes estructuras alineables pueden ser definidas de diversas formas, como un módulo de silicio, un hilo del TRT, una capa o disco completo o incluso un sub-detector entero. El alineamiento se puede realizar utilizando diferentes combinaciones de las estructuras alineables anteriormente mencionadas. Las configuraciones más importantes son llamadas niveles. Estos niveles se definen como:

- Nivel 1: El pixel se considera como una única estructura, el barril y los *end-caps* del SCT y TRT se consideran como estructuras independientes.
- Nivel 2: El pixel y SCT se separan en capas y discos. El TRT se separa en módulos en el barril y ruedas en los *end-caps*.
- Nivel 3: Los módulos del pixel y de SCT y los hilos de TRT se consideran como estructuras alineables.

Se pueden definir otras diferentes sub-estructuras y se pueden combinar para definir nuevos niveles.

6.3.1 Algoritmo de alineamiento

Varios algoritmos basados en trazas se han implementado para ATLAS a lo largo del tiempo. Los finalmente utilizados son los métodos Globalχ^2 y Localχ^2. Ambos se basan en la minimizaron de una función χ^2 construida a partir de los residuos. El Localχ^2 se puede considerar un caso particular del caso Globalχ^2. La función χ^2 se define de forma vectorial como:

$$\chi^2 = \sum_{\text{tracks}} \mathbf{r}^T V^{-1} \mathbf{r} \tag{6.9}$$

donde $\mathbf{r}$ es un vector definido para cada traza con todos los residuos que el sistema puede proporcionar y V una matriz de covariancia construida con las incertidumbres de las medidas. Podemos definir el vector $\mathbf{a}$ como un vector con todos los parámetros de alineamiento que describen la geometría del sistema. Entonces, la minimización del χ^2 con respecto a los parámetros de alineamiento resulta:

$$\frac{d\chi^2}{d\mathbf{a}} = 0 \tag{6.10}$$

Combinando las ecuaciones anteriores llegamos a la ecuación:

$$\sum_{\text{tracks}} \left(\frac{d\mathbf{r}}{d\mathbf{a}} \right)^T V^{-1} \mathbf{r} = 0 \tag{6.11}$$

El objetivo es encontrar la corrección de los parámetros de alineamiento $\delta\mathbf{a}$ que satisfaga esta ecuación. Para ello se calcula la derivada total de $\mathbf{r}$ respecto a $\mathbf{a}$:

$$\sum_{\text{tracks}} \left(\frac{d\mathbf{r}}{d\mathbf{a}}\right)^T V^{-1}\mathbf{r} = \sum_{\text{tracks}} \left(\frac{\partial\mathbf{r}}{\partial\boldsymbol{\tau}}\frac{d\boldsymbol{\tau}}{d\mathbf{a}} + \frac{\partial\mathbf{r}}{\partial\mathbf{a}}\right)^T V^{-1}\mathbf{r} = 0 \tag{6.12}$$

es necesario pues computar la derivada $d\boldsymbol{\tau}/d\mathbf{a}$. Para ello es necesario volver a ajustar las trazas para ver la dependencia de los parámetros de las trazas en función de los parámetros de alineamiento. Finalmente se obtiene:

$$\frac{d\boldsymbol{\tau}}{d\mathbf{a}} = -\mathcal{M}_t^{-1}E^T V^{-1}\left.\frac{\partial\mathbf{r}}{\partial\mathbf{a}}\right|_{\boldsymbol{\tau}=\boldsymbol{\tau}_0} \tag{6.13}$$

donde:

$$\begin{aligned} E &\equiv \left.\frac{\partial\mathbf{r}}{\partial\boldsymbol{\tau}}\right|_{\boldsymbol{\tau}=\boldsymbol{\tau}_0} \\ \mathcal{M}_t &\equiv E^T V^{-1} E \end{aligned} \tag{6.14}$$

Siendo E una matriz de dimensión $N_{\text{Res}}\times N_{\text{Trk}}$ y $\mathcal{M}_t$ una matriz de dimensión $N_{\text{Trk}}\times N_{\text{Trk}}$. Después de determinar los parámetros de la traza, su error y correlaciones pueden ser estimadas por la matriz:

$$\mathcal{C} = \mathcal{M}_t^{-1} = (E^T V^{-1} E)^{-1} \tag{6.15}$$

Las correcciones a los parámetros de la traza calculados anteriormente son usados para encontrar los parámetros de alineamiento minimizando χ^2. Con esto se obtiene la ecuación que nos da la solución para los parámetros de alineamiento:

$$\delta\mathbf{a} = -\mathcal{M}^{-1}v \tag{6.16}$$

donde

$$\begin{aligned} \mathcal{M} &= \left[\sum_{\text{tracks}} \left(\frac{\partial\mathbf{r}}{\partial\mathbf{a}}\right)^T (I - \mathcal{G}_E^T) V^{-1} \left(\frac{\partial\mathbf{r}}{\partial\mathbf{a}}\right)\right] \\ v &= \sum_{\text{tracks}} \left(\frac{\partial\mathbf{r}}{\partial\mathbf{a}}\right)^T (I - \mathcal{G}_E^T) V^{-1}\mathbf{r} \\ \mathcal{G}_E &= E\mathcal{M}_t^{-1}E^T V^{-1} \end{aligned} \tag{6.17}$$

con esta función podemos calcular las nuevas constantes de alineamiento finales ya que $\mathbf{r} = \mathbf{r}(\boldsymbol{\tau}_0, \mathbf{a}_0) + \left.\frac{\partial\mathbf{r}}{\partial\mathbf{a}}\right|_{\mathbf{a}=\mathbf{a}_0} \delta\mathbf{a}$. Este método puede ser aplicado iterativamente repitiendo este procedimiento tantas veces como sea necesario.

La determinación de una solución del alineamiento involucra dos pasos:

- Llenar la matriz y vector de alineamiento ($\mathcal{M}$ y v) a partir de todas las trazas reconstruidas consideradas.
- Resolver el sistema de ecuaciones lineales.

El tamaño de la matriz de alineamiento puede variar en varios ordenes de magnitud. Al alinear grandes estructuras como barriles y/o *end-caps* se consideran unas decenas de grados de libertad, mientras que en el caso de alinear todos los módulos se pueden llegar a miles. En el caso del método Globalχ^2, esta matriz es normalmente muy densa, ya que el método correlaciona las estructuras que participan en la reconstrucción de una misma traza.

Una forma practica de hacer que la matriz de alineamiento sea poco densa es realizando un alineamiento con Localχ^2. En este caso la correlación entre estructuras alineables es descartada y las trazas no son reajustadas. Así que, con este método, cada estructura es alineada localmente con respecto a las otras. El punto principal de este método es que la matriz de alineamiento se convierte en una matriz diagonal a bloques 6×6, con lo que este método es menos exigente en recursos de computación. Por otra parte, la correlación entre estructuras se tiene que recuperar con iteraciones sucesivas, por lo que más iteraciones son necesarias para alcanzar la convergencia.

La solución calculada anteriormente para las constantes de alineamiento no contienen restricciones externas impuestas en la solución. Este tipo de restricciones pueden introducirse en el algoritmo de dos formas diferentes: términos extra en la función χ^2 o con diferentes dependencias para los residuos y multiplicadores de Lagrange.

Estas restricciones se pueden aplicar en forma de restricciones a los parámetros de las trazas por parámetros externos. Se puede utilizar información del *truth* del Monte Carlo (MC) para testar en datos simulados. También se puede usar información del Beam Spot (BS) para restringir los valores de los parámetros de impacto. Incluso se puede utilizar información de los calorímetros para constreñir el momento de las partículas. Algunas muestras físicas pueden ser utilizadas para restringir los parámetros de las trazas gracias a sus observables, como por ejemplo las resonancias del bosón Z.

Además de restricciones a los parámetros de las trazas, también se pueden aplicar a las constantes de alineamiento. Se pueden utilizar medidas realizadas durante el montaje del detector y así limitar el tamaño de las correcciones de alineamiento.

6.3.2 Sistemáticos del alineamiento

El algoritmo de alineamiento es capaz de producir una descripción del detector que proporciona un ajuste de trazas eficiente y de buena calidad. Pero es difícil garantizar que la reconstrucción de los parámetros de las trazas esta libre de sesgos sistemáticos. Es posible encontrar descripciones de la geometría que satisfacen el modelo de trazas asumido pero que llevan a medidas físicas sesgadas. Es lo que se llaman *weak modes* del alineamiento ya que corresponden a modos casi singulares de la solución al problema del alineamiento. Los *weak modes* se pueden definir también como deformaciones de la geometría en las cuales los residuos o el χ^2 del ajuste permanecen invariables. Estos modos pueden aparecer debido a deformaciones del detector real o como artefactos del procedimiento del alineamiento. Los parámetros de las trazas para los cuales es más fácil introducir distorsiones significantes y por lo tanto, tienen más influencia en las medidas físicas son el momento y el parámetro de impacto. Los *weak modes* no pueden ser identificados solamente estudiando la calidad de los ajustes individuales de las trazas. Para ello es necesaria información o medidas adicionales que son dependientes de los parámetros de las trazas. Un ejemplo de estos observables es proporcionado por la masa

invariante de partículas conocidas (p. ej. $Z \to \mu^+\mu^-$, $J/\psi \to \mu^+\mu^-$, $K_S^0 \to \mu^+\mu^-$). Además se puede utilizar el calorímetro electromagnético de ATLAS para proporcionar una medida independiente de la energía de los electrones. A continuación se describen los distintos tipos de sistemáticos que pueden aparecer:

- Deformaciones antisimetricas en carga. Estas deformaciones consisten en movimientos del detector ortogonales a la trayectoria de las trazas que afectan a la curvatura de las trazas de forma opuesta para partículas positivas y negativas.
- Deformaciones simétricas en carga. Un ejemplo de estas deformaciones viene dado por distorsiones radiales. Estas distorsiones afectan el momento medido debido a una expansión o contracción de la trayectoria.
- Orientación del campo magnético. Es un caso especial de distorsión radial que se origina debido al desalineamiento relativo con respecto a la dirección del campo solenoidal.
- Sesgo en el parámetro transversal de impacto. Este sesgo puede aparecer debido a varias deformaciones de la geometría del detector y puede ser asociado con sesgos de otros parámetros de las trazas.

6.4 Rendimiento del alineamiento del detector interno de trazas

6.4.1 Alineamiento inicial con rayos cósmicos

Desde 2008, antes de que los primeros haces circulasen por el LHC, el detector estaba listo y tomando datos. Estos datos provenían de rayos cósmicos y con ellos se realizaron muchas pruebas para comprobar el estado del sistema. También se utilizaron estos datos para realizar el primer alineamiento del detector interno. El invierno del 2008, se registraron más de 200 millones de eventos de rayos cósmicos. Fueron reconstruidos y procesados durante este periodo con diferentes configuraciones del detector e imanes. Casi 7 millones de eventos fueron registrados en el detector interno, con casi 240 mil trazas atravesando el detector pixel. Estos datos fueron utilizados para realizar el primer alineamiento del sistema. En la figura 6.8 se muestra la mejora en los residuales en el barril pixel. Se muestran las distribuciones con la geometría nominal y con la geometría alineada. Para comparar, se muestra también la distribución utilizando un MC con una geometría perfecta. En la figura 6.9 se muestran las mismas distribuciones pero para el SCT. Se puede ver una gran mejora de las distribuciones de los residuos.

En verano del año 2009 otra toma de rayos cósmicos fue realizada. Se recogieron más de 90 millones de eventos. Estos eventos se utilizaron para mejorar el anterior alineamiento utilizando algunas implementaciones nuevas.

6.4.2 Alineamiento con colisiones a 900 GeV

Las primeras colisiones protón-protón registradas por ATLAS se produjeron el 23 de Noviembre durante la puesta en marcha del LHC. Las trazas se reconstruyeron con

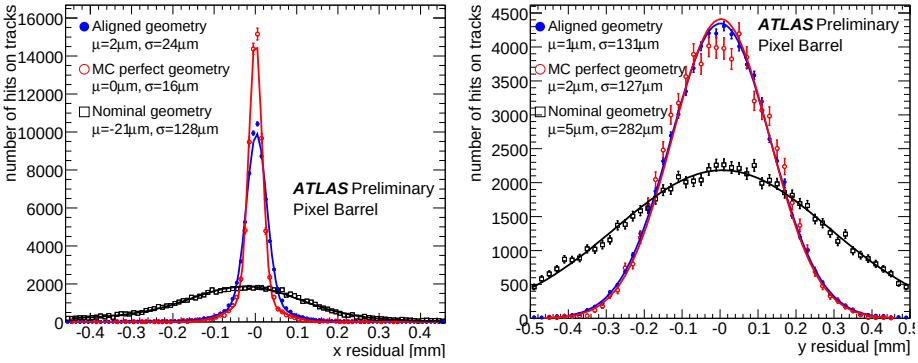

Figure 6.8: Distribuciones de residuos no sesgados en el barril del pixel mostrando la geometría nominal con medidas del Pixel, la geometría alineada y la geometría simulada perfecta (MC).

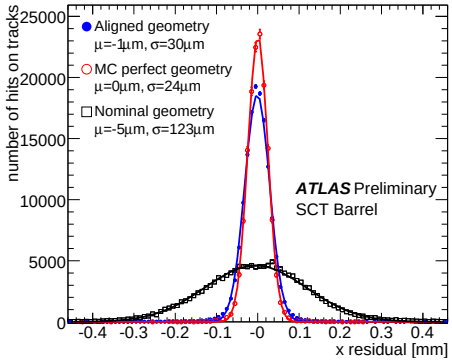

Figure 6.9: Distribuciones de residuos no sesgados en el barril del SCT mostrando la geometría nominal con medidas del Pixel, la geometría alineada y la geometría perfecta (MC).

las constantes obtenidas con los rayos cósmicos. El primer run permitió a ATLAS a registrar casi 1 millón de colisiones a 900 GeV. Estas colisiones se utilizaron para mejorar el alineamiento y calibración de los diferentes sub-detectores de ATLAS. Al final, un nuevo conjunto de constantes de alineamiento fueron obtenidas. El objetivo de este alineamiento era principalmente corregir los end-caps, ya que los rayos cósmicos no los correlaciona entre ellos. Estas constantes serán referidas posteriormente como *Spring 2010 Alignment*.

6.4.3 Alineamiento con colisiones a 7 TeV

El 30 de Marzo del año 2010, ATLAS registró colisiones con una energía en el centro de masas de 7 TeV por primera vez. Durante ese año y el siguiente, el LHC operó a esta energía y ATLAS registró unos 4.5 fb^{-1}. Estos datos además de rayos cósmicos fueron utilizados para el alineamiento, utilizando como geometría inicial las constantes obtenidas con los datos a 900 GeV (*Spring Alignment*). En esta campaña se volvió a alinear todo el detector otra vez, alineando tanto a nivel de estructuras como a nivel de módulos e hilos del TRT. Este alineamiento será referido como *Autumn Alignment*.

6.4.4 Comparación de resultados

En este apartado se mostrará la mejora del alineamiento con datos a 7 TeV respecto al alineamiento anterior. La muestra de datos se reconstruyó con las constantes *Autumn 2010 Alignment* y *Spring 2010 Alignment* para su comparación. En la figura 6.10 se muestran las distribuciones de los residuos para el Pixel, SCT y TRT.

En esta comparación, se observa que las distribuciones con las constantes *Autumn 2010 Alignment* son más estrechas debido a la mejora en general de la resolución del hit en los módulos. Ésta mejora se debe al alineamiento a nivel de módulo realizado.

En la figura 6.11 se muestran figuras comparando los residuos reconstruidos con la geometría *Autumn 2010 Alignment* y una muestra simulada MC con geometría perfecta. Bajo la suposición de que los modelos MC utilizados simulan perfectamente la resolución intrínseca de los hits y la contribución de la dispersión múltiple de Coulomb, la diferencia en la anchura observada de los residuos y la simulada puede ser relacionada directamente con la contribución del desalineamiento el los datos. En el caso de los *end-caps* del Pixel y del SCT y el barril TRT se puede ver que las dos distribuciones tienen una buena concordancia, implicando que la contribución debido a los desalineamientos es despreciable. En cambio, en el caso de los barriles del Pixel y SCT y en los end-capa del TRT se puede observar que los residuos observados son ligeramente más anchos que en la simulación debido a que aun existen pequeños desalineamientos que degradan la resolución.

6.4.5 Estudio de los efectos sistemáticos relacionados con el alineamiento

El bosón Z, con su desintegración a dos muones de carga opuesta, proporciona una clara señal y una poderosa herramienta para estudiar el rendimiento del detector y detectar efectos sistemáticos. Con una bien conocida resolución intrínseca, la resolución estimada de la masa invariante de los dos muones es una medida de los efectos del detector. Los muones provenientes del bosón Z suelen tener un alto p_T y son menos sensibles a los efectos sistemáticos. En la figura 6.12 se muestran las distribuciones de la masa invariable reconstruida del bosón Z para datos antes de corregir los efectos sistemáticos (*Release 16*) y datos perfectamente simulados (MC). La masa en datos se puede ver que es más ancha que el Monte Carlo para todas las regiones del detector.

Los efectos sistemáticos se detectan buscando cambios en la masa invariable en función de varias variables cinemáticas. Para corregir dichos efectos se utilizan var-

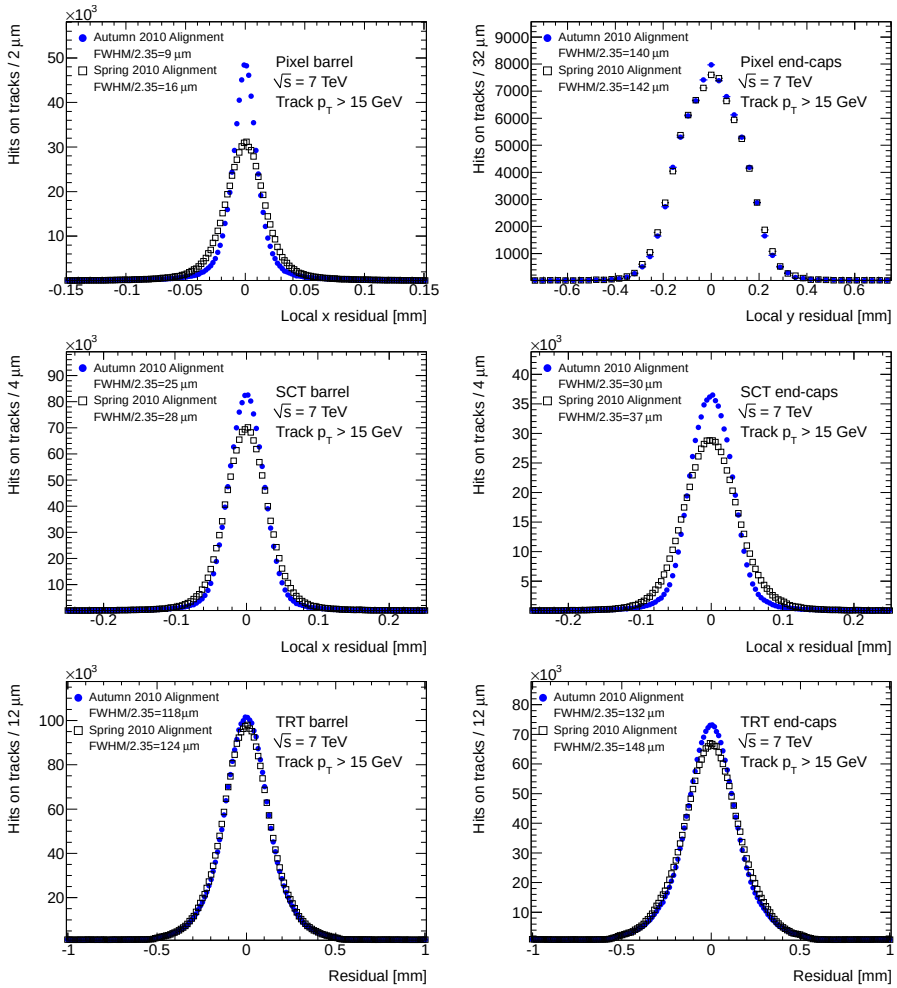

Figure 6.10: Distribuciones de residuos no sesgados obtenidos reconstruyendo la muestra *jet trigger* utilizando las constantes *Spring 2010 Alignment* (cuadrados vacíos) y *Autumn 2010 Alignment* (cuadrados sólidos). Las distribuciones se han integrado sobre todos los hits en las trazas en el barril y *end-caps* del Pixel (arriba), del SCT (centro) y del TRT (abajo).

ios cantidades físicas como restricciones al alineamiento. En concreto se uso la masa invariante de los dos muones en la desintegración del bosón Z y el E/p de los electrones. Esta última cantidad consiste en la razón entre la energía depositada medida en el calorímetro y el momento medido por el detector interno de los electrones. Tras utilizar estos métodos, se vuelven a mostrar en la figura 6.13 las distribuciones de masa del bosón Z con los datos después de aplicar las correcciones de alineamiento de carga

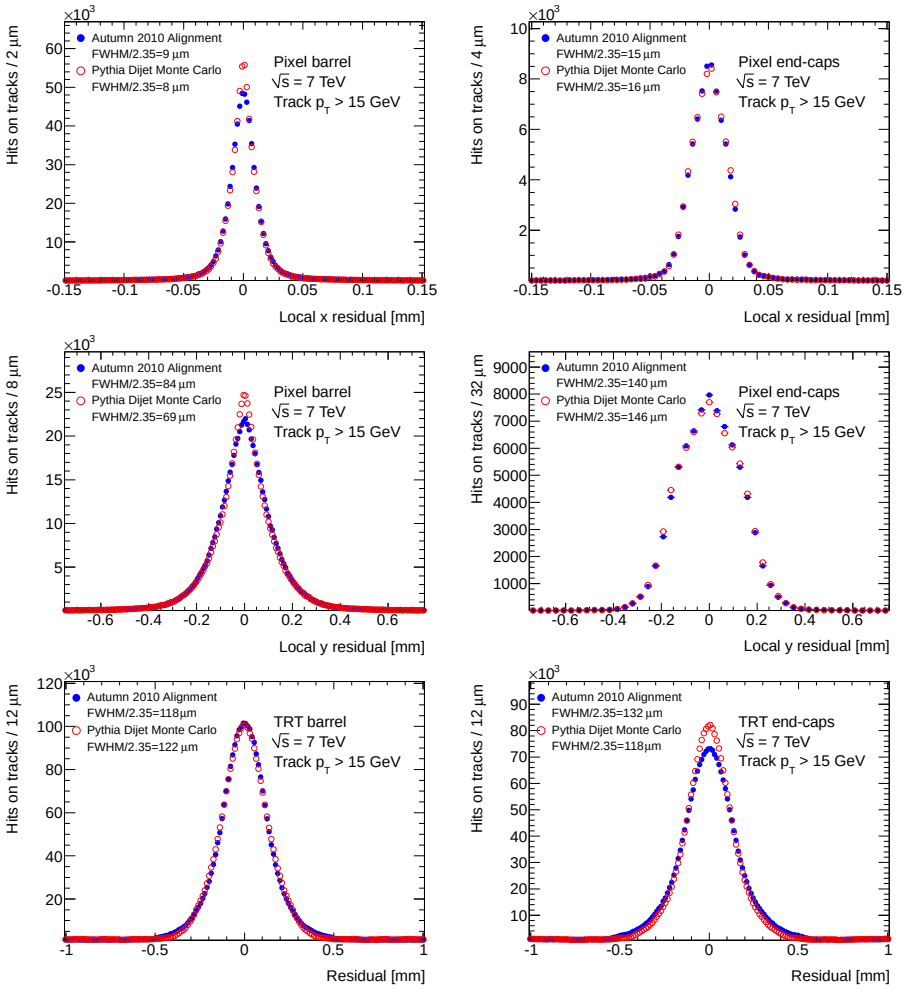

Figure 6.11: Distribuciones de residuos no sesgados obtenidos reconstruyendo la muestra *jet trigger* utilizando las constantes *Autumn 2010 Alignment* (círculos sólidos) comparados con la muestra simulada MC *dijet*. Las distribuciones se han integrado sobre todos los hits en las trazas en el barril y end-caps del Pixel (arriba), del SCT (centro) y del TRT (abajo).

antisimétrica (*Release 17*) comparados con los datos perfectamente simulados. Se observa que el acuerdo es mucho mejor que antes, aunque sigue sin ser perfecto. En todas las regiones, la resolución es ligeramente peor que la predicha por el MC.

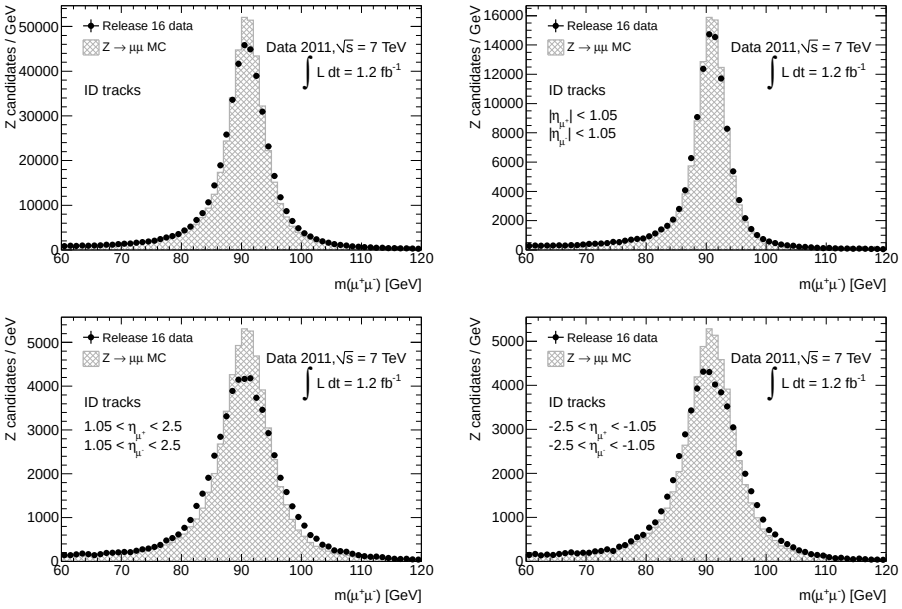

Figure 6.12: Distribuciones de la masa reconstruida del bosón Z mostrando datos antes de las correcciones de alineamiento de carga antisimétrica y un Monte Carlo perfectamente alineado para el todo el detector (arriba izquierda) cuando ambos muones están en el barril del detector (arriba derecha), cuando ambos muones están en el *end-cap* A (abajo izquierda) y cuando ambos muones están en el *end-cap* C (abajo derecha).

6.4.6 Alineamiento run a run.

Empezando con un conjunto fijo de constantes, un simple alineamiento a nivel de estructuras grandes (Pixel, barril y end-capa del SCT y TRT) se realizó para cada run de ATLAS para determinar si el detector se había movido significativamente entre runs. Los resultados obtenidos se monitorizan en una pagina web y si se observa un movimiento significativo, estas constantes son utilizadas para el procesado de los datos. Como ejemplo, en la figura 6.14 se muestra las correcciones en las traslaciones en el eje x respecto la geometría base durante el año 2012. Se puede ver que cambios en las condiciones del entorno pueden llevar a grandes movimientos del detector. Adicionalmente a estos movimientos se observan lentas desviaciones de los sub-detectores.

6.5 Medida de AFBT

En esta sección se presentará la determinación de g_{R} en el experimento ATLAS del LHC. El análisis está basado en la medida de una asimetría en la distribución angular del leptón cargado que proviene de la desintegración del bosón W en eventos single top en el canal de producción t.

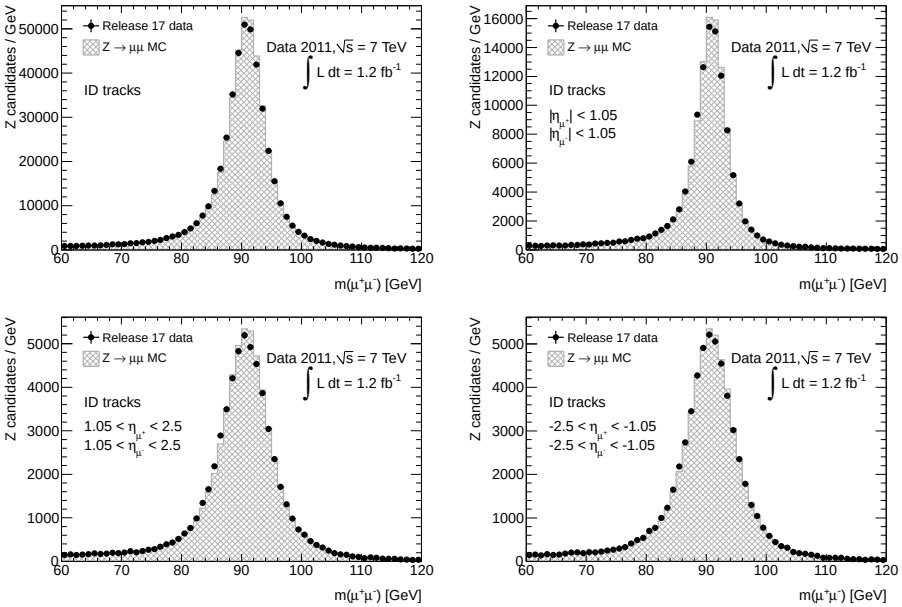

Figure 6.13: Distribuciones de la masa reconstruida del bosón Z mostrando datos con las correcciones de alineamiento de carga antisimétrica y un Monte Carlo perfectamente alineado para el todo el detector (arriba izquierda) cuando ambos muones están en el barril del detector (arriba derecha), cuando ambos muones están en el *end-cap* A (abajo izquierda) y cuando ambos muones están en el *end-cap* C (abajo derecha).

6.5.1 Datos y muestras simuladas

Los datos utilizados en este análisis provienen de las colisiones protón-protón proporcionada por el LHC con una energía en el centro de masas de 7 TeV. La muestra utilizada se filtró exigiendo que los eventos al menos un leptón. La cantidad de datos utilizados en este análisis corresponde a una luminosidad integrada de $4656 \pm 84\text{pb}^{-1}$. Las muestras simuladas de MC fueron producidas utilizando diferentes generadores de eventos conectados con varios generadores de cascadas de partones. Estas muestras se generaron dentro de la producción Montecarlo de ATLAS MC11c, que incluye mucho del conocimiento ganado con los datos de ATLAS recogidos en 2011 sobre alineamiento, distribución del material o eventos subyacentes y ajustes del *mínimum bias*. Los diferentes procesos se agrupan en las siguientes categorías:

- t-channel: el proceso de producción del quark top en el canal t, es decir, la señal a utilizar.
- s-channel, Wt-channel, y par de quarks top: procesos de fondo que incluyen la producción de quarks top.
- W + HF jets: producción de un bosón W real asociado con jets de sabor pesado.

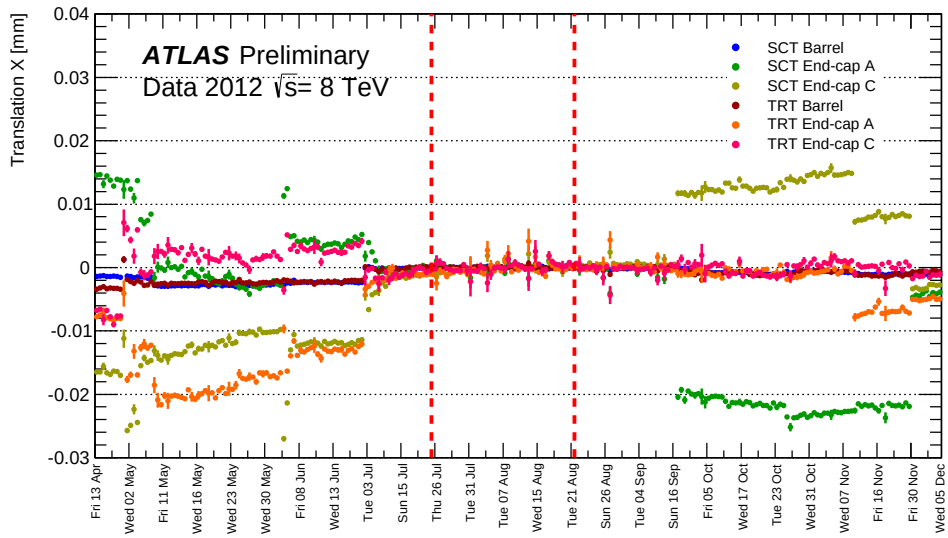

Figure 6.14: Correcciones a la posición X global (T_x) de todos los sub-detectores del detector interno durante 2012. Las lineas verticales indican los periodos en los cuales las constantes base fueron determinadas.

Las muestras simuladas agrupadas son $W + b\bar{b}$, $W + c\bar{c}$ y $W + c$.

- W + light jets: producción de un bosón W real asociado con quarks ligeros.
- Z + jets y dibosón: producción de un boron Z y producción del dibosón WW, ZZ y WZ.
- Multi-jet: eventos con varios jets donde uno de los jets se ha mal identificado como un leptón.

6.5.2 Definición de objetos y selección de eventos

La definición de todos los objetos físicos (electrón, muón, jet, energía faltante,...) sigue las recomendaciones dadas por el grupo de trabajo de la física del top de ATLAS [71]. La selección de eventos sigue la selección básica del grupo de física de la física del single top de ATLAS para la señal leptónica t-channel donde el leptón puede ser un electrón o un muón originado por la desintegración del bosón W. Esta selección aplica diferentes cortes de calidad y limpieza además de cortes derivados de la topología t-channel. Además de esta selección, denotada como pre-selección en este análisis, se aplican unos pocos cortes adicionales para rechazar eventos del fondo. En la pre-selección se aplican los siguientes cortes:

- Criterio de calidad del evento definido en el Good Run List (GRL).

- *Trigger* de un solo leptón.
- Un vértice primario con al menos cinco trazas.
- Al menos un jet bueno con $p_T > 20$ GeV
- Ninguna ráfaga de ruido en el calorímetro de argón líquido.
- Un leptón con $p_{\mathrm{T}} > 25$ GeV y $0 < |\eta| < 1.37$ o $1.52 < |\eta| < 2.47$ para electrones y $|\eta| < 2.5$ para muones.
- Exactamente dos jets buenos con $p_{\mathrm{T}} > 30$ GeV y $|\eta| < 4.5$.
- Una fracción de jet de vértice de más de 0.75.
- En la región donde $2.75 < |\eta| < 3.5$ el corte en p_T se aumenta hasta 35 GeV.
- Un jet marcado por el algoritmo JetFitterCOMBNNc en el punto de trabajo del 55% de eficiencia y con $|\eta| < 2.5$.
- Para rechazar eventos multi-jet se requiere un momento transverso perdido ($E_{\mathrm{T}}^{\mathrm{miss}} >$ 30 GeV) mayor de 30 GeV y una masa del W transversal reconstruida mayor de 30 GeV.
- Un corte adicional de aislamiento: $p_{\mathrm{T}}(\text{leptón}) > 40 \mp (40/\pi - 1)(\Delta\phi(\text{leading-jet}, \text{leptón}) \pm \pi)$.

En la figura 6.15 se muestra la comparación entre los datos y la distribución esperada de $E_{\mathrm{T}}^{\mathrm{miss}}$, $m_{\mathrm{T}}(W)$, η del jet ligero, $\Delta\eta$(jet ligero, jet b), masa del quark top reconstruido y H_{T} para el canal de los electrones en la pre-selección. En la figura 6.16 se muestran las distribuciones angulares en la dirección transversal para electrones y muones en la pre-selección. Se observa un buen acuerdo entre los datos y la predicción del MC.

Después de aplicar la pre-selección, se aplica una selección adicional para separar la señal del fondo. Esta selección consiste en:

- La $|\eta|$ del jet ligero tiene que ser mayor que 2.
- H_T[1] tiene que ser mayor que 210 GeV.
- La masa del quark top reconstruido tiene que estar en el intervalo de 150 GeV a 190 GeV.
- La distancia en η entre el jet ligero y el b-jet tiene que ser superior a 1.

La figura 6.17 muestra la comparación entre los datos y la distribución esperada de $E_{\mathrm{T}}^{\mathrm{miss}}$, $m_{\mathrm{T}}(W)$, η del jet ligero, $\Delta\eta$(jet ligero, jet b), masa del quark top reconstruido y H_{T} para el canal de los electrones para la selección. Adicionalmente, para este análisis, se seleccionan eventos con solo dos jets (*jet-bin*) y se requiere que uno de ellos este marcado como un jet b (*tagged*).

[1] $H_{\mathrm{T}} = p_{\mathrm{T}}(\text{leptón}) + p_{\mathrm{T}}(\text{jet ligero}) + p_{\mathrm{T}}(b\text{-jet}) + E_{\mathrm{T}}^{\mathrm{miss}}$

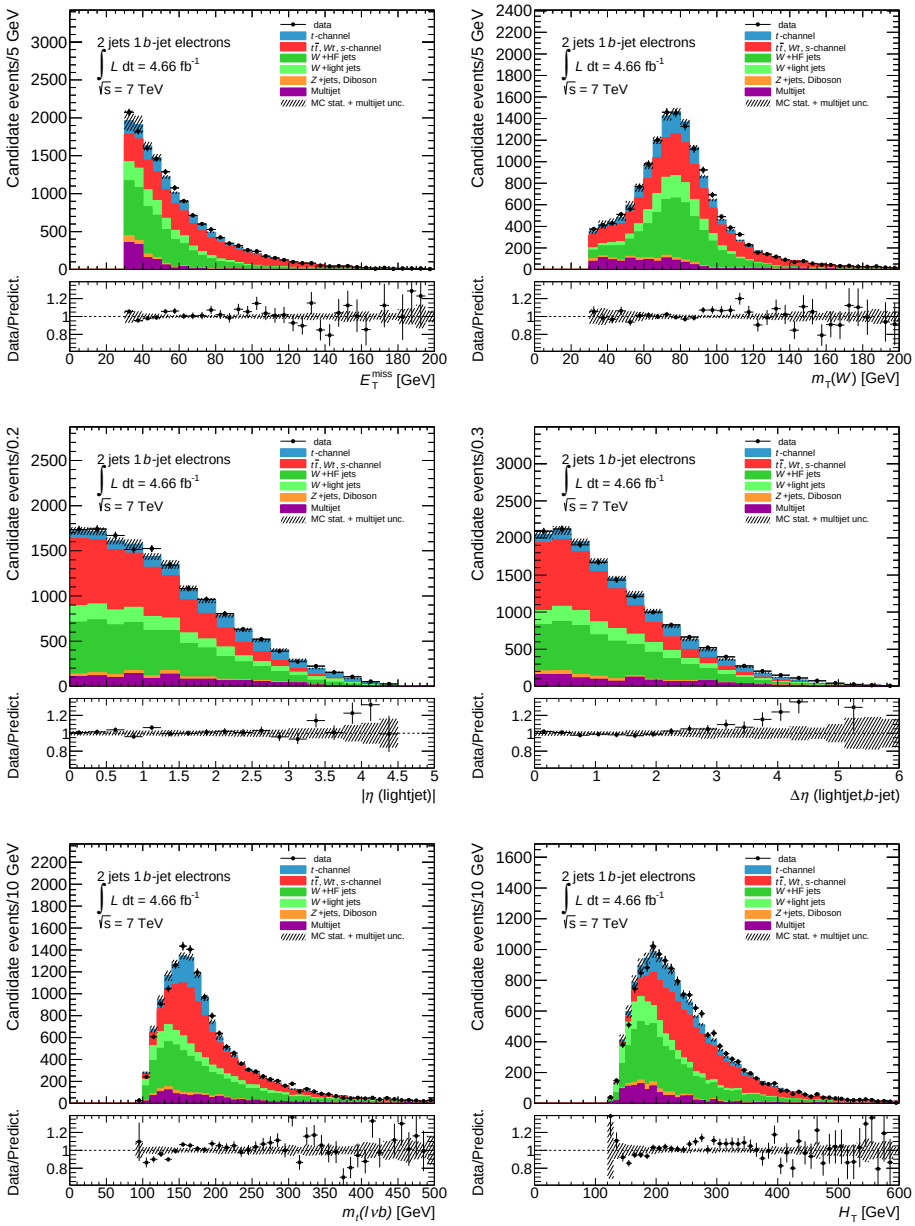

Figure 6.15: Comparación entre los datos y la distribución esperada de MC a nivel de pre-selección en el canal de los electrones. De arriba a la izquierda a abajo a la derecha: $E_{\mathrm{T}}^{\mathrm{miss}}$, $m_{\mathrm{T}}(W)$, η del jet ligero, $\Delta\eta$(jet ligero, jet b), masa del quark top reconstruido y H_{T}.

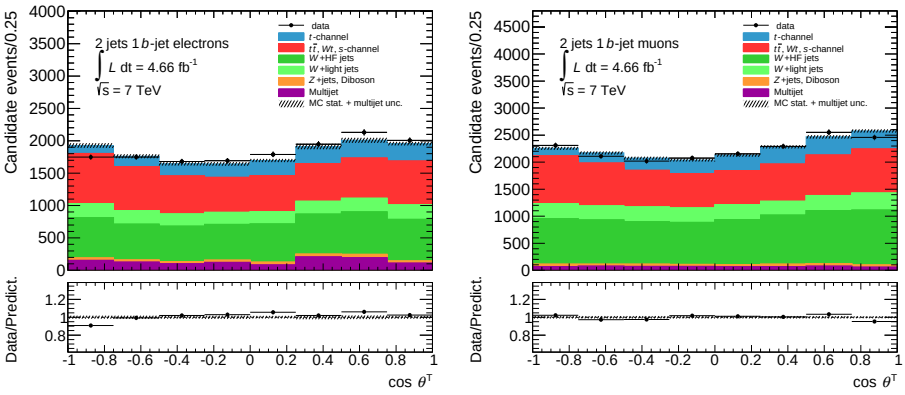

Figure 6.16: Distribuciones angulares en la dirección transversal a nivel de pre-selección para electrones (izquierda) y muones (derecha).

6.5.3 Estimación del fondo y producción de eventos.

El principal fondo del estado final del t-channel viene de la producción del bosón W asociado a jets, multi-jet o eventos QCD y pares de quarks top. Los fondos secundarios se originan de Z más jets, los canales Wt-channel y s-channel y la producción de di-bosones. Los fondos pequeños y los pares de quarks top están modelados usando simulaciones MC y normalizados a la correspondiente predicción teórica. Para multi-jet y W + jets, la normalización se obtiene a partir de los datos mientras que la forma se obtiene de muestras simuladas.

Los eventos multi-jet pueden pasar la selección de eventos si uno de los jets se identifica como un electrón o un muón. Aunque esta probabilidad es muy baja, debido a la larga producción de eventos multi-jet esta contribución es significante como fondo. Para estimar el fondo multi-jet se utilizan dos métodos:

- Para el canal de electrones se utiliza el método jet-electrón [77].
- Para el canal de muones se usa el método matriz [71].

La producción de bosones W junto con jets (ligeros o pesados) tiene una alta producción en el LHC. Los eventos W+jets con estados finales que incluyen leptones, jets y $E_{\mathrm{T}}^{\mathrm{miss}}$son importantes ya que son un fondo dominante en el canal del single top. Para este fondo, la forma de las distribuciones se obtiene de muestras simuladas. Las predicciones se multiplican for factores k para corregir las secciones eficaces con las predicciones NLO previstas por la teoría. Adicionalmente, se utilizan técnicas con datos reales para estimar las diferentes composiciones de sabores y la normalización total. Esto se realiza en una región de control dominada por eventos W+jets, con menos del 5% de contaminación de eventos de la señal.

En la tabla 6.4 se muestran los números de eventos en cada paso del análisis para los canales de electrones y muones en las muestras *tagged* (muestras con un jet identificado

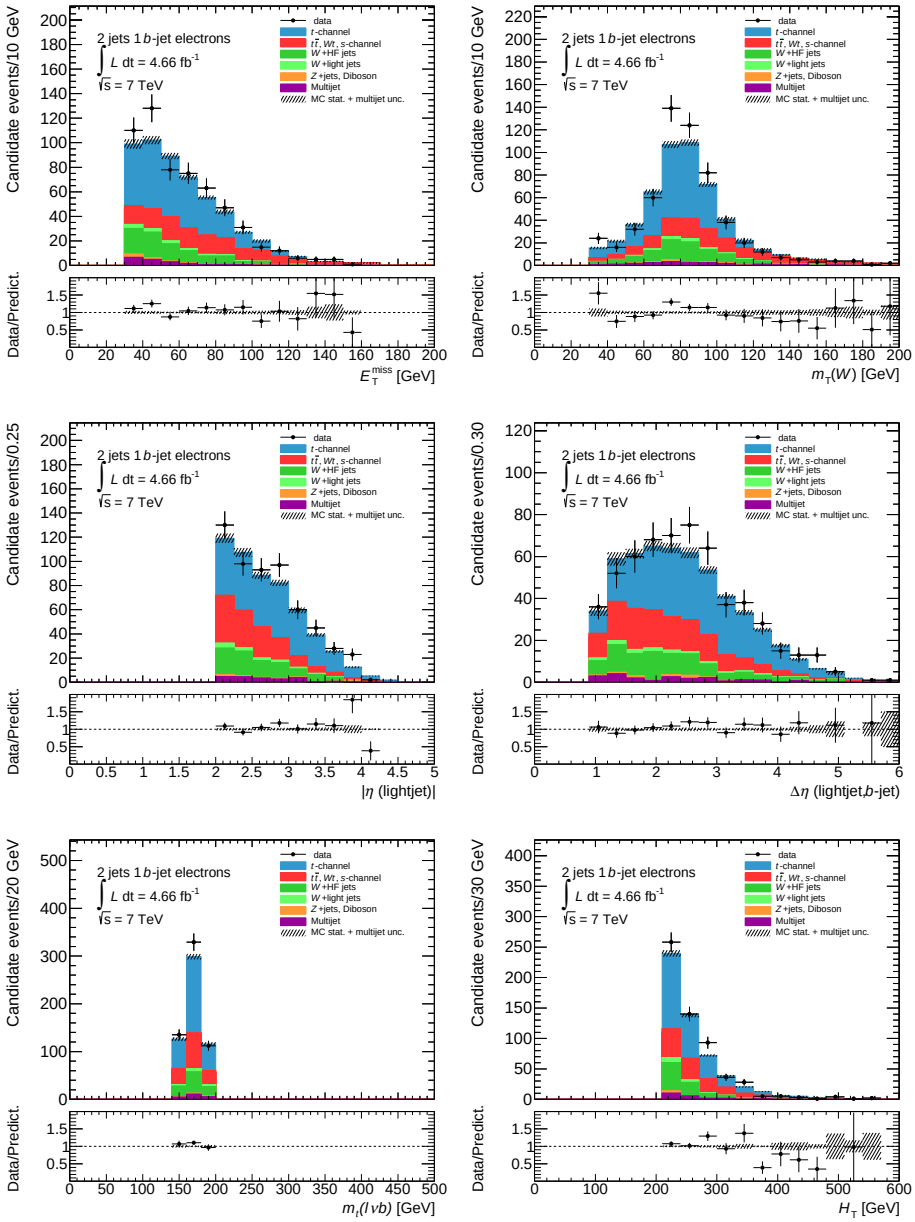

Figure 6.17: Comparación entre los datos y la distribución esperada de MC a nivel de pre-selección en el canal de los electrones. De arriba a la izquierda a abajo a la derecha: $E_{\mathrm{T}}^{\mathrm{miss}}$, $m_{\mathrm{T}}(W)$, η del jet ligero, $\Delta\eta$(jet ligero, jet b), masa del quark top reconstruido y H_{T}.

como proveniente de un *quark b*). Las incertidumbres corresponden a las incertidumbres estadísticas obtenidas a partir del tamaño de las muestras simuladas, mientras que para el multi-jet, estas incertidumbres vienen exclusivamente del método jet-electrón y el método matriz. Ambos canales muestran un buen acuerdo entre los datos y las predicciones.

	Electrón		Muón	
	Pre-selección	Selección	Pre-selección	Selección
t-channel	1717 ± 5	278 ± 2	2076 ± 6	341 ± 2
s-channel	117 ± 1	4 ± 0	151 ± 1	6 ± 0
Wt-channel	585 ± 7	13 ± 1	682 ± 8	16 ± 1
Par de quarks top	4320 ± 14	121 ± 2	5038 ± 15	149 ± 3
Dibosón	121 ± 2	1 ± 0	142 ± 2	2 ± 0
Z + jets	196 ± 9	4 ± 1	190 ± 7	3 ± 1
W + jets pesados	4773 ± 31	86 ± 4	6953 ± 37	109 ± 4
W + jets ligeros	1624 ± 28	15 ± 0	2215 ± 31	23 ± 3
Multijet	1090 ± 545	20 ± 10	550 ± 275	6 ± 3
Total esperado	14544 ± 640	541 ± 15	17997 ± 280	654 ± 7
S/B	0.13	0.95	0.13	0.96
Datos ATLAS	14738	576	17966	691

Table 6.4: Nímero de eventos para los canales de electrones y muones para la preselección y la selección con las muestras *tagged* (un jet b).

6.5.4 Medida de la asimetría adelante-atrás $A_{\mathbf{FB}}^{\mathbf{T}}$

Para calcular la parte real de la constante anomalía de acoplamiento g_{R} del vértice Wtb es necesario medir la asimetría $A_{\mathrm{FB}}^{\mathrm{T}}$ ya que es sensible a ella. La asimetría se calcula a partir de la distribución de $\cos\theta^{\mathrm{T}}$, donde θ^{T} es el ángulo entra la dirección transversa T y el leptón (en el sistema de referencia del W). En la figura 6.16 se puede ver dicha distribución angular al nivel de preselección donde se observa que las distribuciones están dominadas por eventos de fondo.

La figura 6.18 muestra las gráficas equivalentes en el nivel de selección. Se observa el realce de la señal sobre el fondo debido a los cortes adicionales de selección. Estas distribuciones serán las utilizadas para calcular la asimetría $A_{\mathrm{FB}}^{\mathrm{T}}$. Como esta asimetría se calcula contando los números de eventos hacia adelante en θ^{T} ($\cos\theta^{\mathrm{T}} > 0$) y hacia atrás ($\cos\theta^{\mathrm{T}} < 0$), se utilizan las distribuciones con dos bines. Estas distribuciones se muestran en la figura 6.19.

El ángulo θ^{T} se mide utilizando el momento reconstruido del leptón cargado y del bosón W, de modo que la forma de la distribución está convolucionada por los efectos de la reconstrucción del detector (resolución) y la selección. Antes de deducir la asimetría a partir de la figura 6.19, esta tiene que ser deconvolucionada de las distorsiones y llevada a nivel de partones.

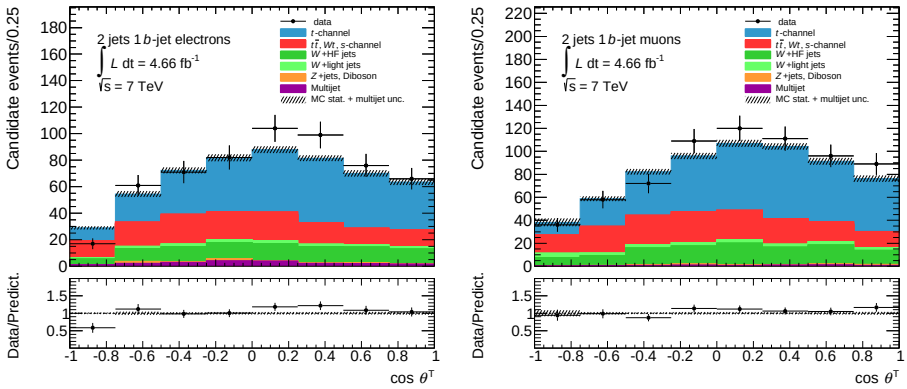

Figure 6.18: Distribuciones angulares en la dirección transversal a nivel de selección para electrones (izquierda) y muones (derecha).

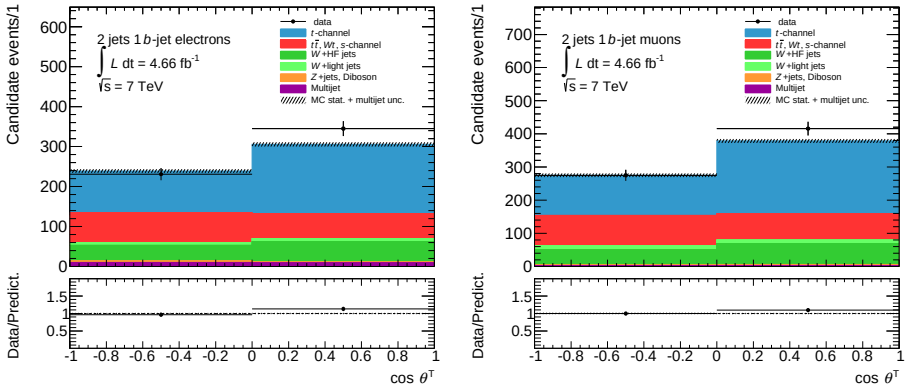

Figure 6.19: Distribuciones angulares con dos bines en la dirección transversal a nivel de selección para electrones (izquierda) y muones (derecha)

Para ello se utilizan simulaciones MC para modelar esos efectos y a continuación revertir esos efectos en los datos reales. El método de deconvolución se realiza utilizando un ajuste a los datos que permite recuperar la distribución de MC de la distribución θ^{T}. Los datos observados tienen que ser corregidos por la aceptancia, los efectos del detector y reconstrucción. Una vez hallada la función para deconvolucionar se realiza un ensayo para comprobar que este método es capaz de reproducir la distribución a novel de generación. Una vez que este procedimiento ha sido validado, se puede utilizar para deconvolucionar la distribución real con el fondo sustraído. Los valores de $A_{\mathrm{FB}}^{\mathrm{T}}$ se muestran en la tabla 6.5 antes y después de la sustracción del fondo y después de la deconvolución para la combinación de electrones y muones. En la figura 6.20 se muestran las diferentes distribuciones así como la comparación con el modelo estándar.

combinado	$A_{\mathrm{FB}}^{\mathrm{T}}$
Datos	0.201 ± 0.028 (data stat.)
Datos (fondo sustraído)	0.357 ± 0.051 (estad. datos) ± 0.015 (fondo MC estad.) = 0.375 ± 0.038 (estad. total)
Data deconv.	0.495 ± 0.090 (estad. datos) ± 0.030 (estad. fondo MC) ± 0.013 (estad. señal MC) = 0.495 ± 0.071 (estad. total)

Table 6.5: Medida de $A_{\mathrm{FB}}^{\mathrm{T}}$ para eventos con dos jets en el canal combinado. Solo se muestran las incertidumbres estadísticas.

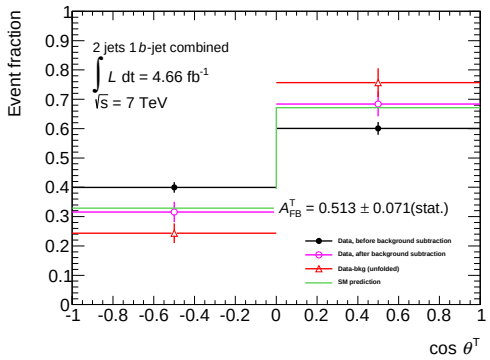

Figure 6.20: Distribuciones angulares deconvolucionadas para la combinación de los canales de los electrones y muones. Las incertidumbres son solo estadísticas.

6.5.5 Incertidumbres sistemáticas.

Hay múltiples efectos sistemáticos que pueden tener un impacto en la medida de $A_{\mathrm{FB}}^{\mathrm{T}}$. Los efectos sistemáticos considerados son los siguientes:

- Factores de escala del *trigger* de leptones, reconstrucción y eficiencia de identificación.
- Momento, escala de energía y resolución de los leptones.
- Escala de energía de los jets.
- Resolución de energía de los jets.
- Eficiencia de reconstrucción de los jets.
- Factores de escala y eficiencia de *b-tagging*.
- Factores de escala del JVF.
- Medida de la $E_{\mathrm{T}}^{\mathrm{miss}}$.
- Apilado e la $E_{\mathrm{T}}^{\mathrm{miss}}$.

- Normalización y forma del fondo de multi-jet.
- Normalización y forma del fondo W+jets.
- Sección eficaz teórica.
- Estados de radiación inicial y final.
- Generador MC.
- Funciones de distribución de los partones.
- Método de deconvolución.
- Luminosidad.

Para calcular las diferentes incertidumbres sistemáticas de $A_{\rm FB}^{\rm T}$, se hace variar la distribución angular $\cos\theta^{\rm T}$ para cada fuente de incertidumbre. El impacto de esas incertidumbres en la asimetría se evalúa utilizando 15 mil pseudo-experimentos. En casa pseudo-experimento, la medida se repite con una muestra simulada utilizando la misma estadística que en la muestra original. La diferencia de la asimetría estimada con y sin variación se toma como la incertidumbre sistemática.

6.5.6 Resultados

El valor final de la asimetría $A_{\rm FB}^{\rm T}$ con sus errores estadísticos y sistemáticos se muestran en la tabla 6.6 para los canales combinados. Se encuentra que los resultados son consistentes con la predicción del modelo estándar ($A_{\rm FB}^{\rm T} = 0.341$) dentro de las incertidumbres totales.

combinado	$A_{\rm FB}^{\rm T}$
Datos (raw)	0.201 ± 0.028 (stat.)
Datos (fondo sustraído)	0.357 ± 0.038 (estad.)
Datos deconv.	0.513 ± 0.088 (estad.) ± 0.115 (sist.)

Table 6.6: Medida de $A_{\rm FB}^{\rm T}$ para eventos con dos jets para el canal combinado. Ambas incertidumbres estadísticas y sistemáticas se muestran para el resultado deconvolucionado.

Appendices

Appendix A

Reconstruction of the top quark

Unlike the reconstruction of the top quarks in $t\bar{t}$ events, in events from the single top quark t-channel there is only one possibility to combine the final physics objects to obtain the top quark. Nevertheless, the reconstruction of the leptonic W boson decay poses a difficult challenge which comes from the kinematics of the neutrino. This is because the neutrino escapes undetected and even if the lepton can be accurately reconstructed from the associated cluster energy and the track direction, the kinematics of the W boson decay is in principle not fully defined. In order to find a solution to this dilemma, the most common assumption for single top quark events is that the $E_{\mathrm{T}}^{\mathrm{miss}}$ of the event corresponds to the transverse momentum of the undetected neutrino (i.e. as the neutrino is massless, $E_{\mathrm{T}}^{\mathrm{miss}} \equiv p_{\mathrm{T}}^{\nu}$). Although it is true that the neutrino is the main contributor to the $E_{\mathrm{T}}^{\mathrm{miss}}$ at LO, there are more contributors, such as extra neutrinos (from B hadron and τ decays), additional p_{T} contributions (ISR/FSR effects, etc), miscalibration of $E_{\mathrm{T}}^{\mathrm{miss}}$, fake missing $E_{\mathrm{T}}^{\mathrm{miss}}$ due to the detector energy resolution and acceptance, etc. Ignoring these additional contributions mean that for the full reconstruction of single top quark events the only decision to be taken is in the solution of the longitudinal momentum of the neutrino, p_z^{ν}, which is derived from the missing energy and using the constraint of the W boson mass when calculating the invariant mass of the lepton and the neutrino.

A.1 Determination of the longitudinal momentum of the neutrino

The four-momentum conservation law for the leptonic W boson decay (i.e. $W \to \ell\nu$, standing ℓ for a lepton) gives the following expression:

$$(p^W)^2 = (p^\ell + p^\nu)^2 \quad \to \quad m_W^2 = m_\ell^2 + 2(E^\ell, \vec{p}^{\,\ell})(E^\nu, \vec{p}^{\,\nu}) = m_\ell^2 + 2(E^\ell E^\nu - \vec{p}^{\,\ell}\cdot\vec{p}^{\,\nu}) \ , \quad \text{(A.1)}$$

where the neutrino mass has been neglected ($m_\nu = 0$). Now, using the hypothesis that

transverse energy in the center of mass of the collision is equal to zero, then the $E_{\mathrm{T}}^{\mathrm{miss}}$ in the detector can be approximated as due just to the neutrino, i.e. $E_{\mathrm{T}}^{\mathrm{miss}} = p_{\mathrm{T}}^{\nu}$. Following with the kinematics, the neutrino energy can be expressed as:

$$(E^{\nu})^2 = (p_x^{\nu})^2 + (p_y^{\nu})^2 + (p_z^{\nu})^2 = (p_{\mathrm{T}}^{\nu})^2 + (p_z^{\nu})^2 \ ,$$

$$E^{\nu} = \sqrt{(E_{\mathrm{T}}^{\mathrm{miss}})^2 + (p_z^{\nu})^2} \ ,$$

and its transverse momentum components are given by:

$$p_x^{\nu} = E_{\mathrm{T}}^{\mathrm{miss}} \cos\phi_{\ E_{\mathrm{T}}^{\mathrm{miss}}} \quad \text{and} \quad p_y^{\nu} = E_{\mathrm{T}}^{\mathrm{miss}} \sin\phi_{\ E_{\mathrm{T}}^{\mathrm{miss}}} \ ,$$

therefore the m_W^2 from expression A.1 becomes:

$$m_W^2 = m_\ell^2 + 2E^\ell E^\nu - 2\left(p_x^\ell p_x^\nu + p_y^\ell p_y^\nu + p_z^\ell p_z^\nu\right) =$$

$$= m_\ell^2 + 2E^\ell\sqrt{(E_{\mathrm{T}}^{\mathrm{miss}})^2 + (p_z^\nu)^2} - 2\left(E_{\mathrm{T}}^{\mathrm{miss}}(p_x^\ell \cos\phi_{\ E_{\mathrm{T}}^{\mathrm{miss}}} + p_y^\ell \sin\phi_{\ E_{\mathrm{T}}^{\mathrm{miss}}}) + p_z^\ell p_z^\nu\right) \ . \quad \text{(A.2)}$$

Since the neutrino stems from an on-shell W boson, one can use the pole-mass of 80.399 ± 0.023 GeV [86] as a reference mass value for m_W, and therefore the only unknown quantity left in Equation A.2 is the neutrino longitudinal momentum (p_z^ν). Working out p_z^ν from formula A.2 a quadratic expression is found:

$$a(p_z^\nu)^2 + bp_z^\nu + c = 0 \quad \rightarrow \quad \begin{cases} a = (E^\ell)^2 - (p_z^\ell)^2 \ . \\ b = p_z^\ell\left(-m_W^2 + m_\ell^2 - 2(p_x^\ell p_x^\nu + p_y^\ell p_y^\nu)\right) \ . \\ c = (E^\ell)^2(E_{\mathrm{T}}^{\mathrm{miss}})^2 - \frac{1}{4}\left(m_W^2 - m_\ell^2 + 2(p_x^\ell p_x^\nu + p_y^\ell p_y^\nu)\right)^2 \ . \end{cases}$$

Being the solutions:

$$p_z^\nu = \frac{-p_z^\ell\left(-m_W^2 + m_\ell^2 - 2(p_x^\ell p_x^\nu + p_y^\ell p_y^\nu)\right)}{2\left((E^\ell)^2 - (p_z^\ell)^2\right)} \pm \sqrt{\Delta} \ , \quad \text{(A.3)}$$

being Δ the discriminant defined as:

$$\Delta \equiv (E^\ell)^2\left[\left(m_W^2 - m_\ell^2 + 2(p_x^\ell p_x^\nu + p_y^\ell p_y^\nu)\right)^2 + 4(E_{\mathrm{T}}^{\mathrm{miss}})^2(-(E^\ell)^2 + \left(p_z^\ell\right)^2)\right] \ .$$

If the two solutions are real, the solution giving the smallest magnitude of the longitudinal neutrino momentum is taken. There are cases where $\Delta < 0$. This is due to the fact that assumption that the neutrino is the only contributor to the $E_{\mathrm{T}}^{\mathrm{miss}}$ is not valid and therefore p_z^ν is overestimated. If that happens, there are several options to solve the problem:

- If a complex solution is found one could claim that this solution is unphysical, assume $\Delta = 0$ and then choose the single p_z^ν value.

- Another solution is decreasing the $E_{\mathrm{T}}^{\mathrm{miss}}$ (i.e. p_{T}^{ν}) step by step until a real pair of solutions is found. This decreasing can be done within the $E_{\mathrm{T}}^{\mathrm{miss}}$ resolution using the MC information as done in Ref. [87] or using the restriction that $m_{\mathrm{T}}(W)$ has to remain below 90 GeV [88].

- Finally, another option is finding for which values of the $E_{\mathrm{T}}^{\mathrm{miss}}$ the Δ term becomes positive. By doing so, one just scales $E_{\mathrm{T}}^{\mathrm{miss}}$ but preserves its direction $(\cos\phi\ _{E_{\mathrm{T}}^{\mathrm{miss}}}, \sin\phi\ _{E_{\mathrm{T}}^{\mathrm{miss}}})$. To do this one can solve the discriminant equation (i.e. $\Delta = 0$) in terms of $E_{\mathrm{T}}^{\mathrm{miss}}$, and denoted as $E_{\mathrm{T}}^{\mathrm{miss}\prime}$. Of course, two solutions will be obtained from this equation as follows:

$$E_{\mathrm{T}}^{\mathrm{miss}\prime} = \frac{-(-m_W^2+m_\ell^2)(p_x^\ell\cos\phi\ _{E_{\mathrm{T}}^{\mathrm{miss}}}+p_y^\ell\sin\phi\ _{E_{\mathrm{T}}^{\mathrm{miss}}})\pm(-m_W^2+m_\ell^2)\sqrt{(E^\ell)^2-(p_z^\ell)^2}}{2\left[(E^\ell)^2-(p_z^\ell)^2-(p_x^\ell\cos\phi\ _{E_{\mathrm{T}}^{\mathrm{miss}}}+p_y^\ell\sin\phi\ _{E_{\mathrm{T}}^{\mathrm{miss}}})^2\right]}\ .$$

  If just one solution is positive, this is the one which is chosen. If the two solutions are positive, the one closer to the initial $E_{\mathrm{T}}^{\mathrm{miss}}$ is chosen. Once this new $E_{\mathrm{T}}^{\mathrm{miss}\prime}$ is calculated it is increased by few eV in order to have $\Delta > 0$ and it is used in Equation A.3 to finally compute the p_z^ν solutions. The selected solution is done following the previous criterion (lowest $|p_z^\nu|$ value).

  In this thesis, this option is used to compute the longitudinal momentum of the neutrino.

A.2 Top quark mass reconstruction

Once the neutrino four-momentum is fully determined, the W boson four-momentum can be reconstructed. Obviously, the leptonic W boson mass reconstructed using the p_z^ν solution of these methods is a Dirac delta distribution, i.e. exactly the W boson pole-mass, as one is computing the neutrino four-momentum which gives this reference mass for the given lepton, event by event. This is completely artificial as it is well known that the W boson has a given lifetime (its decay width is in fact $\Gamma_W = 2.085 \pm 0.042$ GeV [86]) but this result is consistent with the proposed approximation made in this section. Finally the top quark is fully reconstructed from the sum of the four-vectors of the W boson and the selected b-tagged jet.

Appendix B

Control Plots

B.1 Control Plots for the signal region

This section shows all the control plots considered to ensure a good comparison between data and prediction at *pre-selection* and *selection* level in the tagged sample. Figures B.1-B.2 show the angular distributions at *pre-selection* level for electron and muon channels in the tagged sample. Figures B.3-B.4 show the p_T and η of the lepton, the light jet and the b-jet for the electron and muon channels also at *pre-selection* level in the tagged sample. Finally, the shape comparison of the kinematic variables used to define the *selection* cuts for the signal and the main backgrounds (W+jets and top quark pair) are shown in Figure B.5.

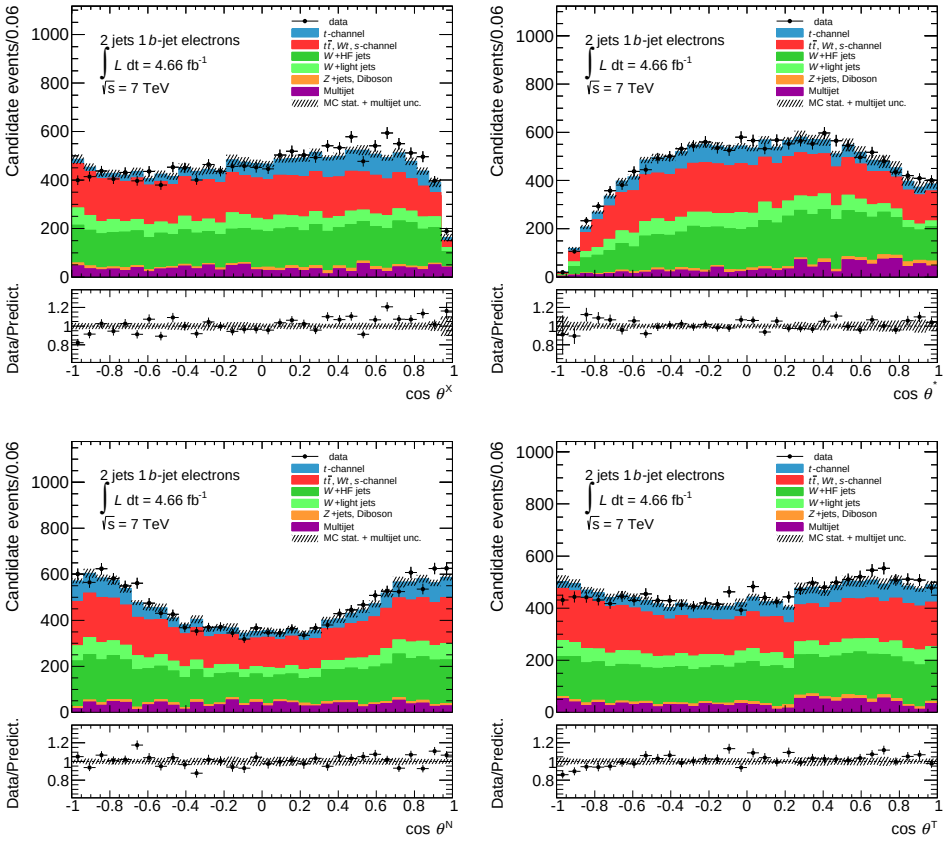

Figure B.1: Angular distributions at *pre-selection* level for electron channel in the tagged sample.

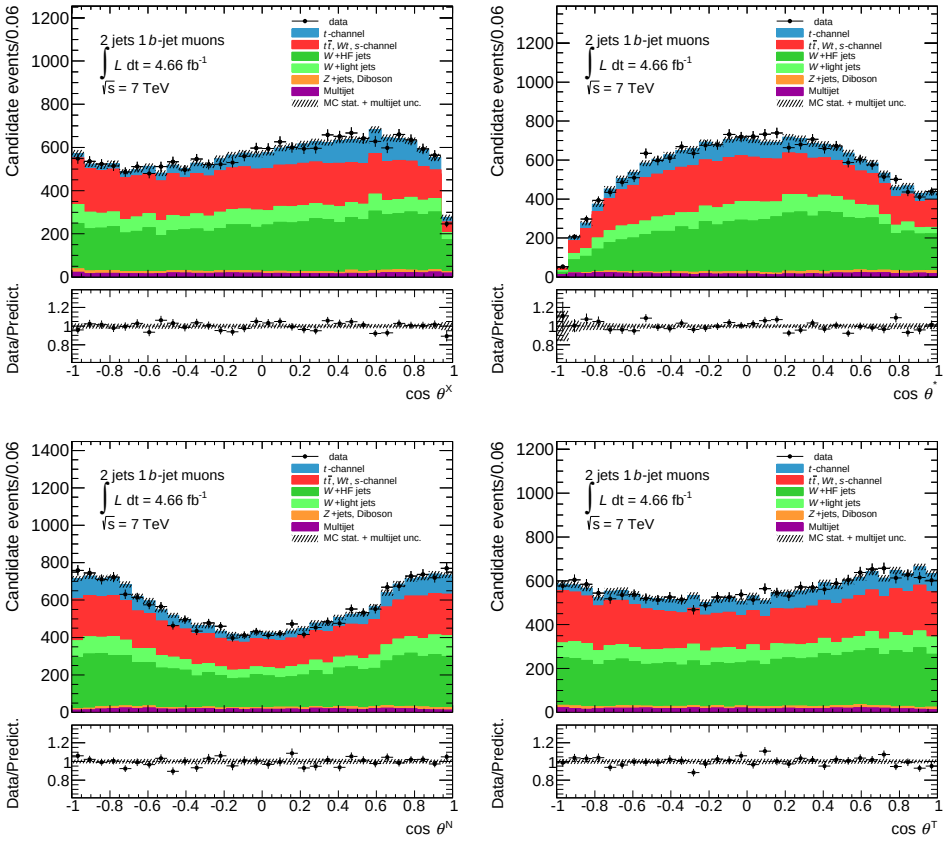

Figure B.2: Angular distributions at *pre-selection* level for muon channel in the tagged sample.

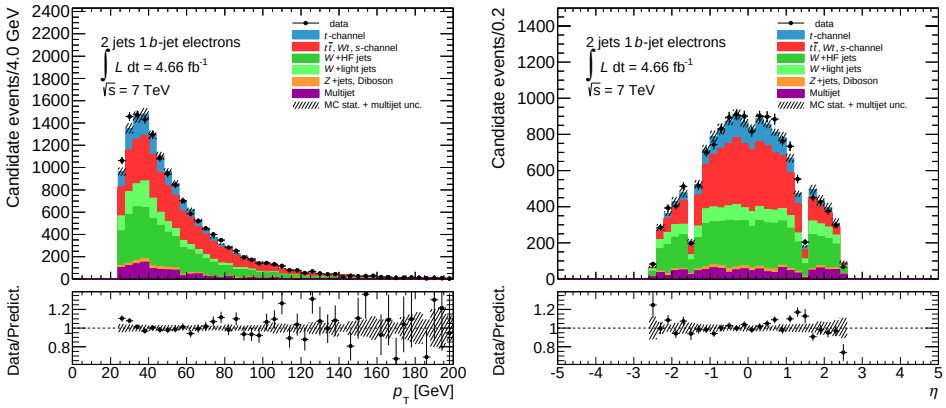

(a) lepton

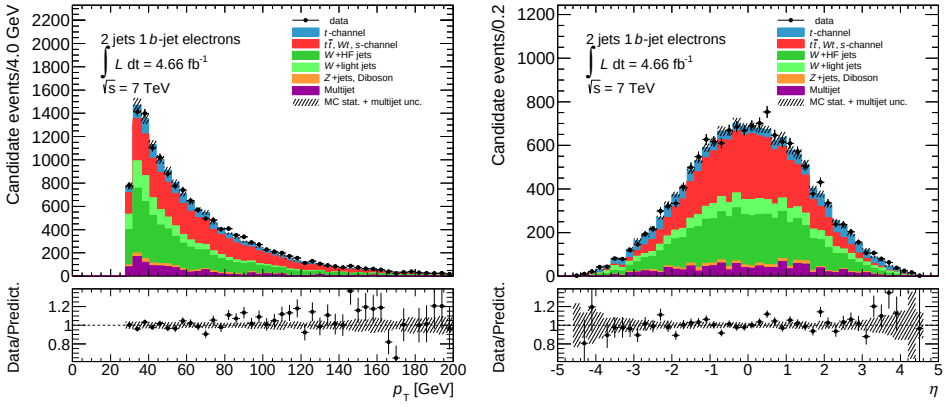

(b) light jet

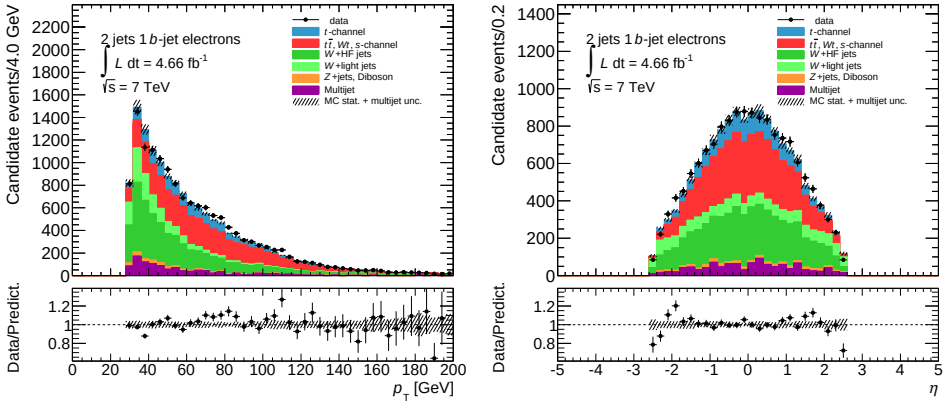

(c) b-jet

Figure B.3: Kinematic distributions p_T (left) and η (right) of final objects for the electron channel at *pre-selection* level in the tagged sample.

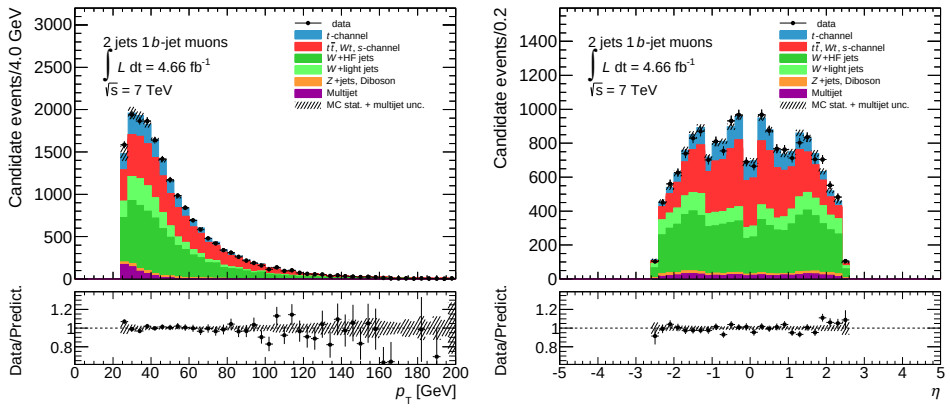

(a) lepton

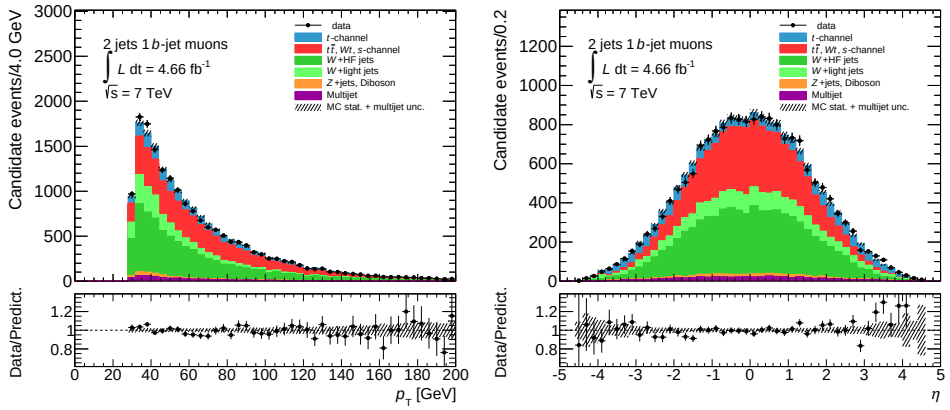

(b) light jet

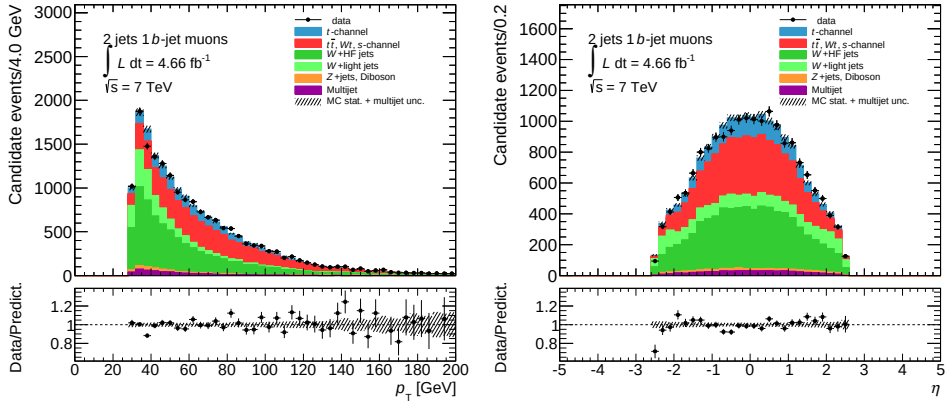

(c) b-jet

Figure B.4: Kinematic distributions p_T (left) and η (right) of final objects for the muon channel at *pre-selection* level in the tagged sample.

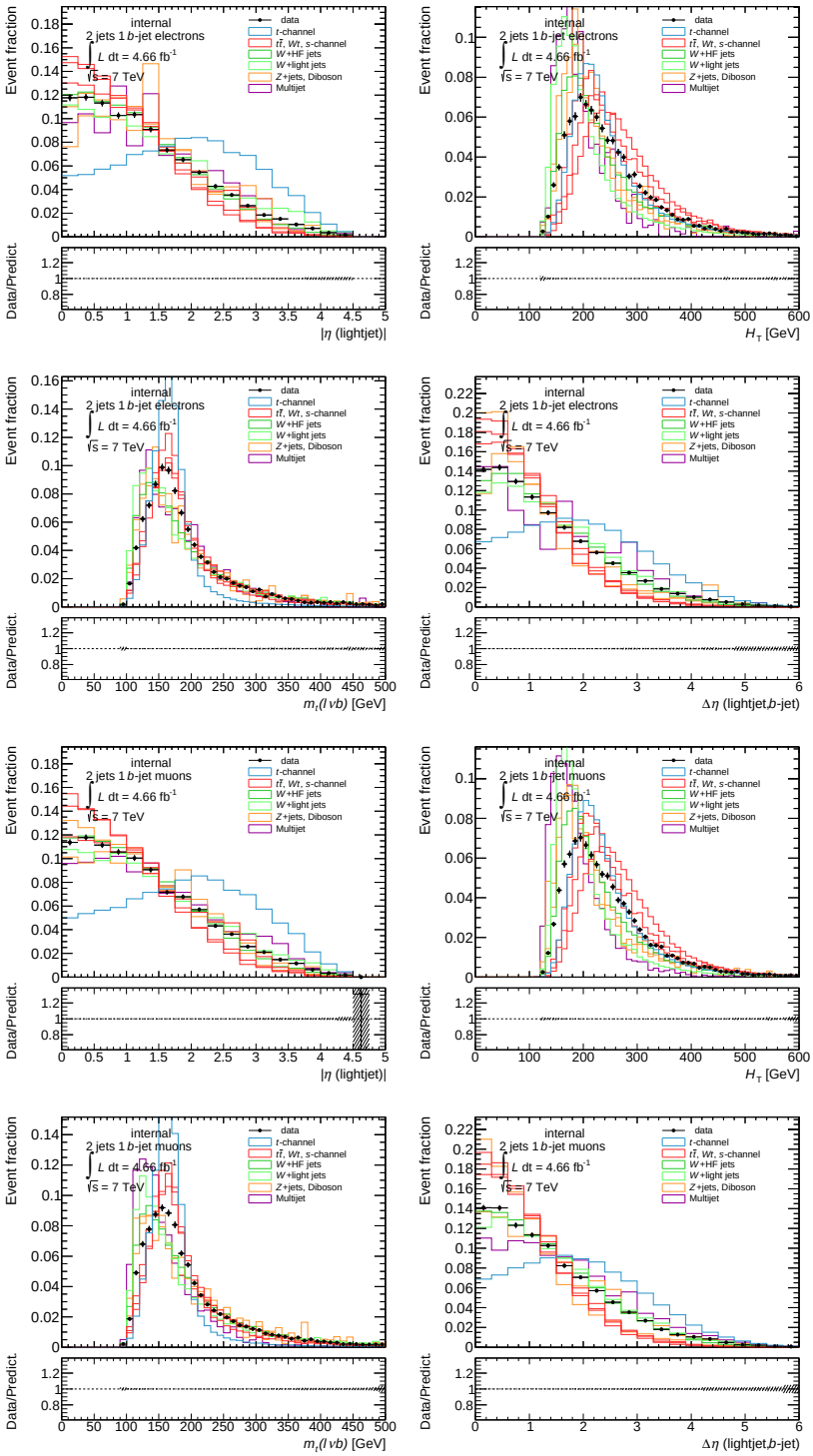

Figure B.5: Shape comparison of the kinematic variables used to define the *selection* cuts for the signal and the main backgrounds (W+jets and top quark pair). From top left to bottom right: η of the light jet (i.e. spectator quark), $\Delta\eta$(light-jet, b-jet), mass of the reconstructed top quark and H_{T} for the electron (top) and muon (bottom) channels.

B.2 Control Plots for the top quark pair control region

This section shows the control plots in the top quark pair (i.e. $t\bar{t}$) control region considered to ensure a good comparison between data and prediction. Figures B.6-B.7 show the different angular distributions including the one used to measure the helicity fraction in the normal direction for the electron and the muon channels. Uncertainties on the prediction are statistical only and for multijet include the 50% normalisation uncertainty.

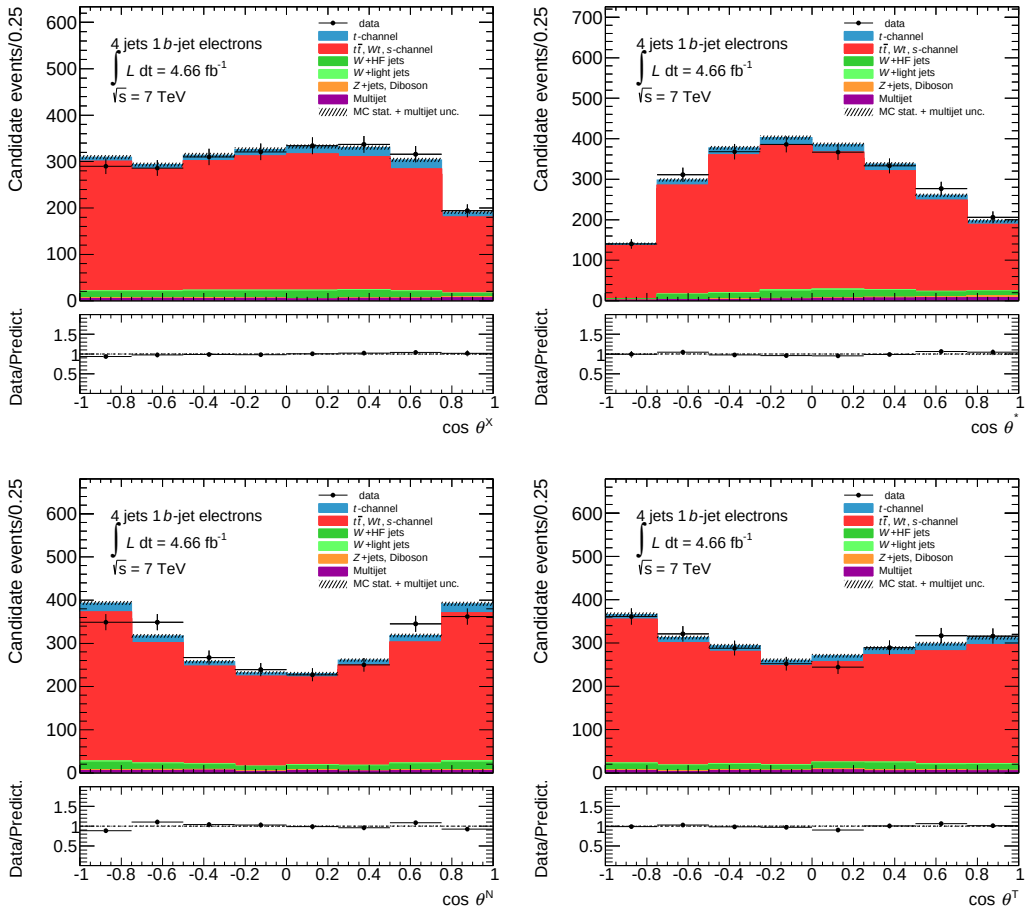

Figure B.6: Angular distributions in the top quark pair enriched region in the electron channel in the tagged sample with exactly four jets.

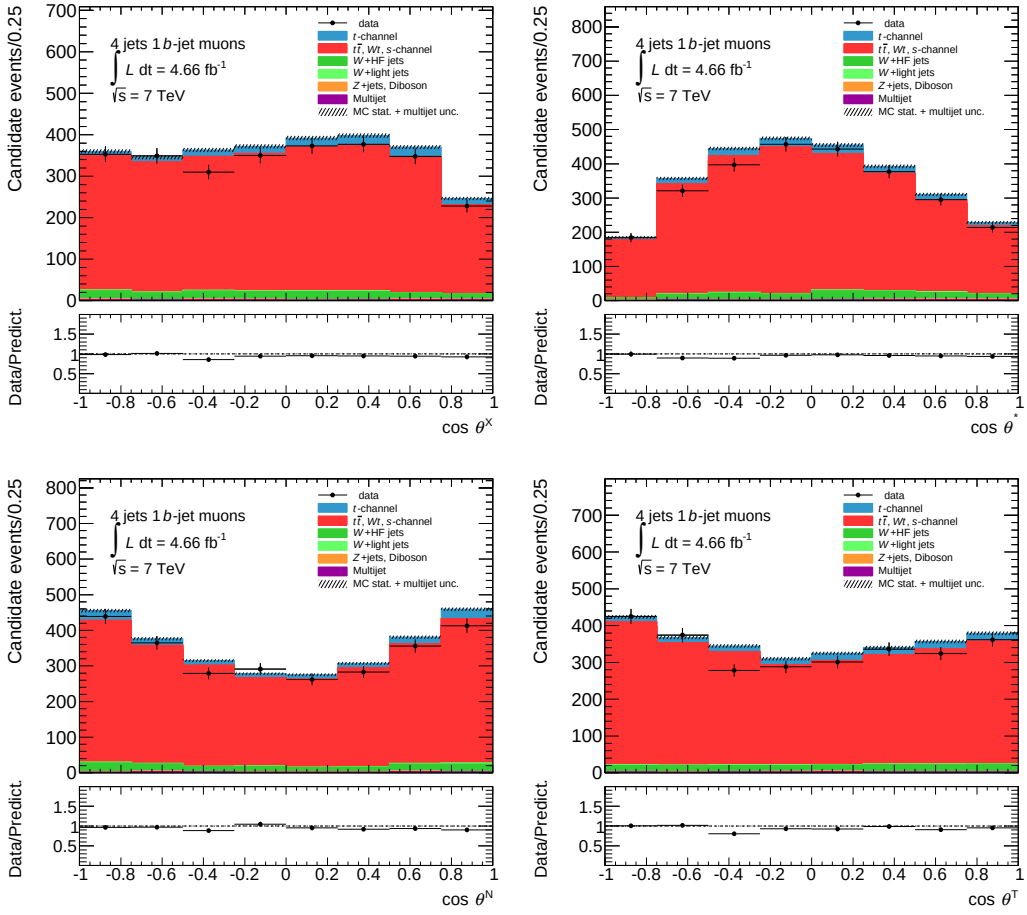

Figure B.7: Angular distributions in the top quark pair enriched region in the muon channel in the tagged sample with exactly four jets.

B.3 Control Plots for the W+jets control region

This section shows all the control plots in the W+jets control region considered to ensure a good comparison between data and prediction. Figures B.8-B.9 show the different angular distributions including the one used to measure the helicity fraction in the normal direction. Good agreement is observed between data and prediction. Uncertainties on the prediction are statistical only and for QCD-multijet include the 50% normalisation uncertainty.

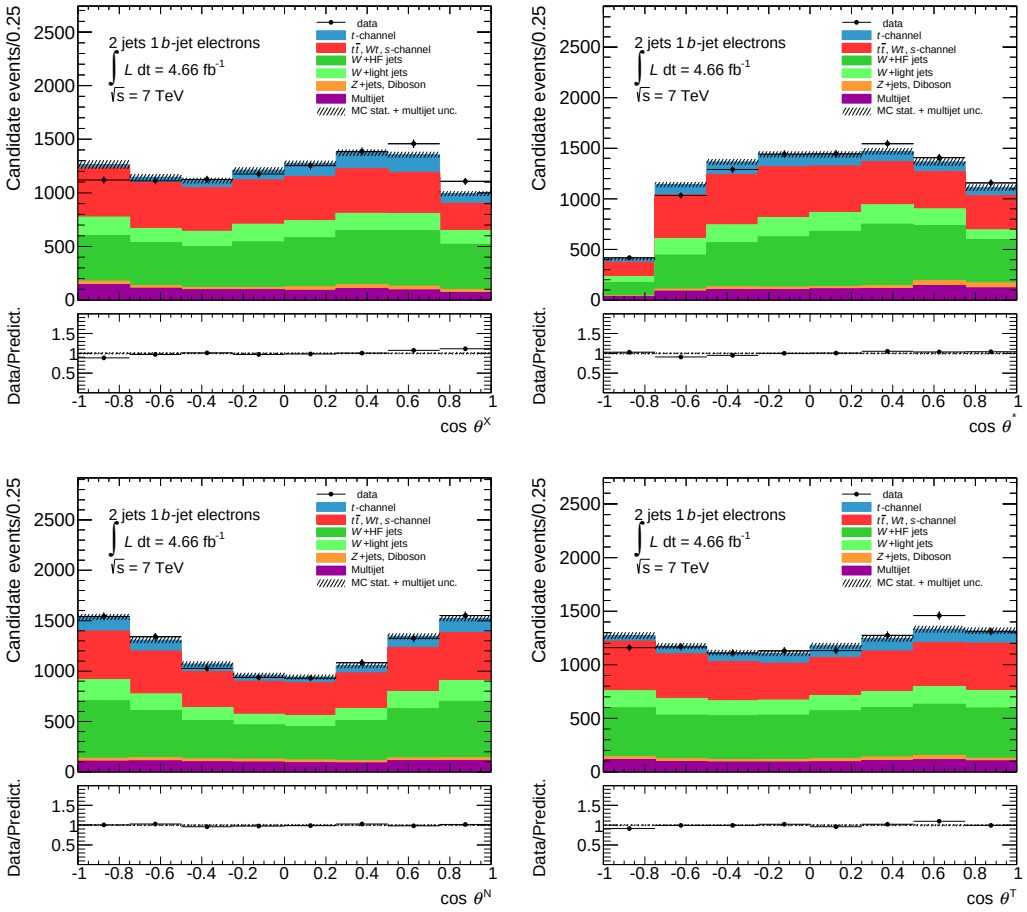

Figure B.8: Angular distributions in the W+jets enriched region in the electron channel in the tagged sample with exactly two jets.

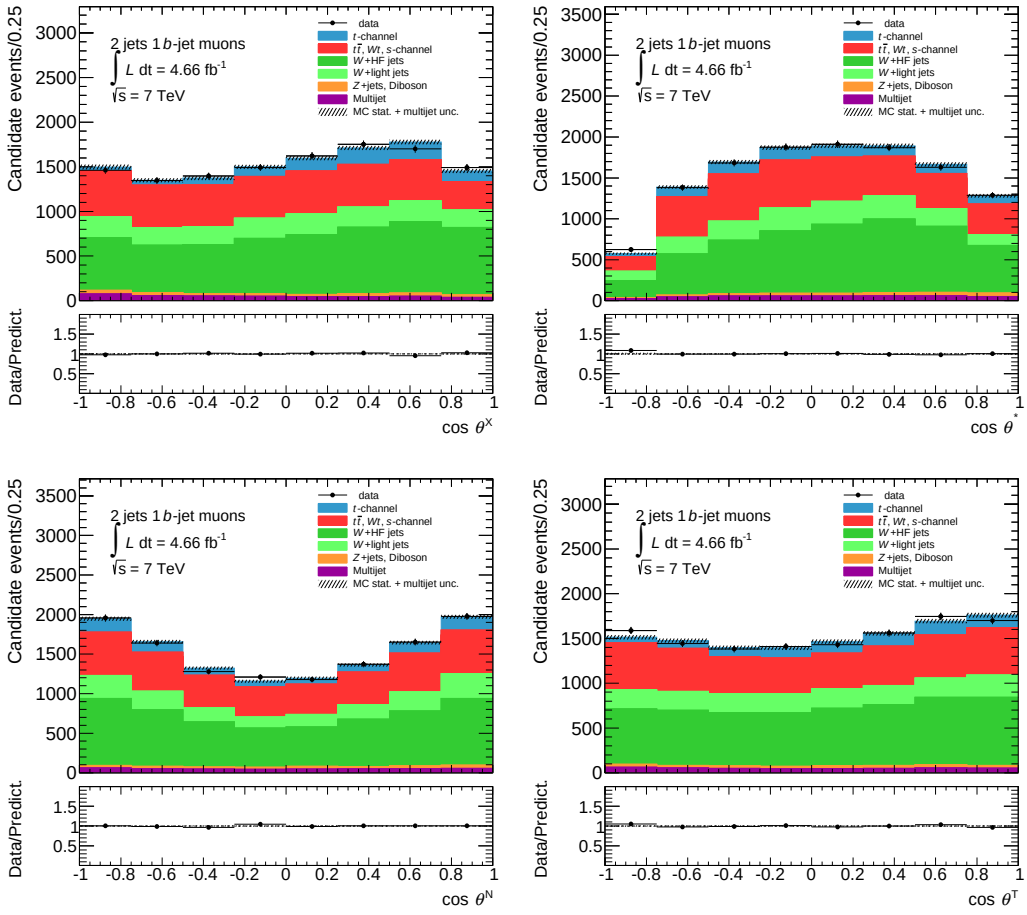

Figure B.9: Angular distributions in the W+jets enriched region in the muon channel in the tagged sample with exactly two jets.

Appendix C

Estimation of the W+jets flavour composition

The method assumes that W+jets contribution is the result of subtracting electroweak (WW, WZ, ZZ, and $Z + jets$), top quark (top quark pair and single top) and QCD-multijet background processes from the data events. An overall normalisation scale factor (denoted by SF) for the W+jets sample is obtained for each jet bin using:

$$\frac{N_{W+jets,Data}}{N_{W+jets,MC}} = \frac{N_{data} - N_{EWK} - N_{top} - N_{QCD}}{N_{W+jets,MC}} \tag{C.1}$$

A single scale factor is derived for each flavour of W+jets events. Both $W+b\overline{b}$ and $W+c\overline{c}$ scale factors are considered the same. These flavour scale factors are extracted using the 1-jet and 2-jet bins of the PreTagged and Tagged data sample. A series of equations can be written using these off-signal regions which can then be solved for the desired scale factors. The number of data events after background subtraction ($N_{data\text{-}bkg}$) is a function of the jet flavour fractions ($F_b b$, F_{cc}, F_c and F_{light}) for different jet bins, and different Tagged samples. For PreTagged events with 1 and 2 jet in the final state, the number of events after background subtraction, $N_{data-bkg}$, is given by:

$$N^{pretag}_{data\text{-}bkg,1} = N^{pretag}_{data\text{-}bkg,1}\left(F^{pretag}_{bb,1} + F^{pretag}_{cc,1} + F^{pretag}_{c,1} + F^{pretag}_{light,1}\right) \ , \tag{C.2}$$

$$N^{pretag}_{data\text{-}bkg,2} = N^{pretag}_{data\text{-}bkg,2}\left(F^{pretag}_{bb,2} + F^{pretag}_{cc,2} + F^{pretag}_{c,2} + F^{pretag}_{light,2}\right) \ . \tag{C.3}$$

The expected number of Tagged events with n jets in flavour sample Φ, ($N^{tag}_{\Phi,n}$), is a function of the number of PreTagged events (N^{pretag}_{n}), the fraction of events of flavour Φ, ($F^{pretag}_{\Phi,n}$) and the average event tagging probability ($P^{tag}_{\Phi,n}$) for each configuration:

$$N^{tag}_{\Phi,n} = N^{pretag}_{n} \cdot F^{pretag}_{\Phi,n} \cdot P^{tag}_{\Phi,n}. \tag{C.4}$$

The event tagging probability ($P^{tag}_{\Phi,n}$) is the fraction of all MC events in the PreTagged sample with configuration (Φ, n) that survive the tagging requirement (exactly 1 tag).

The tag probabilities are determined using the full ALPGEN W+jets MC sample for both electron and muon events. The number of Tagged data events after background subtraction in the 1-jet and 2-jet bin is:

$$N^{tag}_{data\text{-}bkg,1} = N^{pretag}_{data\text{-}bkg,1}\left(F^{pretag}_{bb,1}\cdot P^{tag}_{bb,1} + F^{pretag}_{cc,1}\cdot P^{tag}_{cc,1} + F^{pretag}_{c,1}\cdot P^{tag}_{c,1} + F^{pretag}_{light,1}\cdot P^{tag}_{light,1}\right) , \tag{C.5}$$

$$N^{tag}_{data\text{-}bkg,2} = N^{pretag}_{data\text{-}bkg,2}\left(F^{pretag}_{bb,2}\cdot P^{tag}_{bb,2} + F^{pretag}_{cc,2}\cdot P^{tag}_{cc,2} + F^{pretag}_{c,2}\cdot P^{tag}_{c,2} + F^{pretag}_{light,2}\cdot P^{tag}_{light,2}\right) . \tag{C.6}$$

In writing the full set of equations, certain assumptions must be made to combine the $c\overline{c}$ and $b\overline{b}$ fractions and extract the $b\overline{b}/c\overline{c}$, c, and light samples in the 1-jet bin. Examples include the following:

- F^{pretag}_{cc} is replaced by $k^{pretag}_{cctobb}\cdot F^{pretag}_{bb}$, where k^{pretag}_{cctobb} is the ratio between the $c\overline{c}$ fraction and the $b\overline{b}$ fraction.
- $F^{pretag}_{bb,1}$ is replaced by $k^{pretag}_{bb2to1}\cdot F^{pretag}_{bb,2}$, where k_{bb2to1} is the ratio of $b\overline{b}$ events in the 1 jet bin over the 2 jet bin.

In all such cases the K factors are determined using the full PreTagged MC sample. For PreTagged events with 1 jet in the final state:

$$\begin{aligned} N^{pretag}_{data\text{-}bkg,1} &= N^{pretag}_{data\text{-}bkg,1}\left(F^{pretag}_{bb,1} + k^{pretag}_{cctobb}\cdot F^{pretag}_{bb,1} + F^{pretag}_{c,1} + F^{pretag}_{light,1}\right) \\ &= N^{pretag}_{data\text{-}bkg,1}\left(k^{pretag}_{bb2to1}\cdot F^{pretag}_{bb,2} + k^{pretag}_{cctobb}\cdot k^{pretag}_{bb2to1}\cdot F^{pretag}_{bb,2} + k^{pretag}_{c2to1}\cdot F^{pretag}_{c,2} + k^{pretag}_{l2to1}\cdot F^{pretag}_{light,2}\right) , \end{aligned} \tag{C.7}$$

for Tagged events with 1 jet in the final state:

$$\begin{aligned} N^{tag}_{data\text{-}bkg,1} &= N^{pretag}_{data\text{-}bkg,1}\left(F^{pretag}_{bb,1}\cdot P^{tag}_{bb,1} + k^{pretag}_{cctobb}\cdot F^{pretag}_{bb,1}\cdot P^{tag}_{cc,1} + F^{pretag}_{c,1}\cdot P^{tag}_{c,1} + F^{pretag}_{light,1}\cdot P^{tag}_{light,1}\right) \\ &= N^{pretag}_{data\text{-}bkg,1}\left(k^{pretag}_{bb2to1}\cdot F^{pretag}_{bb,2}\cdot P^{tag}_{bb,1} + k^{pretag}_{cctobb}\cdot k^{pretag}_{bb2to1}\cdot F^{pretag}_{bb,2}\cdot P^{tag}_{cc,1}\right. \\ &\left. + k^{pretag}_{c2to1}\cdot F^{pretag}_{c,2}\cdot P^{tag}_{c,1} + k^{pretag}_{l2to1}\cdot F^{pretag}_{light,2}\cdot P^{tag}_{light,1}\right) , \end{aligned} \tag{C.8}$$

for PreTagged events with 2 jets in the final state:

$$N^{pretag}_{data\text{-}bkg,2} = N^{pretag}_{data\text{-}bkg,2}\left(F^{pretag}_{bb,2} + k^{pretag}_{cctobb}\cdot F^{pretag}_{bb,2} + F^{pretag}_{c,2} + F^{pretag}_{light,2}\right) , \tag{C.9}$$

and for Tagged events with 2 jets in the final state:

$$N^{tag}_{data\text{-}bkg,2} = N^{pretag}_{data\text{-}bkg,2}\left(F^{pretag}_{bb,2}\cdot P^{tag}_{bb,2} + k^{pretag}_{cctobb}\cdot F^{pretag}_{bb,2}\cdot P^{tag}_{cc,2} + F^{pretag}_{c,2}\cdot P^{tag}_{c,2} + F^{pretag}_{light,2}\cdot P^{tag}_{light,2}\right) \tag{C.10}$$

The tag counting method provides four equations and three unknown flavour fractions we want to measure from data: F^{pretag}_{bb}, F^{pretag}_{c} and F^{pretag}_{light}. This system can be

solved algebraically for the flavour fractions. The correction factors, K_{bb}, K_c, and K_{light}, for each W+jets flavour sample are then derived from these fractions. For example, the $b\overline{b}$ correction factor is defined as the number of $W + b\overline{b}$ events in data over the number of $W + c\overline{c}$ events in MC:

$$K_{bb} = \frac{N_{Wbb}^{pretag,data}}{N_{Wbb}^{pretag,MC}} \ , \tag{C.11}$$

and similarly for c and light. For 2-jet events this is:

$$K_{bb,2} = \frac{N_{Wbb,2}^{pretag,data}}{N_{Wbb,2}^{pretag,MC}} = \frac{F_{bb,2}^{pretag,data} \cdot N_{Wjets,2}^{pretag,data}}{F_{bb,2}^{pretag,MC} \cdot N_{Wjets,2}^{pretag,MC}} \ . \tag{C.12}$$

The correction factors for 1, 3 and 4 jet normalisations are derived from the 2-jet correction factors and the W+jets data and MC contributions:

$$K_{bb,i\text{-}jet} = \frac{F_{bb,2}^{pretag,data} \cdot N_{Wjets,i\text{-}jet}^{pretag,data}}{F_{bb,2}^{pretag,MC} \cdot (N_{Wbb,i\text{-}jet}^{pretag,MC} \cdot K_{bb,2} + N_{Wcc,i\text{-}jet}^{pretag,MC} + N_{Wc,i\text{-}jet}^{pretag,MC} + N_{Wlight,i\text{-}jet}^{pretag,MC})} \tag{C.13}$$

The values for these corrections for each systematic are given in the table C.1 for electron channel and C.2 for muon channel.

Systematic	SF	Rel Diff (%)	$K_{bb} = K_{cc}$	Rel Diff (%)	K_c	Rel Diff (%)	K_{light}	Rel Diff (%)
Nominal	0.992	0.000	1.135	0.000	1.423	0.000	0.887	0.000
Lepton reco. eff. up	0.964	-2.812	1.071	-5.677	1.466	3.045	0.887	0.029
Lepton reco. eff. down	1.022	2.959	1.195	5.279	1.386	-2.597	0.886	-0.109
Lepton energy reso. up	0.992	-0.014	1.131	-0.362	1.428	0.354	0.887	-0.056
Lepton energy reso. down	0.992	-0.006	1.149	1.189	1.403	-1.404	0.889	0.271
Lepton energy scale up	0.984	-0.797	1.139	0.308	1.415	-0.576	0.888	0.138
Lepton energy scale down	0.998	0.585	1.152	1.439	1.410	-0.898	0.887	0.046
Jet energy scale up	0.868	-12.533	1.427	25.703	1.349	-5.153	0.864	-2.570
Jet energy scale down	1.076	8.424	0.984	-13.342	1.446	1.651	0.904	1.949
$E_{\mathrm{T}}^{\mathrm{miss}}$: (cellout) up	0.988	-0.418	1.139	0.360	1.417	-0.389	0.888	0.059
$E_{\mathrm{T}}^{\mathrm{miss}}$: (cellout) down	0.993	0.061	1.135	-0.046	1.426	0.206	0.886	-0.074
$E_{\mathrm{T}}^{\mathrm{miss}}$: (pileup) up	0.991	-0.182	1.144	0.777	1.414	-0.621	0.888	0.081
$E_{\mathrm{T}}^{\mathrm{miss}}$: (pileup) down	0.993	0.052	1.152	1.508	1.401	-1.515	0.889	0.232
SF b-tag up	0.992	0.000	0.974	-14.175	1.492	4.857	0.896	1.029
SF b-tag down	0.992	0.000	1.321	16.362	1.343	-5.594	0.876	-1.192
SF c-tag up	0.992	0.000	1.085	-4.413	1.343	-5.600	0.912	2.818
SF c-tag down	0.992	0.000	1.188	4.647	1.516	6.519	0.859	-3.186
SF mistag up	0.992	0.000	1.122	-1.155	1.411	-0.795	0.891	0.502
SF mistag down	0.992	0.000	1.156	1.798	1.428	0.401	0.883	-0.487
JVF SF up	0.985	-0.783	1.108	-2.405	1.436	0.902	0.888	0.151
JVF SF down	1.001	0.826	1.158	1.992	1.412	-0.746	0.886	-0.122
Jet reconstrucction efficiency	0.992	-0.008	1.140	0.435	1.421	-0.128	0.887	-0.043
Jet energy resolution	0.956	-3.678	1.178	3.785	1.401	-1.530	0.886	-0.126
Z+jets norm. up	0.949	-4.414	1.204	6.044	1.432	0.629	0.875	-1.387
Z+jets norm. down	1.036	4.413	1.074	-5.378	1.411	-0.851	0.899	1.336
$t\bar{t}$ norm. up	0.989	-0.301	0.995	-12.377	1.516	6.563	0.888	0.083
$t\bar{t}$ norm. down	0.995	0.302	1.274	12.222	1.331	-6.464	0.886	-0.087
dibosons norm. up	0.992	-0.070	1.134	-0.075	1.423	0.004	0.887	0.013
dibosons norm. down	0.993	0.071	1.135	-0.001	1.423	0.044	0.887	-0.015
W+jets shape (iqopt3)	0.988	-0.431	1.133	-0.198	1.426	0.252	0.887	-0.043
W+jets shape: (ptjmin10)	0.984	-0.813	1.136	0.074	1.422	-0.046	0.887	0.001
QCD norm. up	0.946	-4.691	1.022	-9.963	1.466	3.066	0.895	0.845
QCD norm. down	1.039	4.691	1.237	8.987	1.385	-2.646	0.880	-0.804
Syst. Uncertainty	-	18.425	-	50.667	-	24.107	-	5.380
Stat. Uncertainty	-	0.394	-	9.828	-	6.104	-	0.248
Total Uncertainty	-	18.429	-	51.612	-	24.868	-	5.385

Table C.1: Overall W+jets normalisation scale factors (SF) and flavour fraction scale factors (K_i) for each systematic source of uncertainty for events with 2 jets in the electron channel.

Systematic	SF	Rel Diff (%)	$K_{bb} = K_{cc}$	Rel Diff (%)	K_c	Rel Diff (%)	K_{light}	Rel Diff (%)
Nominal	1.031	0.000	1.413	0.000	1.236	0.000	0.890	0.000
Lepton reco. eff. up	1.014	-1.622	1.385	-1.971	1.253	1.342	0.891	0.082
Lepton reco. eff. down	1.049	1.679	1.448	2.471	1.214	-1.796	0.889	-0.069
Lepton reso. eff: no scale	1.026	-0.477	1.399	-0.964	1.246	0.803	0.890	-0.004
Lepton reso. eff: ID up	1.031	-0.015	1.412	-0.093	1.237	0.070	0.890	-0.000
Lepton reso. eff: ID down	1.031	0.003	1.412	-0.054	1.235	-0.092	0.890	0.041
Lepton reso. eff: MS up	1.031	-0.019	1.413	0.021	1.235	-0.074	0.890	0.014
Lepton reso. eff: MS down	1.031	0.015	1.413	0.001	1.237	0.018	0.890	-0.005
Jet energy scale up	0.912	-11.541	1.741	23.215	1.137	-8.049	0.868	-2.442
Jet energy scale down	1.110	7.615	1.288	-8.820	1.253	1.307	0.903	1.521
$E_{\mathrm{T}}^{\mathrm{miss}}$: (cellout) up	1.027	-0.412	1.404	-0.662	1.249	1.018	0.889	-0.146
$E_{\mathrm{T}}^{\mathrm{miss}}$: (cellout) down	1.034	0.292	1.418	0.372	1.235	-0.107	0.889	-0.045
$E_{\mathrm{T}}^{\mathrm{miss}}$: (pileup) up	1.029	-0.236	1.421	0.556	1.227	-0.782	0.891	0.091
$E_{\mathrm{T}}^{\mathrm{miss}}$: (pileup) down	1.033	0.164	1.416	0.198	1.233	-0.312	0.890	0.061
SF b-tag up	1.031	0.000	1.260	-10.810	1.295	4.776	0.900	1.193
SF b-tag down	1.031	0.000	1.599	13.159	1.159	-6.242	0.878	-1.331
SF c-tag up	1.031	0.000	1.371	-2.997	1.160	-6.155	0.912	2.466
SF c-tag down	1.031	0.000	1.467	3.848	1.316	6.416	0.865	-2.743
SF mistag up	1.031	0.000	1.402	-0.812	1.223	-1.089	0.894	0.503
SF mistag down	1.031	0.000	1.429	1.124	1.245	0.721	0.886	-0.472
JVF SF up	1.023	-0.772	1.387	-1.855	1.247	0.836	0.892	0.204
JVF SF down	1.039	0.798	1.442	2.028	1.220	-1.331	0.889	-0.098
Jet reconstrucction efficiency	1.031	0.012	1.413	0.013	1.235	-0.107	0.890	0.022
Jet energy resolution	1.005	-2.574	1.385	-1.958	1.287	4.134	0.885	-0.597
Z+jets norm. up	1.008	-2.253	1.440	1.892	1.243	0.551	0.884	-0.605
Z+jets norm. down	1.054	2.254	1.388	-1.762	1.229	-0.591	0.895	0.586
$t\bar{t}$ norm. up	1.029	-0.255	1.302	-7.873	1.313	6.208	0.891	0.090
$t\bar{t}$ norm. down	1.034	0.255	1.523	7.786	1.161	-6.124	0.889	-0.093
dibosons norm. up	1.031	-0.064	1.413	0.012	1.235	-0.071	0.890	0.017
dibosons norm. down	1.032	0.064	1.413	-0.012	1.237	0.070	0.890	-0.017
W+jets shape (iqopt3)	1.030	-0.084	1.403	-0.681	1.253	1.347	0.888	-0.266
W+jets shape: (ptjmin10)	1.030	-0.166	1.402	-0.755	1.244	0.607	0.889	-0.077
QCD norm. up	1.024	-0.731	1.356	-4.028	1.233	-0.309	0.899	1.041
QCD norm. down	1.039	0.731	1.469	3.978	1.240	0.281	0.881	-1.021
Syst. Uncertainty	-	15.171	-	47.250	-	21.948	-	4.787
Stat. Uncertainty	-	0.333	-	6.085	-	5.743	-	0.200
Total Uncertainty	-	15.175	-	47.641	-	22.687	-	4.791

Table C.2: Overall W+jets normalisation scale factors (SF) and flavour fraction scale factors (K_i) for each systematic source of uncertainty for events with 2 jets in the muon channel.

C.1 Measurement of AFBT for each lepton channel

This appendix shows the results obtained in the electron and muon channel separately. This allows for a cross-check that the results obtained for the combined channel match with those for the individual channels.

C.1.1 Distortions of the angular distribution $\cos\theta^{\mathrm{T}}$

Figure C.1 shows the event selection efficiency as a function of $\cos\theta^{\mathrm{T}}$ for electrons and muons independently. As in the combined case, a strong suppression of events with $\cos\theta^{\mathrm{T}}$ values in the central region. The reason for this is the same as already discussed in Section 5.4.1.

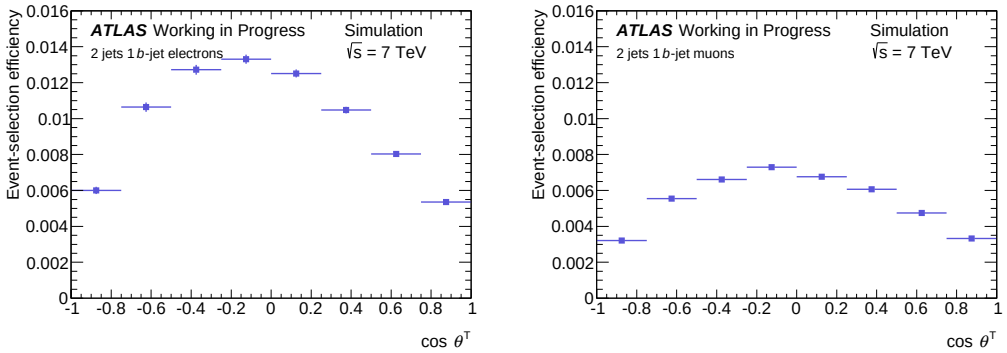

Figure C.1: Event selection efficiency as a function of $\cos\theta^{\mathrm{T}}$ for the electron (left) and the muon (right) channels.

Figure C.2 shows transfer matrix for two different $\cos\theta^{\mathrm{T}}$ (left) bins and probability migration matrix (right) for electrons (top) and muons (bottom). These plots are used to correct for the event reconstruction, i.e. for imperfect measurement of physics objects quantities due to detector acceptance or inefficiencies, the missing energy due to the neutrino and the reconstruction of the top quark.

C.1.1.1 Closure test

The closure test has also been performed for the electron and muon channel independently to check that the procedure is able to reproduce the distribution at generator level. The asymmetry values obtained for the MC signal at reconstructed level can be seen in Table C.3 and the angular distributions in Figure C.3. The resulting unfolded distribution and calculated asymmetries are compatible with the original ones within statistical uncertainties.

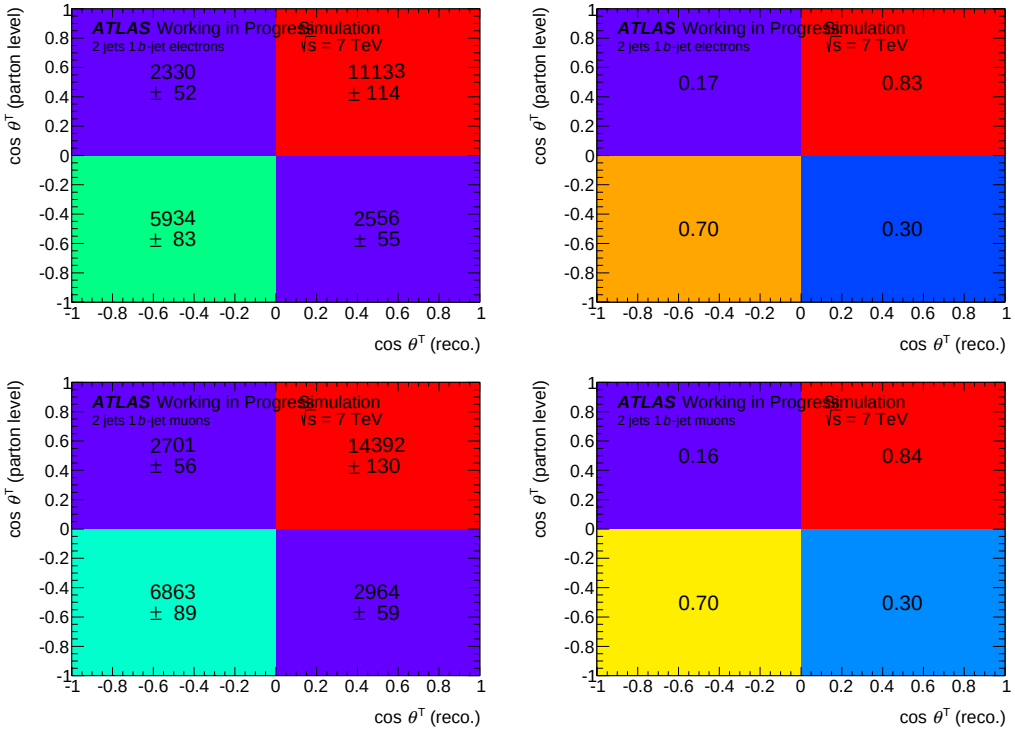

Figure C.2: Transfer matrix T_{ji} (left) and migration matrix M_{ji} (right) for electrons (top) and muons (bottom).

	Electron	Muon
	$A_{\mathrm{FB}}^{\mathrm{T}}$	$A_{\mathrm{FB}}^{\mathrm{T}}$
MC signal (raw)	0.247 ± 0.007 (stat.)	0.290 ± 0.006 (stat.)
MC signal (unfolded)	0.344 ± 0.010 (stat.)	0.345 ± 0.019 (stat.)

Table C.3: Measured value of A_{FB}^{T} for the closure test, obtained for the reconstructed t-channel signal events for electron and muon channel separately. The uncertainty is statistical only.

C.1.2 Unfolded data distribution

The resulting values A_{FB}^{T} are given in Table C.4 before and after background subtraction and after the unfolding for electron and muon channels individually. The unfolded value for the A_{FB}^{T} is showed in Figure C.4 for both channels.

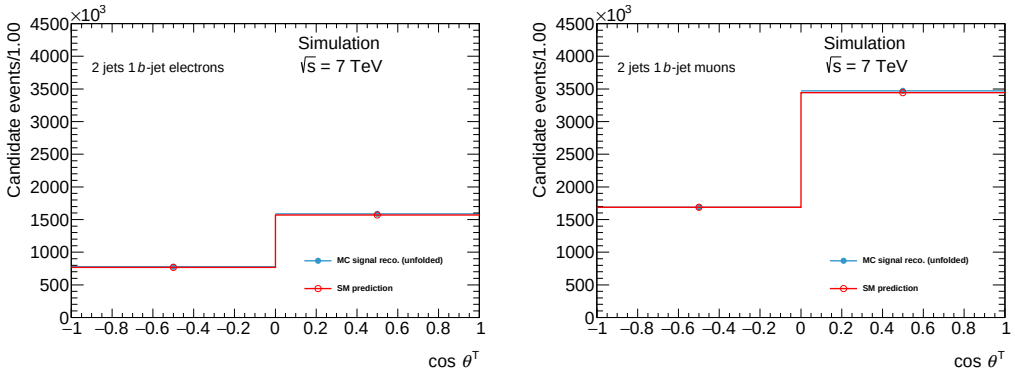

Figure C.3: Unfolded MC signal reconstructed angular distribution for the electron (left) and muon (right) channels.

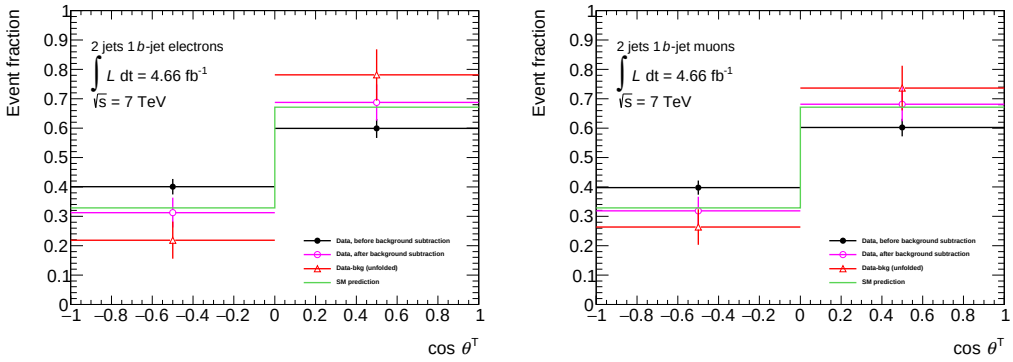

Figure C.4: Unfolded angular distribution for the electron (left) and muon (right) channels. The uncertainties are statistical only.

$A_{\mathrm{FB}}^{\mathrm{T}}$	electron	muon
Data (raw)	0.198 ± 0.041 (stat.)	0.204 ± 0.037 (stat.)
Data (raw, bkg. subtracted)	0.375 ± 0.080 (stat.)	0.363 ± 0.075 (stat.)
Data unfolded	0.562 ± 0.131 (stat.)	0.473 ± 0.120 (stat.)

Table C.4: Measurement of A_{FB}^{T} in the two jets channel for the electron and muon channel. Only the statistical uncertainties are shown.

Acronyms

AD Antiproton decelerator 28

ALICE A Large Ion Collider Experiment 28

ALPHA Antihydrogen Laser Physics Apparatus 25

ATLAS A Toroidal LHC Apparatus 7

BS Beam Spot 71

BT Barrel Toroid 35

CERN European Organization for Nuclear Research 25

CKM Cabibbo–Kobayashi–Maskawa 23

CLIC Compact Linear Collider 28

CL Confidence Level

CMS Compact Muon Solenoid 28

CNGS CERN Neutrinos to Gran Sasso 28

CoG Centre-of-Gravity 76

COMPASS Common Muon and Proton Apparatus for Structure and Spectroscopy 25

CS Central Solenoid 35

DAQ Data Acquisition and Computing 7

DCS Detector Control Systems 85

DOCA distance of closest approach 52

DoF degrees of freedom 52

ECT End-Cap Toroids 35

EDM Event Data Model 49

EDM Event Data Model 49

EW Electro Weak 7

FSI Frequency Scanning Interferometry 56

FWHM full width half maximum 95

GRL Good Run List 168

GUT Grand Unification Theory 19

HLT High Level Trigger 36

HQST InDetAlignHitQualSelTol 87

ID Inner Detector 7

Bibliography

[1] Donald Hill Perkins. *Introduction to high-energy physics; 4th ed.* Cambridge Univ. Press, Cambridge, 2000.

[2] K.A. Olive et al. Review of Particle Physics. *Chin.Phys.*, C38:090001, 2014.

[3] J. Goldstone. Field theories with superconductor solutions. *Il Nuovo Cimento*, 19(1):154–164, 1961.

[4] The ATLAS Collaboration. Observation of a new particle in the search for the standard model higgs boson with the {ATLAS} detector at the {LHC}. *Physics Letters B*, 716(1):1 – 29, 2012.

[5] The CMS Collaboration. Observation of a new boson at a mass of 125 gev with the {CMS} experiment at the {LHC}. *Physics Letters B*, 716(1):30 – 61, 2012.

[6] J.A. Aguilar-Saavedra and J. Bernabéu. W polarisation beyond helicity fractions in top quark decays. *Nucl. Phys.*, B840:349–378, 2010.

[7] Nikolaos Kidonakis. Next-to-next-to-leading-order collinear and soft gluon corrections for t-channel single top quark production. *Phys. Rev.*, D83:091503, 2011.

[8] Nikolaos Kidonakis. NNLL resummation for s-channel single top quark production. *Phys. Rev.*, D81:054028, 2010.

[9] Nikolaos Kidonakis. Two-loop soft anomalous dimensions for single top quark associated production with a W^- or H^-. *Phys. Rev.*, D82:054018, 2010.

[10] J. A. Aguilar-Saavedra. A minimal set of top anomalous couplings. *Nucl. Phys.*, B812:181, 2009.

[11] J. A. Aguilar-Saavedra. A minimal set of top-higgs anomalous couplings. *Nucl. Phys.*, B821:215, 2009.

[12] The ATLAS Collaboration. Measurement of top quark polarisation in $t\bar{t}$ events with the atlas detector in proton-proton collisions at $\sqrt{s} = 7\,\text{TeV}$. Sep 2012. ATLAS-CONF-2012-133.

[13] The ATLAS Collaboration. Measurement of the W boson polarization in top quark decays with the ATLAS detector. *JHEP*, 1206:088, 2012.

[14] G. Mahlon and S. Parke. Single Top Quark Production at the LHC: Understanding Spin. *Phys.Lett.*, B476:323–330, 2000.

[15] R. Schwienhorst, Q.-H. Cao, C.-P. Yuan and C. Mueller. Single top quark production and decay in the t-channel at next-to-leading order at the LHC. *Phys. Rev.*, D83:034019, 2011.

[16] C Lefevre. Lhc: the guide (english version). guide du lhc (version anglaise). Feb 2009.

[17] *LEP design report*. CERN, Geneva, 1984. Copies shelved as reports in LEP, PS and SPS libraries.

[18] The ALICE Collaboration. The alice experiment at the cern lhc. *Journal of Instrumentation*, 3(08):S08002, 2008.

[19] Bryan W. Lynn and Glenn D. Starkman. Chiral symmetry restoration, naturalness and the absence of fine-tuning i: Global theories, 2013.

[20] The ATLAS Collaboration. The atlas experiment at the cern large hadron collider. *Journal of Instrumentation*, 3(08):S08003, 2008.

[21] The CMS Collaboration. The cms experiment at the cern lhc. *Journal of Instrumentation*, 3(08):S08004, 2008.

[22] The LHCb Collaboration. The lhcb detector at the lhc. *Journal of Instrumentation*, 3(08):S08005, 2008.

[23] The LHCf Collaboration. The lhcf detector at the cern large hadron collider. *Journal of Instrumentation*, 3(08):S08006, 2008.

[24] The TOTEM Collaboration. The totem experiment at the cern large hadron collider. *Journal of Instrumentation*, 3(08):S08007, 2008.

[25] Performance of the ATLAS Inner Detector Track and Vertex Reconstruction in the High Pile-Up LHC Environment. Technical Report ATLAS-CONF-2012-042, CERN, Geneva, Mar 2012.

[26] J Bernabeu, J V Civera, M J Costa, C Escobar, J Fuster, C García, J E García-Navarro, F González, S González-Sevilla, C Lacasta, G Llosá, S Marti-García, M Miñano, V A Mitsou, P Modesto, J Nácher, R Rodríguez-Oliete, F J Sánchez, L Sospedra, and V Strachko. Atlas silicon module assembly and qualification tests at ific valencia. *Journal of Instrumentation*, 2(05):T05001, 2007.

[27] http://www.hep.man.ac.uk/atlas/bfield/index.html.

[28] F. Akesson, M.J. Costa, D. Dobos, M. Elsing, S. Fleischmann, et al. ATLAS Inner Detector Event Data Model. 2007.

[29] T Cornelissen, M Elsing, S Fleischmann, W Liebig, E Moyse, and A Salzburger. Concepts, Design and Implementation of the ATLAS New Tracking (NEWT). Technical Report ATL-SOFT-PUB-2007-007. ATL-COM-SOFT-2007-002, CERN, Geneva, Mar 2007.

[30] I Gavrilenko. Description of Global Pattern Recognition Program (XKalman). Technical Report ATL-INDET-97-165. ATL-I-PN-165, CERN, Geneva, Apr 1997.

[31] G. Aad et al. *Expected performance of the ATLAS experiment: detector, trigger and physics*. CERN, Geneva, 2009.

[32] A Andreazza, V Kostyukhin, and R J Madaras. Survey of the ATLAS Pixel Detector Components. Technical Report ATL-INDET-PUB-2008-012. ATL-COM-INDET-2008-006, CERN, Geneva, Mar 2008.

[33] S M Gibson, P A Coe, David Francis Howell, A Mitra, and R B Nickerson. Coordinate measurement in 2-D and 3-D geometries using frequency scanning interferometry. *Opt. Lasers Eng.*, 43:815–831, 2005.

[34] A Bocci and W Hulsbergen. TRT Alignment For SR1 Cosmics and Beyond. Technical Report ATL-INDET-PUB-2007-009. ATL-COM-INDET-2007-011. CERN-ATL-COM-INDET-2007-011, CERN, Geneva, Jun 2007.

[35] P Brückman, A Hicheur, and S J Haywood. Global chi2 approach to the alignment of the atlas silicon tracking detectors. Technical Report ATL-INDET-PUB-2005-002. ATL-COM-INDET-2005-004. CERN-ATL-INDET-PUB-2005-002, CERN, Geneva, 2005.

[36] Roland Härtel and Siegfried Bethke. *Iterative local Chi2 alignment approach for the ATLAS SCT detector*. PhD thesis, Munich, Tech. U., Nov 2005. Presented 28 Nov 2005.

[37] Tobias Göttfert and Siegfried Bethke. *Iterative local Chi2 alignment algorithm for the ATLAS Pixel detector*. PhD thesis, Wurzburg U., May 2006. Presented 26 May 2006.

[38] J. ALISON et al. Study of the systematic effects induced on tracking by the ATLAS Inner Detector alignment. Technical Report ATL-COM-INDET-2011-140, CERN, Geneva, Dec 2011.

[39] The ATLAS Collaboration. *Athena. The ATLAS Common Framework. Developer Guide*, 2004.

[40] O Brandt and P Bruckman de Rentstrom. Hit Quality Selection for Track-Based Alignment with the InDetAlignHitQualSelTool in M8+. Technical Report ATL-COM-INDET-2009-015, CERN, Geneva, May 2009.

[41] G. Aad et al. Charged-particle multiplicities in pp interactions at measured with the atlas detector at the lhc. *Physics Letters B*, 688(1):21–42, 4 2010.

[42] Georges Aad et al. Measurement of the Muon Charge Asymmetry from W Bosons Produced in pp Collisions at $\sqrt{s} = 7$ TeV with the ATLAS detector. *Phys.Lett.*, B701:31–49, 2011.

[43] Characterization of Interaction-Point Beam Parameters Using the pp Event-Vertex Distribution Reconstructed in the ATLAS Detector at the LHC. Technical Report ATLAS-CONF-2010-027, CERN, Geneva, May 2010.

[44] Performance of primary vertex reconstruction in proton-proton collisions at $\sqrt{s}$ =7 TeV in the ATLAS experiment. Technical Report ATLAS-CONF-2010-069, CERN, Geneva, Jul 2010.

[45] Performance of the ATLAS Secondary Vertex b-tagging Algorithm in 7 TeV Collision Data. Technical Report ATLAS-CONF-2010-042, CERN, Geneva, Jul 2010.

[46] Performance of Impact Parameter-Based b-tagging Algorithms with the ATLAS Detector using Proton-Proton Collisions at $\sqrt{\text{s}} = 7$ TeV. Technical Report ATLAS-CONF-2010-091, CERN, Geneva, Oct 2010.

[47] The ATLAS Collaboration. Commissioning of the atlas high-performance b-tagging algorithms in the 7 tev collision data. Jul 2011. ATLAS-CONF-2011-102.

[48] Electron and photon reconstruction and identification in ATLAS: expected performance at high energy and results at 900 GeV. Technical Report ATLAS-CONF-2010-005, CERN, Geneva, Jun 2010.

[49] Georges Aad et al. Electron performance measurements with the ATLAS detector using the 2010 LHC proton-proton collision data. *Eur.Phys.J.*, C72:1909, 2012.

[50] Alignment of the ATLAS Inner Detector Tracking System with 2010 LHC proton-proton collisions at $\sqrt{s} = 7$ TeV. Technical Report ATLAS-CONF-2011-012, CERN, Geneva, Mar 2011.

[51] The ATLAS Collaboration. Luminosity determination in *pp* collisions at $\sqrt{s} = 7$ TeV using the ATLAS detector at the LHC. May 2013.

[52] B. P. Kersevan and E. Richter-Was. The Monte Carlo Event Generator AcerMC versions 2.0 to 3.8 with interfaces to PYTHIA 6.4, HERWIG 6.5 and ARIADNE 4.1. *Comput. Phys. Commun.*, 184(3):919 – 985, 2013.

[53] A. Sherstnev and R. Thorne. Different PDF approximations useful for LO Monte Carlo generators.

[54] B. P. Kersevan, I. Hinchliffe. A Consistent Prescription for the Production Involving Massive Quarks in Hadron Collisions. *JHEP*, 0609:033, 2006.

[55] P. Nason. A new method for combining nlo qcd computations with parton shower simulations. *JHEP*, 11:040, 2004.

[56] H. Lai et al. New parton distributions for collider physics. *Phys.Rev.*, D82:074024, 2010.

[57] M.L. Mangano, M. Moretti, F. Piccinini, R. Pittau, A.D. Polosa. ALPGEN, a generator for hard multiparton processes in hadronic collisions. *JHEP*, 0307, 2003.

[58] J. Aguilar-Saavedra. Single top quark production at LHC with anomalous Wtb couplings. *Nucl. Phys.*, B804:160–192, 2008.

[59] T. Sjostrand, S. Mrenna, and P. Skands. PYTHIA generator version 6.418. *JHEP*, 05:026, 2006.

[60] The ATLAS Collaboration. New atlas event generator tunes to 2010 data. Apr 2011. ATL-PHYS-PUB-2011-008.

[61] Peter Z. Skands. Tuning monte carlo generators: The perugia tunes. *Phys. Rev.*, D82, 2010.

[62] G. Corcella et al. HERWIG 6.5: an event generator for Hadron Emission Reactions With Interfering Gluons (including supersymmetric processes). *JHEP*, 01:010, 2001.

[63] J. M. Butterworth, Jeffrey R. Forshaw, and M. H. Seymour. Multiparton interactions in photoproduction at HERA. *Z. Phys.*, C72:637–646, 1996.

[64] Michelangelo L. Mangano, Mauro Moretti, Fulvio Piccinini, and Michele Treccani. Matching matrix elements and shower evolution for top-quark production in hadronic collisions. *JHEP*, 0701:013, 2007.

[65] The ATLAS Collaboration. The atlas simulation infrastructure. *Eur. Phys. J.*, C70:823, 2010.

[66] The GEANT4 Collaboration. GEANT4: A simulation toolkit. *Nucl. Instrum. Meth.*, A506:205–303, 2003.

[67] M. Aliev, H. Lacker, U. Langenfeld, S. Moch, P. Uwer, et al. HATHOR: HAdronic Top and Heavy quarks crOss section calculatoR. *Comput. Phys. Commun.*, 182:1034–1046, 2011.

[68] C. Anastasiou, L. Dixon, K. Melnikov, F. Petriello. High-precision QCD at hadron colliders: electroweak gauge boson rapidity distributions at NNLO. *Phys.Rev.*, D69:094008, 2004.

[69] J.M. Campbell, R.K. Ellis, C. Williams. Vector boson pair production at the LHC. *JHEP*, 1107:018, 2011.

[70] The common parameters used for ATLAS MC production 2011. `https://twiki.cern.ch/twiki/bin/viewauth/AtlasProtected/McProductionCommonParametersMC1`.

[71] B et at. Acharya. Object selection and calibration, background estimations and mc samples for the autumn 2012 top quark analyses with 2011 data. (ATL-COMPHYS-2012-1197), August 2012.

[72] The ATLAS Collaboration. Measurement of the t-channel single top-quark production cross section in pp collisions at $\sqrt{s} = 7$ TeV with the ATLAS detector. *Phys.Lett.*, B717:330–350, 2012.

[73] The ATLAS Collaboration. Electron performance measurements with the ATLAS detector using the 2010 LHC proton-proton collision data. *Eur.Phys.J.*, C72:1909, 2012.

[74] The ATLAS Collaboration. Measurement of the mistag rate of b-tagging algorithms with 5 fb^{-1} of data collected by the atlas detector. Mar 2012. ATLAS-CONF-2012-040.

[75] The ATLAS Collaboration. Measurement of the b-tag efficiency in a sample of jets containing muons with 5 fb^{-1} of data from the atlas detector. Mar 2012. ATLAS-CONF-2012-043.

[76] K Becker, D Chakraborty, D Hirschbuehl, J Koll, R Schwienhorst, and C Suhr. Measurement of t-channel single top quark production cross section with *oldmathpp* collisions using a cuts-based approach. (ATL-COM-PHYS-2012-1430), Sep 2012.

[77] The ATLAS Collaboration. Mis-identified lepton backgrounds in top quark pair production studies for eps 2011 analyses. (ATL-COM-PHYS-2011-768), September 2011.

[78] The ATLAS Collaboration. Measurement of the t-channel single top-quark and top-antiquark production cross-sections and their ratio in pp collisions at $\sqrt{s} = 7$ tev. Jun 2012. ATLAS-CONF-2012-056.

[79] John M. Campbell, Rikkert Frederix, Fabio Maltoni, and Francesco Tramontano. Next-to-Leading-Order Predictions for t-Channel Single-Top Production at Hadron Colliders. *Phys. Rev. Lett.*, 102:182003, 2009.

[80] Georges Aad et al. Measurements of top quark pair relative differential cross-sections with ATLAS in pp collisions at $\sqrt{s} = 7$ TeV. *Eur.Phys.J.*, C73(1):2261, 2013.

[81] Top Systematic Uncertainties for Winter 2012 (rel17) 5 fb-1 analyses. `https://twiki.cern.ch/twiki/bin/viewauth/AtlasProtected/TopSystematicUncertainties2011`.

[82] M. Botje et al. The PDF4LHC Working Group Interim Recommendations. 2011.

[83] Top PDF Uncertainty Twiki. `https://twiki.cern.ch/twiki/bin/viewauth/AtlasProtected/TopPdfUncertainty`.

[84] Search for $\mathcal{CP}$ violation in single top quark events in pp collisions at $\sqrt{s} = 7$ TeV with the ATLAS detector. 2013.

[85] J. A. Aguilar-Saavedra. TopFit. `http://jaguilar.web.cern.ch/jaguilar/topfit/`.

[86] K. Nakamura et al. (Particle Data Group). Review of Particle Physics. *J. Phys. G*, 37:075021, 2010.

[87] The ATLAS Collaboration. Top Quark Mass Measurements. *ATL-PHYS-PUB-2009-043. ATL-COM-PHYS-2009-111*, 2009.

[88] Expected Performance of the ATLAS Experiment - Detector, Trigger and Physics. 2009.